

**Causes and Mechanisms of  
Remagnetisation in Palaeozoic  
Sedimentary Rocks - a Multidisciplinary  
Approach**

*Inaugural-Dissertation  
zur Erlangung des Doktorgrades  
an der Fakultät für Geowissenschaften der  
Ludwig-Maximilians-Universität München*

*vorgelegt von*  
Alexander Zwing

*4. Juli 2003*

1. Berichterstatter: Prof. Dr. V. Bachtadse
2. Berichterstatter: Prof. Dr. H.C. Soffel

Tag der mündlichen Prüfung: 13.11.2003

# Contents

List of Figures	vi
List of Tables	vii
Abbreviations	viii
Preamble	xi
Zusammenfassung	1
Summary	6
<b>I Introduction</b>	<b>10</b>
<b>1 Remagnetisations: Occurrence and processes</b>	<b>11</b>
1.1 The remagnetisation phenomena . . . . .	11
1.2 Physical mechanisms . . . . .	14
1.3 Chemical processes . . . . .	18
<b>2 Scope of this study</b>	<b>23</b>
<b>3 Methods</b>	<b>26</b>
3.1 Sampling . . . . .	26
3.2 Magnetic methods . . . . .	27
3.3 Clay geochemistry and geochronology . . . . .	28
3.4 Microscopy . . . . .	31
3.5 High gradient magnetic separation . . . . .	31
3.6 Leaching experiments . . . . .	34

<b>II Late Carboniferous Remagnetisation of Palaeozoic Rocks in the NE Rhenish Massif, Germany</b>	<b>41</b>
<b>4 Geology and Sampling</b>	<b>42</b>
4.1 Geological setting and palaeogeography . . . . .	42
4.2 Basin evolution . . . . .	43
4.3 Deformation and diagenesis . . . . .	44
4.4 Sampling area and sample description . . . . .	45
<b>5 Palaeomagnetism</b>	<b>49</b>
5.1 Demagnetisation experiments . . . . .	49
5.2 Tectonic correction and fold tests . . . . .	51
5.3 Interpretation of palaeomagnetic results . . . . .	55
<b>6 Magnetomineralogy</b>	<b>59</b>
6.1 IRM acquisition and demagnetisation . . . . .	59
6.2 Low temperature experiments . . . . .	60
6.3 Hysteresis measurements . . . . .	63
6.4 Viscosity and frequency dependence of susceptibility . . . . .	64
6.5 Interpretation of rock magnetic results . . . . .	66
<b>7 K-Ar dating and trace element geochemistry</b>	<b>69</b>
7.1 Characterisation of clay fractions . . . . .	69
7.2 K-Ar dating of the $< 0.2\mu\text{m}$ fractions . . . . .	73
7.3 Trace and REE geochemistry of the $< 0.2\mu\text{m}$ fractions and leachates	80
7.4 Interpretation of K-Ar ages of $< 0.2\mu\text{m}$ fractions and REE patterns of leachates . . . . .	84
<b>8 Discussion and Conclusions</b>	<b>86</b>
<b>III Dating of remagnetisation events in the Barrandian, Czech Republic and in the Holy Cross Mountains, Poland</b>	<b>90</b>
<b>9 Age of remagnetisation in the Barrandian</b>	<b>91</b>
9.1 Geology and sampling . . . . .	91
9.2 Palaeomagnetism . . . . .	93
9.3 Magnetomineralogy . . . . .	100
9.4 K-Ar dating and trace element geochemistry . . . . .	102
9.5 Discussion of results . . . . .	106

<b>10 Remagnetisations in the Holy Cross Mts.</b>	<b>108</b>
10.1 Geology and sampling . . . . .	108
10.2 Palaeomagnetism . . . . .	110
10.3 Magnetomineralogy . . . . .	116
10.4 K-Ar dating and trace element geochemistry . . . . .	118
10.5 Discussion of results . . . . .	121
<b>IV Final conclusions and implications of this study</b>	<b>123</b>
Bibliography	128
Acknowledgements	141
<b>Appendices</b>	<b>143</b>
A Samples	143
B Palaeomagnetic data	145
C Rock magnetic data	148
D X-ray diffraction data	150
E Geochemical data of clay fractions	152
F Geochemical data of leachates	156
Lebenslauf	159

# List of Figures

1.1	Global distribution of remagnetised Palaeozoic rocks . . . . .	12
1.2	Age of remagnetisation in Palaeozoic rocks . . . . .	13
1.3	Nomograms for magnetite and hematite . . . . .	15
1.4	SEM micrographs of magnetite spheres and pseudoframboids . . . . .	19
2.1	Position of the working areas . . . . .	24
3.1	High gradient magnetic separation device . . . . .	32
3.2	SEM micrograph of magnetic extracts from HGMS . . . . .	33
3.3	Anhyseretic susceptibility and $\text{Fe}_2\text{O}_3$ content of leachates . . . . .	36
3.4	Leaching of $\text{Fe}_2\text{O}_3$ and other oxides . . . . .	37
3.5	Ternary diagrams of cations K, Al, Si, and Ca, Fe, Mg in leachates . . . . .	38
3.6	HREE depletion and REE content versus Th and $\text{P}_2\text{O}_5$ . . . . .	39
4.1	Devonian to Permian palaeogeography . . . . .	43
4.2	Age of deformation in the Rhenish Massif and the Ardennes . . . . .	46
4.3	Geological map of the NE Rhenish Massif . . . . .	47
4.4	Sampling locations in the NE Rhenish Massif . . . . .	48
5.1	Thermal demagnetisation behaviour in orthogonal projection . . . . .	50
5.2	Structural correction of folds with inclined fold axes . . . . .	52
5.3	Fold test results . . . . .	53
5.4	Site mean directions in stereographic projection . . . . .	54
5.5	Anisotropy of magnetic susceptibility . . . . .	55
5.6	Palaeolatitudinal drift history of the NE Rhenish Massif . . . . .	56
6.1	IRM acquisition and thermal demagnetisation of a triaxial IRM . . . . .	60
6.2	Low temperature behaviour . . . . .	62
6.3	Characteristic hysteresis loops . . . . .	63
6.4	Hysteresis ratios $M_{rs}/M_s$ and $H_{cr}/H_c$ . . . . .	64
6.5	Magnetic viscosity of clastic and carbonate rocks . . . . .	65
6.6	$M_{rs}/M_s$ and the intensity decay across the Verwey transition . . . . .	66

7.1	Scanning and transmission electron micrographs . . . . .	71
7.2	Typical XRD patterns for clastic and carbonate rocks . . . . .	72
7.3	Illite crystallinity of $< 0.2\mu m$ and $0.2 - 2\mu m$ fractions . . . . .	73
7.4	K-Ar ages of clay fractions from four pilot samples . . . . .	74
7.5	K-Ar ages and illite crystallinity . . . . .	75
7.6	K-Ar isochrons for isotopic data from $< 0.2\mu m$ fractions . . . . .	77
7.7	Apparent K-Ar ages of $< 0.2\mu m$ fractions . . . . .	80
7.8	REE patterns of untreated $< 0.2\mu m$ fractions . . . . .	81
7.9	Correlation of REE and Fe in the leachates . . . . .	82
7.10	REE patterns of dithionite leachates . . . . .	83
7.11	Correlation of MREE-enrichment with Ba, $Fe_2O_3$ and $CaO + P_2O_5$ . . . . .	84
8.1	Diagenetic and deformation history of the NE Rhenish Massif . . . . .	87
9.1	Geological map of the Barrandian . . . . .	92
9.2	Thermal demagnetisation behaviour . . . . .	94
9.3	Poles of bedding planes in stereographic projection . . . . .	96
9.4	Fold tests results . . . . .	97
9.5	Site mean directions in stereographic projection . . . . .	98
9.6	Palaeolatitudinal drift history of the Barrandian . . . . .	100
9.7	Characteristic hysteresis curves . . . . .	101
9.8	Hysteresis ratios $M_{rs}/M_s$ and $H_{cr}/H_c$ . . . . .	102
9.9	SEM images of Fe-oxides . . . . .	103
9.10	K-Ar isochron and apparent ages of $< 0.2\mu m$ fractions . . . . .	105
9.11	REE patterns of untreated $< 0.2\mu m$ fractions and Fe-oxide leachates . . . . .	106
10.1	Geological map of the Holy Cross Mountains . . . . .	109
10.2	Thermal demagnetisation behaviour . . . . .	111
10.3	Fold test results . . . . .	113
10.4	Palaeopole positions with respect to the APWP for Baltica . . . . .	115
10.5	Characteristic hysteresis curves . . . . .	116
10.6	SEM images of Fe-oxides . . . . .	117
10.7	Illite crystallinity of $< 0.2\mu m$ and $0.2 - 2\mu m$ fractions . . . . .	119
10.8	K-Ar isochron and apparent ages of $< 0.2\mu m$ fractions . . . . .	120
10.9	REE patterns of untreated $< 0.2\mu m$ fractions and Fe-oxide leachates . . . . .	122

# List of Tables

5.1	Unit mean directions from the NE Rhenish Massif . . . . .	54
9.1	Unit mean directions from the Barrandian . . . . .	99
10.1	Unit mean directions from the Holy Cross Mts. . . . .	112
A.1	Sampling locations in the Barrandian and Holy Cross Mountains . . .	143
A.2	Sampling locations in the NE Rhenish Massif . . . . .	144
B.1	Site mean directions (Barrandian and Holy Cross Mountains) . . . .	146
B.2	Site mean directions (Rhenish Massif) . . . . .	147
C.1	Rock magnetic results (Rhenish Massif) . . . . .	149
D.1	Illite crystallinity . . . . .	150
D.2	XRD peaks and mineralogy . . . . .	151
E.1	Major element data of $< 0.2\mu\text{m}$ clay fractions . . . . .	152
E.2	K-Ar data of clay fractions . . . . .	153
E.3	Trace element data of $< 0.2\mu\text{m}$ clay fractions . . . . .	154
E.4	Rare earth element data of $< 0.2\mu\text{m}$ clay fractions . . . . .	155
F.1	Major element data of leachates . . . . .	156
F.2	Trace element data of leachates . . . . .	157
F.3	Rare earth element data of leachates . . . . .	158

# Abbreviations

$(^{40}\text{Ar}/^{36}\text{Ar})_{\text{ini}}$	initial $^{40}\text{Ar}/^{36}\text{Ar}$ ratio
$\alpha_{95}$	radius of cone of 95% confidence
<b>AF</b>	alternating field
<b>AS</b>	Attendorn syncline
<b>AMS</b>	anisotropy of magnetic susceptibility
<b>APWP</b>	apparent polar wander path
<b>ARM</b>	anhysteretic remanent magnetisation
<b>BSE</b>	backscattered electrons
<b>CAI</b>	conodont alteration index
<b>CGS</b>	Centre de Géochimie de la Surface, Strasbourg
<b>CNSC</b>	Cretaceous normal geomagnetic superchron
<b>CRM</b>	crystallisation remanent magnetisation
<b>Dec</b>	declination
$\delta$	density
<b>dm, dp</b>	semiaxes of oval of 95% confidence
<b>EDX</b>	energy dispersive x-ray spectroscopy
<b>fd</b>	full data fold test
<b>FWHM</b>	full width at half maximum
<b>GPMDB</b>	Global Palaeomagnetic Database
$H_c$	coercivity
$H_{cr}$	remanence coercivity
<b>HCM</b>	Holy Cross Mountains, Poland
<b>HGMS</b>	high gradient magnetic separation
<b>HREE</b>	heavy rare earth elements
<b>ICI</b>	illite crystallinity index
<b>Inc</b>	inclination
<b>io</b>	inclination only fold test
<b>IRM</b>	isothermal remanent magnetisation
<b>IRM<sub>RT</sub></b>	isothermal remanent magnetisation acquired at room-temperature
<b>IRM<sub>10K</sub></b>	isothermal remanent magnetisation acquired at 10K

<b>k</b>	FISHER (1953) precision parameter
<b>K<sub>1</sub></b>	axis of maximum susceptibility
<b>K<sub>2</sub></b>	axis of medium susceptibility
<b>K<sub>3</sub></b>	axis of minimum susceptibility
<b>k<sub>0</sub></b>	initial susceptibility
<b>k<sub>a</sub></b>	anhysteretic susceptibility
<b>k<sub>an</sub></b>	mass normalised anhysteretic susceptibility
<b>k<sub>f</sub></b>	ferromagnetic susceptibility
<b>k<sub>fd</sub></b>	frequency dependence of susceptibility
<b>ka</b>	thousand years
<b>Lat</b>	latitude
<b>Long</b>	longitude
<b>LREE</b>	light rare earth elements
<b>LS</b>	Lüdenscheid syncline
<b>μ</b>	magnetic permeability
<b>M</b>	magnetic moment
<b>M<sub>rs</sub></b>	saturation remanence
<b>M<sub>s</sub></b>	saturation magnetisation
<b>Ma</b>	million years ago
<b>MAD</b>	medium angle of deviation
<b>MD</b>	multi-domain
<b>MPMS</b>	Magnetic Properties Measuring System
<b>MREE</b>	middle-heavy rare earth elements
<b>MSWD</b>	mean square of weighted deviates
<b>My</b>	million years
<b>n</b>	number of specimens
<b>N</b>	number of samples yielding palaeomagnetic results
<b>N'</b>	number of site mean directions
<b>N<sub>o</sub></b>	number of samples obtained in the field
<b>NASC</b>	North American shale composite
<b>NL</b>	laboratory for rock- and palaeomagnetism of the University of Munich in Niederlippach
<b>NRM</b>	natural remanent magnetisation
<b>PCRS</b>	Permo-Carboniferous reversed geomagnetic superchron
<b>PLAT</b>	latitude of palaeopole
<b>PLONG</b>	longitude of palaeopole
<b>PRM</b>	piezo-remanent magnetisation
<b>PSD</b>	pseudo-single-domain

<b>pTRM</b>	partial thermal remanent magnetisation
<b>RA</b>	Remscheid anticline
<b>REE</b>	rare earth elements
<b>R<sub>max</sub></b>	vitronite reflectance
<b>S</b>	magnetic viscosity coefficient
<b>SD</b>	single-domain
<b>SE</b>	secondary electrons
<b>SP</b>	superparamagnetic
<b>SEM</b>	scanning electron microscope
<b>SIRM</b>	saturation isothermal remanent magnetisation
<b>STEM</b>	scanning transmission electron microscope
<b>t</b>	time period
<b><math>\tau</math></b>	relaxation time
<b>T</b>	temperature
<b>T<sub>b</sub></b>	blocking temperature
<b>T<sub>c</sub></b>	Curie-temperature
<b>T<sub>r</sub></b>	remagnetisation temperature
<b>T<sub>ub</sub></b>	laboratory unblocking temperature
<b>TEM</b>	transmission electron microscope
<b>TRM</b>	thermal remanent magnetisation
<b>V</b>	Volume
<b>VpTRM</b>	viscous partial thermalremanent magnetisation
<b>VSM</b>	vibrating sample magnetometer
<b>WS</b>	Wittgenstein syncline
<b>XRD</b>	X-ray diffraction

# Preamble

For this work, a variety of experiments and measurements were carried out in different laboratories. All palaeomagnetic experiments, IRM and ARM acquisition, IRM demagnetisation and anisotropy of susceptibility measurements were conducted at the laboratory for rock- and palaeomagnetism of the University of Munich in Niederlippach (NL). All other rock magnetic experiments (hysteresis curves, low temperature and viscosity measurements, frequency dependence of susceptibility) were carried out at the Institute for Rock Magnetism, University of Minnesota, Minneapolis. This visit was partly funded by a visiting fellowship to the Institut for Rock Magnetism. The preparation of clay minerals, their characterisation with electron microscopy and XRD and all isotopic and geochemical measurements of clay fractions and iron-oxides leachates were carried out in cooperation with Prof. Dr. N. Clauer and Dr. N. Liewig at the Centre de Géochimie de la Surface (CGS), Université Louis Pasteur, Strasbourg.

Parts of this thesis are based on, or directly taken from papers published, or to be published in scientific journals. Below, these papers are listed in order of their appearance in the text:

Zwing, A., Bachtadse, V. and Soffel, H.C., 2002, Late Carboniferous Remagnetisation of Palaeozoic Rocks in the NE Rhenish Massif, Germany, *Phys. Chem. Earth*, Vol. 27/25-31 pp. 61-70

Zwing, A., Rock magnetic properties of remagnetised Palaeozoic sediments from Middle and Eastern Europe, *The IRM Quarterly*, Winter 2001 - 2002, Vol. 11, No. 4, p. 8

Zwing, A., Matzka, J., Bachtadse, V., Soffel H.C., Rock magnetic properties of remagnetised Palaeozoic clastic and carbonate rocks from the NE Rhenish Massif, Germany, submitted to *Geophys. J. Int.*

Zwing, A., Liewig, N., Clauer, N., Bachtadse, V., K-Ar dating and trace element geochemistry of authigenic illites and Fe-oxide leachates from remagnetised sediments, NE Rhenish Massif, Germany, in preparation.

Some results of this work were presented as contributions to national and international meetings, which are listed in temporal order in the following. The abstracts are documented in the abstract volumes of the meetings.

Zwing, A., Bachtadse, V., Soffel, H.C., Liewig, N. und Clauer, N., 2000, Remagnetisierung von devonischen und unterkarbonischen Sedimenten des Rechtsrheinischen Schiefergebirges und ihre mögliche Ursache, 60. Jahrestagung der Deutschen Geophysikalischen Gesellschaft, München.

Zwing, A., Bachtadse, V., Liewig, N., Clauer, N. and Soffel, H.C., 2001, Remagnetisation of Paleozoic sediments in the NE Rhenish Massif and its possible causes, 26th General Assembly of the European Geophysical Society, Nice.

Zwing, A., Schätz, M., Bachtadse, V. and Tait, J.A., 2001, Paleomagnetism of Late Devonian carbonates in the Holy Cross Mountains, Poland: Trying to unravel the tectonic and magnetisation histories, American Geophysical Union Spring Meeting, Boston.

Zwing, A., Matzka, J., Bachtadse, V. and Soffel, H.C. Rock magnetic properties of remagnetised Devonian and Carboniferous carbonate and clastic rocks from the NE Rhenish Massif, Germany, 27th General Assembly of the European Geophysical Society, Nice.

Zwing, A., Liewig, N., Clauer, N. and Bachtadse, V. K-Ar dating and trace element geochemistry of authigenic illites and iron oxide leachates from remagnetised Palaeozoic sediments, NE Rhenish Massif, Germany, EGS-AGU-EUG Joint Assembly 2003, Nice.

# Zusammenfassung

In der vorliegenden Arbeit wurden die magnetischen und geochemischen Eigenschaften von remagnetisierten paläozoischen Gesteinen Mittel- und Osteuropas untersucht. Hierzu wurden paläomagnetische und gesteinsmagnetische Methoden mit der Mineralogie und Isotopie (K-Ar) von Tonmineralen und Geochemie (Seltene Erden) von Eisenoxiden kombiniert. Drei Arbeitsgebiete (Rheinisches Schiefergebirge, Barrandium und Heilig-Kreuz-Gebirge) wurden ausgewählt, in denen die Ursachen spätpaläozoischer Remagnetisierungen bisher noch ungeklärt waren. Die Ergebnisse liefern wichtige Informationen über die Prozesse und Mechanismen, die möglicherweise für die spätpaläozoischen Remagnetisierungen in den Arbeitsgebieten verantwortlich sind.

**Rheinisches Schiefergebirge:** In spätpaläozoischen Karbonaten und klastischen Gesteinen des nordöstlichen Rheinischen Schiefergebirges wird eine spätkarbonische Remagnetisierung (Komponente B) beobachtet. Drei regionale Falten-tests zeigen eine charakteristische Variation des Remagnetisierungsalters relativ zum Alter der Faltung. Im Süden des Arbeitsgebietes ist die Remagnetisierung älter als die Faltung, aber syntektonisch im Norden des rechtsrheinischen Schiefergebirges. Demnach wird der zeitliche Ablauf der Remagnetisierung durch das Alter der Faltung eingegrenzt, welches im Rheinischen Schiefergebirge die Migration der Deformationsfront von Süden nach Norden im Zeitbereich von 325 Ma bis 300 Ma reflektiert. Der Vergleich der resultierenden Paläobreite des Rheinischen Schiefergebirges mit der erwarteten paläogeographischen Driftgeschichte der Region ergibt ein Alter der Remagnetisierung von ca. 315 - 300 Ma, das mit dem Alter der Deformation vergleichbar ist. Die Übereinstimmung der Paläoinklination im gesamten Arbeitsgebiet deutet an, dass die Gesteine in einem relativ kurzen Zeitbereich von wenigen Millionen Jahren remagnetisiert wurden. Die thermische Stabilität der Remanenz bis 550 °C, die relativ niedrigen Paläotemperaturen im Arbeitsgebiet und die kurze Dauer des Remagnetisierungsereignisses implizieren einen chemischen Prozess der Remagnetisierung.

Gesteinsmagnetische Untersuchungen belegen die komplexe Mineralogie der magnetischen Träger in den remagnetisierten Gesteinen des Rheinischen Schieferge-

birges. Der wichtigste Träger der karbonischen Remagnetisierung ist Magnetit, während Pyrrhotit und Hämatit nur in einigen Karbonatgesteinen und in roten Sandsteinen sowie in roten Knollenkalken als Magnetisierungsträger auftreten. Die Hystereseeigenschaften, magnetische Viskosität und das Remanenzverhalten bei niedrigen Temperaturen der Karbonatgesteine deuten auf die Anwesenheit von sehr feinkörnigen (superparamagnetischen) magnetischen Mineralen hin. Dieses Material ist vermutlich auch für ähnliche gesteinsmagnetische Eigenschaften von siliziklastischen Gesteinen verantwortlich. Durch den großen Gehalt an detritischem MD-Magnetit und paramagnetischen Mineralen, ist diese Interpretation für die klastischen Gesteine allerdings nicht eindeutig. Während die Hystereseeigenschaften von mittel und grobkörnigen klastischen Gesteinen in das Feld von MD-Magnetit fallen, sind die Hystereseeigenschaften der biogenen Kalke charakteristisch für remagnetisierte Karbonate. Die Eigenschaften feinkörniger Klastika und Kalkturbidite liegen dazwischen. Dies deutet das Vorkommen von superparamagnetischem Magnetit in allen Lithologien an, die magnetische Signatur dieses sehr feinkörnigen Materials wird allerdings von MD-Magnetit in klastischen Gesteinen überdeckt. Die Anwesenheit von superparamagnetischem Material ist ein Hinweis für die Neubildung von magnetischen Mineralen und die Entstehung einer CRM.

Die K-Ar Datierungen von  $< 0.2\mu m$  Tonfraktionen deuten zwei diagenetische Ereignisse im nordöstlichen Rheinischen Schiefergebirge an. Die Beobachtung von K-Ar Isochronen schließt eine Kontamination mit detritischem Material oder den Verlust von radiogenem  $^{40}\text{Ar}$  aus. Mitteldevonische klastische Gesteine werden durch ein diagenetisches Ereignis bei  $336 \pm 6.2$  Ma charakterisiert, welches möglicherweise mit einem magmatischen Ereignis in der Mitteldeutschen Kristallinschwelle vor ca 340-330 Millionen Jahren in Zusammenhang steht. Die zweite Illitisation bei  $312 \pm 10$  Ma geschah zeitgleich mit der Deformation im nordöstlichen Rheinischen Schiefergebirge und wird nur in oberdevonischen und unterkarbonischen Gesteinen beobachtet. Dies deutet an, dass die metamorphen Bedingungen nicht ausgereicht haben, um die ältere Illitgeneration in den tiefer versenkten mitteldevonischen Gesteinen zu rekristallisieren. Das jüngere diagenetische Ereignis geschah zeitgleich mit der syn-tektonischen Remagnetisierung, die allerdings nicht auf die oberen Einheiten des Rheinischen Schiefergebirges beschränkt ist und auch die mitteldevonischen Sequenzen erfasst hat.

Die durch chemische Lösungsexperimente extrahierten Eisenoxide und andere leicht lösliche Minerale zeigen eine charakteristische Anreicherung an mittelschweren Seltenen Erden, die in den mitteldevonischen klastischen Gesteinen stärker ausgeprägt ist und mit dem Gehalt an Ba korreliert. Dies belegt, dass Ba während des älteren Diageneseereignisses mobilisiert wurde und vermutlich aus synsedimentären

mentären Baryt-Lagerstätten (SEDEX) stammt. Die jüngere Illitgeneration wird durch niedrigere Gd/La-Verhältnisse in den leicht löslichen Mineralen charakterisiert, die auf die Bildung von Eisenoxiden und Apatit mit flachen, NASC normalisierten Mustern der Seltenen Erden hinweisen. Die Muster der Seltenen Erden deuten daher die Überlagerung von zwei Mineralisationen unterschiedlichen Alters an. Zudem zeigen die Muster der Seltenen Erden Variationen in den Gehalten an Eu und Ce, was auf unterschiedliche Redox-Bedingungen in den untersuchten Lithologien hinweist. Von einer weiträumigen Migration orogener Fluide wird eher die Homogenisierung der geochemischen Signaturen leichtlöslicher Minerale erwartet. Daher kann eine weiträumige Fluidmigration nicht die Ursache der Remagnetisierung in Rheinischen Schiefergebirge gewesen sein. Im Gegensatz zu den oberdevonischen und unterkarbonischen Gesteinen, besteht für die mitteldevonischen Einheiten kein zeitlicher Zusammenhang zwischen Diagenese von Tonmineralen und Remagnetisierung. Die Umwandlung von Smectit zu Illit kann hier nicht die Ursache der Remagnetisierung sein. Da die Remagnetisierung und die Deformation im Rheinischen Schiefergebirge ein ähnliches Alter haben, könnte die Ursache der Remagnetisierung mit lokaler Drucklösung und Änderung des Porenwasserdruckes in Zusammenhang stehen.

**Barrandium:** Im Barrandium (Tschechische Republik) kann eine Remagnetisierung identifiziert werden, die vornehmlich von Magnetit getragen wird. Die Auswertung von Faltentests und der Vergleich der resultierenden Paläobreite mit der Polwanderkurve lässt keine eindeutige Interpretation zu. Aufgrund paläomagnetischer Ergebnisse kann die Remagnetisierung entweder während der Spätphase der variszischen Deformation im späten Devon oder lange nach der Faltung im späten Karbon erworben worden sein. Die K-Ar Alter der  $< 0.2\mu\text{m}$  Tonfraktionen weisen auf ein diagenetisches Ereignis um ca. 390 - 365 Ma hin. Dieses Zeitintervall ist beinahe identisch mit dem Alter der Deformation im Barrandium und die Illit-Diagenese steht vermutlich mit der Deformation in Zusammenhang. Die Muster der Seltenen Erden leicht löslicher Minerale zeigen eine charakteristische Anreicherung an mittelschweren Seltenen Erden, die mit dem Gehalt an Ba korreliert. Elektronenmikroskopische Untersuchungen zeigen Hinweise für die Oxidation von framboidalem Pyrit zu Magnetit in grauen spätsilurischen Kalksteinen und die Bildung von Eisenoxiden in roten devonischen Kalksteinen. Die Magnetit-Pseudoframboide bilden typische Paragenesen mit neugebildetem Illit. Da die Oxidation von framboidalem Pyrit eine mögliche Ursache für die Remagnetisierung sein kann, wird angenommen, dass die K-Ar Alter der Illite die Remagnetisierung auf den Zeitraum des späten Devons eingrenzen.

**Heilig-Kreuz Gebirge:** Die paläomagnetischen Ergebnisse von spätdevonischen Kalksteinen des Heilig-Kreuz Gebirges (Polen) lassen auf eine komplexe Remagnetisierungsgeschichte schließen. Zwei Remagnetisierungen wurden nach der Faltung im späten Paläozoikum (Komponente A) und im Mesozoikum (Komponente B) erworben. Eine dritte magnetische Komponente (C) ist syntektonischen Ursprungs. Obwohl die Magnetisierungen A und B sehr wahrscheinlich im späten Paläozoikum erworben wurden sind, ist eine exakte Bestimmung der Remagnetisierungsalter mit paläomagnetischen Methoden nicht möglich. Beide Komponenten der Magnetisierung werden von Magnetit getragen und elektronenmikroskopischen Untersuchungen belegen die Oxidation von framboidalem Pyrit zu Magnetit. Die triassische Remagnetisierung (C) wird von Hämatit getragen, der in Form sekundärer Bildungen in Hohlräumen beobachtet werden kann. Die K-Ar Alter und isotopengeochemische Zusammensetzung der  $< 0.2\mu\text{m}$  Tonfraktionen deuten eine Mischung unterschiedlicher Generationen von Schichtsilikaten an. Diese Ergebnisse können mit dem Vorkommen einer Illitgeneration, jünger als 290 Ma und ihrer Kontamination mit unterschiedlichen Mengen von älterem authigenem oder detritischem Material erklärt werden. Allerdings kann ein Verlust von radiogenem  $^{40}\text{Ar}$  nicht ausgeschlossen werden. Für ein besseres Verständnis der Diagenesegeschichte der spätdevonischen Kalksteine im Heilig-Kreuz Gebirge sind weitere Untersuchungen nötig.

**Remagnetisierungsprozesse:** Die Ergebnisse der vorliegenden Arbeit belegen die komplexe Natur der Prozesse und Mechanismen, die zu den Remagnetisierungen in den Arbeitsgebieten führten. Eine weiträumige Migration orogener Fluide wird als Ursache der weitverbreiteten Remagnetisierungen in paläozoischen Gesteinen Nordamerikas angenommen (z.B. STAMATAKOS *et al.*, 1996). Eine solche regionale Fluidmigration kann für das Rheinische Schiefergebirge ausgeschlossen werden und wird auch durch die Beobachtungen im Barrandium und Heilig-Kreuz-Gebirge nicht belegt. In den spätdevonischen und frühkarbonischen Gesteinen des Rheinischen Schiefergebirges könnten chemische Prozesse während der Umwandlung von Smectit in Illit zur Bildung von Magnetit und zur Remagnetisierung geführt haben. In den Kalksteinen des Barrandiums und Heilig-Kreuz-Gebirges belegen Magnetit-Pseudoframboide die Oxidation von Pyrit zu Magnetit als eine mögliche Ursache der Remagnetisierung. Die für diesen Prozess notwendigen Fluide könnten aus Porenwässern oder lokaler Fluidmigration auf Klüften oder Störungen stammen. In den mitteldevonischen Einheiten des Rheinischen Schiefergebirges erfolgten die Illitierung und die Remagnetisierung nicht zeitgleich und auch die Oxidation von Pyrit konnte nicht beobachtet werden. Ein möglicher Mechanismus der Remagnetisierung in diesen Einheiten könnte mit Drucklösung und der Veränderung des Porenwasser-

druckes während der Deformation in Zusammenhang stehen. Die mesozoischen Remagnetisierungen im Rheinischen Schiefergebirge und dem Heilig-Kreuz-Gebirge werden von Hämatit getragen. Sie wurden entweder durch Hämatit-Vererzungen während Hebungsphasen im Mesozoikum oder durch deszendente, oxidierende Fluide verursacht, die von der Verwitterungszone entlang Zonen erhöhter Wegsamkeiten in das Gestein eingedrungen sind.

# Summary

The present work combines palaeomagnetic and rock magnetic methods with clay mineralogy, isotope geochemistry of clay minerals and trace element geochemistry of Fe-oxide leachates to study remagnetised sedimentary rocks from Palaeozoic outcrops in Middle and Eastern Europe. Three areas were selected (NE Rhenish Massif, Barrandian and Holy Cross Mountains), where the causes of Late Palaeozoic remagnetisations are yet unclear. The results yield important implications for the processes and mechanisms responsible for the remagnetisations in the areas studied.

**NE Rhenish Massif:** A Late Carboniferous remagnetisation (component B) is identified in Late Palaeozoic carbonate and clastic rocks from the NE Rhenish Massif. Three individual incremental regional fold tests across the area show a unique and distinctive variation in timing of remagnetisation relative to the age of folding. The remagnetisation is postfolding in the South and of synfolding origin in the North of the area. Consequently, the timing and the duration of the remagnetisation event is constrained by the age of folding, which varies throughout the area and reflects a northward migration of the deformation front during 325 Ma to 300 Ma. Comparison of the resulting palaeolatitude of the NE Rhenish Massif with the palaeolatitudinal drift history for the region yields an estimate for the age of remagnetisation of ca. 315 - 300 Ma, which is in good agreement with the age of deformation. The concordance of the magnetic palaeoinclinations obtained from the entire area indicates that the rocks were remagnetised during a relatively short period of only a few My. The thermal stability of the remanence up to 550 °C, the comparably low palaeotemperatures in the studied region and the short duration of the remagnetisation event favour a chemical remagnetisation process.

Rock magnetic experiments reveal a complex magnetomineralogy of the remagnetised Palaeozoic sediments from the NE Rhenish Massif. The dominant carrier of the Carboniferous magnetisation component is magnetite, but pyrrhotite and hematite accompany magnetite as carrier of the NRM in some grey carbonates and red sandstones or red nodular limestones, respectively. The hysteresis ratios, magnetic viscosity and low temperature behaviour of the carbonate rocks give strong evidence for the presence of very fine grained (superparamagnetic) magnetic min-

erals. This material is also thought to be responsible for similar rock magnetic properties of siliciclastic rocks. This interpretation, however, is not unique for the siliciclastic rocks, due to the predominance of detrital MD magnetite and the high amount of paramagnetic material. The hysteresis ratios from medium to coarse grained rocks and reef carbonates fall in or close to the fields of MD magnetite and remagnetised carbonates, respectively. The fine grained clastic rocks (siltstones) and limestone turbidites have intermediate hysteresis properties. This implies the presence of very fine grained magnetic material in all lithologies of the NE Rhenish Massif, which is indicative for authigenic growth of magnetic minerals and formation of a CRM. However, the magnetic fingerprint of SP grains gets increasingly disguised with increasing amount of detrital MD magnetite in clastic rocks.

K-Ar dating of  $< 0.2\mu\text{m}$  clay fractions indicates two diagenetic events in the NE Rhenish Massif. The observation of K-Ar isochrons rules out contamination from detrital sources and preferential loss of radiogenic  $^{40}\text{Ar}$  from authigenic illites. Middle Devonian clastic rocks are characterised by an illitisation event at  $336 \pm 6.2$  Ma, which is probably connected to a major magmatic event at ca. 340 - 330 Ma in the Mid-German Crystalline Rise. The second period of illite formation at  $312 \pm 10$  Ma is coeval to the northward migration of deformation through the Rhenish Massif and is only recorded by Upper Devonian and Lower Carboniferous rocks. This indicates that the metamorphic conditions were not sufficient to recrystallise the earlier illite generation in the more deeply buried Middle Devonian rocks. The age of the younger illitisation event is not significantly different from the age of the pervasive, syntectonic remagnetisation. However, the remagnetisation event was not restricted to the upper part of the fold and thrust belt and also affected the Middle Devonian strata.

A characteristic enrichment in MREE is observed in Fe-oxide leachates, which is more pronounced in the Middle Devonian clastic rocks and which is correlated to the amount of Ba in the leachates. This indicates, that Ba was mobilised during the older diagenetic event and probably originates from synsedimentary (SEDEX), baryte-bearing deposits. The younger illite generation is characterised by lower Gd/La ratios in leachates, which are thought to reflect the formation of Fe-oxides and apatite with flat NASC normalised REE patterns. Consequently, the REE patterns of leachates indicate the interference of two mineralisations of different ages. Furthermore, the REE patterns from different samples show a variation of Eu and Ce, which indicates varying redox conditions in the lithologies studied. This is taken as evidence against a pervasive migration of orogenic fluids on a regional scale as a cause of remagnetisation in the NE Rhenish Massif. While a temporal relationship between clay diagenesis and remagnetisation is observed in Upper Devonian and

Lower Carboniferous rocks, the remagnetisation is not related to clay diagenesis in Middle Devonian rocks. Here, the transformation of smectite to illite cannot account for the growth of authigenic magnetic minerals, which must have been triggered by a different mechanism. Since the ages of remagnetisation and main deformation are generally similar, this mechanism could be related to localised pressure solution and changing pore fluid pressure due to tectonic stress. However, this raises the question, why the remagnetisation occurred during different stages of folding in the northern and southern parts of the NE Rhenish Massif.

**Barrandian:** In the Barrandian, Czech Republic, a remagnetisation is identified, which is predominantly carried by magnetite. Fold test analysis and comparison of the resulting palaeolatitude with the palaeomagnetic reference frame yields ambiguous results. Based on palaeomagnetic evidence, the remagnetisation event could have occurred during the late stage of the Variscan deformation in the Late Devonian or the remagnetisation could be postfolding in origin and of Late Carboniferous age. The apparent K-Ar ages of  $< 0.2\mu\text{m}$  fractions indicate a diagenetic event around 390 - 365 Ma. This age interval is almost identical with the age of deformation in the Barrandian and the illite diagenesis is likely to be related to the deformation. The REE patterns of Fe-oxide leachates show a distinct enrichment in MREE, which is generally correlated to the Ba-content. SEM studies indicate oxidation of framboidal pyrite to magnetite in grey Late Silurian limestones and the formation of Fe-oxides in red Devonian limestones. Magnetite pseudoframboids and authigenic illite form a characteristic parageneses. Since oxidation of framboidal pyrite is a possible mechanism of remagnetisation, the K-Ar ages of illite are thought to constrain the remagnetisation to be Late Devonian in age. The SEM studies also indicate, that authigenesis of magnetic minerals in red Devonian limestones is related to dissolution of baryte.

**Holy Cross Mountains:** The palaeomagnetic results from Late Devonian limestones from the Holy Cross Mountains, Poland, reveal a complex (re-)magnetisation history. Two remagnetisations are identified, which are postfolding in origin and were acquired in Late Paleozoic (component A) and Mesozoic (component C) times. A third component of magnetisation (B) yields synfolding results during fold test analysis. Although remagnetisations A and B are likely to be Late Palaeozoic in age, the exact timing of remanence acquisition remains unclear. Components A and B are carried by magnetite and SEM studies indicate the oxidation of framboidal pyrite to magnetite. The Triassic remagnetisation (C) resides in hematite, which is observed as secondary coatings of spherical pore spaces. The apparent K-Ar ages and isotopic compositions of  $< 0.2\mu\text{m}$  fractions indicate a mixture of different

generations of sheet silicates. These results can be explained by the presence of a illite generation younger than ca. 290 Ma years, which is contaminated by different amounts of detrital material (muscovite) or an older authigenic illite generation. However, diffusive loss of  $^{40}\text{Ar}$  from the illite crystal lattice subsequent to illite formation cannot be ruled out. Further studies are needed to better understand the diagenetic history of the Late Devonian limestones in the Holy Cross Mountains.

**Remagnetisation processes:** The results of this study imply, that the processes and mechanism responsible for the remagnetisations in the areas studied are rather complex. The regional migration of orogenic-type fluids, which is thought to be responsible for widespread remagnetisations in Palaeozoic rocks of the Hercynian realm of North America (e.g. STAMATAKOS *et al.*, 1996, and references therein), can be excluded for the NE Rhenish Massif and is not supported by the observations made in rocks from the Barrandian and the Holy Cross Mountains. Chemical changes associated with the smectite/illite transition could be responsible for the remagnetisation of Late Devonian and early Carboniferous rocks from the NE Rhenish Massif. In limestones from the Barrandian and the Holy Cross Mountains, the observation of pseudoframboidal magnetite indicates the oxidation of pyrite to magnetite as a possible remagnetisation mechanism. This process requires the presence of a fluid phase, which could originate from pore fluids or local migration of fluids on fractures and faults. In the Middle Devonian sequences of the NE Rhenish Massif the illite generation and the remagnetisation are not contemporaneous and oxidation of pyrite was not observed. Here, the remagnetisation must be related to a different mechanism. It can be speculated, that the remagnetisation mechanism in the Middle Devonian sequences could be related to pressure solution and changing pore fluid pressure during deformation. The Mesozoic remagnetisations in the NE Rhenish Massif and the Holy Cross Mountains are carried by hematite and are either related to hematite bearing mineralisation events during phases of uplift in the Mesozoic or caused by oxidising fluids percolating from the weathering surface and penetrating zones of enhanced permeability.

# Part I

## Introduction

# Chapter 1

## Occurrence and processes of remagnetisations

### 1.1 The remagnetisation phenomena

Since the first magnetic measurements on rocks in the beginning of the 20th century, palaeomagnetism has become a powerful method, which is widely-used in modern Earth Sciences. The identification and directional analysis of ancient magnetisation components is crucial for the reconstruction of the distribution of continents and oceans in the geological past and is invaluable to understand plate tectonic processes. Besides the data gathered by observatories in the past, the magnetic polarity and intensity record of sedimentary and volcanic rocks is the major foundation, upon which the knowledge of the mechanisms controlling the Earth's magnetic field is based. Consequently, the correct interpretation of age, intensity and direction of the magnetisation of rocks is of utmost importance.

One prerequisite for this task is the successful separation of different components of magnetisation. This has been promoted by analytical advances concerning stepwise demagnetisation, magnetometer sensitivity and data analysis techniques in the last decades. On the other hand, the understanding of the processes by which rocks become magnetised is equally important. These processes are reasonably well known for magnetisations, which were acquired during rock formation. However, the primary magnetic information can be partly or completely destroyed by a secondary magnetic overprint, acquired at any time after the formation of a rock. The processes controlling the acquisition of secondary magnetisations are still poorly understood.

Secondary magnetic overprints are observed in many different rock types, including all major sedimentary, magmatic and metamorphic lithologies. Rocks of all ages are affected, however, Proterozoic and Palaeozoic lithologies suffered remagnetisation events more prevalently than their younger equivalents. A query of the

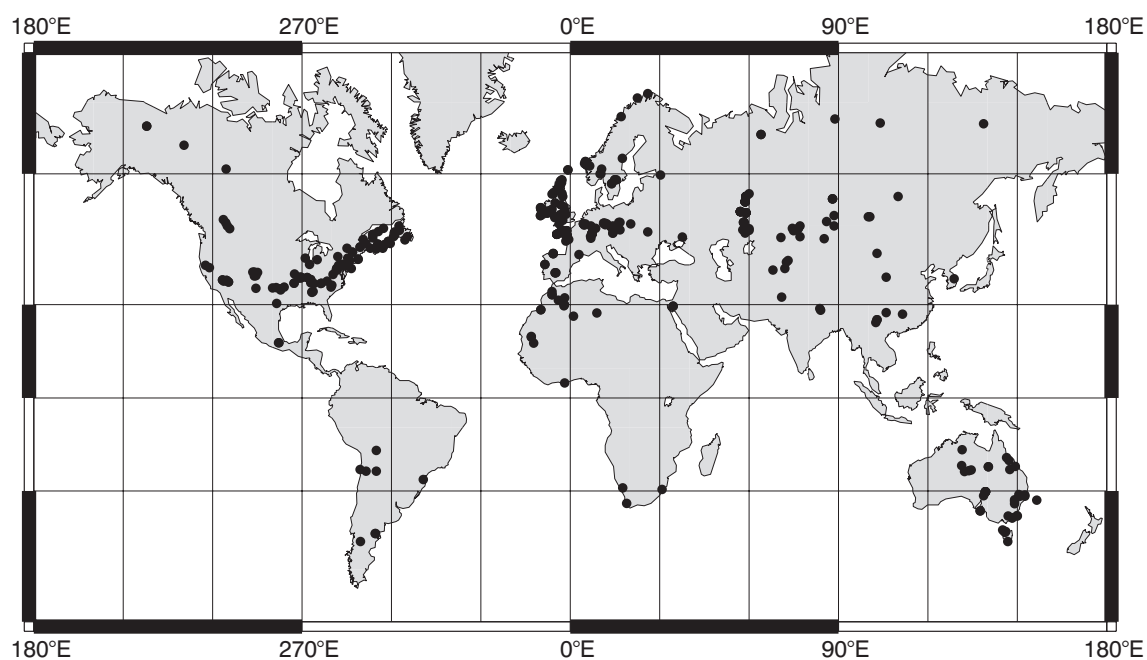


**Figure 1.1** Global distribution of remagnetised Palaeozoic rocks. Search results from the GPMDB 2000 (MCELHINNY & LOCK, 1990). The distribution roughly maps the occurrence of Palaeozoic rocks in the major orogenic belts.

Global Palaeomagnetic Database (GPMDB 2003, MCELHINNY & LOCK, 1990) for remagnetised Palaeozoic rocks yields more than 400 results. Their worldwide distribution (Fig. 1.1) roughly maps the distribution of major Palaeozoic orogenic belts and illustrates the widespread nature of remagnetisations in Pre-Triassic rocks.

The main handicap in the interpretation of secondary magnetic overprints is the uncertainty associated with the timing and duration of the remagnetisation event. Sophisticated sampling strategies allow the use of field test in order to determine the remagnetisation age relative to geological events, such as sedimentation hiatuses, intrusion of magmatic rocks or folding and tilting. However, up to now, the timing of remagnetisation is only estimated by comparing the directions of the magnetic components to existing palaeomagnetic data from the same crustal unit or terrane.

Besides the large uncertainties associated with those age estimates, the age distribution of the magnetic overprints (Fig. 1.2) reveals that 66% of the events recognised in Palaeozoic rocks occurred in the time interval from 350 Ma to 250 Ma. Within this time falls the climax of the Hercynian orogeny resulting in the final assembly of Pangaea. This coincides with the Permo-Carboniferous Reversed Geomagnetic Superchron (PCRS), a long period of reverse polarity of the Earth's magnetic field, which spans approximately 58 My from the Namurian to the Late Permian (OPDYKE & CHANNELL, 1996). Almost 90% of Late Palaeozoic remagnetisations yield a reversed polarity of the Earth's magnetic field. It is notable, that far less records

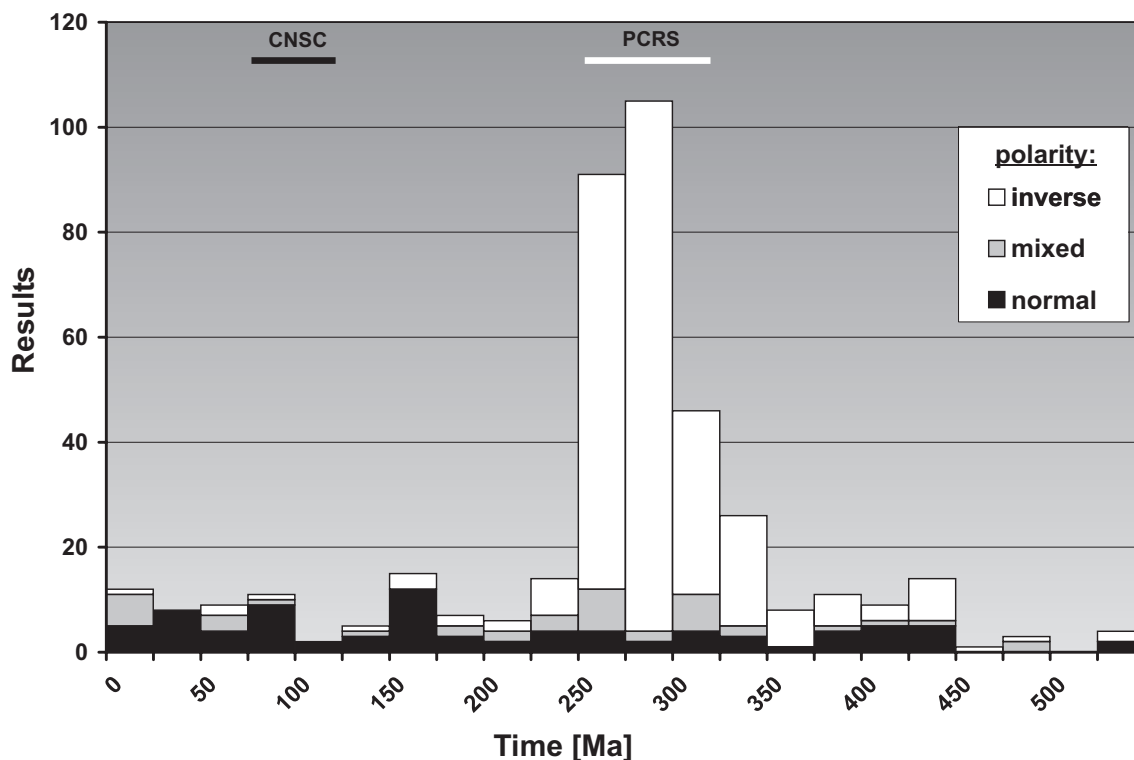


**Figure 1.2** Remagnetisation age in Palaeozoic rocks. The majority of Palaeozoic rocks were remagnetised during the Permo-Carboniferous reversed geomagnetic superchron (PCRS) and yield an inverse polarity of the Earth's magnetic field.

indicate the remagnetisation of Palaeozoic rocks during the Cretaceous Normal Geomagnetic superchron (CNSC, Fig. 1.2), suggesting a link between Late Palaeozoic orogenesis and remagnetisation.

Since the earliest identifications of magnetic overprints in the mid-1960s, it has been shown that remagnetisations are the rule rather than the exception in Palaeozoic rocks. However, the mechanisms responsible for this Late Palaeozoic remagnetisation event are still discussed rather controversially. Both, the long period of reverse polarity during the PCRS and the Hercynian orogeny are only two amongst a variety of factors that are thought to have caused Late Palaeozoic remagnetisation.

CREER (1964) was among the first to suspect a Late Palaeozoic remagnetisation event, when he recognised the similarity of many North American and European palaeopoles from Early Palaeozoic rocks with those of Late Palaeozoic age. He suggested, that the remagnetisation resulted from secondary iron oxides (hematite) in red beds, which formed during weathering, while Laurasia occupied the tropical weathering zone during Late Palaeozoic times (CREER, 1968). This early interpretation became known as the "remagnetisation hypothesis".

The general validity of the remagnetisation hypothesis was challenged when

MCELHINNY & OPDYKE (1973) reported a remagnetisation from the Ordovician Trenton Limestone (New York State, USA) with a direction similar to those from remagnetised North American red beds. Here, the carrier of magnetisation was shown to be magnetite, which could not have formed by oxidative weathering as proposed by CREER (1968). Later, VAN DER VOO & FRENCH (1977) related remagnetisations in orogenic belts to thermal and chemical processes during burial diagenesis, rather than to near-surface weathering.

Since the 1980s a large number of remagnetised rocks were studied in detail in order to better understand remagnetisation mechanisms. Two general types of processes can be distinguished: 1) physical processes, where the magnetisation of existing minerals is reset by temperature, its direction changed by rotational deformation or a new magnetisation imprinted by differential stress and 2) chemical processes, which cause the growth of new magnetic minerals and might dissolve existing magnetic grains.

## 1.2 Physical mechanisms

### 1.2.1 Thermoviscous remagnetisation

Temperature is one of the most important physical parameters, controlling magnetisation and magnetic properties of natural magnetic minerals. A single-domain (SD) grain of magnetite, cooled through its blocking temperature  $T_b$  in an external magnetic field ( $H_o$ ), will acquire a thermal remanent magnetisation (TRM).  $T_b$  is controlled by the chemical composition, the volume  $V$  and coercivity  $H_c$  of the grain. A large SD magnetite grain or an elongated grain with high  $H_c$  has a high  $T_b$ , while  $T_b$  is low for small, euhedral SD grains. The temperature, at which the TRM is demagnetised in the laboratory is called the unblocking temperature ( $T_{ub}$ ). For ideal SD magnetite and low external fields during TRM acquisition,  $T_b$  and  $T_{ub}$  are equal.

Natural rocks contain magnetic minerals in a wide variety of grain sizes and shapes, which can be described by a distribution of grain volume and coercivity. Consequently, a single-domain TRM of rocks has a spectrum of blocking temperatures and the total TRM equals the sum of partial thermal remanent magnetisations (pTRM), each carried by grain assembles with similar volume and coercivity.

While an individual SD grain is always magnetised to saturation, a population of identical SD grains can attain a state of zero magnetisation, in which the magnetic vectors of the individual grains are randomly oriented. This magnetic equilibrium is achieved by gradual relaxation of the initial magnetisation due to random thermal excitations. The relaxation time ( $\tau$ ) is the time an ensemble of SD magnetite grains

takes to reach the magnetic equilibrium. For small SD grains,  $\tau$  exceeds the age of the Earth at room temperature, but is reduced to a few minutes at several hundred °C.

Rocks, which are exposed to elevated temperatures (e.g. 300 °C) over long periods of time by regional metamorphism or other geological processes, will acquire a viscous partial thermoremanent magnetisation (VpTRM) carried by SD grains with a certain combination of  $T_b$  and  $\tau$ . Due to the much shorter time periods of the demagnetisation experiments, the  $T_{ub}$  of this VpTRM observed in the laboratory will be significantly higher than the maximum palaeotemperature (300 °C). The relationship between  $T_b$  at a time interval of geological length and  $T_{ub}$  during the demagnetisation experiment in the laboratory was first described by PULLAIAH *et al.* (1975) for magnetite and hematite, based on Neel's (1949) single-domain theory and is visualised in nomograms (blocking diagrams, Fig. 1.3). Lines on the diagrams connect combined temperature and relaxation time conditions that can unblock the magnetisation in a given population of SD grains. An equivalent relationship was reported for SD pyrrhotite by DUNLOP *et al.* (2000).

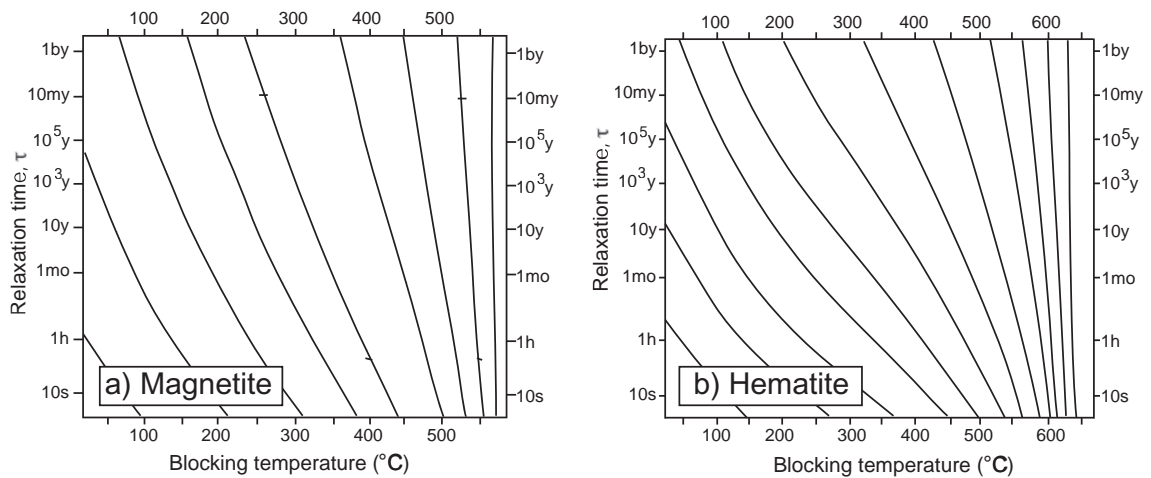


**Figure 1.3** Nomograms for a) magnetite and b) hematite. Lines on the diagrams connect combined temperature and relaxation time  $\tau$  conditions that can unblock the magnetisation in a given population of SD grains. Redrawn from PULLAIAH *et al.* (1975)

The nomograms (Fig. 1.3) illustrate, that the thermal stability of a TRM overprint depends on both, the remagnetisation temperature  $T_r$  and the duration of the time interval, during which the rocks were subjected to  $T_r$  and a small external field. A remagnetisation carried by SD magnetite with a  $T_{ub}$  of 350 °C in the laboratory could be caused by either the contact aureole of a magmatic dyke, which heated the sample to 250 °C for a couple of years or by deep burial, slightly above 150 °C for several My. Although palaeomagnetic and rock magnetic methods cannot differen-

tiate between the two processes, basin evolution or petrological studies of mineral thermometers can help to constrain the temperature history of remagnetised rocks.

In the Early Triassic Milton Monzonite of the Sydney Basin, Australia, pyrrhotite carries a well-studied example of a thermal remagnetisation. Here, the magnetic overprint records a heating event about 100 Ma ago. The inferred remagnetisation temperature corresponds well to results from vitrinite reflectance ( $R_{max}$ ) data and constrains the palaeotemperatures and the uplift history of the basin (DUNLOP *et al.*, 1997b, 2000). Frequently, the combination of low palaeotemperatures, indicated by CAI and  $R_{max}$  data and high  $T_{ub}$ , is taken as evidence against a thermal remagnetisation after comparison with the relevant blocking diagram (e.g. JACKSON *et al.*, 1988; ELMORE *et al.*, 1993).

However, since the PULLAIAH *et al.* (1975) nomograms are based on Néel's (1949) TRM theory, they are only valid for SD grains and cannot be applied to rocks with a complex grain-size distribution of magnetic minerals. A thermal activation model for grain-size distributions (WALTON, 1980) yields higher unblocking temperatures for a TRM than the model for SD particles. If the magnetic carriers obey Walton's (1980) theory, the palaeotemperatures, which are required for a thermal overprint are overestimated by the PULLAIAH *et al.* (1975) nomogram. This is the case for the remagnetised Devonian limestones in New York State (USA), where a thermal remagnetisation has been excluded on the basis of low palaeotemperatures and high  $T_{ub}$  of the remagnetisation component (KENT, 1985, and references therein). The  $T_{ub}$  of a postglacial, 10 ka old thermoviscous magnetic overprint in Devonian limestone cobbles from glacial deposits is higher than derived from the original PULLAIAH *et al.* (1975) nomogram and closer to the temperatures predicted by the blocking diagram from MIDDLETON & SCHMIDT (1982) based on Walton's (1980) theory. KENT (1985) suggested reconsidering the possibility of a thermal event as the origin of the Late Palaeozoic remagnetisation in the region. Since then, it has been recognised, that the estimation of palaeotemperatures based on  $T_{ub}$  is hampered by the presence of multi-domain (MD) grains. The  $T_{ub}$  of a TRM carried by e.g. MD magnetite is significantly higher than its  $T_b$  (DUNLOP & XU, 1994). As a result, the palaeotemperatures required for such a TRM are overestimated.

### 1.2.2 Long interval of constant geomagnetic polarity

The age distribution of remagnetisation events in Paleozoic rocks and the duration of the Permo-Carboniferous reversed superchron show a striking similarity (Fig. 1.2). This can be taken as an indication for a generic connection between long periods of constant polarities and magnetic overprints, as a thermoviscous remagnetisation over tens of My can be caused by relatively low palaeotemperatures. The  $T_{ub}$  of most

Late Palaeozoic remagnetisation components in carbonates is higher than 450 °C. Assuming the validity of Néel's (1949) theory in rocks, where SD magnetite is the dominating carrier of magnetisation, a thermal overprint requires palaeotemperatures above 300 °C over several tens of My. However, such temperatures are more typical for low regional metamorphic conditions and well above the palaeotemperatures recorded by both, CAI and  $R_{max}$  from the sections studied. Therefore, a long-lasting thermal remagnetisation event at low temperatures during the PCRS or the CNSC is rather unlikely.

On the other hand, the palaeomagnetic signature of a remagnetisation event which spans one or more reversals of the geomagnetic field is likely to be rather complex (CROUZET *et al.*, 2001). The correct interpretation of such a remagnetisation will be difficult or even impossible with standard palaeomagnetic methods. Consequently, magnetic overprints are more likely to be identified from time intervals with constant polarity of the Earth's magnetic field, while the processes responsible for remagnetisations might be connected to geological processes (e.g. orogeny), which were active throughout the geological history.

### 1.2.3 Stress and Strain

Pressure and deformation can change the magnetisation of a rock in various ways. Strain such as simple shear causes rotation of magnetic grains and their magnetic moments. In numerical models, the amount of rotation varies with the type of deformation (constant volume or volume loss, continuous or discontinuous deformation) and the way the magnetisation is treated: as a passive marker (like a pencil mark on the rock before deformation) or as a vector carried by rigid, mechanically active spheres (KODAMA, 1988). Although those extra granular effects do not remagnetise individual magnetic minerals, they change the direction of magnetisation and can rotate a prefolding magnetisation to appear synfolding in age.

Deformation experiments on artificial rock analogues demonstrate that magnetite and pyrrhotite grains are partly demagnetised by hydrostatic pressure and acquire a new piezo-remanent magnetisation (PRM) when exposed to high differential stress (BORRADAILE, 1994; ROBION & BORRADAILE, 2001). Such a PRM is thought to have remagnetised detrital Ti-magnetite in a Jurassic sandstone in the Wyoming-Idaho-Utah Thrust Belt during folding and movement upon thrust ramps (HUDSON *et al.*, 1989).

## 1.3 Chemical processes

### 1.3.1 Crystallisation remanent magnetisation

A crystallisation remanent magnetisation (CRM) is the result of the formation of a new magnetic mineral in the presence of a magnetic field. The commonly used term chemical remanent magnetisation is not always strictly accurate, as recrystallisation does not necessarily involve chemical changes (e.g. transformation of  $\gamma\text{Fe}_2\text{O}_3$  with spinel structure to rhombohedral  $\alpha\text{Fe}_2\text{O}_3$ ). Two different crystallisation processes can be distinguished, which are commonly caused by diagenesis, metamorphism or metasomatism.

Existing magnetic minerals can be altered by oxidation, reduction and dehydration processes or by a reorganisation of the crystal lattice during phase transformation. A well-known example for alteration of existing magnetic minerals is the low-temperature oxidation of titanomagnetite to titanomaghemite in ocean-floor basalts (e.g. MATZKA, 2001). During alteration, newly formed magnetic minerals acquire a magnetisation (two-phase CRM), with a direction, which is not necessarily parallel to the ambient field. In fact, the direction of the two-phase CRMs is frequently influenced by exchange coupling with the NRM of the primary magnetic phase. For example, after low temperature oxidation of titanomagnetite (by oxygen addition), the resulting CRM differs only in intensity from the initial magnetisation. The direction of magnetisation is not affected by the alteration (DUNLOP & ÖZDEMİR, 1997a, p. 374, and references therein). Other processes were found to produce intermediate directions of the external field and the parent remanence (e.g. oxidation of magnetite to hematite, HEIDER & DUNLOP, 1987). This makes the directional interpretation of those two-phase CRM rather difficult. However, many alteration processes require relatively high temperatures (300 °C - 600 °C), which exceed the maximum palaeotemperatures of many remagnetised sediments. Low-temperature oxidation of titanomagnetite starts soon after cooling of the magmatic rock and is usually completed when the magnetic minerals are introduced into the sedimentary cycle.

Probably more important for the remagnetisation of (very-low grade meta-) sediments is the precipitation and nucleation of new magnetic minerals. When those authigenic minerals grow beyond the superparamagnetic (SP) - SD threshold, they record the ambient geomagnetic field. During this process, the rocks acquire a grain-growth or single-phase CRM. Laboratory experiments have shown, that the single-phase CRM direction is always parallel to the direction of the ambient field (DUNLOP & ÖZDEMİR, 1997a, p. 372f and references therein). The authigenesis of magnetic minerals is often triggered by the presence of fluids, which are impor-

tant carriers for Fe-ions (often in form of Fe-complexes). However, fluids can also promote the dissolution of existing magnetic minerals and thus erase a pre-existing NRM.

### 1.3.2 Authigenic growth of magnetic minerals

Magnetic extracts of remagnetised Palaeozoic carbonates frequently contain magnetite spheres (Fig. 1.4a), which are consistent with a diagenetic origin and were first observed by MCCABE *et al.* (1983). However, the magnetic properties of those magnetite spherules suggest, that they resemble MD magnetite and are too large to record ancient magnetisations (XU *et al.*, 1994).

Scanning electron microscope (SEM) and scanning transmission electron microscope (STEM) investigations of magnetic extracts from remagnetised carbonates reveal the presence of pseudoframboidal magnetite (Fig. 1.4b), which formed by oxidation of framboidal pyrite (SUK *et al.*, 1990, 1993a; LU *et al.*, 1990). Additionally, aggregates of spherical magnetite grains about 200 nm in diameter were observed and the rock magnetic properties of the magnetic extracts suggest the presence of even smaller magnetic material with SP properties (SUK *et al.*, 1993a; SUN & JACKSON, 1994). Further evidence for the authigenic nature of magnetite is the cogenetic relationship between magnetite and other minerals known to be authigenic (dolomite, illite and K-feldspar), inclusions of authigenic minerals within magnetite, absence of Ti in magnetite and textural features, including spherical aggregates (SUK *et al.*, 1991).

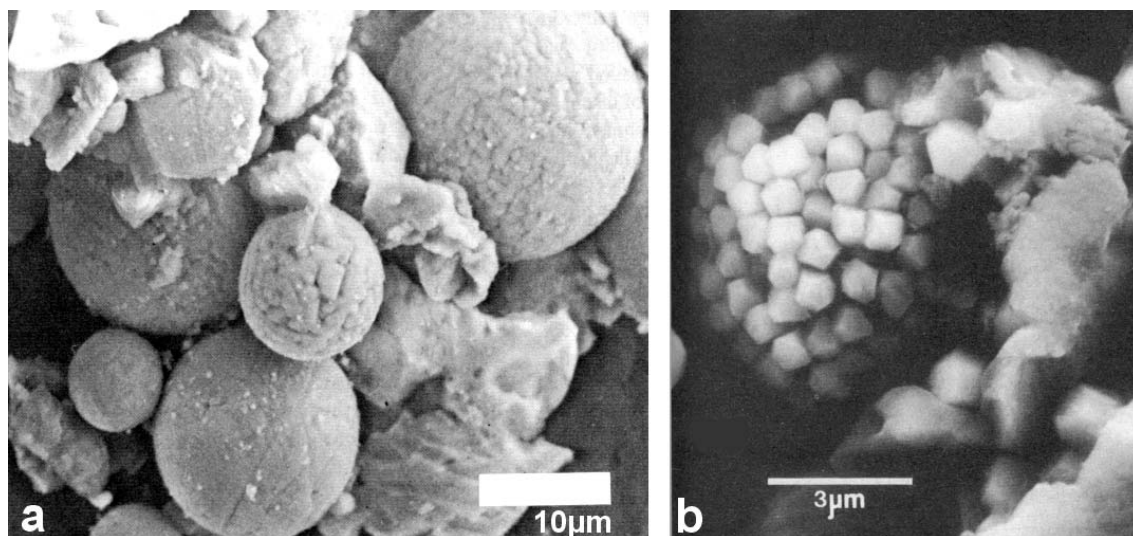


**Figure 1.4** Scanning electron micrographs of a) magnetite spheres extracted from a remagnetised Cambrian Dolomite (MCCABE *et al.*, 1983) and b) a magnetite pseudoframboid, where pyrite is replaced by magnetite (SUK *et al.*, 1993a).

The presence of very fine grained, authigenic magnetic material in many remagnetised carbonates is also indicated by distinct rock magnetic properties, such as unusually high hysteresis ratios and a high frequency dependence of susceptibility  $k_{fd}$  (JACKSON *et al.*, 1993). The high hysteresis ratios  $H_{cr}/H_c$  and  $M_{rs}/M_s$  are diagnostic for remagnetised Palaeozoic carbonates (MCCABE & CHANNELL, 1994). They indicate the presence of SP grains and SD magnetite dominated by magnetocrystalline anisotropy, which is characteristic for small euhedral magnetite grains (JACKSON, 1990).

Since the formation of authigenic magnetite generally involves dissolution of a precursor phase (e.g. pyrite, Fe-rich smectite) and crystallisation of magnetite, the presence of a fluid phase is required. The theoretical stability relations of iron oxides and sulphides in water are well known and the conversion from pyrite or Fe-rich smectite to magnetite was demonstrated experimentally (BROTHERS *et al.*, 1996; HIRT *et al.*, 1993). However, the origin and chemistry of the fluids involved is still a matter of debate.

### 1.3.3 Tectonically driven fluid flow

OLIVER (1986) postulated fluid migration during orogenesis from the foldbelts into the foreland and mid-continent, driven by plate tectonic processes. This hypothesis was based on hydrocarbon migration patterns, the distribution of Mississippi Valley type lead-zinc mineralisations, fluid inclusions and palaeomagnetic results from the Hercynian foldbelts of Eastern and Central North America. Further evidences for such a fluid flow event are the anomalous thermal history of shallow buried sediments, epigenetic dolomite deposits and the regional potassium metasomatism (BETHKE & MARSHAK, 1990). Thrusting and tectonic compression, sediment compaction or orogen topography could all have triggered fluid flow. Catastrophic release of heat from the crust by free convection, induced by fracturing and faulting related to continental collision was suggested to have maintained the fluid flow (DEMING, 1992). However, the mechanistic link between tectonic deformation and brine migration is poorly understood (BETHKE & MARSHAK, 1990).

A significant correlation between magnetite concentration and the amount of illite in the clay fraction was observed (JACKSON *et al.*, 1988) along a several hundred km long, east-west transect across New York State, USA. Both, magnetite content and degree of illitisation generally increase in the foreland (West) towards the fold and thrust belt in the East. Furthermore, the amount of magnetite is correlated with the K/Al ratio along this profile (LU *et al.*, 1991). As the K/Al ratio is thought to reflect the incorporation of exotic K from fluids into aluminosilicates during diagenesis, magnetite authigenesis seems to be connected to K-metasomatism

and is described by two chemical models (LU *et al.*, 1991):

1. Fe-bearing smectite + K-rich fluid  $\rightarrow$  illite-smectite + magnetite + quartz + fluids
2. Fe-bearing smectite + K-rich fluid  $\rightarrow$  K-feldspar + magnetite + quartz + fluids

Comparison of palaeopole positions from remagnetised Palaeozoic rocks of fold-belts in the Eastern and Central USA with a time averaged reference apparent polar wander path (APWP) for North America, yields remagnetisation ages of 255 - 275Ma (STAMATAKOS *et al.*, 1996). Fold tests suggest a rapid remagnetisation event: the magnetic overprint is postfolding in the hinterland, synfolding in the central fold and thrust belt and prefolding in the foreland (STAMATAKOS *et al.*, 1996). This constrains the timing of a proposed fluid flow event relative to the tectonic history and suggests that fluid migration was not directly related to the emplacement of individual thrust sheets.

Despite the general agreement between the fluid migration hypothesis and many observations from remagnetised rocks, some aspects remain unclear. This is best exemplified by a study on two Devonian lithologies from the Valley and Ridge Province, West Virginia, USA (ELMORE *et al.*, 2001). Here, a Late Palaeozoic magnetic overprint was observed in a profile with carbonate rocks in the lower part and clastic rocks at the top. While the sandstones carry evidence for extensive fluid flow and are regarded as a palaeoaquifer, the carbonate rocks show no sign of fluid alteration. This is supported by  $^{87}Sr/^{86}Sr$  values of calcite, which are coeval with respect to Early Devonian seawater (ELMORE *et al.*, 2001). Consequently, fluid flow caused remagnetisation of the sandstone, while another, yet unknown mechanism is responsible for the magnetic overprint in the carbonates.

### 1.3.4 Maturation of organic matter and clay diagenesis

A connection between magnetite authigenesis and hydrocarbon migration was proposed by SUK *et al.* (1993b) for Ordovician carbonates of the Michigan Basin, where the magnetite concentration and negative  $\delta^{13}C$  values of calcite are strongly correlated. The formation of magnetite and carbonates with negative  $\delta^{13}C$  values requires the presence of hydrocarbons within an oxidising diagenetic system. This can occur where hydrocarbons intermix with oxidising fluids. The Michigan basin is confined by arches that restrict the influx of fluids, which are unlikely to be of tectonic origin. Here, basinal brines, mixing with meteoric recharge are thought to have acted as oxidising fluids (SUK *et al.*, 1993b).

The timing of CRM acquisition in Early Carboniferous sediments from Colorado, USA, ranges from Late Palaeozoic to Cretaceous and coincides with the modelled

timing of organic matter maturation (BANERJEE *et al.*, 1997). Here, palaeomagnetic results from calcite veins precipitated during fluid migration, suggest that the magnetisation was not affected by exotic fluids. The remagnetisation is thought to be related to diagenetic reactions, such as maturation of organic matter during low to moderate burial temperatures (50 °C – 100 °C).

In a study of remagnetised Jurassic and Cretaceous sediments from the Vocontian Trough, SE France, KATZ *et al.* (2000) related a pre-Eocene remagnetisation event to the burial diagenetic alteration of smectite. Again, a contribution from orogenic-type fluids is unlikely, as  $^{87}\text{Sr}/^{86}\text{Sr}$  values and stable isotopes of carbon and oxygen show no evidence for alteration. Pore fluids are the possible origin for the fluid phase, which is required to trigger the formation of magnetite (SUK *et al.*, 1991). Studies by WOODS *et al.* (2002) on the Isle of Skye and results from GILL *et al.* (2002) on Cretaceous sedimentary rocks in NW Montana, USA also suggest a connection between magnetite authigenesis and smectite to illite conversion.

### 1.3.5 Weathering processes

Although it is clear by now that the Late Palaeozoic remagnetisation event itself was not caused by surficial weathering as proposed by CREER (1968), there are many examples, where weathering processes control the growth of magnetic minerals, in most cases hematite or goethite. The resulting remagnetisation is nonpervasive and connected to palaeosoils, erosional discordances or zones of increased permeability, such as karst or faults. An example of a remagnetisation caused by weathering in Late Carboniferous/Early Permian times and carried by hematite is described by NICK & ELMORE (1990) from a Cambrian dolomite in southern Oklahoma, USA.

# Chapter 2

## Scope of this study

As described in the previous section, several studies in the past have proposed a genetic link between remagnetisations and fluid flow on regional scales, hydrocarbon migration or clay diagenesis. The formation of authigenic mica-type sheet silicates is a common process during fluid triggered alteration or burial diagenesis. Although the isotopic and geochemical signatures of clay minerals can potentially constrain the timing of and conditions during such events, systematic investigations of clay minerals in remagnetised sedimentary rocks are rare. Furthermore, despite presence-absence tests of chemical remagnetisations and clay authigenesis, no direct evidence for the cogenetic growth of magnetic minerals and mica-type sheet silicates has yet been presented.

This work aims towards a better understanding of the diagenetic processes during remagnetisation events by combining the identification and rock magnetic characterisation of chemical remagnetisations with isotopic and geochemical studies on the authigenic clay minerals in the same sample material (for description of methods used see chapter 3, page 26ff). In order to do this, three areas were selected in Central and Eastern Europe (NE Rhenish Massif, Barrandian and Holy Cross Mountains, see Fig. 2.1), where Late Palaeozoic remagnetisations were reported from Palaeozoic rocks, in which the palaeotemperatures did not exceed very low-grade metamorphic conditions. The origin and mechanisms of the remagnetisations in the studied areas are as yet unclear.

A Late Palaeozoic remagnetisation was reported by BACHTADSE *et al.* (1983) and WILKEN (1995) overprinting the primary magnetic information in rocks from the NE Rhenish Massif. The geodynamic evolution and deformation history of the Rhenish Massif was subject of numerous studies in the past (e.g. AHRENDT *et al.*, 1983; ONCKEN *et al.*, 1999; PLESCH & ONCKEN, 1999; FRANKE, 2000, and references therein). Therefore, the Rhenish Massif was chosen as the main study area to test the combination of palaeomagnetism, rock magnetism and isotope geochemistry on

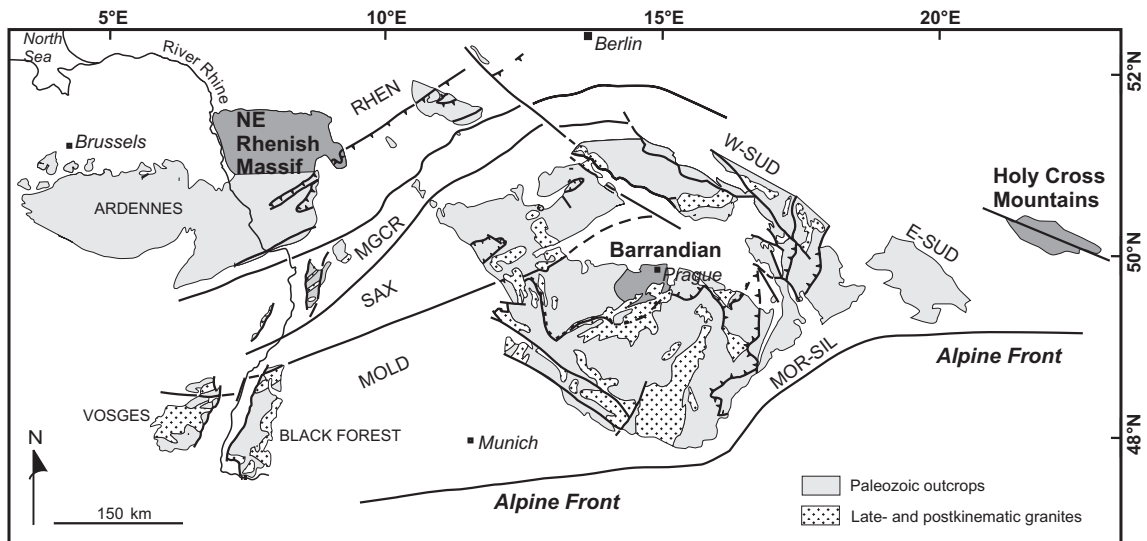


**Figure 2.1** Position of the studied areas (dark grey) in the Variscides of Middle and Eastern Europe. RHEN: Rhenohercynian, MGCR: Mid-German Crystalline Rise, SAX: Saxothuringian, MOLD: Moldanubian, MOR-SIL: Moravo-Silesian, W-SUD: Western Sudetes, E-SUD: Eastern Sudetes.

Middle Devonian to Early Carboniferous clastic and carbonate rocks.

In Silurian and Devonian carbonate and volcanic rocks of the Barrandian, Czech Republic, a secondary magnetisation event partly overprints Silurian carbonate and volcanic rocks (TAIT *et al.*, 1994b). While the Silurian remanence could still be separated from these sequences, the primary magnetisation is completely erased in the Devonian limestones from the same area (J. TAIT, unpublished data).

Multiple remagnetisations were reported from Devonian carbonate rocks in the western Holy Cross Mountains (HCM), Poland (GRABOWSKI & NAWROCKI, 2001, 1996, SCHÄTZ, unpublished data). Here, large-scale Variscan rotations are discussed to indicate a dextral strike-slip movement along the Trans-European Suture Zone (TESZ). Due to these possible rotations, comparison of palaeopoles with the apparent polar wander path (APWP) for Baltica is not possible. An independent age constraint of the magnetisations would yield important information about the tectonic evolution of the TESZ in the Late Palaeozoic.

This study includes various disciplines of geophysical and geochemical research, which were applied to samples from all studied areas. New palaeomagnetic results were obtained for detailed fold test analysis to constrain the remagnetisation age relative to the Variscan deformation. Rock magnetic measurements were carried out to identify the mineral carriers of magnetisation and authigenic magnetic minerals (magnetite) with superparamagnetic properties. The separation and characterisation of clay minerals was a crucial step for the preparation and selection of clay fractions for geochemical and isotopic (K-Ar) analysis. For comparison of geochem-

ical signatures of authigenic clay minerals and magnetic mineral, Fe-oxides were leached from clay fractions and analysed for trace and rare earth elements.

An important aim of this study is to contribute to the development of methods by which the age of remagnetisation can be constrained, if no palaeomagnetic reference frame (APWP) is available. Independent dating of remagnetisations would greatly enhance their use for palaeogeographical reconstructions and the interpretation of age and duration of tectonic events. In many cases, the dating of remagnetisation is difficult, even if an APWP is available. In orogenic belts, where local rotations about vertical axes are common, comparison of palaeopoles with the APWP relies heavily on the inclination information. However, if the palaeolatitudinal drift of studied orogenic belt was small in a certain time interval, comparison of palaeopoles with the APWP yields ambiguous results. This is the case for the Variscan/Hercynian belt in North America and Baltica for Late Devonian and Early Carboniferous times.

On the other hand, the palaeomagnetic reference frame is well constrained for many time intervals and areas. Once a direct genetic link between remagnetisation and diagenetic events has been identified, the age of diagenesis can be estimated with palaeomagnetic methods. This is of great interest, since palaeomagnetism is less time consuming and costly than separation and isotopic dating of authigenic clay minerals.

# Chapter 3

## Methods

In the course of this study, a wide variety of physical and chemical methods was applied to characterise the palaeomagnetic, rock magnetic, isotopic and chemical fingerprints of remagnetised rocks. A detailed description of the fundamental principals of the methods used is beyond the scope of this text. Generally, methods described in texts such as BUTLER (1992), DUNLOP & ÖZDEMİR (1997a), BRINDLEY & BROWN (1980) and CLAUER & CHAUDHURI (1995) have been used throughout this study. The following sections give more detailed information on sampling and sample preparation techniques, experimental parameters, data analysis. They also report the techniques used for clay mineral and iron oxide separation.

### 3.1 Sampling

Sampling locations (sites) were selected on different limbs of small and large scale folds to apply palaeomagnetic fold tests. Exposures with macroscopic evidence for fracturing, internal deformation (foliation) or weathering were not sampled. For palaeomagnetic and standard rock magnetic measurements, 5 to 15 cores of 2.54 cm diameter were drilled at each site with a petrol driven drill and oriented with a magnetic compass. Whenever possible, additional sun compass readings were taken to check for local magnetic declination. The cores were cut into 2.54 cm x 2.2 cm laboratory specimens. For clay and iron oxide geochemistry, hand samples or drill cores of 3.20 cm diameter were taken directly adjacent to the palaeomagnetic sampling locations.

## 3.2 Magnetic methods

### 3.2.1 Palaeomagnetic methods

Palaeomagnetic specimens were subjected to stepwise demagnetisation experiments. Thermal demagnetisation was carried out using two Schonstedt TSD-1 furnaces (residual fields less than 5nT), while for alternating field (AF) demagnetisation a 2G Enterprises AF demagnetiser was used. All measurements of remanent magnetisation were carried out using a 2G Enterprises DC-SQUID magnetometer which, together with the demagnetisation equipment, is housed in a magnetically shielded room in the laboratory for rock- and palaeomagnetism of the Department for Earth and Environmental Sciences, University of Munich in Niederlippach (NL).

The intensity of the initial natural remanent magnetisation of the specimens is generally in the range between  $10^{-3}$  A/m and  $10^{-4}$  A/m and well above the magnetometer's lower sensitivity level of about  $10^{-7}$  A/m. The magnetic susceptibility of the specimens was monitored after each heating step with a Minikappa KLF-3 (Geofyzika Brno). The sensitivity of the KLY-3 is sufficient to detect changes in susceptibility due to chemical alteration of the samples during heating.

The results of the demagnetisation experiments were plotted in orthogonal projection (ZIJDERVELD, 1967, Fig. 5.1). Linear segments and remagnetisation circle trajectories were identified by eye and subjected to principal component analysis (KIRSCHVINK, 1980). Linear segments and remagnetisation circles with median angle of deviation (MAD)  $> 15^\circ$  were excluded from further analysis. Mean site directions for great circle or combined great circle and stable endpoint data were determined using the algorithm given by MCFADDEN & MCELHINNY (1988).

### 3.2.2 Rock magnetic methods

Acquisition of the anhysteretic remanent magnetisation (ARM) and isothermal remanent magnetisation (IRM) to palaeomagnetic specimens (ca.  $11 \text{ cm}^3$ ) and thermal demagnetisation of a three component IRM at 0.12 T, 0.4 T and 2.6 T (LOWRIE, 1990) was carried out in NL. For ARM acquisition, small magnetic fields (10 nT - 40 nT) were applied with a DC-field coil in a alternating field of 150 mT. The anisotropy of magnetic susceptibility (AMS) was measured in NL on selected specimens with a KLY-2 KappaBridge (Geofyzika Brno). All other magnetomineralogical investigations were conducted at the Institute for Rock Magnetism (IRM), University of Minnesota. The hysteresis parameters of palaeomagnetic specimens were measured using a Vibrating Sample Magnetometer (VSM, Princeton Measurements). The VSM was also used to determine the ferromagnetic susceptibility and to monitor

the viscous decay of an IRM for 5 min. Since a finite time is needed to reduce the applied field of the VSM to zero, the remanence measurements were started 10s after IRM acquisition, allowing for 290s of measuring time. Smaller specimens (ca. 0.2 cm<sup>3</sup>) were prepared for low temperature experiments (10 K - 300 K) with a Magnetic Properties Measurement System (MPMS-XL5, Quantum Designs). The frequency dependence of susceptibility ( $k_{fd}$ ) of small specimens was determined using a Lakeshore Cryotronics susceptometer.

### 3.3 Clay geochemistry and geochronology

#### 3.3.1 Characterisation of illite formation

The formation of authigenic mica-type sheet silicates is a common process during very low-grade metamorphism of sedimentary and volcanic rocks. The thermally induced transition from mixed-layer illite-smectite to illite-mica has been studied many times in the last decades and serves as an indicator for very low-grade conditions (CLAUER & CHAUDHURI, 1999, and references therein). The crystallo-chemical changes during this transition involve changes of isotopic and geochemical signatures, which can be used to constrain the timing of and conditions during diagenetic events.

In order to study a specific diagenetic event, successful separation of the characteristic mineral generation is crucial to eliminate the contamination from other phases, such as detrital micas. In general, the probability of the presence of contaminating minerals is lower for the smallest grain size fractions. Therefore, the separation and characterisation of illite generations is a fundamental step in the proper selection of size fractions for isotopic analysis. The techniques and methods used for separation and characterisation of the samples for isotopic analysis are described in the following sections.

The preparation of clay fractions, their characterisation with electron microscopy and all isotopic and geochemical measurements on clay fractions and iron-oxide leachates were done in collaboration with N. Clauer and N. Liewig at the Centre de Géochimie de la Surface (CGS), Université Louis Pasteur, Strasbourg.

#### 3.3.2 Sample preparation

During preparation of clay fractions, great care was taken to prevent contamination with detrital minerals by overcrushing of the samples, dissolution of iron oxides and contamination with anthropogenic magnetic material. Hand samples or drill cores were cleaned with distilled water, dried and crushed using a hydraulic press to

produce 2-4 cm sized rock fragments, which were again cleaned with distilled water. Gentle disaggregation of the rock fragments using repetitive freezing-thawing cycles for three months (LIEWIG *et al.*, 1987) was tested on four pilot samples (ALB1, ATT1, HAC, LET). Due to the high degree of cementation and low permeability of the rocks studied, however, this disaggregation method was not successful. All samples were then carefully crushed in an agate hand mortar and a mortar grinder with agate grinding sets (Retsch RM 100).

Carbonate was dissolved using a buffered solution of sodium acetate and acetic acid, yielding a minimal pH of 4.5. The fraction, containing clay minerals  $< 2\mu\text{m}$  (in the following called " $< 2\mu\text{m}$  fraction") with a density of  $\delta = 2.6$  (e.g. illite) was extracted by repeated sedimentation in distilled water according to Stokes law. The  $0.2 - 2\mu\text{m}$  and  $< 0.2\mu\text{m}$  fractions were separated from a part of the  $< 2\mu\text{m}$  fraction by ultra high-speed centrifugation (overflow centrifuge) following the procedure described by LARQUE & WEBER (1978). The separated fractions were examined with a scanning electron microscope (SEM) for semiquantitative analyses and a transmission electron microscope (TEM) to assess the clay mineral morphologies and grain size distributions (see chapter 3.4).

### 3.3.3 Mineralogical investigation

The  $0.2 - 2\mu\text{m}$  and  $< 0.2\mu\text{m}$  fractions of all samples and the  $< 2\mu\text{m}$  fraction of selected samples were analysed with a Philips Sigma 2070 X-ray diffractometer from  $2.3^\circ$  to  $34^\circ 2\Theta$  (Co  $K_\alpha$ , 40 kV, Fe-filter,  $0.2-1^\circ$  slits). Smear samples were prepared on glass slides and analysed four times: (1) untreated, (2) after 12 hours in ethylene-glycol atmosphere for identification of mixed-layer minerals (e.g. illite-smectite), (3) after 4 hours at  $490^\circ\text{C}$  to destroy swelling layers in mixed-layer minerals, and (4) after 12 hours in hydrazine atmosphere to differentiate kaolinite from chlorite. The XRD patterns were recorded on paper with a Servogor XY 733 plotter.

The illite crystallinity index (ICI) was measured to evaluate diagenetic effects and very low-grade metamorphic effects. For quantification of the ICI, the Kübler index (KÜBLER, 1966) was used, which is defined by the full width at half maximum (FWHM) of the first illite basal reflection ( $10\text{\AA}$ ). Here, the FWHM was measured on plotter paper in mm with an accuracy of 0.5 mm. The diagenetic (non-metamorphic)/anchizone and anchizone/epizone boundaries for  $< 2\mu\text{m}$  air dried clay fractions are defined at 5.75 mm and 3.5 mm, respectively (LARQUE & WEBER, 1978). An ICI of 1mm equals  $0.1^\circ 2\Theta$ , Cu  $K_\alpha$ , however it should be noted, that the width of the  $10\text{\AA}$  peak depends on sample preparation and the experimental setup. Consequently, comparison with IC data from other laboratories should be treated with caution.

### 3.3.4 Chemical analyses

Major and trace elements, including rare earth elements (REE), were determined of very fine  $< 0.2\mu\text{m}$  fractions of all samples. Ca. 20 mg of untreated sample were dissolved first in a mixture of 4 ml 40 % HF and 14N HNO<sub>3</sub> for 36 hours at 100 °C and after evaporation of the acids in 0.5 ml 70% HClO<sub>4</sub> and 0.5 ml 14N HNO<sub>3</sub> for 24 hours at 100 °C. The dried material was dissolved in 1.5 ml HNO<sub>3</sub> and diluted with bidistilled water to 100ml in volumetric flasks. The solutions were then analysed by ICP-MS (JY124) and ICP-AES (VG PQ2+). The analytical uncertainty was controlled by determination of the BE-N (basalt, GOVINDARAJU & ROELANDST, 1993) and GL-O (glauconite, GOVINDARAJU, 1994) geostandards.

Potassium for the K-Ar age determinations was measured by atomic absorption spectroscopy using a Hitachi Z-8200, calibrated to an internal potassium standard solution. The reproducibility of the potassium determination was better than  $\pm 1.5\%$ .

REE concentrations in the  $< 0.2\mu\text{m}$  fractions and in leachates were normalised using the North American shale composite (NASC), given by MCLENNAN (1989). The Eu and Ce anomalies were calculated by comparison with the arithmetic means of the normalised values of the neighbouring elements (Eu\*, Ce\*, TAYLOR & MCLENNAN, 1985). The analytical error of the REE concentrations in the NASC is considered small relative to that of the investigated samples (10%) and is neglected. Consequently, the maximum relative error for the Ce/Ce\* and Eu/Eu\* ratios is about 20% and samples with ratios between 0.8 and 1.2 yield no Ce or Eu anomalies.

### 3.3.5 Geochronology

Ar isotope determinations for K-Ar ages were performed on  $0.2 - 2\mu\text{m}$  and  $< 0.2\mu\text{m}$  fractions of all samples and the  $< 2\mu\text{m}$  fraction of the pilot samples following a procedure close to that described by BONHOMME *et al.* (1975). The samples were preheated to 80 °C for several hours to reduce the amount of atmospheric argon absorbed by the clay mineral surfaces during sample preparation. After fusion of the sample by a radio frequency induction coil at temperatures up to 1600 °C, the released gas was led through a Pyrex line with high-vacuum metal valves beyond a Cu<sub>2</sub>O and TiO<sub>2</sub> getter for purification of the noble gases. After addition of a <sup>38</sup>Ar spike aliquot, the argon isotope ratios were measured on a VG1200 mass spectrometer and corrected for blank and mass discriminations. The results were controlled by repetitive analysis of the GL-O standard (ODIN, 1976) which averaged  $24.67 \pm 0.18 \times 10^{-6} \text{cm}^3/\text{g STP}$  ( $2\sigma$ ) of radiogenic <sup>40</sup>Ar for 12 determinations. The atmospheric <sup>40</sup>Ar/<sup>36</sup>Ar ratio was also measured periodically and averaged  $300.8 \pm 7.9$ .

K-Ar ages are calculated using the formula of COX & DALRYMPLE (1967) with the decay constant recommended by STEIGER & JÄGER (1977). The errors during sample weighting,  $^{38}\text{Ar}/^{36}\text{Ar}$  and  $^{40}\text{Ar}/^{38}\text{Ar}$  measurements and  $\text{K}_2\text{O}$  analysis were taken into account for calculation of age uncertainties. K-Ar isochrons were calculated using the software package Isoplot (v. 2.49), provided by K. Ludwig (LUDWIG, 2001). Whenever reasonable, the algorithm given by YORK (1969) was used for error estimation. This method weights the data points proportional to the inverse square of the scatter, assuming that the assigned analytical errors are the only reason for the observed scatter. However, considering the natural inhomogeneity of sediments, isochrons were also calculated from data, where analytical errors are obviously not the only reason for the observed scatter. In this case, equal weights and zero error-correlation is assigned to each data point. The isochron errors are given as 95%-confidence errors.

### 3.4 Microscopy

Polished thin sections were prepared from all samples and observed under transmitted and reflected light to identify the main rock-forming minerals as well as sufficiently large ( $> 10\mu\text{m}$ ) ferromagnetic minerals of detrital origin.

After coating with carbon, polished thin sections and freshly broken rock fragments were studied in secondary mode using a SEM (JEOL JSM 840, equipped with a energy dispersive X-ray analyser, TRACOR 5500). The morphology, composition and distribution of authigenic clay minerals and their genetic association with authigenic ferromagnetic grains was investigated with secondary electrons (SE). For detection of very fine grained iron oxides (magnetite, hematite) and iron sulphides (pyrite, pyrrhotite), imaging of density sensitive backscattered electrons (BSE) was used. The SEM was also applied to determine the composition of magnetic concentrates (see chapter 3.5).

Clay fractions and fine grained material released from rock fragments by ultrasonic treatment of rock fragments were studied with TEM (PHILIPS CM12) to characterise the morphologies of clay minerals and the grain-size distributions of clay fractions.

### 3.5 High gradient magnetic separation

Magnetic minerals were separated from nonmagnetic matrix material using the high gradient magnetic separation (HGMS) technique (HILLIER & HODSON, 1997, and references therein). This method allows separation of relatively large amounts of

magnetic material, which is required for chemical analyses ( $> 10$  mg). The HGMS technique is significantly faster than the separation methods, were the material is forced to pass along a permanent magnet (VON DOBENECK, 1985; MCCABE *et al.*, 1983). This requires the circulation of the sample in aqueous suspension for several days up to one week, enhancing the possibility of chemical alteration (oxidation) of the magnetic minerals (R. LØVLIE, pers. comm.).

A HGMS device was designed in the Department for Earth and Environmental Sciences in Munich following the experimental setup by HILLIER & HODSON (1997). The device consists of a funnel connected to a glass tube, which passes vertically between the poles of an electromagnet ( $H_{max} = 650$  mT) and is connected to a separation flask via a silicon tube (Fig. 3.1). The funnel, tubes and flask are filled with a standing column of distilled water. The glass tube contains an irregularly wound wire of a magnetically highly permeable material ( $\mu_{max} = 4.5 \cdot 10^5$ ), which is held in place by the magnetic field.

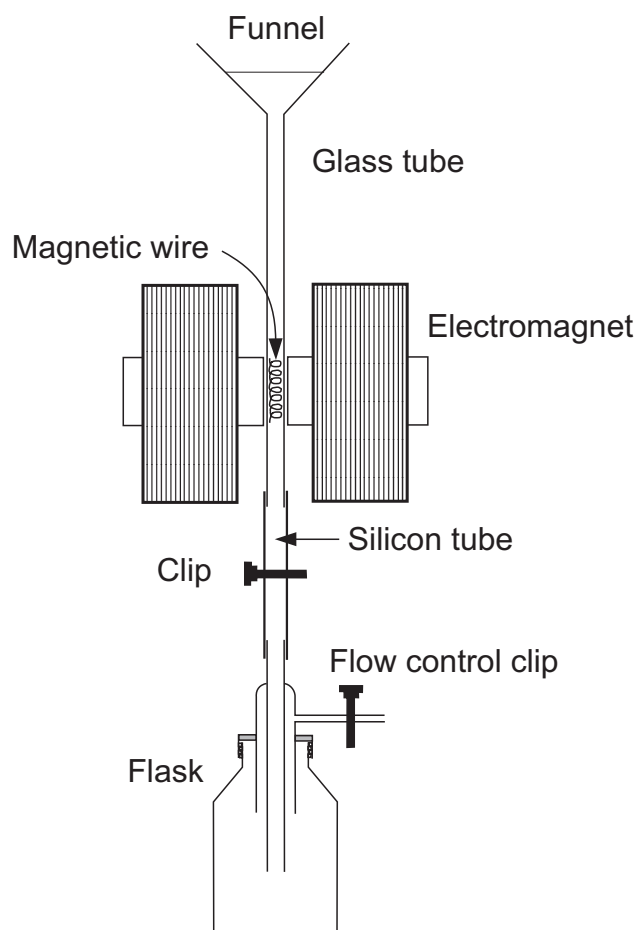


**Figure 3.1** The HGMS device consists of a funnel connected to a glass tube, which passes vertically between the poles of a electromagnet. A magnetic wire in a magnetic field of less than 50 mT captures ferromagnetic and paramagnetic grains.

The samples are brought in aqueous suspension and poured into the funnel. Fields of about 50 mT are applied to extract paramagnetic and ferromagnetic material, which is captured by the magnetic wire and on the glass tube adjacent to the pole edges of the electromagnet. The clip connected to the flask is used to set a constant flow rate (ca. 1-2 l/hr) through the glass tube. Before the top of the water column reaches the magnetic wire, the magnetic field is set to the maximum value (650 mT) to prevent loss of magnetic material during outflow of the suspension. The silicon tube is then closed with a clip, the flask containing the nonmagnetic fraction removed and the magnetic concentrate collected in a new flask. Depending on the flow rate, the separation experiment takes 30 min to 1 hr. To increase recovery, the experiments were repeated once or twice.

For this study, the grain size fractions  $< 1.2\mu\text{m}$ ,  $1.2 - 6\mu\text{m}$ ,  $6 - 10\mu\text{m}$ ,  $10 - 20\mu\text{m}$  and  $20 - 40\mu\text{m}$  for magnetite ( $\delta = 5.2$ ) were prepared by repeated sedimentation experiments for four pilot samples at the CGS in Strasbourg. The amount of magnetic material collected from the medium size fractions ( $6 - 10\mu\text{m}$  and  $< 10 - 20\mu\text{m}$ ) is relatively high (10-20 mg) and sufficient for chemical analyses. Spherules of iron oxide, most likely magnetite, were observed by SEM and EDX analysis (Fig. 3.2a). However, the  $< 1.2\mu\text{m}$  magnetite fraction, which contains the magnetic minerals relevant for the acquisition of stable NRMs yields very small amounts of magnetic material ( $< 1\text{mg}$ ).

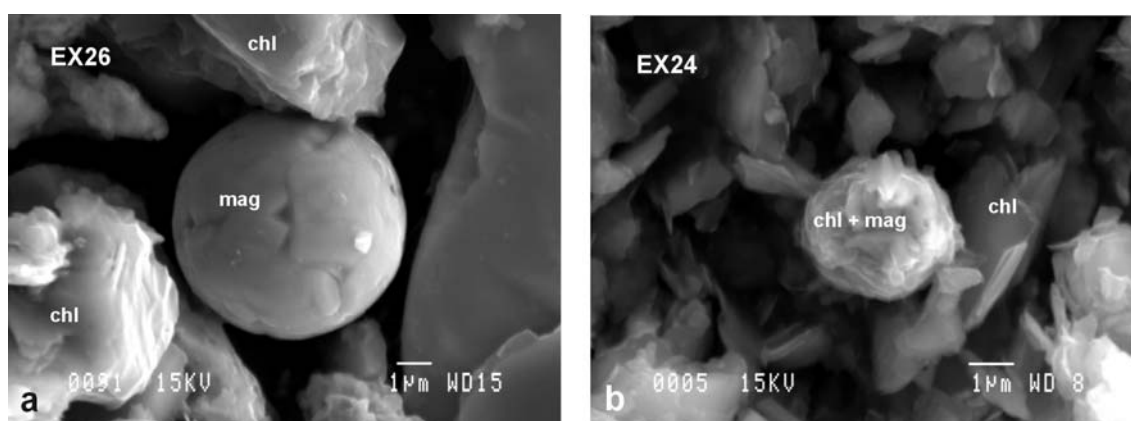


**Figure 3.2** SEM micrographs of magnetic extracts from a Carboniferous greywacke sample (OLP, NE Rhenish Massif): a) a magnetite sphere (mag) from the  $6 - 10\mu\text{m}$  magnetite grain size fraction and b) a sphere of small chlorite grains, which agglomerated on magnetic iron oxides ( $< 1.2\mu\text{m}$  magnetite grain size fraction). All magnetic extracts are contaminated by paramagnetic minerals, such as chlorite (chl).

In addition, the extracted ferromagnetic material is heavily contaminated by paramagnetic minerals (Fig. 3.2). SEM observation and EDX analysis of the magnetic separates indicate the presence of Fe and Mg bearing sheet silicates (chlorites).

The occurrence of chlorite in the clay fractions from the NE Rhenish Massif is confirmed by XRD analysis. In the larger grain size fractions ( $6 - 40\mu m$ , Fig. 3.2a), the high amount of chlorite might result from ferromagnetic inclusions within the crystal lattice of the sheet silicates. In the small grain size fractions, spheres of agglomerated chlorite were observed (Fig. 3.2b). The Fe content in these agglomerates is significantly higher than in the surrounding chloritic material and indicates the presence of very small iron oxides (magnetite) either in form of ferromagnetic impurities or as very small independent grains, which are not visible under the SEM. Lower magnetic fields during the separation experiment did not reduce significantly the paramagnetic contamination. Therefore, the HGMS method is not suitable for the preparation of pure ferro(i)magnetic extracts, which are required for chemical analysis, but was used for preparation of magnetic concentrates for SEM observations.

## 3.6 Leaching experiments

### 3.6.1 The dithionite-leaching method

Iron oxides were leached from the  $< 0.2\mu m$  fractions at the CGS in Strasbourg using dithionite ( $\text{Na}_2\text{S}_2\text{O}_4$ ) as a reducing agent, buffered to a constant pH of 7.3. This procedure is highly effective in the dissolution of free iron oxides, without extracting Fe from silicate crystal lattices (MEHRA & JACKSON, 1960). The treatment with acetic acid during sample preparation did not or only partly dissolve iron oxides, as is demonstrated by SEM observation of fine grained iron oxides in magnetic concentrates. Due to the higher density of iron oxides (e.g. magnetite:  $\delta = 5.2$ ), the  $< 0.2\mu m$  clay fractions contain iron oxide grains  $< 0.12\mu m$ . This size fraction contains magnetite and hematite SD grains, which might carry ancient magnetisations and includes potentially existing superparamagnetic grains, characterising chemical remagnetisation.

Iron oxides were leached according to the procedures described by MEHRA & JACKSON (1960). About 100 - 120 mg of clay sample were suspended in centrifugation tubes with 4 ml of 0.3M Na-Citrate<sub>aq</sub> and 0.5 ml 1M NaHCO<sub>3aq</sub> and heated to 80 °C. Then, a weighted amount (ca. 100 mg) of Na<sub>2</sub>S<sub>2</sub>O<sub>4</sub> was added and the tube shaken for 15 min. After addition of 1 ml saturated NaCl<sub>aq</sub>, the suspension was centrifuged at 4000 rpm and poured into teflon containers. The dried material was dissolved first in 4 ml 10N HCl and 2 ml 14N HNO<sub>3</sub> (aqua regia) and then in 2 ml 14N HNO<sub>3</sub> after evaporation at 100 °C. The solution was diluted with bidistilled water in volumetric flasks and analysed by ICP-MS and ICP-AES for major and trace elements (except Na), respectively.

Not available in highly purified quality, dithionite contains relatively large amounts of Zn, Cr, Ni, Cu, Mo and Sr ( $> 0.5$  ppm). Therefore, contamination by dithionite and other reagents used was controlled by preparing and analysing a complete reaction without any sample powder. Due to possible precipitation of S from the solution (MEHRA & JACKSON, 1960), estimate of the amount of leached material by weighting the residue is problematic. Therefore, the elemental oxide contents in the leachate are given relative to the total amount of clay, which was leached with dithionite. The blank-corrected results are listed in Tables F.1, F.2 and F.3.

### 3.6.2 Efficiency of Fe-oxide leaching

In order to control the efficiency of the leaching process, the amount of magnetite in the samples was estimated using the anhysteretic susceptibility  $k_{an}$  as a proxy. While the initial susceptibility  $k_0$  is controlled by all magnetic (ferro(i)-, para-, and diamagnetic) material present in the sample,  $k_{an}$  reflects only the amount of ferromagnetic minerals. Furthermore,  $k_{an}$  depends on grain size and is about an order of magnitude greater in  $0.1\mu\text{m}$  magnetite grains than in  $1\mu\text{m}$  magnetite (DUNLOP & ÖZDEMİR, 1997a, p. 299). Consequently, the mass normalised anhysteretic susceptibility  $k_{an}$  of a whole-rock sample is a good measure for the magnetite content in the  $< 0.2\mu\text{m}$  fraction, where the magnetite grains are  $< 0.12\mu\text{m}$  (Fig. 3.3). Since the alternating field intensity during ARM acquisition was set to 150 mT, only magnetic minerals with coercivities below 150 mT (e.g. magnetite) contribute to  $k_{an}$ .

For samples, in which magnetite is the predominant ferro(i)magnetic mineral, the  $\text{Fe}_2\text{O}_3$  content of the leachates is correlated to  $k_{an}$  (circles in Fig. 3.3). Considering natural inhomogeneities (the ARM measurements and leaching experiments were made on different sample aliquots) and the effects from large magnetite grains, which contribute to the ARM but are not present in the  $< 0.2\mu\text{m}$  fractions, this correlation is reasonably good ( $r^2 = 0.75$ ). The magnetite minerals, which can carry a remanent magnetisation, were not removed during the preparation of the clay fractions, but were completely dissolved during the leaching process. The leachates of samples for which rock magnetic experiments indicate the presence of hematite (crosses in Fig. 3.3), contain more  $\text{Fe}_2\text{O}_3$  than predicted by  $k_{an}$ . This indicates, that hematite, which does not contribute to  $k_{an}$ , is also dissolved by the dithionite treatment.

Although the relation between  $k_{an}$  and the  $\text{Fe}_2\text{O}_3$  content of the leachates show that dithionite leaching is very effective in dissolving magnetite and hematite, still Fe may not be completely removed from the clay. During centrifuging, small amounts of leachate were absorbed by the clay residue and could not be completely removed. While this effect might cause minor differences in Fe-content of clay fractions and

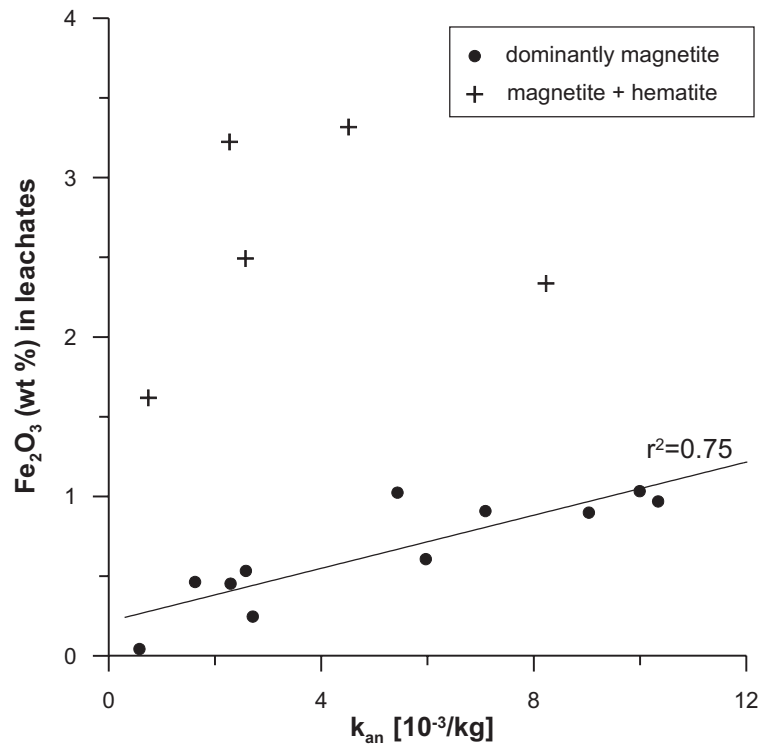


**Figure 3.3** The  $\text{Fe}_2\text{O}_3$  content of the leachates is correlated to the mass normalised anhysteretic susceptibility  $k_{an}$  in samples, where magnetite is the predominant ferromagnetic mineral (circles). Since hematite does not contribute to  $k_{an}$ , samples containing hematite plot above this correlation line (crosses). The  $\text{Fe}_2\text{O}_3$  content of the leachates is given relative to the mass of the clay fractions, which were leached with dithionite.

leachates, it cannot account for the observation, that leachates from some clastic rocks contain less than 10% Fe of the untreated clay fractions (Fig. 3.4 a).

In fact, the relative amount of leached Fe is controlled by the lithology and provenance of the samples: it is generally higher than 50% for carbonate rocks from the NE Rhenish Massif (40% - 83%, filled circles in Fig. 3.4 a), but significantly lower in the clay fractions of clastic rocks from the NE Rhenish Massif (8% - 30%, open circles in Fig. 3.4 a). For most rocks from the Barrandian (diamonds in Fig. 3.4 a) and Holy Cross Mountains (crosses in Fig. 3.4 a) about 25% - 50% of the Fe in the clay fractions is removed by the leaching process.

The different degrees of Fe-leaching indicate varying amounts of other Fe-bearing minerals in the different rock types and sampling areas, which are less or not soluble by dithionite. Fe-chlorite was identified by XRD in rocks from the NE Rhenish Massif (see section 7.1.2) and is thought to be an important source of insoluble Fe in the siliciclastic rocks, while its absence in carbonate rocks explains the higher degree of Fe-leaching in those lithologies. Other insoluble or less soluble Fe-bearing minerals, which are thought to be present in small amounts in the clay fractions are

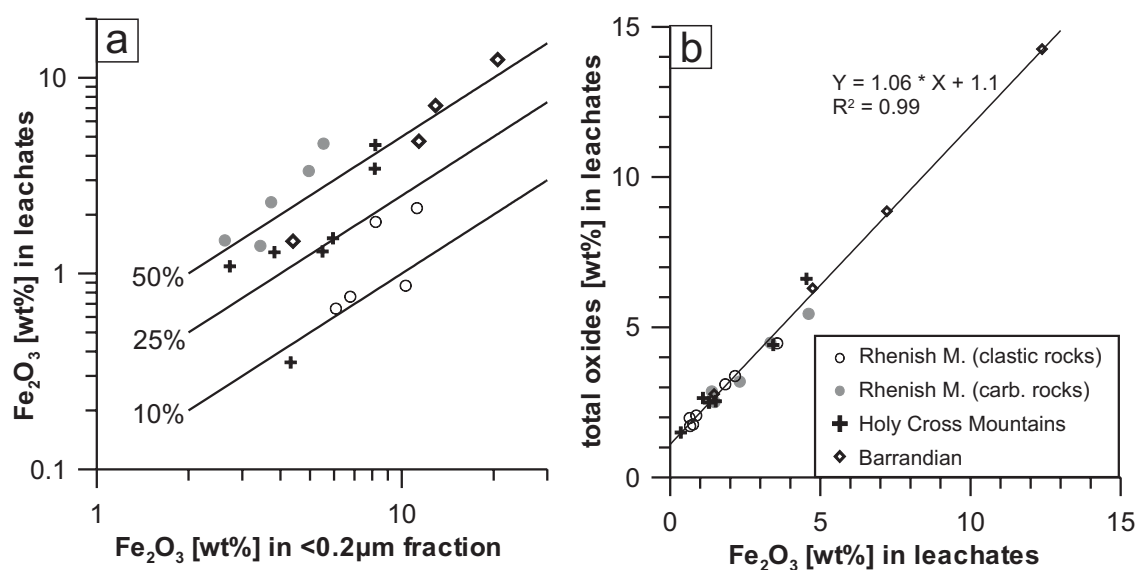


**Figure 3.4** Leaching of  $\text{Fe}_2\text{O}_3$  and other oxides. a) the amount of  $\text{Fe}_2\text{O}_3$  leached from the clay fractions depends on lithology and sampling area and suggests different amounts of insoluble Fe-bearing minerals. b) The total amount of oxides in the leachates is linearly correlated to the amount of leached  $\text{Fe}_2\text{O}_3$ . The intercept with the ordinate at ca. 1.1% total oxides indicates dissolution of a constant amount of Fe-free phases (e.g. carbonates, phosphates, Al-oxy-hydroxides) during leaching. The oxide concentrations in the leachates is given relative to the mass of untreated clay fractions.

biotite and glauconite.

### 3.6.3 Dissolution of other minerals

Besides  $\text{Fe}_2\text{O}_3$ , the leachates contain significant amounts of oxides from other major elements (mainly  $\text{SiO}_2$ ,  $\text{Al}_2\text{O}_3$ ,  $\text{MgO}$ ,  $\text{K}_2\text{O}$ ,  $\text{CaO}$  and  $\text{P}_2\text{O}_5$ ), indicating dissolution of other mineral phases during the leaching process. The sum of those elements is almost constant in all samples, as shown by the linear correlation between the total amount of oxides and the amount  $\text{Fe}_2\text{O}_3$  of all samples in Fig. 3.4 b. The intercept of the fitted line ( $r^2 = 0.99$ ) with the ordinate indicates, that the amount of additional soluble mineral phases, leached from the total untreated clay fractions represents about 1 wt%. The dissolution of  $\text{SiO}_2$  and  $\text{Al}_2\text{O}_3$  from soils by iron oxide leaching with dithionite and other reagents is described by MEHRA & JACKSON (1960).

The Al/Si ratios of the leachates show a wide variation (0.63 - 7.7), however, they are generally higher than for a mixture of illite, smectite and chlorite which are the most common clay minerals in the  $< 0.2\mu\text{m}$  fractions (shaded area in Fig. 3.5 a). This is taken as a convincing proof that no clay material was dissolved or altered during the leaching procedure. Given the similar mineralogy of the clay fractions and the uniform conditions during leaching, a differential dissolution of clay minerals

from samples where the leachates plot into the clay field is unlikely (Fig. 3.5 a). The variation in Al/Si ratios of the leachates rather reflects the presence of more soluble amorphous silica (chert) and Al-oxi-hydroxides in different proportions in the clay fractions. It should be noted, that although the dissolved mineral phases yield a strong relationship among Al and K, dissolution of K-feldspar is not indicated by the Al/K ratios of the leachates (Fig. 3.5 a).

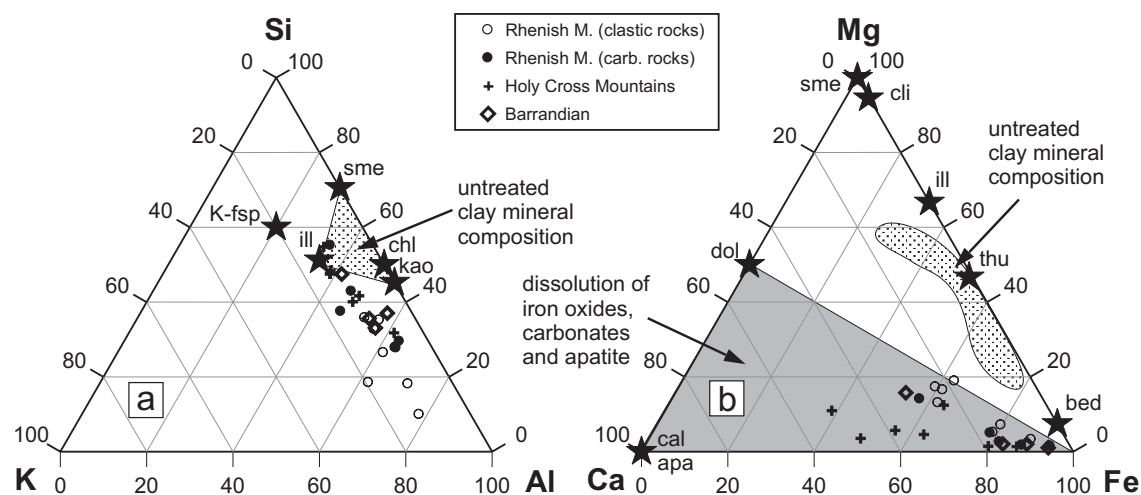


**Figure 3.5** Ternary diagrams of cations Al, Si, K and Ca, Fe, Mg in leachates. a) Leachates (symbols) have higher Al/Si ratios than untreated clay fractions (stippled area), while the K/Al ratios are similar for leachates and clay fractions. b) The Ca, Fe, Mg composition of leachates indicates dissolution of Fe-oxi-hydroxides, dolomite, calcite and apatite (grey area). The stippled area indicates the composition of untreated clay fractions. Average mineral compositions after CLAUER & CHAUDHURI (1995). apa: apatite, bed: beidellite (Fe-smectite), cal: calcite, chl: chlorite, cli: clinocllore (Mg-chlorite), dol: dolomite, ill: illite, kao: kaolinite, K-fsp: K-feldspar, sme: smectite, thu: thuringite (Fe-chlorite).

In the Ca, Fe, Mg ternary diagram, all leachates fall into a field including the compositions of Fe-oxi-hydroxides, dolomite, calcite and apatite (light shaded area in Fig. 3.5 b). This indicates dissolution of these minerals during leaching. The contribution from calcite is thought to be minimal, since the clay fractions were treated with acetic acid before leaching. The composition of the untreated clay fractions (dark shaded area in Fig. 3.5 b) is significantly different with higher Mg/Fe and Mg/Ca ratios. In general, clay minerals and other silicates are not affected by the treatment, while oxo-hydroxides, carbonates, phosphates and possibly sulfates are dissolved. Consequently, the leachates represent a mixture of Fe-oxides and other soluble minerals in the  $< 0.2\mu\text{m}$  fractions.

### 3.6.4 Sources of rare earth elements in leachates

Fe-oxi-hydroxides are important carriers (scavengers) of REE in sedimentation and diagenetic environments. Therefore, the analysis and interpretation of REE patterns in Fe-oxide leachates is a potential method to characterise the geochemical events, causing formation of authigenic magnetic minerals. Since the leachates represent a mixture of Fe-oxides and other soluble minerals, this relies on the assumption, that the majority of REE in the leachates originates from authigenic minerals. In chemically remagnetised rocks, this assumption is feasible for fine grained Fe-oxides and other highly soluble minerals as baryte, which are likely to be mobilised during diagenesis and fluid migration.

However, REE-rich minerals of detrital origin can severely contaminate the authigenic REE pattern, if present in the  $< 0.2\mu\text{m}$  fractions and dissolved during leaching. Possible candidates for those REE-rich minerals are apatite, zircon and monazite, which were observed by SEM of rock fragments and polished surfaces as accessory minerals in clastic rocks from the NE Rhenish Massif. While zircon ( $\text{ZrSiO}_4$ ) and other REE carrying silicates (sphene, allanite) are very resistant to chemical weathering and unlikely to be dissolved during leaching, detrital monazite ( $(\text{Ce,REE})\text{PO}_4$ ) might contaminate the REE composition of the leachates.

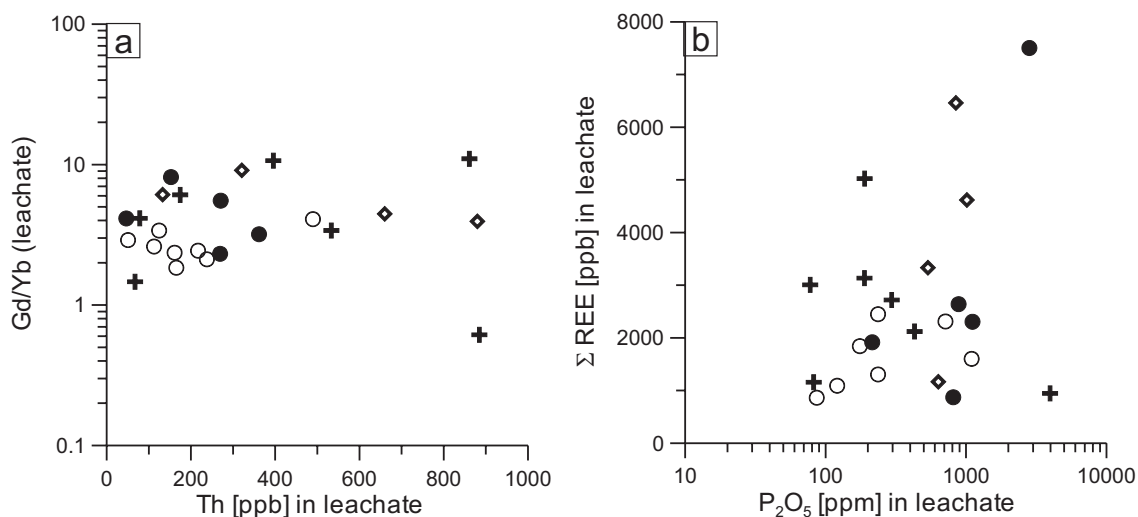


**Figure 3.6** HREE depletion and REE content versus Th and  $\text{P}_2\text{O}_5$  in leachates. a) Gd/Yb ratio as a measure for HREE depletion in monazite versus Th. b) REE content versus  $\text{P}_2\text{O}_5$  in leachates. Symbols as in Fig. 3.5.

Monazite is typically depleted in heavy rare earth minerals (HREE,  $\text{Gd/Yb} = 27.2$ ) and contains more than 6% Th (LEE & BASTRON, 1967), which can be used to identify any contribution from these minerals to the REE concentrations of the leachates. If monazite is present in the  $< 0.2\mu\text{m}$  fractions and dissolved during

leaching, a positive correlation would be expected for the Gd/Yb ratio and the Th concentration. However, this trend is not observed in a plot of Gd/Yb versus Th (Fig. 3.6 a). The Gd/Yb ratio, ranging from 1 to 10 for the majority of samples is rather evenly distributed for all Th concentrations. This is taken as strong evidence, that monazite is not present in the  $< 0.2\mu\text{m}$  fractions or was not dissolved during leaching.

Detrital apatite is more difficult to identify, since its trace element composition and REE pattern both vary significantly with magmatic host-rock types (BELOUSOVA *et al.*, 2002) and sediments contain a mixture of apatite detritus from different sources with spatial and temporal variations. However, the total content of REE is not directly correlated to the  $\text{P}_2\text{O}_5$  concentration in the leachates from the Barrandian, Holy Cross Mountains and carbonate rocks of the NE Rhenish Massif (Fig. 3.6 b). This indicates that apatite is not a major source of the REE in leachates from these areas and lithologies. A weak correlation ( $r^2 = 0.28$ ) of REE and  $\text{P}_2\text{O}_5$  contents is only observed for clastic rocks from the NE Rhenish Massif. However, all apatite grains, which were identified by SEM in this group of samples were larger than  $5\mu\text{m}$  and are not expected in the  $< 0.2\mu\text{m}$  fractions. Therefore, a contamination of the REE patterns of leachates by detrital apatite cannot be ruled out, but is thought to be unlikely.

## Part II

# Late Carboniferous Remagnetisation of Palaeozoic Rocks in the NE Rhenish Massif, Germany

# Chapter 4

## Geology and Sampling

### 4.1 Geological setting and palaeogeography

The eastern Rhenish Massif is part of the Rhenohercynian fold belt (RHEN in Fig. 2.1), forming the northernmost tectonostratigraphic unit of the Central European Variscides as defined by KOSSMAT (1927). In more recent plate tectonic concepts, the Rhenohercynian belt is seen as the foreland fold and thrust belt thrust onto the southern margin of the Avalonian microcontinent during the Variscan orogeny. To the south, the Rhenohercynian is bordered by the relics of magmatic arcs (Mid-German Crystalline Rise, MGCR in Fig. 2.1), which were active during most of the Palaeozoic. The adjacent Saxothuringian unit (SAX in Fig. 2.1) is part of the Amorican Terrane Assemblage (Armorica), which comprises several tectonostratigraphic terranes (e.g. Ibero-American belt, Saxothuringian, Barrandian). These semi-autonomous terranes underwent similar latitudinal drift histories in the Early Palaeozoic but different extents of block rotation (TAIT *et al.*, 1997, and references therein).

The Avalonian and Amorican microplates are derived from the northern continental margin of Gondwana, from where they rifted off in the Early Palaeozoic. In the Late Silurian, the Avalonian microcontinent had almost completed its northward drift and was situated in the close vicinity to Laurentia and Baltica at low latitudes (Fig. 4.1 a). Armorica was still located further to the south until the closure of the Rheic Ocean, which reopened in Early-Mid Devonian times with the development of the Rhenohercynian basin (TAIT *et al.*, 1997). Although the Late Devonian latitudinal position of the northern Armorican margin is constrained by palaeomagnetic data, the width of this oceanic basin is still debatable, as the APWP of Baltica is poorly defined for this time period (ZWING & BACHTADSE, 2000, and references therein).

The formation of the European Variscan Fold Belt, triggered by the closure of the Rheic and Rhenohercynian oceans in the Devonian reached its peak during the collision of Gondwana with the northern continents (Laurentia, Baltica, Avalonia and Armorica) in the Late Carboniferous. The consolidation of the European Variscan Fold Belt until its final configuration within the supercontinent Pangaea (WEGENER, 1912) lasted until the Permian (Fig. 4.1 b).

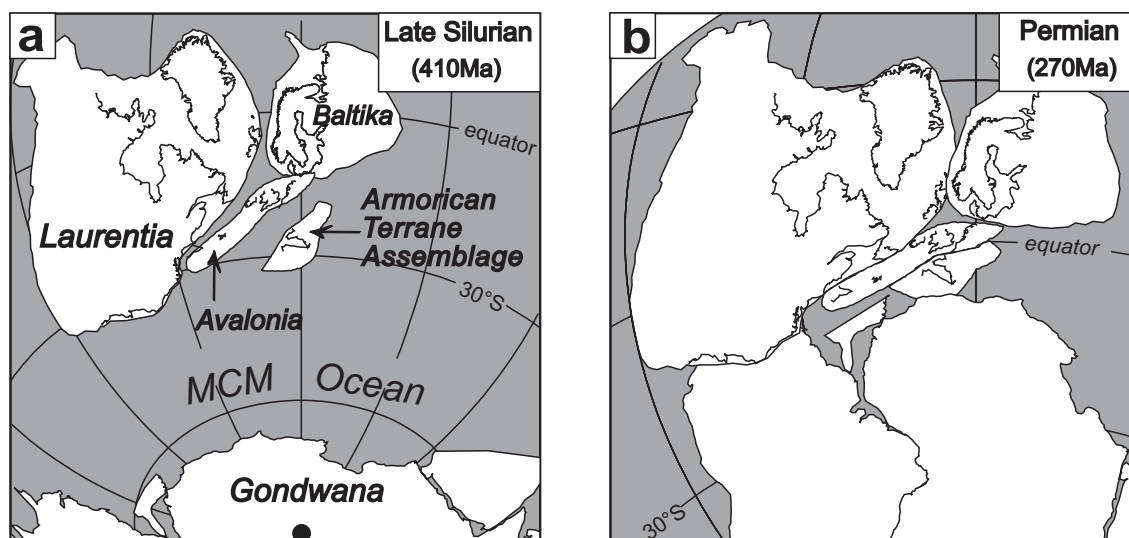


**Figure 4.1** Palaeogeography of the Circum-Atlantic continents before and after the assembly of Pangaea in the (a) Late Silurian (after TAIT et al., 1997) and (b) Permian (after BACHTADSE, 1994)

## 4.2 Basin evolution

The eastern Rhenish Massif is dominated by Devonian and Carboniferous sediments, which developed from a sedimentary prism on the southern, passive continental margin of the Old Red Continent. The sedimentation in a neritic facies during the Lower and Middle Devonian is characterised by thick clastic deposits and the occurrence of red-beds, conglomerates and root horizons. These represent a deltaic sedimentation, ranging from the delta front in the north to the proximal part of the delta plain in the south, which was occupied by plants growing partly below the water level. The facial development and distribution of the neritic sediments indicate the existence of a giant deltaic system, delivering siliciclastic debris from the north (WALLISER, 1981). K-Ar ages on detrital micas ranging from 459 Ma to 409 Ma indicate Caledonian sources for the clastic sedimentation (FRANKE, 2000, and references therein).

During subsidence of the shelf, the neritic facies gave way to hemipelagic and pelagic environments. The pelagic sediments are characterised by fine grained siliciclastic rocks, occasionally intercalated with nodular limestones and were deposited in a relatively shallow basin. This is indicated by numerous bioherms, which developed in the photic zone on top of submarine seamounts of a few hundred meters height (WALLISER, 1981). The clastic input was reduced during a transgressive phase in the Givetian, which enhanced the growth of carbonate reefs on the continental shelf. Due to the peak in basic volcanic activity and the growth of reefs, the sea floor morphology and facies differentiation reached a maximum during this time interval.

In the Late Devonian, the continuous facial development was interrupted by several black shale events of global scale, the best known being the Late Frasnian Kellwasser horizon (BUGGISCH, 1972), which marks a global extinction of reefs and is present in many sections all over the world. The high topographic relief in the Famennian was reduced by high sedimentation rates in the lower parts of the basin.

The transgression at the Devonian-Carboniferous boundary almost completely terminated the clastic sedimentation and led to the deposition of alum shales, bedded cherts, dark shales and the formation of a carbonate platform in the north, which extended westwards into the British Isles (FRANKE, 2000). Closure of Rhenohercynian oceanic basin caused the formation of a Late Devonian flysch trough, which propagated north-westward during the Early Carboniferous. The flysch sediments were derived from the Mid German Crystalline Rise in the south and consist of limestone turbidites in the lower parts and massive greywackes towards the top. After the main flysch phase in the Late Viséan, the Namurian is marked by molasse-type deposits, defining the main orogenic phase. The high sedimentation rate in the Late Namurian exceeded the rate of subsidence and resulted in the formation of the paralic, coal-bearing sequences of the Subhercynian molasse foredeep (WALLISER, 1981).

### 4.3 Deformation and diagenesis

Southward subduction of the oceanic basin beneath the Mid German Crystalline Rise and the final collision of the bordering continental blocks resulted in an overall shortening of about 50% (200km) within the Rhenohercynian zone (ONCKEN *et al.*, 1999). The resulting structural style of the Rhenish Massif east of the river Rhine is characterised by thin-skinned imbricate thrust sheets in the south and thick-skinned tectonics with NNW facing, symmetric fault propagation folds further in the north (ONCKEN *et al.*, 2000). First order folds have wavelengths of tens of km with ENE plunging fold axes. Subsidiary folds with wavelength of tens to hundreds of me-

ters are plunging both to ENE and WSW with varying dips, reaching  $60^\circ$  within the cores of first order structures. The structural development of both first order and subsidiary structures in the region is related to a single continuous deformation path with progressive rotational deformation and consistently NE-trending fold axes (FRANKE, 1990). The subhorizontal ( $3^\circ$  max. dips) Upper Permian Zechstein deposits of the Hessian trough unconformably overlie the Rhenish Massif towards the East. Consequently, no significant tilt of the Rhenish Massif occurred after Late Permian times.

In the last decades, the kinematic evolution of the Rhenohercynian foldbelt has been studied by a variety of methods, including strain measurements, metamorphic petrology and geochronology. Isotopic ages from synkinematically grown phyllosilicates (white mica, illite) were first published by AHRENDT *et al.* (1983) from the eastern Rhenish Massif, indicating a northward propagation of the deformation front. More recent data (e.g. REUTER, 1987; REUTER & DALLMEYER, 1989) show, that the deformation started at around 320Ma in the south and migrated northwards until 300 Ma (Fig. 4.2, PLESCH & ONCKEN, 1999). It is important to note, that the samples, chosen for these studies, show a distinct cleavage: mica formation and recrystallisation is related to the peak deformation and cleavage formation (REUTER, 1985).

Conodont alteration indices (CAI, EPSTEIN *et al.*, 1977) from Devonian and Carboniferous carbonate rocks (KÖNIGSHOF, 1992) and vitrinite reflectance data (PAPROTH & WOLF, 1973, and references therein) indicate a general increase in palaeotemperatures from diagenetic and very low-grade conditions in the north to epizonal conditions in the south (Fig. 4.3). In the northern part of the eastern Rhenish Massif, the vitrinite reflectance is correlated to the stratigraphic level and the  $R_{max}$  isolines are folded and offset across faults. This indicates the preservation of a thermal state related to maximum burial near the onset of deformation. In the southern Rhenish Massif, the  $R_{max}$  isolines are not folded and cut through stratigraphic levels. Here, the average vitrinite reflectance is relatively high (5-7%  $R_{max}$ ) within even the youngest pre-tectonic sediments. Consequently, a major tectonic overburden caused the synkinematic resetting of the maximum palaeotemperatures (PLESCH & ONCKEN, 1999, and references therein) in the southern part of the Rhenish Massif.

## 4.4 Sampling area and sample description

Based on information from CAI and  $R_{max}$  data, sampling for palaeomagnetic and geochemical studies was restricted to the northern part of the Rhenish Massif, where

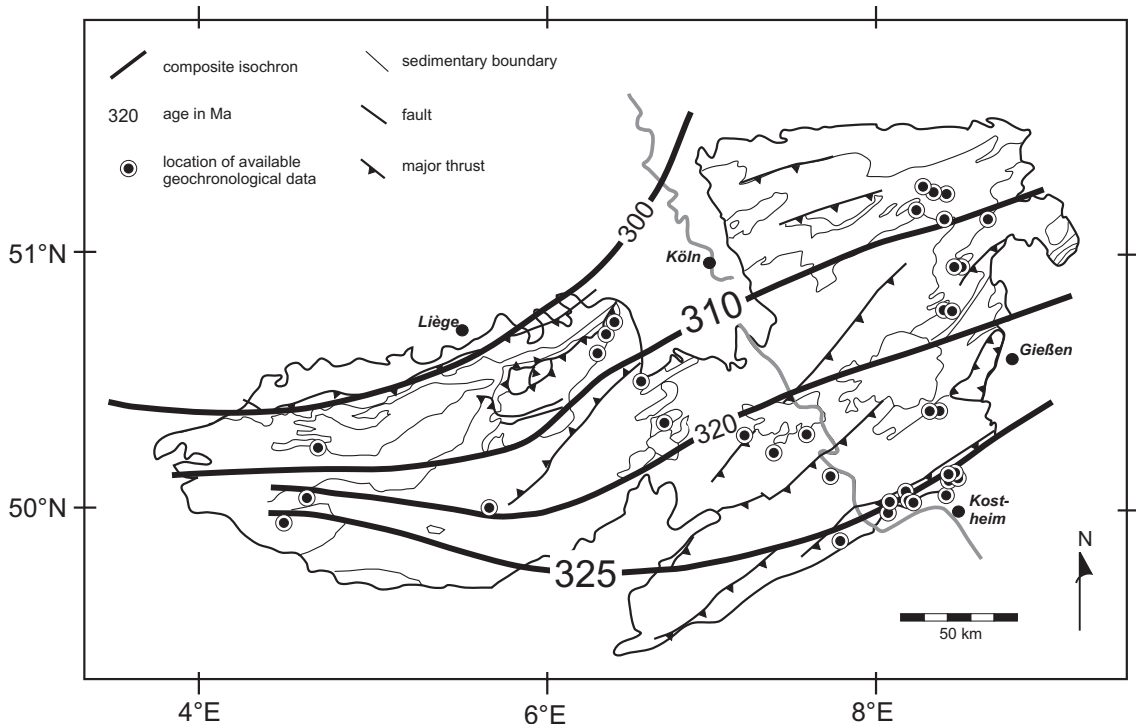


**Figure 4.2** Age of deformation in the Rhenish Massif and the Ardennes. Composite isochrons of progressive deformation are tentatively constructed from available geochronologic data of Variscan age. Modified after PLESCH & ONCKEN (1999).

palaeotemperatures and the amount of discontinuous deformation are significantly lower than further to the south. With exception of the Remscheid Anticline (RA, Fig. 4.3) in the northernmost part, samples were preferably taken from synclinal structures: Lüdenscheid Syncline (LS), Attendorn Syncline (AS), Wittgenstein Syncline (WS) and Paffrath Syncline (PS). In all studied areas, the palaeotemperatures are below  $300^{\circ}\text{C}$  ( $\text{CAI} < 4$ ,  $R_{\text{max}} < 3.5\%$ ).

A total of 331 oriented palaeomagnetic cores were taken at 37 sites from Lower Devonian to Lower Carboniferous rocks. The palaeomagnetic sampling locations are indicated with circles on the geological map of the NE Rhenish Massif in Fig. 4.4 and are listed in Table A.2. Great care was taken to sample rock types without macroscopic evidence for internal deformation (foliation), hydrothermal mineralisations or weathering. Sampling was concentrated on various limbs from small and large-scale folds, where the plunge of fold axes does not exceed  $35^{\circ}$ .

The sediments from the Rhenish Massif are dominated by clastic deposits and most samples were taken from siltstones, (quartzitic) sandstones and greywackes of Eifelian, Givetian and Namurian age. Carbonates associated with reef complexes of Upper Devonian age were sampled at five localities (GRU, STC, AFI2, AFI7,

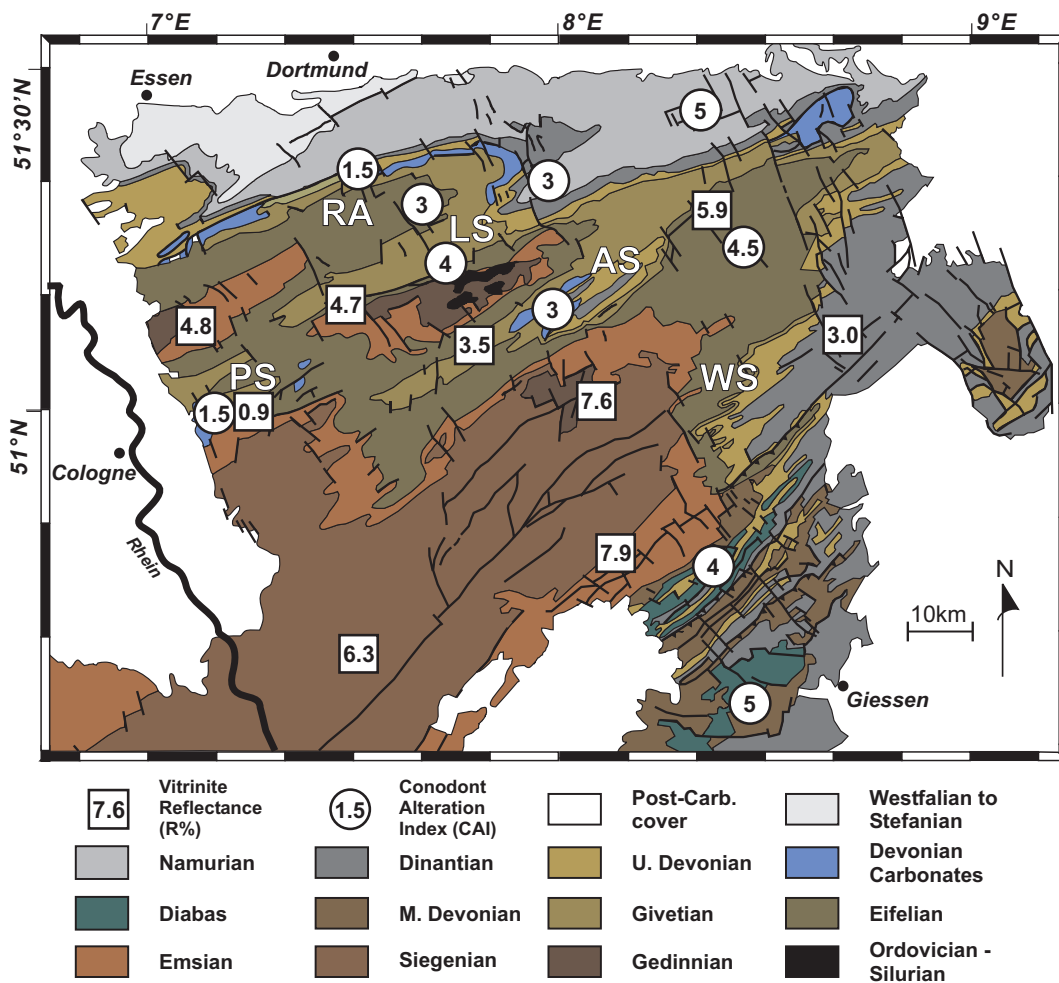


**Figure 4.3** Geological map of the NE Rhenish Massif with conodont alteration (CAI) and vitrinite reflectance (R%) data. Palaeotemperatures are lowest in the north and in the youngest sediments. Main structural units where sampling was carried out: Remscheid Anticline (RA), Lüdenscheid Syncline (LS), Attendorn Syncline (AS) and Wittgenstein Syncline (WS), Paffrath Syncline (PS).

ATT2). At five sites (HEN, LET2 & 3, STU, HAC), samples were taken from Tournaian and Viséan carbonates, which were deposited on the Early Carboniferous carbonate platform. Given the terrigenous source of the detritus and relatively high flow regimes in the vicinity of the delta fan, the clastic rocks are likely to contain rather coarse grained magnetic minerals (magnetite, maghemite, hematite) of detrital origin, which has strong impact on the rock magnetic properties of the sediments (see Chapter 6). During formation of reef complexes and the carbonate platform, the input of terrestrial material was restricted and the amount of detrital magnetic minerals is expected to be smaller. For rock magnetic studies, the sediments were subdivided into three major groups: a) siliciclastic rocks (quartzitic sandstones, sandstones and siltstones) with high amount of terrigenous detritus, b) platform carbonates, dominated by calcareous detritus with less input of terrigenous material

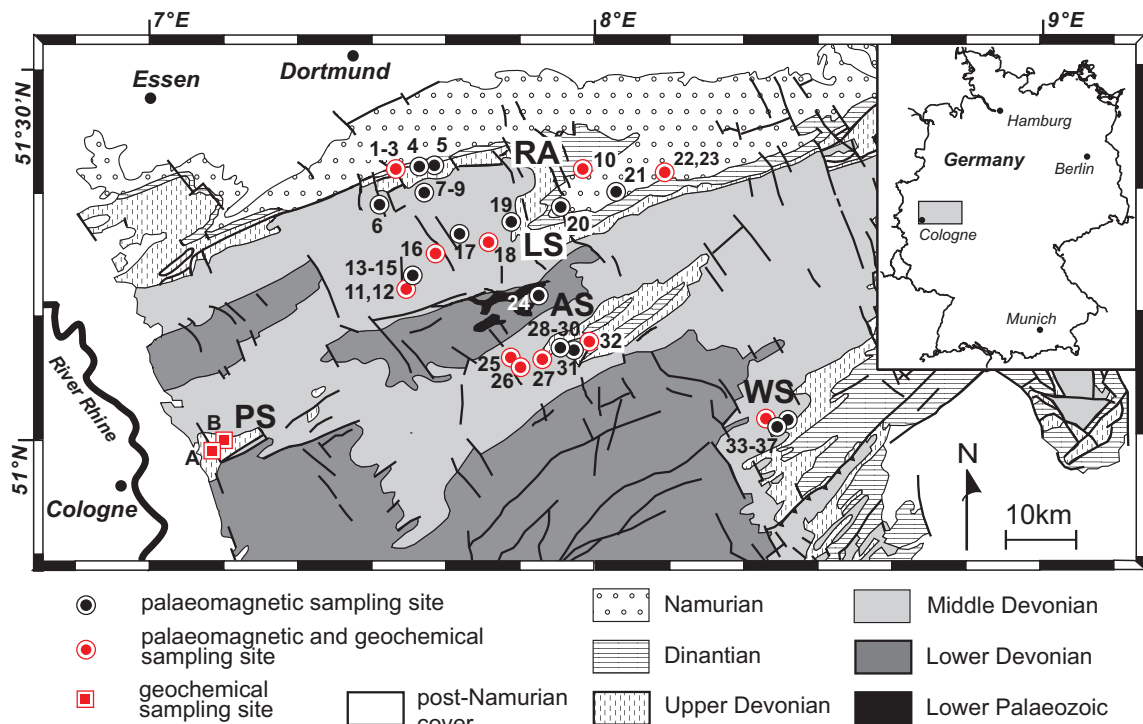


**Figure 4.4** Geological sketch map of the NE Rhenish Massif with palaeomagnetic sampling locations. Main structural units where sampling was carried out: Remscheid Anticline (RA), Lüdenscheid Syncline (LS), Attendorn Syncline (AS) and Wittgenstein Syncline (WS). The numbers refer to the first column of Table B.2.

and c) reef carbonates with very little detritus.

Samples for clay and iron oxide geochemistry were taken at selected palaeomagnetic sampling sites across the NE Rhenish Massif, which are indicated in red in Fig. 4.4. Hand samples or drill cores of 3.20 cm diameter were generally taken directly adjacent to the palaeomagnetic sampling locations from the same lithology. At locality BOH, a green crystal tuff was sampled for geochemical studies, while the palaeomagnetic samples were taken from a quartzitic sandstone in the hanging wall of the tuff layer. Hand samples for geochemical studies were also taken from reef carbonates at two locations (LER, UTH) in the Paffrath syncline (red squares A and B in Fig. 4.4), where the palaeotemperatures are minimal ( $CAI = 1.5$ ,  $R_{max} = 0.9\%$ ). Here, a previous palaeomagnetic study indicates a synfolding remagnetisation of Late Palaeozoic age (FÖRSTER, 1997, and U. Hambach, pers. comm.).

# Chapter 5

## Palaeomagnetism

### 5.1 Demagnetisation experiments

Stepwise thermal demagnetisation was generally successful in completely separating the magnetic components present, although many specimens from clastic rocks and a few from carbonate rocks show severe mineralogical alterations by heating above 450 °C. Due to the presence of high coercivity minerals such as hematite and/or goethite, alternating field treatment (AF) generally yielded incoherent directional results or did not succeed in resolving the complete directional spectrum. This is also the case for combined AF and thermal demagnetisation experiments. Alternating field demagnetisation, however, was successful in specimens from Carboniferous carbonate rocks in the RA and here both thermal and AF treatment yield similar directional results. The palaeomagnetic results are shown in Table B.2.

Three distinct components of magnetisation (A, B, C) can be identified in the sample set. After removal of an erratic viscous remanence at 100 °C, component A is identified in about 60% of the specimens between 100 °C and 150 °C. Its direction is similar to that of the present day geomagnetic field in the sampling area, and component A is therefore interpreted to be of recent origin (Fig. 5.1 b,d).

A second component, B, can be identified in 242 specimens from 34 sites. In the majority of specimens, component B is observed during thermal demagnetisation between 260 °C and 550 °C and is carried by magnetite (Fig. 5.1 a). The unblocking temperature of component B in carbonate rocks from the RA is slightly lower (ca. 500 °C, Fig. 5.1 b) than in clastic rocks from the same unit. A sharp decrease in intensity during demagnetisation at about 320 °C occurs sporadically in both carbonate and clastic rocks, but is not accompanied by a change in direction of the demagnetisation vector. In those specimens, component B is thought to be carried by both, magnetite and pyrrhotite. This interpretation is supported by thermal demagnetisation experiments of a three component isothermal remanent magnetisation

(IRM, LOWRIE, 1990). Here, the low coercivity component ( $< 120\text{mT}$ ) is demagnetised at  $580^\circ\text{C}$  and the intermediate coercivity component ( $120\text{mT} - 400\text{mT}$ ) shows a significant decrease in intensity at  $320^\circ\text{C}$ .

In specimens, which are affected by mineralogical alterations during heating, the identification of component B is limited to the temperature range between  $260^\circ\text{C}$  and  $450^\circ\text{C}$ , above which the specimens show erratic directional behaviour. The magnetic carrier of component B in these specimens is thought to be magnetite, as the shape of decay curve of the NRM up to  $450^\circ\text{C}$  is very similar to that of samples in which complete demagnetisation was achieved at  $550^\circ\text{C}$ . In samples displaying this type of behaviour, component B was identified by principal component analysis (KIRSCHVINK, 1980) based on a minimum of three consecutive demagnetisation steps.

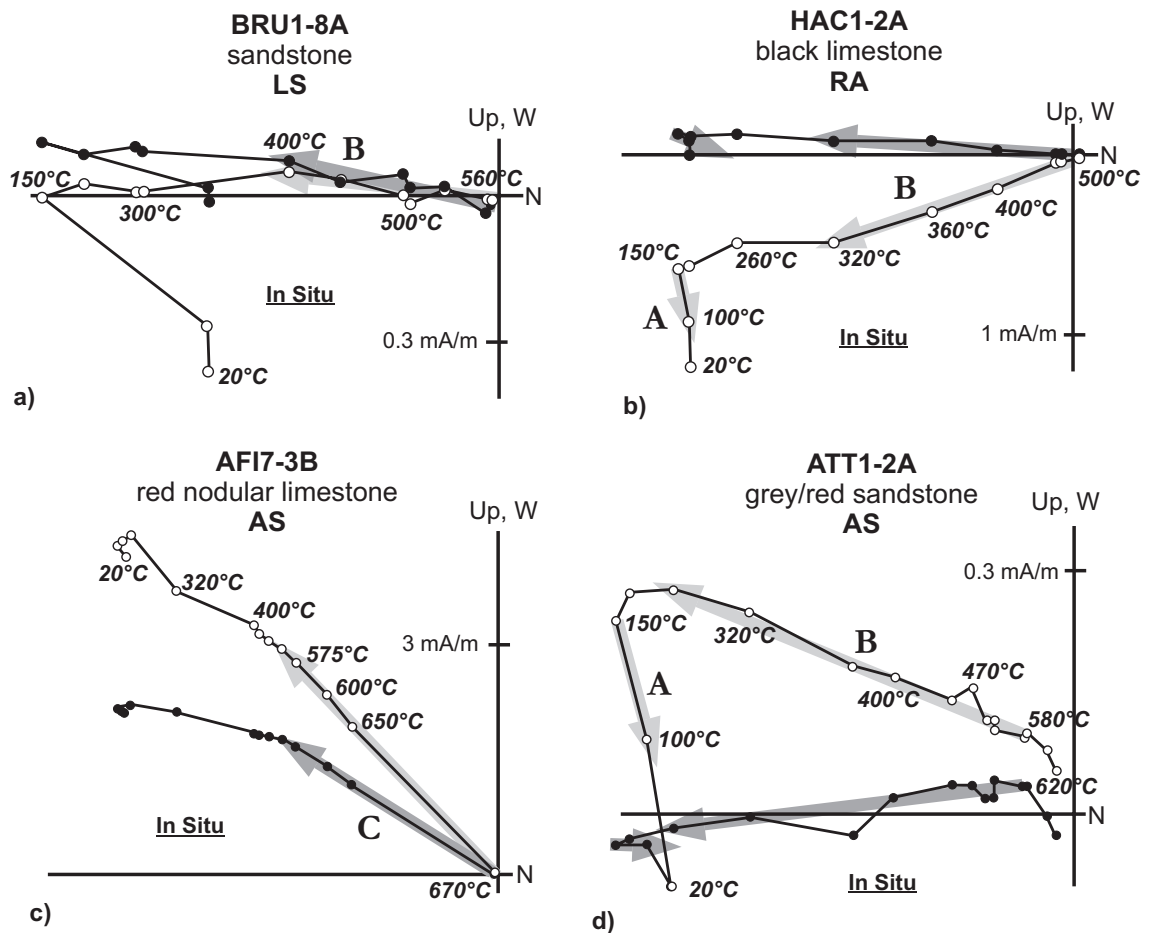


**Figure 5.1** (a-d) Thermal demagnetisation behaviour in orthogonal projection (ZIJDERVELD, 1967) of four representative specimens from carbonate and clastic rocks of the Remscheid Anticline (RA), Lüdenscheid Syncline (LS) and Attendorn Syncline (AS) in geographic coordinates (open and solid circles are projection on the vertical and horizontal plane, respectively) showing remanence components A, B, and C.

In red nodular limestones (AFI2) and red siltstones (PLE) from the AS, component B is carried by magnetite and hematite, as is indicated by unblocking temperatures close to 580 °C and 670 °C. The in situ direction of component B with generally southerly declinations and shallow positive and negative inclinations shows decreasing variation and dependency on bedding orientation from north (RA) to south (LS, AS and WS; see below).

In 22 specimens from 3 sites of the AS (AFI7, ATT2, ATT4) a third component C is observed as a stable endpoint direction at demagnetisation temperatures up to 670 °C, indicating hematite as the predominant carrier of this magnetisation (Fig. 5.1 c). The in situ direction of component C with southerly declinations and intermediate negative inclinations is significantly different from the in situ direction of component B in AS and LS. Component C is generally the only magnetisation component that can be reliably identified in sites AFI7, ATT2 and ATT4. However, 12 specimens from sites GAR and ATT1 are not completely demagnetised after removal of component B at 580 °C, indicating the presence of a high unblocking temperature component carried by hematite (Fig. 5.1 d). Although erratic demagnetisation behaviour due to alteration during heating above 580 °C prevents the direct observation of this component, use of the great circle intersection technique (HALLS, 1978) yields an in situ direction that is very similar to the direction of component C. The sites where component C is identified lie within zones of very tight folding in the AS and LS, as is indicated by near vertical or overturned bedding planes and plunges of the fold axis up to 35 °.

GAR and ATT1 are the only sites, where two components of magnetisation (B and C) can be identified within single specimens above demagnetisation temperatures of 260 °C. The combination of a low temperature component between 300 °C and 375 °C and a high temperature component stable up to 550 °C, as described by MOLINA GARZA & ZIJDERVELD (1996) from carbonate rocks in the Ardennes, is not observed in rocks from the Rhenish Massif.

## 5.2 Tectonic correction and fold tests

The conventional tilt correction in palaeomagnetism is intended to correct for bedding tilt, assuming horizontal fold axes. If applied to folds with inclined fold axis, conventional tilt correction produces declination anomalies in palaeomagnetic vectors which resemble effects of tectonic rotation (MACDONALD, 1980). Therefore, tectonic correction was performed by combining unplunging and untilting procedures in areas, where structures show significant plunge of fold axis of greater than 5 °. In a first step, bedding planes and palaeomagnetic directions were rotated from

the in situ position (IS in Fig. 5.2) into a tectonic position with horizontal fold axes (plunge corrected, PC in Fig. 5.2). In a second step, the unplunged palaeomagnetic directions were bedding corrected using the plunge corrected bedding planes (tilt and plunge corrected, TPC in Fig. 5.2). The site mean directions of B and C in geographical coordinates and after plunge and tilt correction are listed in Table B.2.

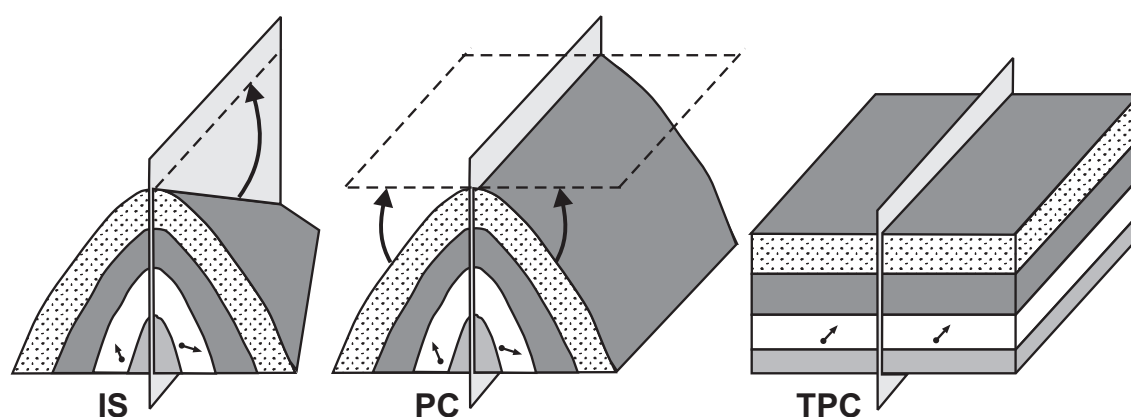


**Figure 5.2** Structural correction of folds with inclined fold axes. In situ (IS) bedding planes and magnetic directions were first corrected for plunge of fold axes. The unplunged magnetic direction (PC) were then tilt corrected (TPC) using the plunge corrected bedding planes

Fold tests using parametric resampling (WATSON & ENKIN, 1993) were performed with the ENKIN (1990) software package with stepwise rotation of the in situ directions (IS) into the plunge and tilt corrected directions (TPC) of magnetisation (Fig. 5.3). This procedure simulates unplunging of the fold axis and untilting of the bedding planes simultaneously and has been judged to be an adequate method to correct for the dominantly single-phase deformation in the Rhenish Massif.

Based on the fact that the in situ directions of component B are controlled by the geographical position of the sampling site, the sampling area was subdivided into three domains (RA, LS, AS & WS) and separate regional fold tests were performed for each domain.

After simultaneous unplunging and untilting, the site mean directions of the RA and LS show large deviations in declination at the optimum degree of unfolding (Fig. 5.4). This scatter is interpreted to be a result of post-orogenic rotations around vertical axes after remanence acquisition. Consequently, the site mean directions do not follow a Fisherian distribution and the data of the RA and LS were reanalysed using an inclination-only fold tests (ENKIN & WATSON, 1996).

Although the standard and inclination-only fold tests yield very similar results for the degree of unfolding and the resulting mean inclination, the significance of the tests for the RS and LS is highly increased by the inclination-only fold test. The behaviour of FISHER'S (1953) precession parameter  $k$  for 20 resampled datasets

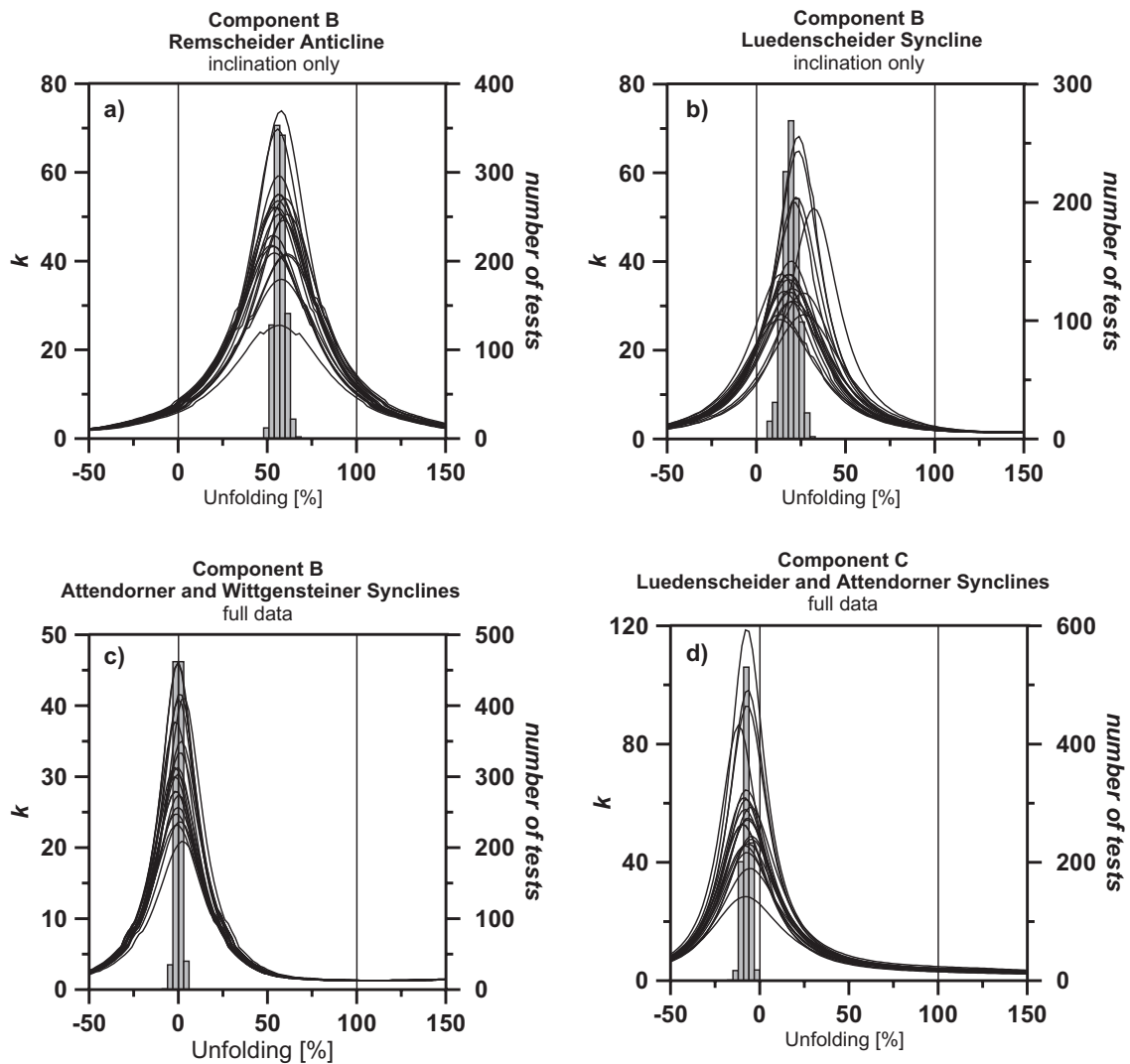


**Figure 5.3** (a-d) Fold test results for components B and C. The continuous curves show the value of FISHER'S (1953) precision parameter  $k$  as a function of unfolding degree for 20 examples of parametric resampling. The histograms give the distribution of the maxima from 1000 trials in groups of 3%. Accuracy of bedding attitude was estimated to be within  $3^\circ$ .

during unfolding is shown in Figs. 5.3 a-d (continuous lines) for each domain. The histograms in Figs. 5.3 a-d show the distribution of the maxima of  $k$  of 1000 resampling trials in 3% increments of unfolding. Bedding orientation was assumed to be accurate within  $3^\circ$ .

At the 95% level of confidence, the optimum degree of unfolding for component B decreases from 52% - 63% (RA, Fig. 5.3 a) in the north to 11% - 27% (LS, Fig. 3b) and -3% - 4% (AS & WS, Fig. 3c) further to the south. This suggests that the acquisition of component B occurred during folding in the RA and LS, whereas component B is clearly a postfolding remagnetisation in the AS & WS (Table 5.1). Despite the variation in degree of unfolding, the unit mean directions of component

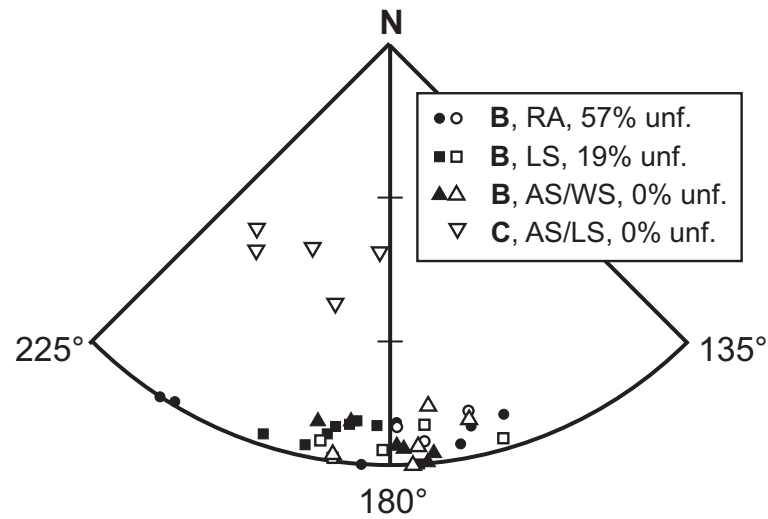


**Figure 5.4** Stereographic projection of site mean directions of component B from the Remscheid Anticline (RA), Lüdenscheid Syncline (LS) and the Attendorn and Wittgenstein Synclines (AS & WS) after optimum degree of unfolding. The directions correspond well in inclination but show a large scatter in declination (see text for discussion). The in situ site mean directions of component C are significantly different from B (open and solid symbols are upper and lower hemispheres, respectively).

Area	N'	oduf	95% confidence	Dec [°]	Inc [°]	k	$\alpha_{95}$ [°]	PLAT	PLONG	dp [°]	dm [°]	Palaeo-latitude	fold test
<b>Component B</b>													
RA	10	57%	52% - 63%	*	1	49	+5/-5	*	*	*	*	1°S +2°/-3°	io
LS	13	19%	11% - 27%	*	4	43	+5/-4	*	*	*	*	2°S +3°/-2°	io
AS & WS	11	0%	-3% - 4%	179	1	52	6	38°S	9°E	3	6	1°S +3°/-4°	fd
<b>Component C</b>													
LS & AS	5	-7%	-12% - -3%	202	-45	52	11	64°S	34°W	10	15	27°N +10°/-8°	fd

**Table 5.1** Mean direction with resulting palaeopole position (south pole) for the components of magnetisation identified in the rocks from the north-eastern part of the Rhenish Massif. Here: RA, Remscheid Anticline; LS, Lüdenscheid Syncline; AS, Attendorn Syncline; WS, Wittgenstein Syncline; N', number of site mean directions used; oduf, optimum degree of unfolding with its interval of 95% confidence and corresponding declination (Dec), inclination (Inc), radius of cone of 95% confidence ( $\alpha_{95}$ ) and Fisher precision parameter (k); PLAT and PLONG, latitude and longitude of the palaeo(south)pole; dp and dm, semiaxes of the oval of 95% confidence; io, inclination-only fold test (ENKIN & WATSON, 1996); fd, full data fold test. \*no declination information available.

B from the three units are not significantly different in inclination. The optimum degree of untilting of component C (-7%) indicates a postfolding origin of component C (Fig. 5.3 d).

The anisotropy of the magnetic susceptibility (AMS) in 12 samples covering all

structural domains does not show any evidence for significant internal deformation. The results yield an oblate magnetic fabric where the directions of the minimum susceptibilities ( $K_3$ ) are perpendicular to the planes of bedding. The intermediate ( $K_2$ ) and maximum susceptibilities ( $K_1$ ) are distributed along a girdle parallel to the bedding orientation (Fig. 5.5). The directions of  $K_1$  in geographic coordinates show no similarity to the orientation of the fold axes and consequently the AMS results are interpreted to reflect a primary sedimentary fabric.

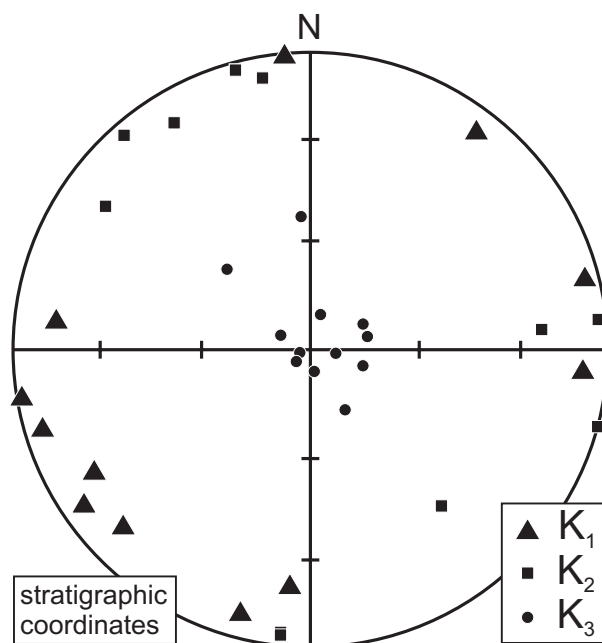


**Figure 5.5** Orientation of the principle axes of anisotropy of magnetic susceptibility (AMS) in stereographic projection (stratigraphic coordinates). The minimum susceptibilities ( $K_3$ , circles) are perpendicular to the bedding orientation. Maximum ( $K_1$ , triangles) and intermediate ( $K_2$ , squares) susceptibilities are distributed in a girdle parallel to the bedding.

### 5.3 Interpretation of palaeomagnetic results

Based on the results of demagnetisation experiments and AMS measurements, incomplete separation of magnetisation components and/or rotation of magnetic grains due to internal deformation can be ruled out. Incremental fold tests indicate that component B was acquired during various deformation stages in the area. In the south (AS & WS), B postdates folding, while B is of synfolding age in the northernmost part of the sampling area (RA and LS).

These observations agree with tectonic models, postulating northward migration of the deformation from 315 Ma to 300 Ma in the NE Rhenish Massif (AHRENDT

*et al.*, 1983). Furthermore, the almost identical regional mean directions of component B (Table 2) obtained in all structural domains strongly suggest that remagnetisation occurred in a very tight time window, lasting only a few My. A similar temporal relationship between folding and magnetic overprint was described by STAMATAKOS *et al.* (1996) for a orogenic remagnetisation of Permian age in the central Appalachian fold belt.

The distribution of the site mean directions of component B shows a large scatter in magnetic declination, which is interpreted to reflect late-/post-orogenic block rotations, locally compensating for regional tectonic movements.

The unit mean directions of component B yield low palaeolatitudes (RA:  $1^{\circ}\text{S} +2^{\circ}/_{-3^{\circ}}$ ; LS:  $2^{\circ}\text{S} +3^{\circ}/_{-2^{\circ}}$ ; AS/WS:  $1^{\circ}\text{S} +3^{\circ}/_{-4^{\circ}}$ ) and are in good agreement with the predicted palaeolatitude of the sampling area (Fig. 5.6; reference point: Cologne  $51^{\circ}\text{N}$ ,  $7^{\circ}\text{E}$ ) in the Late Carboniferous, based on the mean palaeopoles for Baltica and Laurentia (VAN DER VOO, 1990).

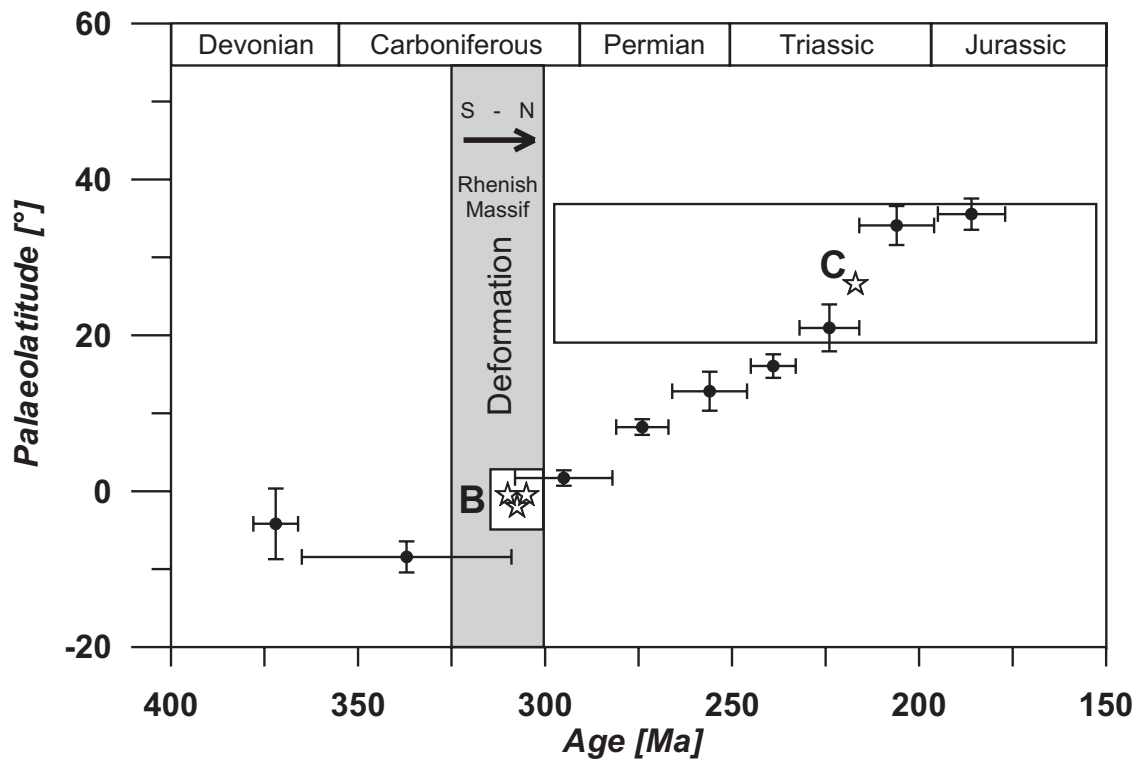


**Figure 5.6** Palaeolatitudes for components B and C (stars) plotted against the predicted palaeolatitudinal drift history for the Rhenish Massif (reference location: Cologne,  $51^{\circ}\text{N}$ ,  $7^{\circ}\text{E}$ ), based on mean palaeopoles for Baltica and Laurentia (VAN DER VOO, 1990) which are shown with their errors ( $\alpha_{95}$ ) and the time span over which the poles have been averaged. The shaded area indicates the age of deformation, which migrated northwards through the Rhenish Massif from 325 Ma to 300 Ma. The white rectangles indicate the latitudinal errors of components B and C and their relative ages with respect to the deformation.

A chemical event, possibly triggered by fluid migration is favoured as the mechanism of this remagnetisation by the observations that component B is predominantly carried by magnetite with unblocking temperatures of 550 °C and that the magnetisation was acquired within a few My. The occurrence of hematite as a carrier of the Carboniferous remagnetisation is restricted to two localities of red carbonate rocks and siltstones. In both localities, the red carbonate and siltstone layers parallel the bedding and are thought to reflect oxidative conditions during sedimentation and/or early diagenesis. The fact that hematite carries component B in these lithologies, indicates that hematite was not reduced to magnetite, but recrystallised during remagnetisation.

Thermal demagnetisation results sporadically suggest the simultaneous formation of pyrrhotite and magnetite in carbonate and clastic rocks. It can be speculated that this is connected to the alteration of pyrite, which is omnipresent in the samples studied.

The theory of thermal activation for grain size distributions (WALTON, 1980) predicts higher unblocking temperatures for a viscous partial thermal remanent magnetisation (VpTRM), than the model SD particles of PULLAIAH *et al.* (1975). Even if the magnetic carriers of B follow the relaxation time - unblocking temperature relationship given by MIDDLETON & SCHMIDT (1982), which are based on WALTON'S (1980) theory, a VpTRM acquired during a few My would require palaeotemperatures well above 400 °C to explain the observed unblocking temperatures of 550 °C. However, neither CAI (KÖNIGSHOF, 1992) nor vitrinite reflectance data (PAPROTH & WOLF, 1973) indicate palaeotemperatures above 300 °C in the area studied. In the Carboniferous carbonate rocks of the RA, where unblocking temperatures of component B are around 500 °C, the palaeotemperatures did not exceed 200 °C. Therefore a VpTRM is not considered as an important mechanism of the remagnetisation in the NE Rhenish Massif.

The mean direction of component B (Inc: 1° - 4°) is similar to the direction of a high temperature component (Inc: 2°) reported by MOLINA GARZA & ZIJDERVELD (1996) from the Ardennes and the Brabant Massif. This indicates a similar age of a Late Carboniferous remagnetisation event in the Palaeozoic Massif on both sides of the Rhine river. However, according to MOLINA GARZA & ZIJDERVELD (1996), the high temperature component in the Ardennes and the Brabant Massif predates the deformation. If both components are coeval and are related to the same remagnetisation event, this would imply a different timing of the deformation in both regions, which is indicated by the different spacing of the deformation isochrons in the Ardennes and the Rhenish Massif (Fig. 4.2). The Late Carboniferous to Early Permian low temperature component (Inc: 10°) described by MOLINA GARZA &

ZIJDERVELD (1996), is not observed in the NE Rhenish Massif. In a recent study, ZEGERS *et al.* (2003) demonstrated that the relative intensity of this component shows a marked spatial correlation with a Mississippi Valley-type (MVT) ore district in the Ardennes, suggesting a direct genetic link between MVT fluids and this remagnetisation component. The absence of MVT ore deposits in the NE Rhenish Massif explains the fact, that the younger magnetic overprint is not observed in the samples from this region.

The postfolding component C yields a palaeolatitude of  $27^{\circ}\text{N}^{+10^{\circ}}/_-8^{\circ}$  indicating a Late Triassic to Early Jurassic age of this remagnetisation (Fig. 5.6). This overprint is mainly carried by hematite and could be the result of hematite-bearing mineralisations, which occur in rocks of the Rhenish Massif and are connected to uplift of the Rhenish Shield during Mesozoic times (WERNER, 1990). However, no direct evidence for those mineralisations was observed in the samples during field work or by light microscopy. Component C is exclusively observed within zones of tight folding and steep to overturned bedding planes and could alternatively be caused by oxidising fluids, migrating from the Mesozoic weathering surface along zones of increased permeability into the Palaeozoic strata.

# Chapter 6

## Magnetomineralogy

### 6.1 IRM acquisition and demagnetisation

Three characteristic shapes of IRM acquisition curves were observed, indicating a varying contribution of high coercivity phases in the sample set (Fig. 1a). The majority of specimens reach saturation at fields of 0.3 - 0.5 T (ALB3-8B in Fig. 6.1 a). During demagnetisation of a triaxial IRM (0.12 T, 0.4 T, 2.6 T; LOWRIE, 1990), the low coercivity component is most prominent and is removed at 600 °C, indicating the predominance of magnetite (Fig. 6.1 b).

In samples from red nodular limestones and red sandstones, the IRM acquisition behaviour indicates the simultaneous presence of a low and high coercivity phase (PLE1-4B in Fig. 6.1 a). The low and high coercivity components are demagnetised at ca. 580 °C and 670 °C, respectively, confirming the coexistence of magnetite and hematite, which both carry the Palaeozoic remagnetisation component (Fig. 6.1 c) in those lithologies.

In a few samples, magnetite is accompanied by pyrrhotite, which is indicated by the significant decrease in intensity of the medium coercivity component at about 350 °C (Fig. 6.1 d). The field to be applied in order to reach magnetic saturation of natural pyrrhotites is grain size dependent and varies between ca. 0.25 T and 2 T (DEKKERS, 1988). Therefore, the incomplete saturation at fields above 2 T (BOH1-5B in Fig. 6.1 a) is thought to be caused rather by traces of goethite or hematite than by pyrrhotite. In most carbonates a distinct decrease in NRM and IRM (high coercivity component) intensity is observed at ca. 150 °C, which indicates the presence of goethite.

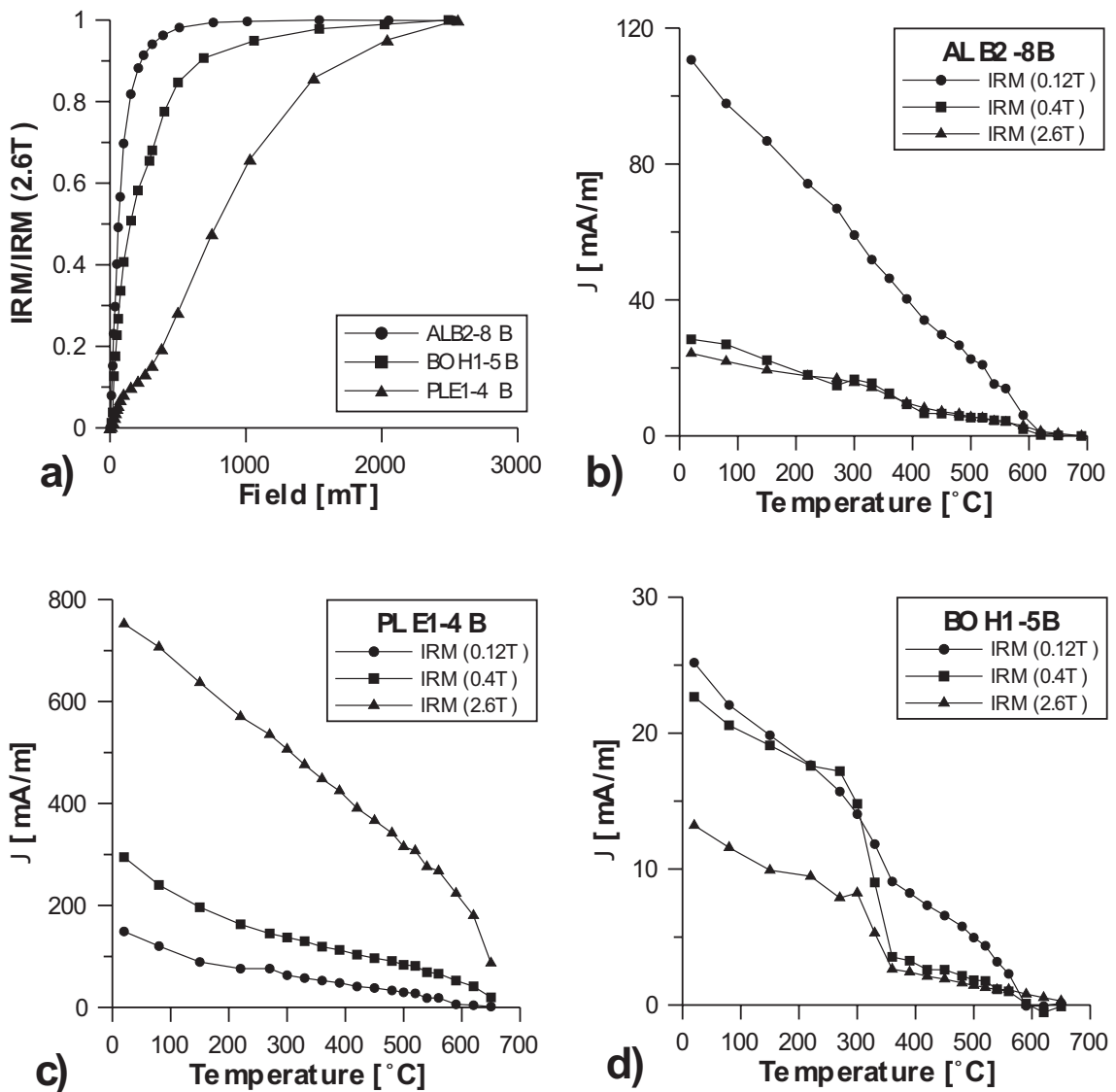


**Figure 6.1** IRM acquisition (a) and thermal demagnetisation of a triaxial IRM (0.12 T, 0.4 T, 2.6 T) of samples from b) siltstones (ALB3-8B), c) red sandstones (PLE1-4B) and d) quartzites (BOH1-5B). Magnetite ( $T_c$ : 580°C) is present in all samples and is accompanied by hematite ( $T_c$ : 670°C) in red sandstones (PLE1-4B) and pyrrhotite ( $T_c$ : ca. 320°C) in some siliciclastic rocks (BOH1-5B) and carbonates.

## 6.2 Low temperature experiments

The results of low temperature measurements carried out at the Institute for Rock Magnetism in Minneapolis, USA are shown in Fig. 6.2 for representative samples from different lithologies. The cooling of an IRM applied at room temperature (2.5 T at 300 K,  $IRM_{RT}$ ) from 300 K to 10 K (crosses in Fig. 2) and the thermal demagnetisation of a low temperature IRM (2.5 T at 10 K after zero-field cooling,  $IRM_{10K}$ ) from 10 K to 300 K (circles in Fig. 6.2) were observed in zero-field. Changes

of the thermal demagnetisation curve are accentuated by the first derivative of the magnetic moment over temperature ( $\log \left| \frac{\partial M}{\partial T} \right|$ , dashed lines in Fig. 6.2).

All samples are characterised by a sharp decrease in magnetisation during heating of the  $IRM_{10K}$  from 10 K to ca. 100 K. In carbonates (HEN1-5, Fig. 6.2 a), this is generally thought to reflect the presence of ultrafine magnetic material with very low  $T_{ub}$ . In clastic rocks (ALB1, BOH1-13, PLE1-4, Figs. 6.2 b-d), however, this behaviour could also be caused by iron-bearing silicates, which are paramagnetic at room-temperature, but magnetically ordered at very low temperatures (COEY, 1988, and references therein). The sharp increase in intensity of the  $IRM_{RT}$  on cooling below 30 K in samples ALB1 and BOH1-13 (Figs. 6.2 b,c) is probably caused by the combination of magnetic ordering and magnetic blocking in a small residual field within the MPMS (ca. 0.1 mT)

Although the NRM is carried by magnetite (and occasionally by magnetite and pyrrhotite/hematite) in carbonate rocks, samples from those lithologies show no distinct Verwey-transition at 120 K (HEN1-5, Fig. 6.2 a). However, a marked transition is observed in all clastic rocks. It is weakly developed in fine grained rocks (siltstones: ALB1, Fig. 6.2 b) and more pronounced in coarser lithologies (quartzitic sandstones: BOH1-13, Fig. 6.2 c; red sandstones: PLE1-4, Fig. 6.2 d). The Verwey-transition is also clearly developed during cooling of a room temperature IRM in the clastic lithologies (crosses in Figs. 6.2 b-d). The absence of the Verwey-transition in the carbonate rocks can be caused by either very small particle sizes or partly oxidised magnetite grains. Compared to the clastic lithologies, however, the carbonate rocks show no indications for intensified chemical alteration. Consequently, non-stoichiometric, oxidised magnetite is not expected to be solely responsible for the low temperature behaviour of the carbonates.

The presence of goethite in many carbonates is indicated by the increase in magnetisation during zero-field cooling of a  $IRM_{RT}$  (DEKKERS, 1989a, HEN1-5, crosses in Fig. 2a). The hypothetical maximum blocking temperature for goethite in sample HEN1-5 from a qualitative estimate shown as a dotted line in Fig. 6.2 a is about 360 K and somewhat lower than the Néel-temperature (393K) of pure goethite. This implies a small amount of isomorphous substitution of  $Fe^{3+}$  by e.g.  $Al^{3+}$  in the crystal lattice (DEKKERS, 1989a).

The occurrence of pyrrhotite in the samples from site BOH is reflected in the sharp decrease in IRM intensity on cooling at the pyrrhotite transition temperature (32 K, Fig. 6.2 c). The broad maximum between 150 K and 200 K of the IRM intensity during cooling has also been attributed to the presence of pyrrhotite (DEKKERS, 1989b; JACKSON *et al.*, 1993).

In none of the hematite bearing lithologies (e.g.: PLE1-4, Fig. 6.2 d) a signifi-

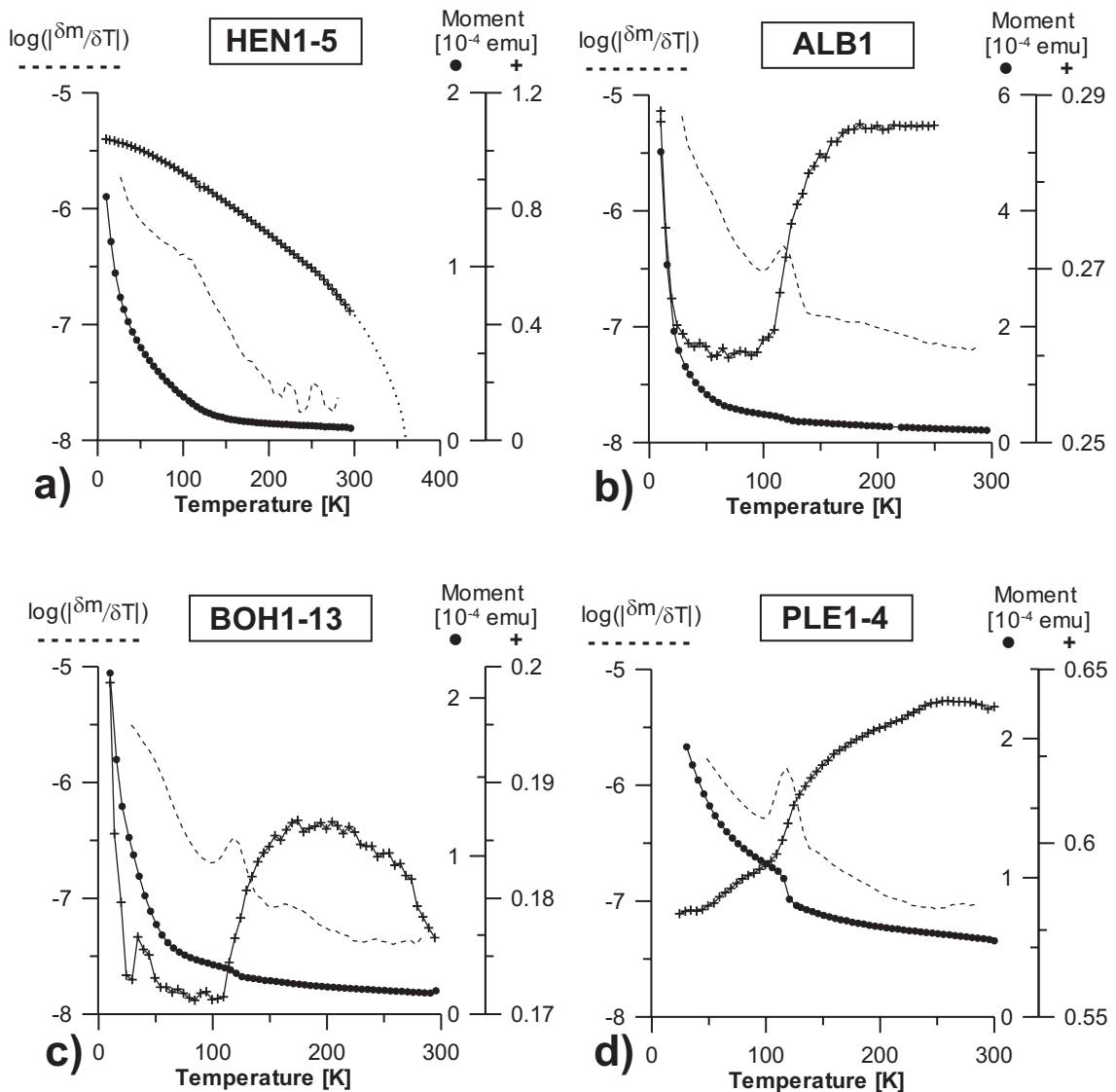


**Figure 6.2** Low temperature behaviour of a) carbonate rocks (HEN1-5, platform carbonate), b) siltstones (ALB1), c) quartzites (BOH1-13) and d) red sandstones (PLE1-4). Thermal demagnetisation of an IRM (2.5 T) acquired at 10K and cooling of an IRM (2.5 T) acquired at room temperature is shown with circles and crosses, respectively. The dashed lines mark the first derivative (log) of the heating curve and highlight the occurrence of the Verwey transition.

cant change in magnetisation occurs at the hematite transition temperature (Morin-transition, ca. 255 K - 265 K). However, the Morin-transition is very sensitive to impurities in the hematite crystal lattice and is suppressed by small amounts (e.g. 1 atom % Ti substitution) of foreign-ion substitution (MORRISH, 1994, and references therein). The temperature and height of the Morin-transition also depend on the particle size; it is completely absent in hematite grains with diameters less than  $0.1\mu\text{m}$  (BANDO *et al.*, 1965).

### 6.3 Hysteresis measurements

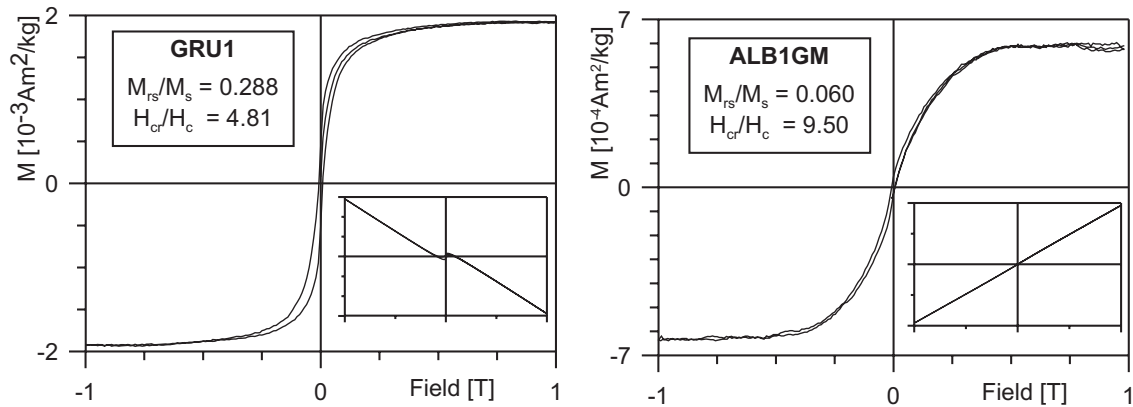


**Figure 6.3** Hysteresis curves of two samples from reef carbonates (GRU1) and siltstones (ALB1GM). The hysteresis curves of carbonates are often wasp-waisted, whereas the siliciclastic rocks are characterised by very slim loops. The insets show the original shape of the hysteresis loops before correction for diamagnetism (GRU1) and paramagnetism (ALB1GM).

Prior to interpretation, the hysteresis loops were corrected for paramagnetic or diamagnetic components. Reef carbonates (GRU1-8, Fig. 6.3 a) have "wasp-waisted" hysteresis loops, which are narrow at low external fields and wider at medium fields, whereas loops from clastic lithologies are generally very slim and not constricted (ALB1GM, Fig. 6.3 b). The misfit between the individual hysteresis branches at high fields in Fig. 6.3 b is a result of the large amount of paramagnetic material and a small systematic temperature change of the sample during measurement. A correction was made for this misfit during data analysis. The results from hysteresis measurements are shown in Table C.1.

Hysteresis results from samples, which did not reach complete saturation or where the IRM acquisition and demagnetisation and/or low temperature behaviour yield evidence for the presence of a high coercivity magnetic phase (goethite, hematite) or the predominance of pyrrhotite (e.g. sample BOH1-5B, Fig. 6.2 d) were rejected. Due to the presence of goethite in many carbonate rocks, only few results from carbonate lithologies are shown in Fig. 6.4.

The hysteresis ratios of the magnetite bearing sediments display a distinct relation to lithology. Samples from reef carbonates (squares in Fig. 6.4) have characteristically high hysteresis ratios, which fall on the mixing line ( $M_{rs}/M_s = 0.89 \cdot (H_{cr}/H_c)^{-0.6}$ , line a in Fig. 6.4), observed by JACKSON (1990) in remagnetised carbonates from North America. The hysteresis ratios of most clastic rocks fall on the mixing line of SD and MD magnetite (PARRY, 1982, line b in Fig. 6.4). Here, the high values of  $H_{cr}/H_c$  and low values of  $M_{rs}/M_s$  indicate the predomi-

nance of MD magnetite. The platform carbonates (triangles in Fig. 6.4) and some fine-grained clastic rocks (siltstones) have significantly higher hysteresis ratios than SD-MD mixtures and fall between the two groups described above (line c in Fig. 6.4). This relation between hysteresis ratio and lithology is also observed in samples where IRM demagnetisation and low temperature measurements indicate that magnetite is accompanied by small amounts of pyrrhotite (open symbols in Fig. 6.4; sample BOH1-5B from Fig. 6.2 d is not included here).

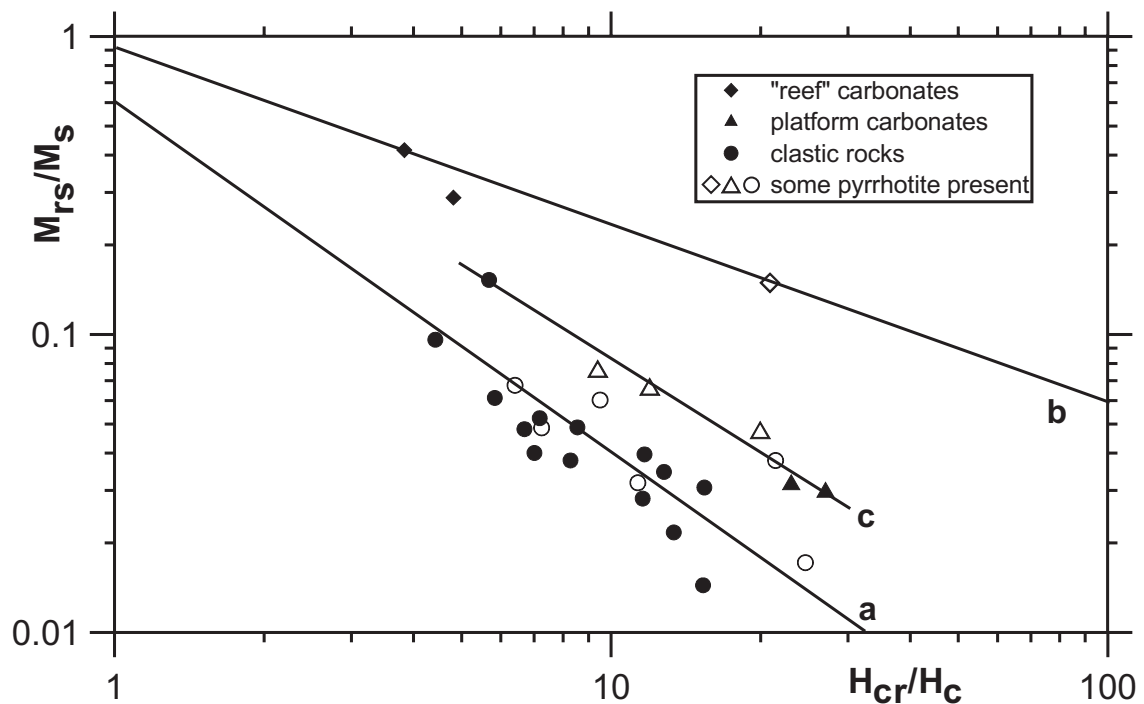


**Figure 6.4** Plot of the hysteresis ratios  $M_{rs}/M_s$  and  $H_{cr}/H_c$ . The majority of siliciclastic rocks (circles) fall on the SD-MD mixing line after PARRY (1982, line a), whereas reef carbonates (diamonds) have hysteresis properties similar to those obtained from North American remagnetised carbonates (JACKSON, 1990, line b). Fine grained clastic rocks and platform carbonates (triangles) fall both groups described above (line c). Samples, where a small contribution from pyrrhotite was observed during thermal demagnetisation of a triaxial IRM and heating of a  $IRM_{10K}$  (open symbols), show a similar relation between lithology and hysteresis ratios.

## 6.4 Viscosity and frequency dependence of susceptibility

The viscous decay of an IRM (1 T) was observed for 300 s. The measurement was started 10 s after IRM acquisition to allow for decay of the magnetic field induced by the solenoid. The remanence decreases between 2% and 7% during the experiments in samples from all lithologies (Fig. 6.5 a). This decay is caused by

thermally activated domain wall jumps in MD particles or by grains just above the superparamagnetic threshold that have relaxation times in the order of tens of seconds (DUNLOP & ÖZDEMİR, 1997a). It can be described by the viscosity coefficient  $S = \left| \frac{\partial M}{\partial \log(t)} \right|$ , normalised by the initial remanence  $M_r(10s)$ .

The magnetic viscosity coefficient (Fig. 6.5 b) of most carbonate rocks and hematite-bearing lithologies (e.g. ATT2-7 in Fig. 6.5 a) varies between  $0.025 \text{ s}^{-1}$  and  $0.03 \text{ s}^{-1}$  and is significantly higher than for the majority of clastic rocks (ca.  $0.01 - 0.02 \text{ s}^{-1}$ , e.g. LOS3-4 in Fig. 6.5 a). The observation of a higher magnetic viscosity in lithologies with few or no amounts of MD magnetite indicates a significant contribution from very fine grained magnetite.

A significant change (4% - 8%) in susceptibility during frequency sweeps from 40 Hz to 4000 Hz (AC field:  $200 \text{ Am}^{-1}$ ) at room temperature was observed only in carbonate rocks and few clastic rocks. Although the bulk susceptibilities of the clastic samples are relatively high ( $10^{-3}$  to  $10^{-5}$  SI), the changes with frequency were mostly below the sensitivity of the Lakeshore susceptometer, which was estimated by repeated measurements of a paramagnetic material ( $\text{Gd}_2\text{O}_3$ ). The small frequency dependence of the clastic rocks is thought to result from a very small contribution of superparamagnetic material to the bulk susceptibility, which is dominated by paramagnetic minerals and MD magnetite. This is also reflected by a low ratio of ferromagnetic to paramagnetic susceptibility of less than 5%.

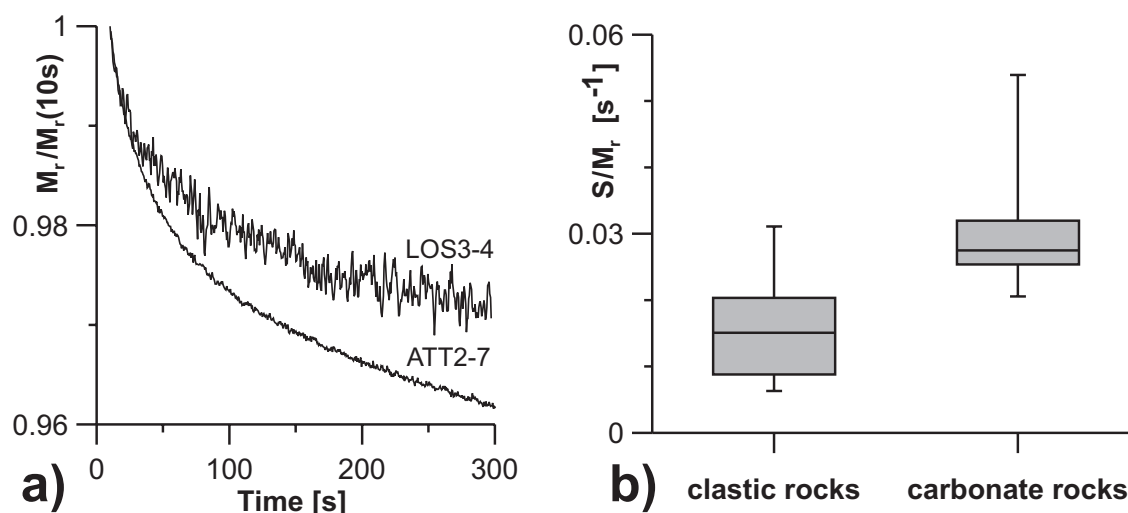


**Figure 6.5** a) Viscose decay of an IRM (1 T) for two samples from siliciclastic rocks (LOS3-4) and red nodular limestones (ATT2-7); b) median (horizontal line), range of mean 50% of results (shaded boxes) and extreme values (caps) of the viscosity coefficient for clastic and carbonate rocks.

## 6.5 Interpretation of rock magnetic results

The remagnetised rocks from the NE Rhenish Massif yield a wide spectrum of rock magnetic properties. The appearance of the Verwey transition, which is prominent in clastic rocks but suppressed or absent in carbonate rocks indicates different amounts of MD magnetite of detrital origin in siliciclastic rocks, platform carbonates and reef carbonates. This is supported by the ratio  $M_{rs}/M_s$ , which is high ( $> 0.15$ ) for reef carbonates and low ( $< 0.08$ ) for clastic rocks, with intermediate values for detrital carbonates.

The different lithologies studied here can be discriminated in a plot of  $M_{rs}/M_s$  against the relative change in magnetisation across the Verwey-transition ( $\frac{M(100K)-M(130K)}{M(100K)}$ , Fig. 6.6). The trend from high  $M_{rs}/M_s$  and an absent Verwey transition in reef carbonates to low  $M_{rs}/M_s$  and a distinct Verwey transition in siliciclastic rock reflects an increasing contribution from detrital MD magnetite.

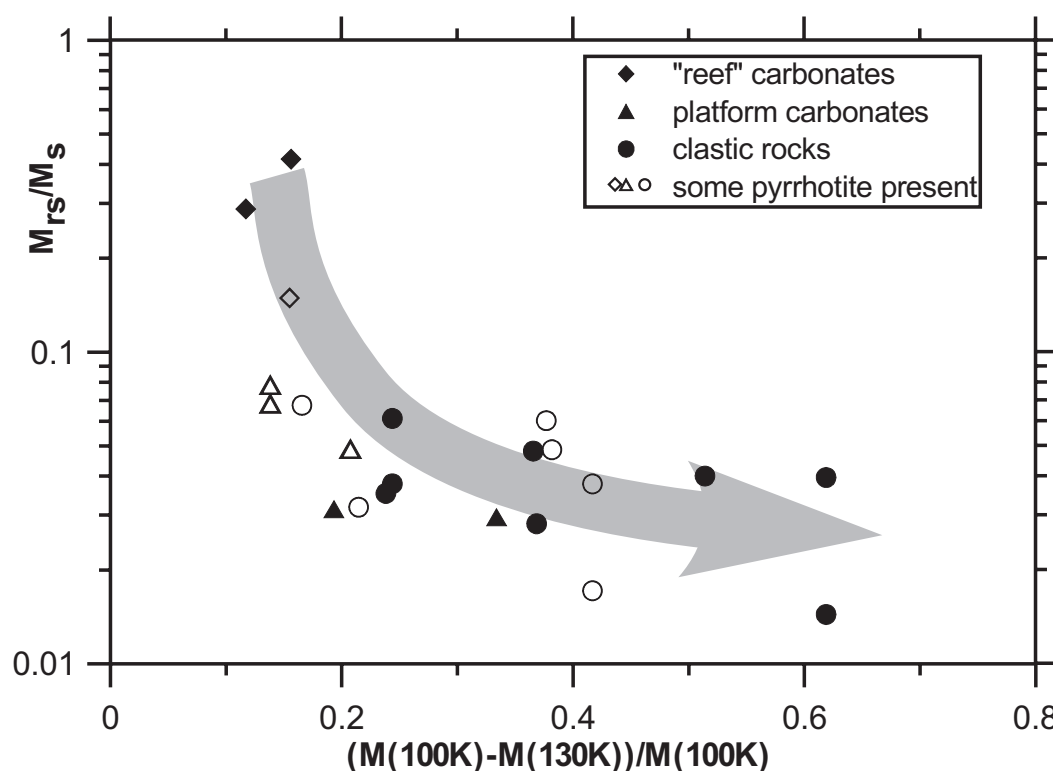


**Figure 6.6** The ratio  $M_{rs}/M_s$  plotted against the intensity decay across the Verwey transition during heating of an  $IRM_{10K}$  in zero field. The arrow indicates the trend of increasing amount of MD magnetite with decreasing  $M_{rs}/M_s$  and increasing size of the Verwey transition.

Detrital input and contribution from MD magnetite is low in carbonate rocks. Their rock magnetic properties ( $IRM_{10K}$  intensity decrease between 10 K - 100 K, frequency dependence of susceptibility) are indicative for the presence of very fine

grained material. Particularly, the high magnetic viscosity and high  $M_{rs}/M_s$  ratios in the carbonates with few or no contribution from MD magnetite evidence the existence of very fine grained magnetic material with relaxation times in the order of tens of seconds or below. Reef carbonates have hysteresis ratios which correlate with values reported by JACKSON (1990) for remagnetised carbonates from the North American Hercynian foldbelt.

The high detrital input of the siliciclastic rocks is reflected in low hysteresis ratios and in a high paramagnetic susceptibility, which are indicative of a large amount of MD magnetite and paramagnetic silicate minerals, respectively. Instead of being indicative of the presence of very fine grained magnetite, the decrease in  $IRM_{10K}$  in those rocks could be caused by paramagnetic minerals, which magnetically order at very low temperatures. The magnetic viscosity in the siliciclastic rocks might result from the movement of domain walls in MD magnetite, rather than viscous unblocking of magnetite, close to the SP-SD grain size threshold. Consequently, the massive contribution of paramagnetic minerals and MD magnetite to the rock magnetic properties of the siliciclastic rocks disguises any possible contribution from fine grained material.

The hysteresis properties of platform carbonates and some fine grained clastic rocks (siltstones) fall between the values of the lithologies described above. Their hysteresis ratios are lower than those of the reef carbonates and significantly higher than those of most siliciclastic rocks and pure MD-SD magnetite mixtures. Compared to medium to coarse grained siliciclastic rocks (sandstones, greywackes), terrigenous material is expected to be less abundant in platform carbonates and more fine grained in siltstones. Therefore, the amount (and total volume) of magnetite grains above the SD-MD boundary is expected to be smaller in both lithologies. The observation of intermediate hysteresis results in those rocks indicates the coexistence of two generations of magnetite in the sediments of the NE Rhenish Massif: a) detrital magnetite, predominantly in MD state and b) authigenic mixtures of SD magnetite dominated by magnetocrystalline anisotropy and ultrafine (SP) magnetite. Based on the observation of intermediate hysteresis results in some fine grained siliciclastic rocks, it seems reasonable to predict the existence of the authigenic magnetite generation in the clastic rocks in general, although it is often disguised by MD magnetite.

The thermal demagnetisation behaviour of the NRM indicates, that pyrrhotite and hematite carry the remagnetisation component in some samples (ZWING *et al.*, 2002). The presence of pyrrhotite in some rocks from the NE Rhenish Massif is confirmed by the thermal demagnetisation pattern of a triaxial IRM and the observations of the low temperature transition of pyrrhotite at 35 K during the low

temperature experiments. Where it is present in small amounts only, pyrrhotite does not significantly affect the hysteresis results (Fig. 6.4).

Despite the identification of hematite during thermal demagnetisation of the triaxial IRM, the Morin transition was never observed during the low temperature experiments and is thought to be suppressed by very small particle sizes and small amounts of foreign-ion substitution.

# Chapter 7

## K-Ar dating and trace element geochemistry of authigenic illites and Fe-oxide leachates

### 7.1 Characterisation of clay fractions

#### 7.1.1 Microscopic observations

Transmitted light microscopy of polished thin sections showed no evidence for pervasive internal deformation in the rocks studied, while primary sedimentary fabrics, such as bioturbation and imbrication of sheet silicates and shell fragments are preserved in many rock types. Bioclasts and oolites in carbonates are undeformed and recrystallised into sparitic calcite and dolomite. Lamination in siltstone results from varying amounts of quartz grains in a clay matrix (chlorite), which is characterised by irregular textures. Formation of foliation by oriented recrystallisation or alignment of sheet silicates is not observed. However, pressure solution along grain boundaries is common in quartz-rich lithologies. The samples are generally characterised by high compaction and very low porosities. The intergranular pore spaces in sandstones and early intraparticle and vuggy porosities in carbonate rocks are filled with calcite and dolomite cements. Small amounts of free intergranular porosity was only observed in greywackes.

Two different types of illite were identified by SEM observations. Subhedral and irregular illite crystals occur as overgrowth of detrital and authigenic minerals. In carbonates, illite coats large grains of authigenic kaolinite ( $< 10\mu m$ ), which occurs in calcite veins (LET, Fig. 7.1 a). Overgrowth of subhedral illite was also observed on detrital muscovites of siltstones and sandstones. Illite with lamellar to fibrous textures fills small intergranular pores in greywackes (OLP, Fig. 7.1 b).

The clay fractions are generally characterised by irregular illite morphologies, while idiomorphic hexagonal or elongated shapes are rare. The grain size distribution of the illite grains in the  $< 2\mu\text{m}$  fractions is highly inhomogeneous and even the smallest grains have irregular morphologies (HAC, Fig. 7.1 c). This supports either illite growth hindered by highly constricted interstitial space or grain destruction during sample preparation by overcrushing. However, the irregular illite morphologies and inhomogeneous grain sizes are observed in both the clastic and carbonate lithologies. While overcrushing is a well-known problem in clastic rocks, the final disaggregation of carbonates is done by dissolution with acetic acid, which cannot account for the observed morphologies of the clay minerals. In addition, the clay minerals released from washed rock fragments of sample HAM after short ultrasonic treatment (1 min) show the same characteristics as the  $< 2\mu\text{m}$  fractions (Fig. 7.1 d). This strongly attests against significant effects of sample preparation on the morphologies and grain sizes of the clay minerals and indicates a highly restricted interstitial volume during illite growth.

TEM studies demonstrate the presence of large amounts of clay minerals with particle sizes  $< 0.2\mu\text{m}$  (Fig. 7.1 c,d) in all studied lithologies from the NE Rhenish Massif. Due to its low contamination by detrital sources, this grain size fraction is thought to represent best the authigenic clay minerals and it was used for K-Ar age determinations and trace element geochemistry after separation from a part of the  $< 2\mu\text{m}$  fraction by ultra high-speed centrifugation (overflow centrifuge) following the procedure described by LARQUE & WEBER (1978).

### 7.1.2 Mineralogy and illite crystallinity

XRD analysis show that illite and chlorite are the dominant minerals of the  $< 0.2\mu\text{m}$  fractions. Illite was identified by strong reflections at  $10\text{\AA}$  (001),  $5\text{\AA}$  (002) and  $3.3\text{\AA}$  (003), while chlorite is characterised by peaks at  $14\text{\AA}$  (001),  $7\text{\AA}$  (002),  $4.7\text{\AA}$  (003) and  $3.5\text{\AA}$  (004). The presence of kaolinite in one sample (LET) is indicated by a reflection at  $7\text{\AA}$  and its change after treatment with hydrazine. In many samples, weak reflections at  $4.26\text{\AA}$  and  $3.15\text{\AA}$ -  $3.21\text{\AA}$  indicate the presence of small amounts of quartz and feldspars, respectively. Feldspar is mostly identified in the  $< 0.2 - 2\mu\text{m}$  and  $< 2\mu\text{m}$  fractions of some samples, while not observed in the  $< 0.2\mu\text{m}$  fractions. It should be mentioned that the identification of small amounts of K-feldspar by XRD in samples containing large amounts of illite is generally difficult. The mineralogy of the  $< 0.2\mu\text{m}$  fractions resulting from the XRD patterns is given in Tab. D.2.

The XRD patterns of the  $< 0.2\mu\text{m}$  and  $< 2\mu\text{m}$  fractions are significantly different, depending on the clastic or carbonate lithology of the rocks. The  $< 2\mu\text{m}$

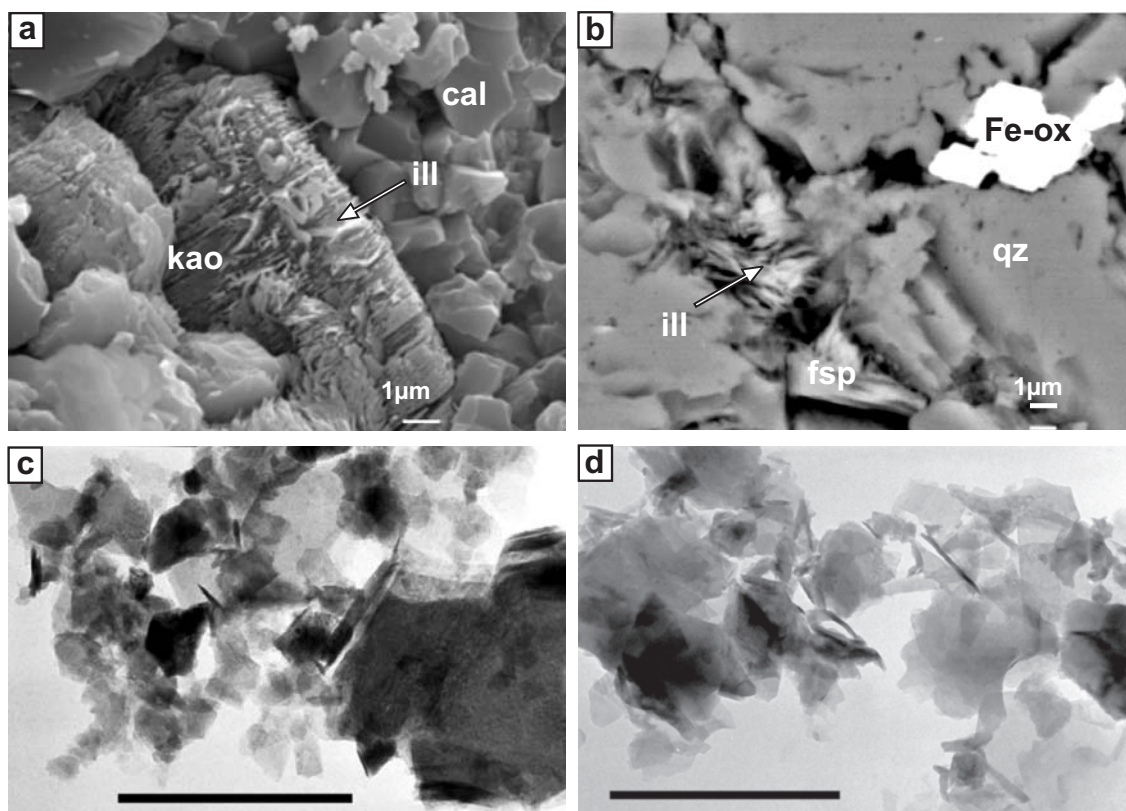


**Figure 7.1** Scanning (SEM) and transmission (TEM) electron micrographs. a) SE image of a fragment from sample LET; ill, illite; kao, kaolinite; cal, calcite. b) BSE image of a polished thin section of sample OLP; qz, Quartz; fsp, feldspar; Fe-ox, iron oxide (magnetite). c) TEM image of the  $< 2\mu\text{m}$  fraction from sample HAC. d) TEM image of fine grained material released from washed rock fragments of sample HAM after ultrasonic treatment (1 min). c,d) Length of bar is  $1\mu\text{m}$ .

fractions from clastic rocks (e.g. ALB3, Fig. 7.2 a) contain illite, chlorite and small amounts of quartz and albite. In the very fine fractions ( $< 0.2\mu\text{m}$ ), the relative intensities of the  $10\text{\AA}$  and  $14\text{\AA}$  peaks indicate a higher amount of illite and lower, but still considerable quantities of chlorite (ca. 25% - 40%). Here, the intensities of the  $14\text{\AA}$  peak increase after heating to  $490^\circ\text{C}$ , which is indicative of Fe-rich chlorites. In the  $< 2\mu\text{m}$  and  $< 0.2\mu\text{m}$  fractions from carbonate rocks, illite is the predominant mineral and the amounts of chlorite and of other accessory minerals are very small (e.g. STC, Fig. 7.2 b).

The (001) reflection is generally asymmetrical with a tail towards lower diffraction angles and moves to slightly higher diffraction angles (max.  $0.4^\circ 2\theta$ , Cu  $K_\alpha$ ) after treatment with glycol. Both, the asymmetry and the change in peak position are more pronounced in carbonate rocks and are characteristic for illite - smectite interstratification (BRINDLEY & BROWN, 1980). However, the difference in width of the  $10\text{\AA}$  peak from untreated and glycolated samples does not exceed 1 mm and in

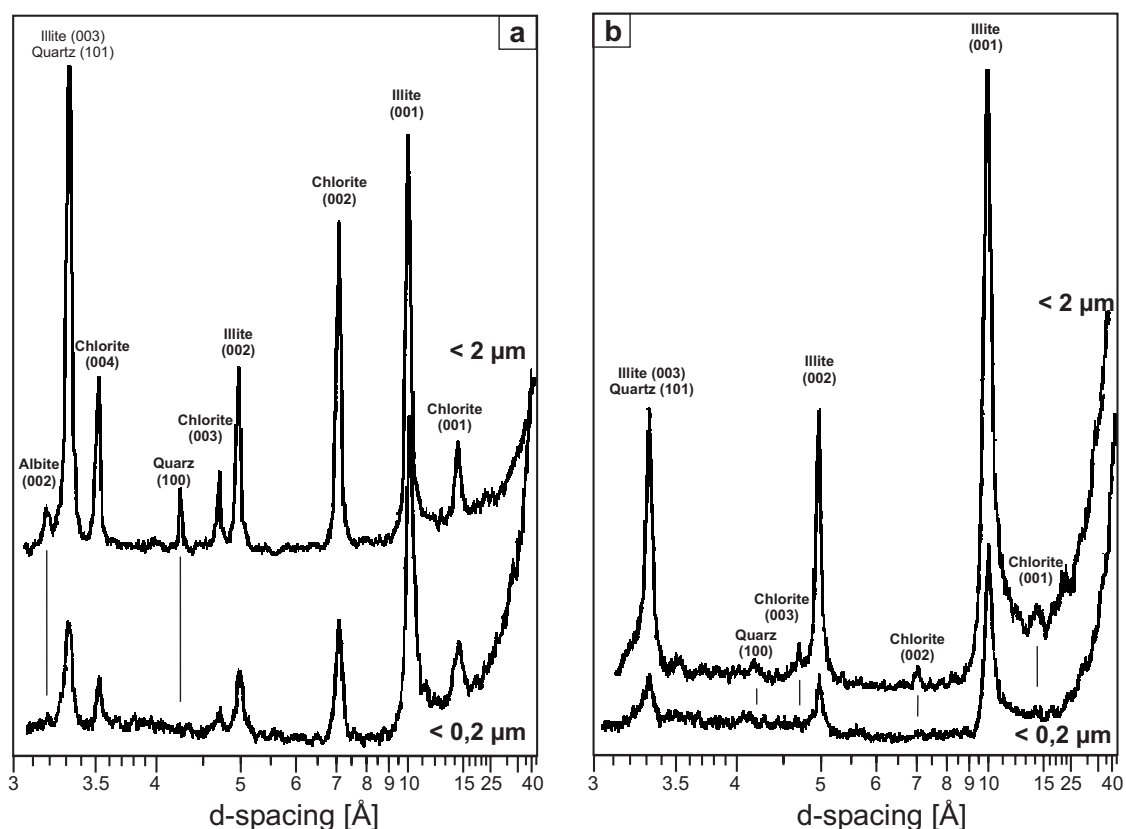


**Figure 7.2** XRD patterns for the  $< 0.2\mu\text{m}$  and  $< 2\mu\text{m}$  fractions from (a) the sandstone sample ALB3 and (b) the carbonate STC. The amount of detrital minerals, such as quartz and albite is significantly smaller in the fine fractions.

some samples the  $10\text{\AA}$  peak is slightly sharper after treatment with ethylene-glycol (Fig. 7.3). Compared to the relatively low accuracy of the width measurements ( $0.5\text{ mm}$ ), the differences in the  $10\text{\AA}$  peak width of untreated and glycolated samples are not significant, which indicates only very small amounts of smectite interstratification.

The ICI of the  $0.2 - 2\mu\text{m}$  air-dried fractions ranges from 3 mm to 8 mm FWHM ( $0.3 - 0.8^\circ 2\theta$ , Cu  $K_\alpha$ , Fig. 7.3, Table D.1). It is lowest in carbonate samples from the Remscheid Anticline and Paffrath Syncline (7 - 8 mm FWHM, RA and PS in Fig. 7.3) and significantly higher in the clastic rocks from the Lüdenscheid, Attendorn and Wittgenstein Synclines (3 - 4.5 mm FWHM, LS and AS/WS in Fig. 7.3). The clay fraction from a tuff layer (BOH) has an unusually low ICI (7.5 mm FWHM). The ICI of the  $< 0.2\mu\text{m}$  air dried fractions is generally lower with a FWHM up to 10 mm (sample LER), but follows the same trend as the coarser fractions.

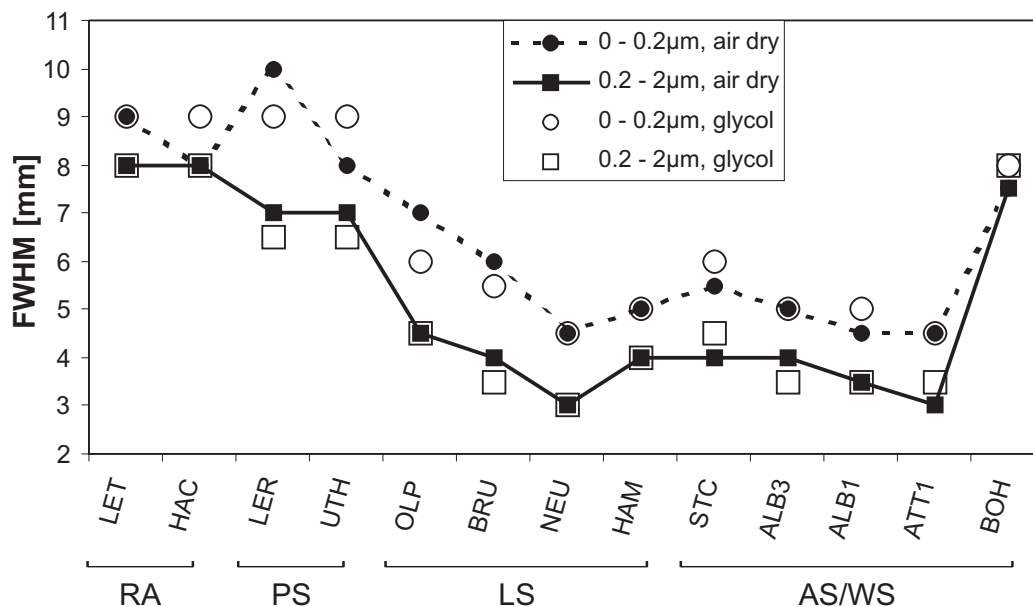


**Figure 7.3** The full width at half maximum (FWHM) of the illite  $10\text{\AA}$  peak in mm as a measure of the illite crystallinity index (ICI) of  $< 0.2\mu\text{m}$  (circles) and  $0.2 - 2\mu\text{m}$  (squares) fractions without treatment (solid symbols) and after treatment with ethylene-glycol (open symbols). 1 mm equals  $0.1^\circ 2\theta$ , Cu  $K\alpha$ . Glycol treatment did not significantly change the width of the  $10\text{\AA}$  peak. RA, Remscheid Anticline; PS, Paffrath Syncline; LS, Lüdenscheid Syncline; AS/WS, Attendorn and Wittgenstein Synclines.

## 7.2 K-Ar dating of the $< 0.2\mu\text{m}$ fractions

### 7.2.1 Effects of sample preparation and grain size on the apparent K-Ar ages

The influence of different disaggregation methods on the apparent K-Ar ages was studied on clay fractions of four samples (LET, HAC, ALB1, ATT1). A first set of clay fractions ( $< 2\mu\text{m}$ , in the following called LETa, HACa, ALB1a, ATT1a and  $< 0.2\mu\text{m}$ , LETb, HACb, ALB1b, ATT1b) was extracted after gentle disaggregation of rock pieces using repetitive freezing-thawing cycles for three months (LIEWIG *et al.*, 1987). Due to the high degree of cementation and low permeability of the rocks, the repetitive freezing-thawing cycles were not successful and the samples had to be crushed in an agate hand mortar and a mortar grinder with an agate grinding set (Retsch RM 100). Carbonate was dissolved with 1N hydrochloric acid. Except for clay fraction HACa, the  $< 2\mu\text{m}$  fractions yield the highest apparent K-Ar ages in the sample set (open circles in Fig. 7.4). The apparent age of ALB1a ( $388 \pm 9$  Ma) is close to the age range of detrital muscovites from the Rhenish Massif (409 - 459

Ma; FRANKE, 2000, and references therein). This clearly reveals contamination by detrital muscovite or K-feldspar, which is also indicated by the XRD patterns of some  $< 2\mu\text{m}$  fractions.

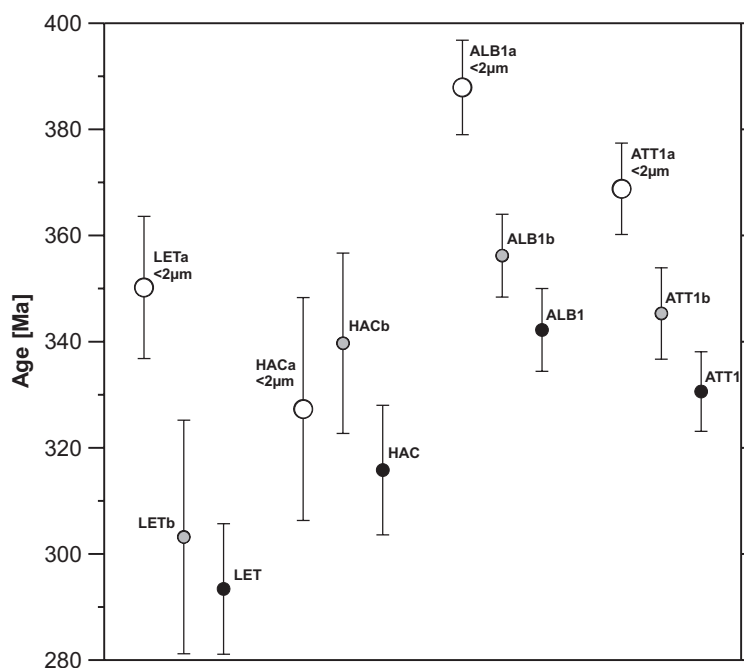


**Figure 7.4** K-Ar ages with uncertainties of clay fractions from four pilot samples. From each sample, three fractions were analysed to evaluate the effects of grain size and disaggregation method on the K-Ar ages. Open and grey circles:  $< 2\mu\text{m}$  and  $< 0.2\mu\text{m}$  fractions after freezing-thawing experiments, grinding and treatment with 1N hydrochloric acid; black circles:  $< 0.2\mu\text{m}$  fractions after gentle grinding and treatment with a buffered solution of acetic acid. For sample description see Table A.2.

The apparent K-Ar ages of the  $< 0.2\mu\text{m}$  fractions (grey and black circles in Fig. 7.4) are significantly lower than those of the corresponding  $< 2\mu\text{m}$  fractions, suggesting a lower influence of the detrital material. However, the samples from carbonate rocks yield quite large uncertainties (LETb:  $303 \pm 22$  Ma, HACb:  $340 \pm 17$  Ma), which are caused by low potassium contents and by high amounts of atmospheric Ar, which is probably absorbed during sample preparation (see Table E.2 for K-Ar analytical data). Due to the large uncertainties, the K-Ar results of the clay fractions LETb and HACb were discarded from further interpretation.

A second set of  $< 0.2\mu\text{m}$  fractions was separated from the pilot samples after gentle crushing with the Retsch RM 100 mortar grinder and treatment with a buffered solution of acetic acid for removal of carbonate minerals. These clay fractions (black circles in Fig. 7.4, in the following called LET, HAC, ALB1 and ATT1) yield similar K-Ar ages (within analytical uncertainty) and smaller uncertainties than the first set

of separates and the comparison outlines similar effects of the two separation procedures on the  $< 0.2\mu\text{m}$  fractions. It was therefore decided to use the gentle crushing and treatment with acetic acid for all samples from the NE Rhenish Massif.

## 7.2.2 Apparent K-Ar ages of $< 0.2\mu\text{m}$ fractions

All apparent K-Ar ages of the  $< 0.2\mu\text{m}$  fractions fall within the range from  $293 \pm 12$  Ma (LET) to  $359 \pm 8$  Ma (HAM, Table E.2) and are younger than the sedimentation age of the respective rock samples, indicating the dominant authigenic nature of the clay minerals. The relation between apparent K-Ar age, lithology and illite crystallinity is given in Fig. 7.5. The samples follow a general trend of increasing apparent age with increasing ICI (decreasing FWHM in Fig. 7.5). With the exception of samples LER and OLP, the  $< 0.2\mu\text{m}$  fractions from clastic rocks with high illite crystallinity (FWHM: 4 - 6 mm, circles in Fig. 7.5) yield higher apparent ages ( $331 \text{ Ma} \pm 8$  to  $345 \text{ Ma} \pm 9$ ) than the  $< 0.2\mu\text{m}$  fractions from carbonate rocks ( $293 \pm 12$  Ma to  $320 \pm 8$  Ma), where the ICI is comparably low (FWHM: 5.5 - 9 mm, diamonds in Fig. 7.5).

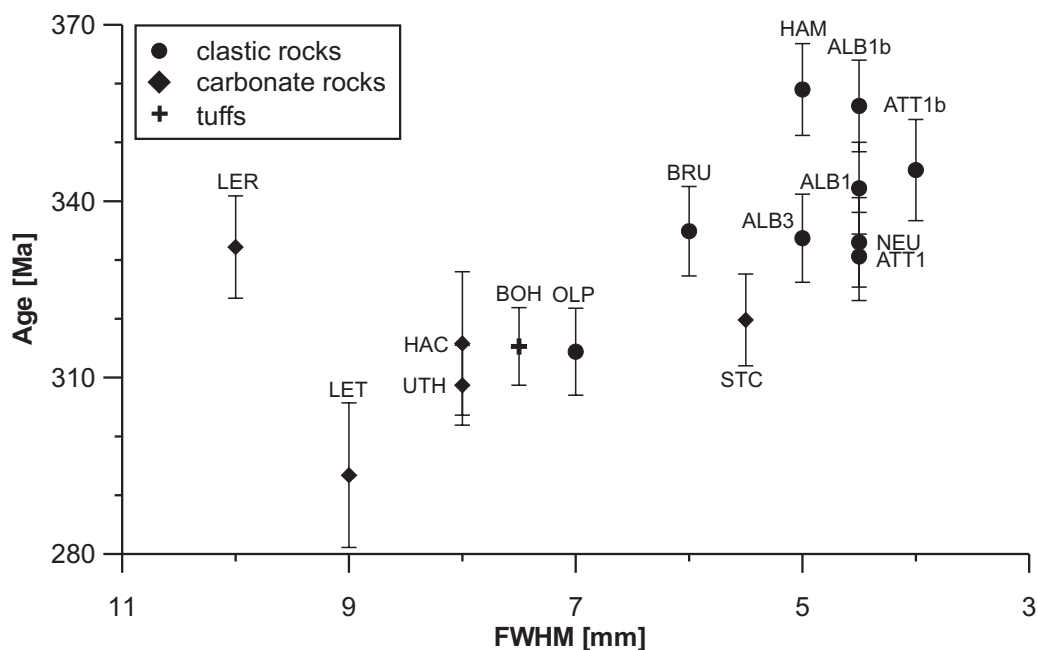


**Figure 7.5** Plot of apparent K-Ar ages versus FWHM of the  $10 \text{ \AA}$  peak as a measure of the illite crystallinity index. With exception of LER, the samples follow a general trend of increasing apparent age with increasing illite crystallinity (decreasing FWHM). See text for further discussion.

The sample distribution in Fig. 7.5 suggests that the apparent ages of the clay fractions, which span the entire time period from 293 Ma to 359 Ma are related to the illite crystallinity of the samples. This could be interpreted to indicate preferential

loss of  $^{40}\text{Ar}$  from less well crystallised illites with low ICI after a single crystallisation event at ca. 350 Ma. However, within the group of Mid-Devonian clastic rocks (circles in Fig. 7.5 except sample OLP), the correlation between apparent age and illite crystallinity is not observed. Alternatively, the higher apparent ages and ICI in clastic rocks could reflect significant contamination by detrital components. In order to identify possible loss of radiogenic  $^{40}\text{Ar}$  or the presence of detrital components, the K-Ar dates were analysed using isochron plots.

### 7.2.3 Definition of K-Ar isochrons

Mixtures of two or more mineral parageneses with different formation ages or loss of radiogenic  $^{40}\text{Ar}$  from illite lattices can usually be identified by the  $^{40}\text{Ar}/^{36}\text{Ar}$  intercepts of a regression line in a plot of  $^{40}\text{Ar}/^{36}\text{Ar}$  versus  $^{40}\text{K}/^{36}\text{Ar}$  and the amount of scatter of the data along the regression line. As the proportions of the different mineral parageneses or the amount of  $^{40}\text{Ar}$  lost by diffusion are likely to vary from sample to sample, the resulting regression in a plot of  $^{40}\text{Ar}/^{36}\text{Ar}$  versus  $^{40}\text{K}/^{36}\text{Ar}$  is a mixing line. The  $^{40}\text{Ar}/^{36}\text{Ar}$  intercept of a mixing line is likely to be different from the initial isotopic composition of the mineral parageneses, which is similar to the present-day atmospheric  $^{40}\text{Ar}/^{36}\text{Ar}$  ratio in most cases (295.5, CLAUER & CHAUDHURI, 1995, and references therein). Furthermore, the observed scatter of the data, defining a mixing line is much larger than the analytical scatter, which results in large values of the mean square of weighted deviates (MSWD). Ideally, real isochrons should have an MSWD of 1.0 or less. Due to the limited number of samples in a normal data-set, the MSWD is often larger than 1.0 and BROOKS *et al.* (1972) suggested that 2.5 is an acceptable cut-off for the definition of an isochron. However, it should be kept in mind, that the natural inhomogeneities of sediments can cause additional scatter and higher MSWD values.

In a plot of  $^{40}\text{Ar}/^{36}\text{Ar}$  versus  $^{40}\text{K}/^{36}\text{Ar}$ , the analytical K-Ar data of most samples fall on or close to one of two regression lines. Both regression lines yield low MSWD values and initial  $^{40}\text{Ar}/^{36}\text{Ar}$  ratios close to the present-day value (295.5), which are given by the intercept of the regression line with the ordinate. Therefore, the regression lines are interpreted as isochrons (isochrons A and B; Fig. 7.6).

Isochron A is defined by  $< 0.2\mu\text{m}$  fractions of the Middle Devonian clastic rocks (ALB1, ATT1, ATT1b, BRU, NEU and ALB3; closed circles in Fig. 7.6) and yields an age of  $348 \pm 7.2$  Ma. The initial  $^{40}\text{Ar}/^{36}\text{Ar}$  ratio ( $(^{40}\text{Ar}/^{36}\text{Ar})_{ini}$ ) is  $284 \pm 40$  and the MSWD is close to unity (0.97). It should be mentioned, that the fractions ATT1 and ATT1b, which both enter the calculation of isochron A, were extracted from the same sample by different separation procedures and are not strictly independent. Fraction ATT1b was extracted with the procedure using repetitive freezing-thawing

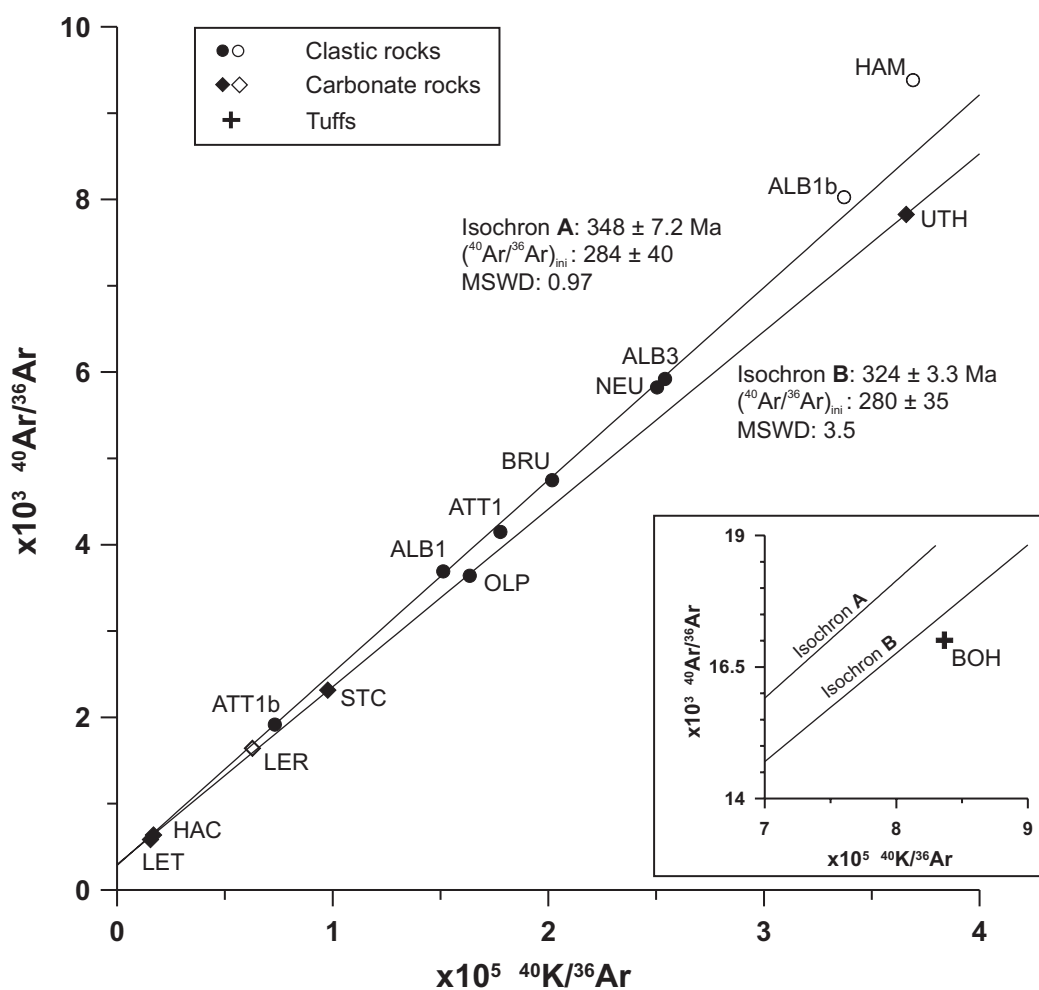


**Figure 7.6** K-Ar isochrons for isotopic data from  $< 0.2\mu\text{m}$  fractions. The data plot along two different isochrons: Isochron A for Middle Devonian clastic rocks (closed circles) and isochron B for Upper Devonian and Lower Carboniferous carbonate rocks (closed diamonds) and a Namurian greywacke (OLP). Clay fractions ALB1b, HAM and LER (open symbols) are contaminated by detrital material and were not used for the isochron determination. The clay fraction from tuff sample BOH is characterised by exceptionally high ratios of  $^{40}\text{Ar}/^{36}\text{Ar}$  and  $^{40}\text{K}/^{36}\text{Ar}$  (cross, see inset for an expansion of main diagram) and plots below both isochrons. The analytical errors are smaller than the size of the symbols.

cycles and hydrochloric acid. If ATT1b is omitted, the resulting isochron is less reliable and has large uncertainties ( $333 \pm 22$  Ma,  $(^{40}\text{Ar}/^{36}\text{Ar})_{\text{ini}}: 473 \pm 220$ , MSWD: 0.42). Due to the large error, the age is not significantly different from the age of isochron A. Isochron B is defined by the  $< 0.2\mu\text{m}$  fractions of the Upper Devonian and Lower Carboniferous carbonate rocks (LET, HAC, STC and UTH; closed diamonds in Fig. 7.6) and one sample from Namurian greywackes (OLP) and gives an age of  $324 \pm 3.3$  Ma with a MSWD of 3.5 and  $(^{40}\text{Ar}/^{36}\text{Ar})_{\text{ini}}$  of  $280 \pm 35$ .

Four samples do not follow the observed trend and were not used for isochron determination. The clay fractions of two sandstone samples (ALB1b, HAM; open

circles in Fig. 7.6) both plot clearly above isochron A. This could be caused either the presence of a second, older paragenesis of K-bearing minerals or by excess  $^{40}\text{Ar}$  during illite formation. Excess  $^{40}\text{Ar}$  can result from  $^{40}\text{Ar}$  mobilisation from older minerals during diagenesis and incorporation of  $^{40}\text{Ar}$  into the crystal structure of authigenic illites during crystallisation (inherited  $^{40}\text{Ar}$ ). However, the clay fraction ALB1, which was separated from the same rock sample as ALB1b, falls onto isochron A and shows no evidence for excess  $^{40}\text{Ar}$  during illite formation. Furthermore, such a mechanism would be expected to affect other samples with similar lithology (BRU) or provenance (ALB3), which is not the case. The more likely cause for the high  $^{40}\text{Ar}$  contents and high apparent ages of clay fractions ALB1b and HAM is a contamination by small amounts of detrital material. For both samples, the ICI is not higher than for samples from similar lithologies (Fig. 7.3), excluding the presence of significant amounts of detrital muscovite. The high apparent ages are probably caused by detrital K-feldspar, although K-feldspar reflections were not identified by XRD. However, since the major K-feldspar and illite reflections partly overlap, identification of K-feldspar with XRD is difficult in illite-rich samples.

The  $< 0.2\mu\text{m}$  fraction from carbonate LER (open diamond in Fig. 7.6) plots slightly above isochron B. Although the slope of isochron B does not change significantly, if sample LER is included in its calculation ( $323 \pm 5.5$  Ma,  $(^{40}\text{Ar}/^{36}\text{Ar})_{\text{ini}}: 297 \pm 57$ ), it yields a high MSWD (16). Here, the cause for the high  $^{40}\text{Ar}$  content and apparent age is ambiguous. Detrital contamination is unlikely, since the carbonate contains almost no siliciclastic material. On the other hand, no evidence for inherited  $^{40}\text{Ar}$  is observed in the clay fraction from the carbonate sample UTH, which was sampled only few km further East.

The  $< 0.2\mu\text{m}$  fraction of the Middle Devonian tuff (BOH) from the Wittgenstein syncline (WS in Fig. 4.4) yields the highest potassium content of all samples (8.48 wt%  $\text{K}_2\text{O}$ ) and has exceptionally high isotope ratios ( $^{40}\text{Ar}/^{36}\text{Ar}: 17.0 \times 10^3$ ;  $^{40}\text{K}/^{36}\text{Ar}: 8.37 \times 10^5$ ). However, the isotope ratios plot clearly below isochron B (cross in inset of Fig. 7.6). This is consistent with the low apparent K-Ar age of sample BOH, which is significantly younger than the apparent ages of the other  $< 0.2\mu\text{m}$  fractions from Middle Devonian rocks (Fig. 7.5). The younger age of the  $< 0.2\mu\text{m}$  fraction from sample BOH is thought to reflect diffusive loss of  $^{40}\text{Ar}$  from an illite generation, which originally had an isotope composition similar to that of the samples plotting on isochron A or B. In a previous study of tuff layers from the Wittgenstein syncline, REUTER (1987) also reported unusually young ages for the smaller grain size fractions ( $< 0.63\mu\text{m}$ ), while the ages of the coarser fractions agree with the ages of size fractions from metapelites. REUTER (1987) concluded, that the illites in the  $< 0.63\mu\text{m}$  fractions from tuffs experienced diffusive loss of radiogenic

$^{40}\text{Ar}$  during decline of metamorphic temperatures and that the apparent K-Ar ages have no geologic significance.

### 7.2.4 Age of illite formation

The  $^{40}\text{Ar}/^{36}\text{Ar}$  ratios close to the present-day value and the comparably low MSWD values are taken as strong evidence, that isochrons A and B characterise two distinct generations of authigenic illite. Isochron B is not considered to reflect mixing of different generations of authigenic illite, although the MSWD of isochron B (3.5) is slightly higher than the value suggested by BROOKS *et al.* (1972). This scatter in the K-Ar data is thought to be caused by natural inhomogeneities in the sedimentary rocks.

This implies two different events of illite formation in the rocks of the NE Rhenish Massif: an older event in the Middle Devonian clastic rocks (isochron A) and a later illite formation in the Upper Devonian and Lower Carboniferous carbonate rocks and the Namurian greywackes (isochron B). Furthermore, observation of isochrons A and B rules out mixture of detrital and authigenic components or preferred loss of radiogenic  $^{40}\text{Ar}$  from less well crystallised illites in the majority of samples. According to the characteristic isochron, the mineral parageneses resulting from the two events are called illite generation A and B in the following.

Since the  $^{40}\text{Ar}/^{36}\text{Ar}$  intercepts of isochrons A and B are not significantly different from each other (A:  $284 \pm 40$ , B:  $280 \pm 35$ ) and from the present-day atmospheric  $^{40}\text{Ar}/^{36}\text{Ar}$  ratio (295.5), the weighted mean apparent ages are thought to represent best the formation ages of illite generations A and B. The clay fractions from clastic rocks (NEU, BRU, ALB3, ATT1, ATT1n, ALB1), which represent the illite generation A yield a weighted mean apparent age of  $336 \pm 6.2$  Ma (group A in Fig. 7.7). This is significantly different from the weighted mean apparent age from samples of group B (carbonate rocks LET, HAC, LER, UTH, STC and greywacke OLP, group B in Fig. 7.7), which is  $312 \pm 10$  Ma. The individual apparent ages from this group show a relatively large scatter, which is thought to reflect the relatively low illite crystallinity of those clay fractions.

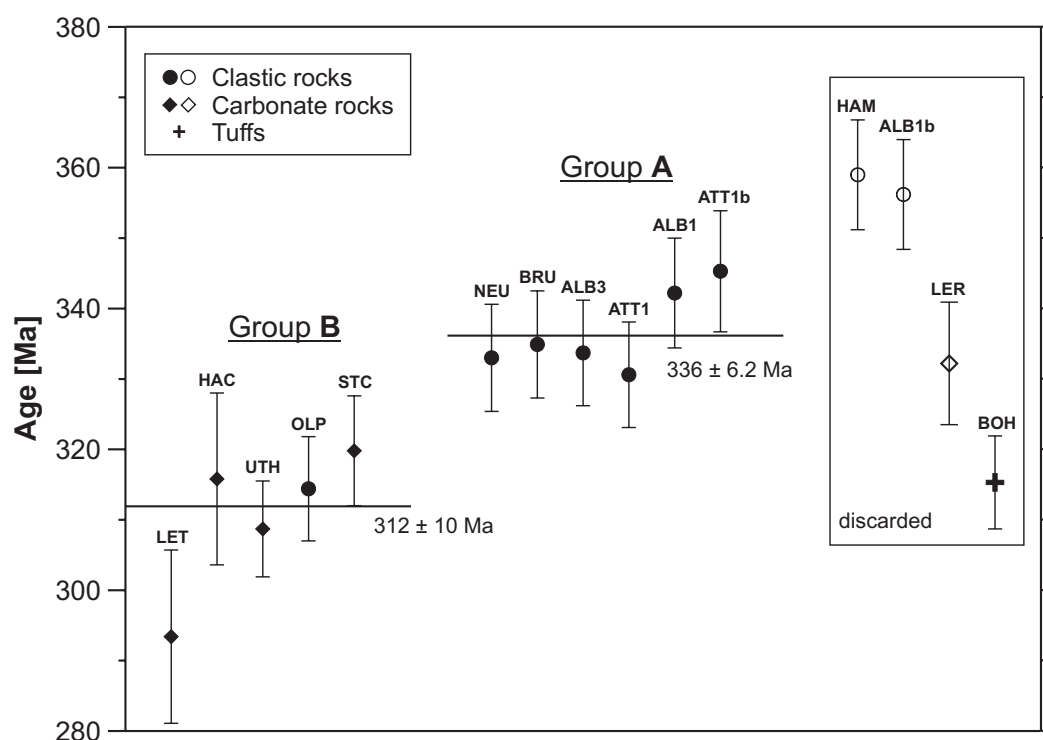


**Figure 7.7** Apparent K-Ar ages of  $< 0.2\mu\text{m}$  fractions. Two groups of ages are distinguished by analyses of K-Ar isochrons: Clastic rocks yield an weighted mean apparent age of  $336 \pm 6.2$  Ma, while carbonate rocks and greywacke OLP have a weighted mean of  $312 \pm 10$  Ma. Due to possible contamination by detrital material, samples HAM, ALB1 and LER1 were discarded. Sample BOH is thought to have experienced loss of  $^{40}\text{Ar}$  and was rejected from further interpretation.

## 7.3 Trace and REE geochemistry of the $< 0.2\mu\text{m}$ fractions and leachates

### 7.3.1 REE patterns of the untreated $< 0.2\mu\text{m}$ fractions

The NASC normalised REE patterns of the untreated  $< 0.2\mu\text{m}$  fractions are generally flat, but show varying relative amounts of REE (Fig. 7.8, see also Table E.4). The majority of fractions from clastic rocks contain less REE than the NASC (clay/NASC = 0.5 - 0.8), which reflects dilution of REE-carrying minerals by quartz. The NASC-normalised REE contents of carbonate rocks (0.3 - 1.5) show significant variation, which is thought to be caused by highly varying amounts of REE-poor minerals (dolomite, calcite, quartz).

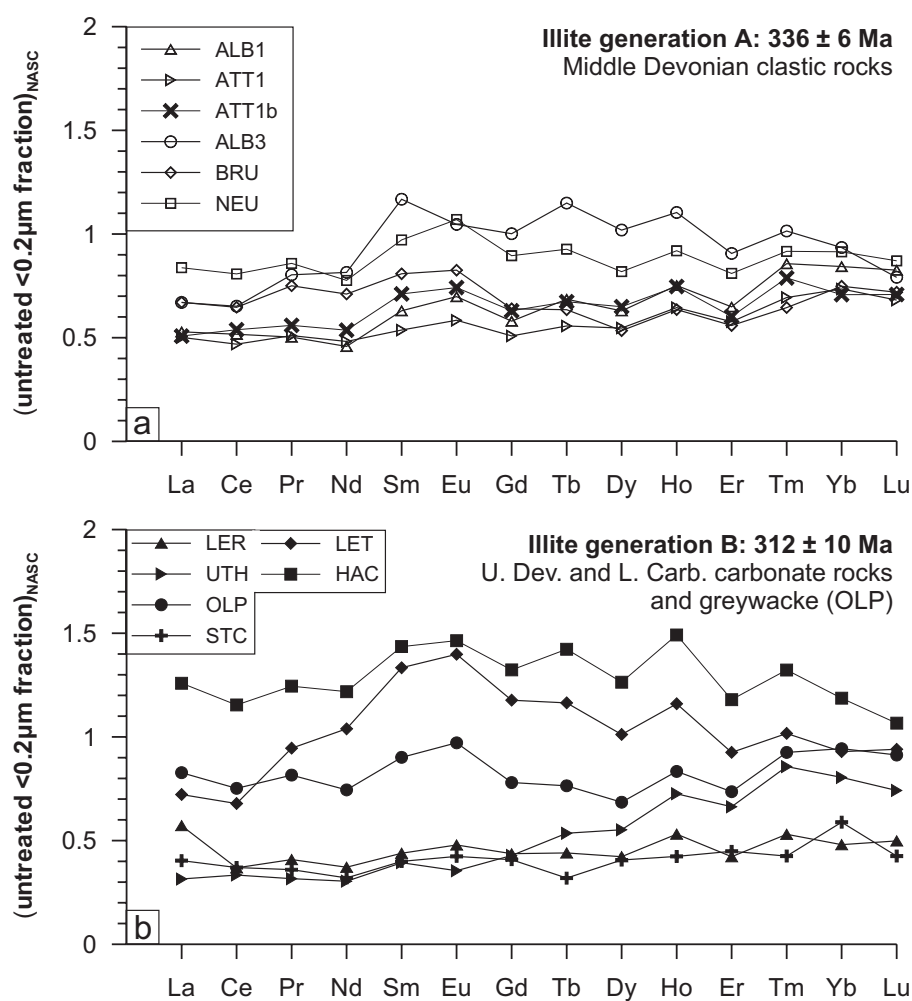


**Figure 7.8** NASC-normalised REE patterns of untreated  $< 0.2\mu\text{m}$  fractions from a) Middle Devonian clastic rocks (illite generation A) and b) Upper Devonian and Lower Carboniferous carbonate rocks and greywackes (illite generation B).

Beside these differences in relative amounts of REE, which are mainly controlled by lithology, the patterns from the two groups of fractions, which represent illite generation A and B are not significantly different. Few samples from both groups show an enrichment in the heavy REE (HREE), which is most pronounced for the carbonate UTH and is related to the presence of organic material. Sample LET is slightly enriched in middle-heavy REE (MREE: Sm, Eu, Gd, Tb). The variations of Eu and Gd are generally not significant, except sample LER, which has a negative Ce anomaly.

### 7.3.2 REE patterns of Fe-oxide leachates

The amounts of REE in the leachates are rather low and range from 0.4% to 4.3% of the total REE in  $< 0.2\mu\text{m}$  fractions. This indicates that most REE in the clay

fractions are carried by minerals that are not dissolved during the leaching procedure. The relative and absolute amounts of soluble REE and Fe are strongly correlated (Fig. 7.9 a,b), indicating a strong affinity of REE towards Fe-oxides and Fe-carrying insoluble minerals.

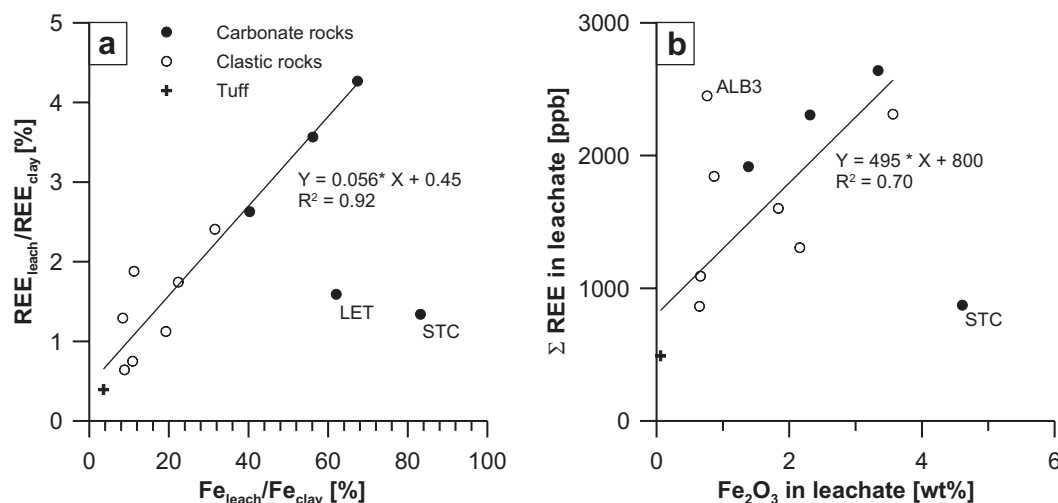


**Figure 7.9** Correlation of REE and Fe in the leachates. a) The relative amounts of soluble REE and Fe are correlated (except for samples STC and LET). b) Relation of total amounts of REE to  $Fe_2O_3$  in leachates (ALB3 and STC are not included in calculation of the regression).

The low amounts of soluble REE in clastic rocks (open circles in Fig. 7.9 a) correspond to the low efficiency of Fe-leaching in these lithologies, which reflects the presence of insoluble Fe-chlorite (see section 7.1.2). This suggests that insoluble REE are preferentially carried by Fe-rich clay minerals. Except for samples LET and STC, the carbonates are characterised by high relative amounts of soluble Fe and REE. Similarly, the absolute amounts of soluble REE and Fe are correlated (except for samples ALB3 and STC), indicating that the majority of soluble REE is related to Fe-oxides (Fig. 7.9 b).

The REE patterns of the leachates are shown in Fig. 7.10 a,b. For most leachates, the concentrations of Tm and Lu were below the detection limit of the ICP-MS (see Table F.3). The REE patterns of the samples HAC, NEU, HAM and BOH show large scatters and were not used for further interpretation. Sample LER was added to the group of Upper Devonian and Lower Carboniferous carbonate rocks and greywackes, which are characterised by illite generation B ( $312 \pm 10$  Ma), however, it should be noted that LER plots slightly above isochron B in a  $^{40}Ar/^{36}Ar$  versus  $^{40}K/^{36}Ar$  plot (Fig. 7.6).

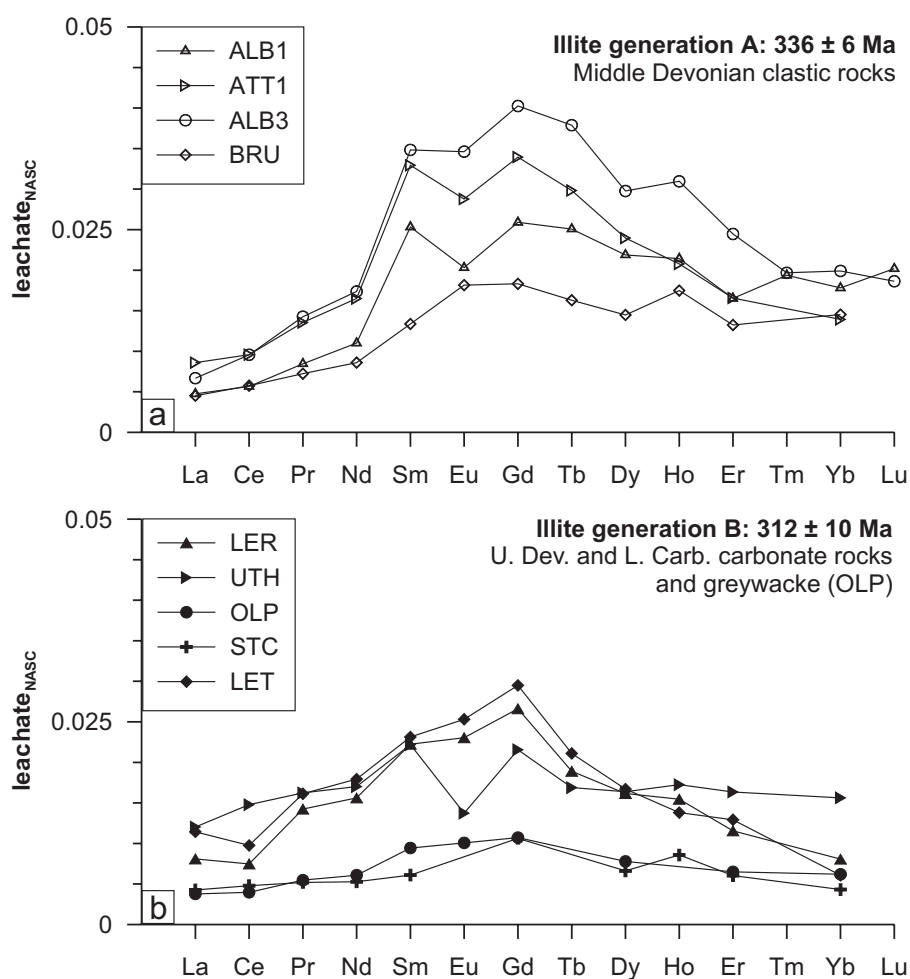


**Figure 7.10** NASC-normalised REE patterns of leachates from a) Middle Devonian clastic rocks (illite generation A) and b) Upper Devonian and Lower Carboniferous carbonate rocks and greywackes (illite generation B).

The REE patterns of the leachates are characterised by varying degrees of enrichment in MREE (Nd - Dy, Fig. 7.10) and show significant differences between the two groups of samples, which are characterised by illite generations A and B. The enrichment in MREE is more pronounced in the leachates of the Middle Devonian clastic rocks (illite generation A, Fig. 7.10 a), while the REE patterns of leachates from Upper Devonian and Lower Carboniferous carbonate rocks and greywackes are generally flatter (illite generation B, Fig. 7.10 b). This fractionation, which can be quantitatively described by the ratio of Gd/La is directly correlated with the Ba-content of the leachates (Fig. 7.11 a). In samples from group B with low MREE enrichment and low Ba-contents, the ratio of Gd/La shows an inverse correlation to  $\text{Fe}_2\text{O}_3$  and  $\text{CaO} + \text{P}_2\text{O}_5$  (Fig. 7.11 b).

The relation between MREE-enrichment and Ba,  $\text{Fe}_2\text{O}_3$  and  $\text{CaO} + \text{P}_2\text{O}_5$  contents of the leachates is interpreted to reflect two mineralisation processes: early

crystallisation of MREE enriched baryte during formation of illite generation A ( $336 \pm 6$  Ma) and growth of Fe-oxides and apatite with low Gd/La ratios ( $\leq 1$ ) during formation of illite generation B ( $312 \pm 10$  Ma).

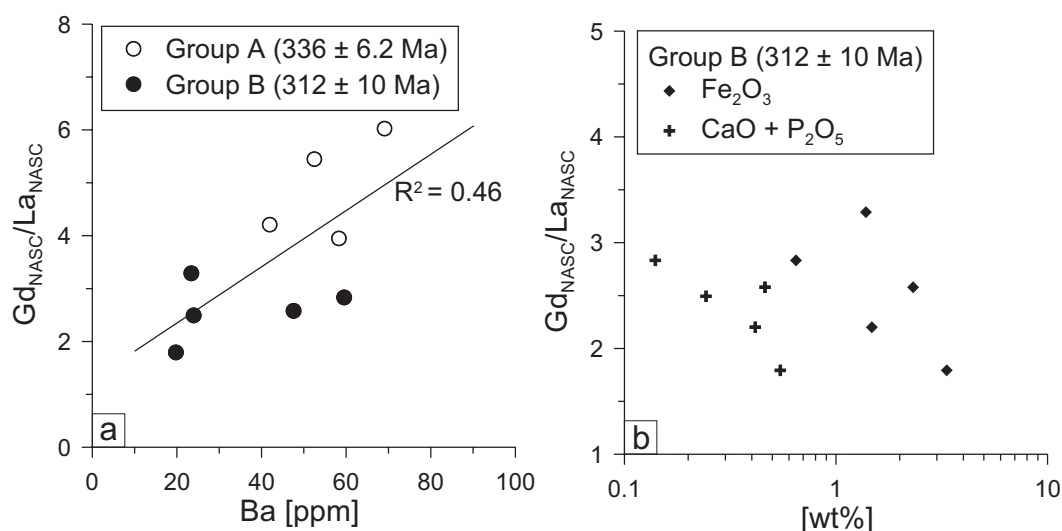


**Figure 7.11** a) The ratio of Gd/La as a measure of MREE enrichment is directly correlated to the Ba-content of the leachates, while b) samples from group B (illite generation B,  $312 \pm 10$  Ma) show inverse correlation of Gd/La with Fe<sub>2</sub>O<sub>3</sub> and CaO + P<sub>2</sub>O<sub>5</sub>

For most leachates, the variation in Ce and Eu, which can attain two valence-states (Ce<sup>3+</sup> and Ce<sup>4+</sup>; Eu<sup>2+</sup> and Eu<sup>3+</sup>) is not significant. However, leachates ATT1, ALB1 and UTH have negative Eu-anomalies, while LET has a negative Ce-anomaly. This is thought to reflect different redox conditions during precipitation of REE carrying minerals, such as Fe-oxides and apatite.

## 7.4 Interpretation of K-Ar ages of $< 0.2\mu\text{m}$ fractions and REE patterns of leachates

The relation between apparent K-Ar ages of  $< 0.2\mu\text{m}$  fractions and the stratigraphic age and provenance of the samples, indicate that an illitisation event at  $336 \pm 6.2$  Ma affected deeply buried Middle Devonian (and possibly also older) rocks and led to the formation of well crystallised illite in the siliciclastic rocks of the Lüdenscheid and Attendorn synclines. This diagenetic event could be related to a major magmatic event at ca. 340-330 Ma in the Mid-German Crystalline Rise (KREUZER & HARRE, 1975; TODT *et al.*, 1995), which was located in close proximity south of the NE Rhenish Massif at that time (FRANKE, 2000). If the Upper Devonian and Carboniferous rocks, which were located at more shallow depths did record this early

illitisation event, the isotopic system of the illite in those rocks was completely reset during the event at  $312 \pm 11$  Ma.

The second event did not recrystallise illite in the Middle Devonian clastic rocks, indicating that the temperatures did not reach the maximum metamorphic temperatures of the first event in the more deeply buried Middle Devonian sequences. The different diagenetic conditions during the two illitisation events are also reflected in the ICI of the  $< 0.2\mu\text{m}$  fractions, which are significantly higher in Middle Devonian clastic rocks and lower in the younger units.

The occurrence of Ba and the enrichment in MREE, which is more pronounced in Middle Devonian clastic rocks, indicate that the early illitisation event was accompanied by mineralisation of Ba-minerals (baryte). Thermally driven fluid flow could have mobilised Ba from SEDEX deposits, which frequently occur along synsedimentary fault zones in the NE Rhenish Massif (e.g. Meggen ore deposit, WERNER, 1989). The characteristic enrichment in MREE in the leachates with high Ba-contents is probably inherited from those synsedimentary mineral deposits.

The inverse correlation of MREE-enrichment and  $\text{Fe}_2\text{O}_3$  and  $\text{CaO} + \text{P}_2\text{O}_5$  contents in leachates of samples that were affected by the later illitisation event, indicates mineralisation of Fe-oxides and possibly apatite with flat REE patterns. This diagenetic event is coeval to the deformation in the region and could have caused the chemical remagnetisation in the Upper Devonian and Lower Carboniferous units.

The REE patterns in the leachates from different lithologies of the NE Rhenish Massif show varying occurrences of Eu (and Ce) anomalies. This indicates varying redox conditions in the different lithologies during mineralisation of soluble phases such as baryte, Fe-oxides and apatite. A pervasive migration of fluids on a regional scale is expected to homogenise the trace and REE signatures of soluble minerals. The observation of two mineralisation events of different ages and the different redox conditions during diagenesis are taken as strong evidence against regional fluids flow in the NE Rhenish Massif.

# Chapter 8

## Discussion and Conclusions

A pervasive remagnetisation (component B), predominantly carried by magnetite is identified in Late Palaeozoic carbonate and clastic rocks from the NE Rhenish Massif. The age of this remagnetisation event is well constrained to the time span of 315 - 300 Ma by the age of deformation (AHRENDT *et al.*, 1983) and comparison of the resulting palaeolatitudes for the region with its palaeolatitudinal drift history (VAN DER VOO, 1990). The concordance of the magnetic inclinations obtained from the entire area suggests that the rocks were remagnetised during a relatively short time-period of only a few My. The thermal stability of the remanence up to ca. 550 °C, the comparably low palaeotemperatures in the studied region and the short duration of the remagnetisation event, favour a chemical remagnetisation process. Authigenesis of magnetic minerals (magnetite) is indicated by the presence of SP magnetite, which is identified by hysteresis ratios, magnetic viscosity and low temperature behaviour of carbonate rocks.

K-Ar dating of  $< 0.2\mu\text{m}$  fractions indicates two diagenetic events in the region studied. The observation of K-Ar isochrons rules out contamination from detrital sources and preferential loss of radiogenic  $^{40}\text{Ar}$  from authigenic illites. Middle Devonian clastic rocks are characterised by an illitisation event at  $336 \pm 6.2$  Ma ( $I_1$  in Fig. 8.1 a), which is probably connected to a major magmatic event at ca. 340 - 330 Ma in the Mid-German Crystalline Rise (KREUZER & HARRE, 1975; TODT *et al.*, 1995), located in close proximity south of the NE Rhenish Massif at that time (FRANKE, 2000). During this event, fluids are thought to have mobilised sulphates from SEDEX deposits, which occur along major synsedimentary fault zones (WERNER, 1989). The characteristic enrichment in MREE in leachates with high Ba-contents is probably inherited from those synsedimentary mineral deposits.

The second period of illite formation ( $312 \pm 10$  Ma,  $I_2$  in Fig. 8.1 b) is coeval to the northward migration of deformation through the Rhenish Massif and is only recorded by Upper Devonian and Lower Carboniferous rocks. This indicates, that

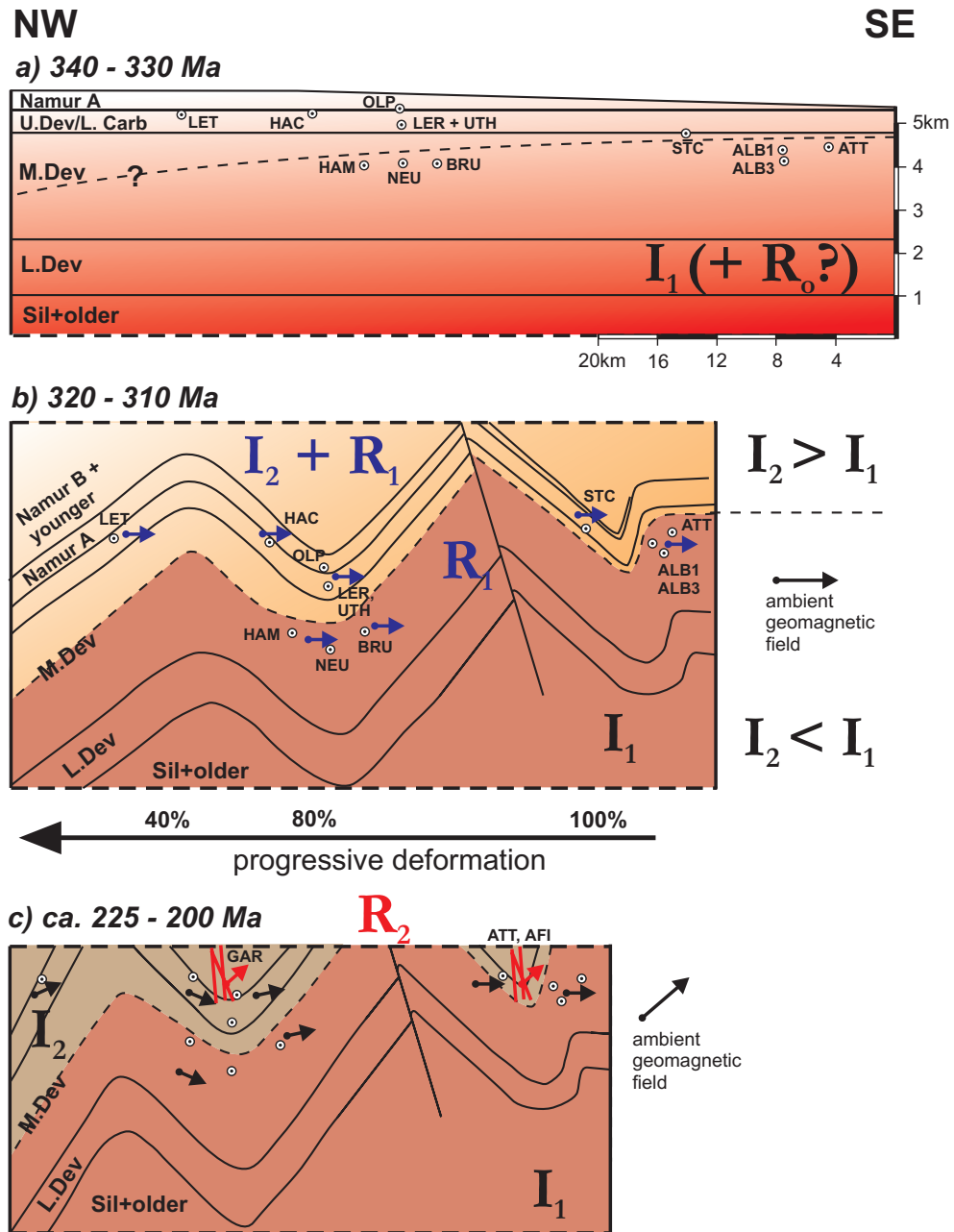


**Figure 8.1** Diagenetic and deformation history of the NE Rhenish Massif. a) A diagenetic event ( $I_1$ ) at  $336 \pm 6.2$ , connected to the intrusion of plutonic rocks in the Mid-German Crystalline Rise caused formation of illite generation A in Middle Devonian rocks. During this time, the rocks could have acquired a thermoviscous remagnetisation ( $R_0$ ), which was completely erased during the later chemical remagnetisation. b) The second diagenetic event ( $I_2$ ) at  $312 \pm 10$  Ma affected only Upper Devonian and Lower Carboniferous strata and is coeval with the deformation and the pervasive remagnetisation ( $R_1$ ), which is observed in all stratigraphic units. c) A late Triassic remagnetisation ( $R_2$ ) is exclusively observed within zones of tight folding and steep to overturned bedding planes and could be caused by oxidising fluids, migrating from the mesozoic weathering surface along zones of increased permeability into the Palaeozoic strata. Vertical scale in (a) after WALLISER (1981), fold and fault geometry in b,c) modified after a balanced cross-section by ONCKEN et al. (2000).

the metamorphic conditions were not sufficient to recrystallise the earlier illite generation in the more deeply buried Middle Devonian rocks. This is supported by the low illite crystallinity of Upper Devonian and Lower Carboniferous rocks. The boundary below which the earlier illite generation was not affected by  $I_2$  is tentatively drawn in Fig. 8.1 a,b. However, it should be noted, that this boundary was folded during the Variscan deformation. This is supported by the fact, that the vitrinite reflectance in the NE Rhenish Massif is correlated to the stratigraphic level and that the the  $R_{max}$  isolines are folded and offset across faults (PAPROTH & WOLF, 1973). Consequently, the first illite generation and the vitrinite reflectance preserved a thermal state related to the maximum burial and the magmatic event in the Mid-German Crystalline Rise.

The age of the illitisation event  $I_2$  is not significantly different from the age of the pervasive, syntectonic remagnetisation ( $R_1$  in Fig. 8.1 b). In contrast to  $I_2$ , the remagnetisation event was not restricted to the upper part of the fold and thrust belt and also affected the Middle Devonian strata, erasing any previous (thermoviscous) remagnetisation ( $R_0$  in Fig. 8.1 a), possibly caused by the earlier thermal event. The younger illite generation is characterised by lower Gd/La ratios in leachates, which are thought to reflect the formation Fe-oxides and apatite with flat NASC normalised REE patterns.

The pervasive migration of fluids on regional scales is expected to homogenise the trace and REE signatures of soluble minerals. However, the REE patterns of leachates indicate the interference of two mineralisations of different ages. Furthermore, the REE patterns from different samples show a variation of Eu and Ce, which indicates varying redox conditions in the lithologies studied. This is taken as evidence against a pervasive migration of orogenic fluids on a regional scale as a cause of remagnetisation in the NE Rhenish Massif. In the Ardennes, an Early Permian remagnetisation is related to fluid migration during formation of Mississippi Valley-type deposits (ZEGERS *et al.*, 2003). The absence of such syn- to late orogenic deposits in the NE Rhenish Massif further supports the evidence against regional migration of orogenic fluids in NE Rhenish Massif.

A temporal relationship between clay diagenesis and remagnetisation is observed in Upper Devonian and Lower Carboniferous rocks. On the other hand, the remagnetisation is not related to clay diagenesis in Middle Devonian rocks, since they have preserved an older diagenetic event. Here, the transformation of smectite to illite cannot account for the growth of authigenic magnetic minerals, which must have been triggered by a different mechanism. Since the ages of remagnetisation and main deformation are generally similar, this mechanism could be related to localised pressure solution and changing pore fluid pressure due to tectonic stress. However,

this raises the question of why the remagnetisation occurred during different stages of folding in the northern and southern parts of the NE Rhenish Massif.

A second remagnetisation (component C) is recorded in rocks from the cores of first-order structures with steeply dipping bedding planes and is predominantly carried by hematite. Being of Late Triassic to Early Jurassic age, this remagnetisation event is either related to hematite bearing mineralisation events during the uplift of the Rhenish shield in the Mesozoic or caused by oxidising fluids percolating from the weathering surface and penetrating zones of enhanced permeability (Fig. 8.1 c).

## Part III

Dating of remagnetisation events  
in the Barrandian, Czech Republic  
and in the Holy Cross Mountains,  
Poland

# Chapter 9

## Age of remagnetisation in the Barrandian, Czech Republic

### 9.1 Geology and sampling

The Barrandian Basin forms a syncline within the gently folded Cadomian basement of central Bohemia (Fig. 9.1). The sedimentary and volcanic evolution of Ordovician to Middle Devonian rocks reflects subsidence and extension in an intra-continental or passive margin setting. Lower Cambrian conglomerates are overlain by Ordovician clastic rocks with Hirnantian age glacio-marine horizon, which are followed by Silurian and Devonian shales and carbonates. Givetian rocks are unconformably overlain by Famennian age sediments (CHLŮPÁČ, 1994). Effusive basalts persisted from Late Wenlockian to the Ludlovian and are associated with a subsurface sill emplacement.

Synsedimentary faulting and related folding occurred in the Ordovician and continued during Silurian and Devonian times (HAVLÍČEK, 1981). The Variscan deformation and (very) low-grade metamorphism is bracketed between the late Givetian and late Famennian, i.e. between 385 Ma and 365 Ma (FRANKE, 2000). Isotopic  $^{40}\text{Ar}/^{39}\text{Ar}$  dating on hornblendes and white micas from surrounding areas in the Teplá-Barrandian yielded ages ranging from 382 Ma to 362 Ma (DALLMEYER & URBAN, 1998). The resulting structural style of the Barrandian is dominated by open, upright folds with wavelengths in the km scale.

The geodynamic evolution of the region was subject of a series of palaeomagnetic studies, which demonstrate the continuous northwards drift of central Bohemia from the northern margin of Gondwana in Early Ordovician times to a position adjacent to the southern margin of Baltica in the Late Silurian (TAIT *et al.*, 1994a,b, 1995). Palaeomagnetic data from Late Silurian rocks indicate, that the Bohemian Massif underwent major anticlockwise rotation in the order of  $140^\circ$  prior to consolidation

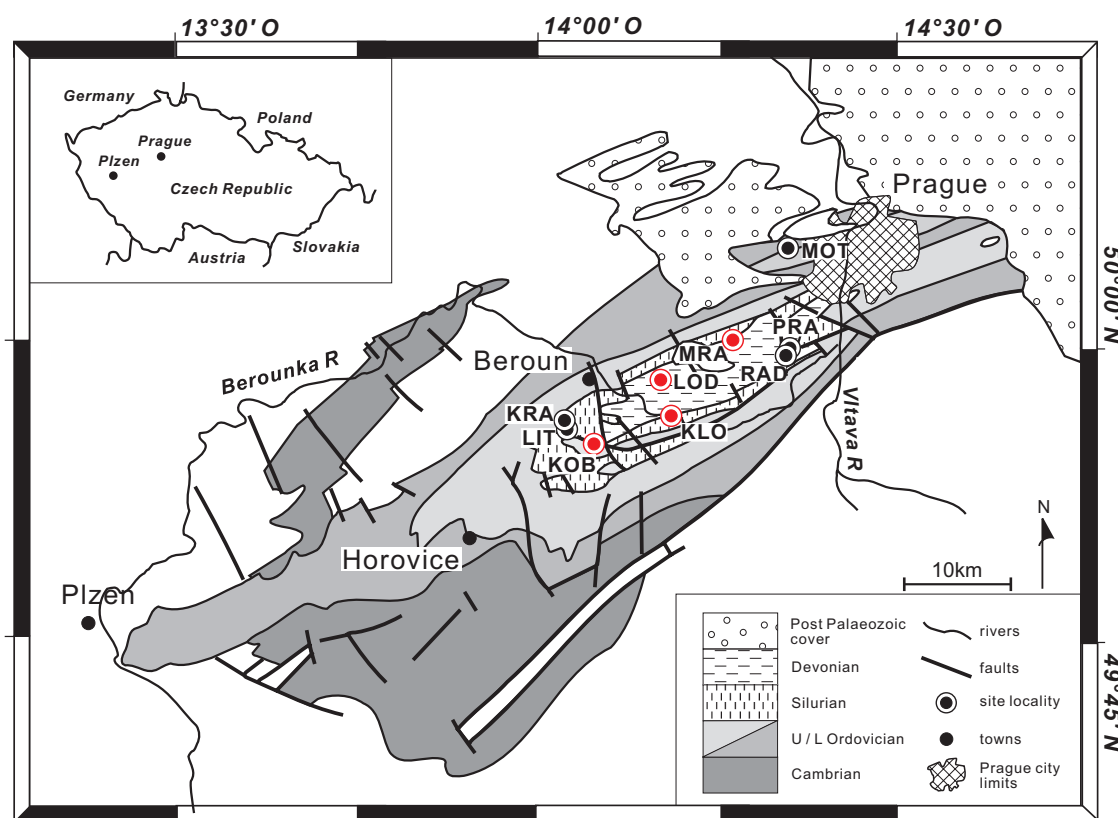


**Figure 9.1** Geological sketch map of the Barrandian and location of palaeomagnetic sampling sites, discussed in the text. Sites, where samples were taken for palaeomagnetic and geochemical studies are shown in red.

of Hercynian Europe. Lower Ordovician and Upper Silurian rocks are partially overprinted by a secondary component, which was interpreted by TAIT *et al.* (1994b) to be Late Carboniferous in age. While the primary magnetisation could still be identified at higher demagnetisation temperatures in the Ordovician and Silurian rocks, the original magnetisation of Devonian carbonates in the Barrandian seems to be completely erased by this remagnetisation (J. TAIT, unpublished data).

In order to study this Late Palaeozoic remagnetisation event, unpublished demagnetisation data from J. TAIT of five sites from Devonian limestones (LODJ, KOBJ, MRAJ, PRAJ and RADJ in Table B.1) was analysed. Additionally, new samples were taken at those sites and the auxiliary type section of the Silurian/Devonian boundary (KLO in Fig. 9.1), which was previously studied by TAIT *et al.* (1994b). Hand samples for isotopic and geochemical studies of clay minerals were taken from four sites (KLO, MRA, LOD and KOB, red circles in Fig. 9.1). For detailed fold test analysis the site mean directions with  $\alpha_{95} < 16^\circ$  of the remagnetisation component (component B) from Silurian rocks given by TAIT *et al.* (1994b) were reanalysed. Those sites are indicated with an asterisk in Tables A.1 and B.1. The locations of

the sampling sites discussed here are indicated in Fig. 9.1.

Site KOB was the only locality, where evidence for alteration by fluids was observed in the field. Here, a ca. 10m thick sequence of red limestones was sampled (KOBAA). The reddish colour of the limestone is delimited by bedding surfaces and also includes sparitic calcite in cavities of bioclasts. This indicates primary or early diagenetic oxidation of Fe-oxides. Along fractures, the red limestone is altered to greenish colours, however, the cavities of bioclasts are still filled with red sparitic calcite. This is thought to indicate a later migration of reducing fluids along fractures.

## 9.2 Palaeomagnetism

### 9.2.1 Demagnetisation behaviour

Most samples measured show a multicomponent behaviour during stepwise thermal demagnetisation and tend to undergo mineralogical alteration during thermal treatment. As a result, the demagnetisation vectors of more than 80% of the samples show large scatter above demagnetisation temperatures of 480 °C, which severely hampers the interpretation of the demagnetisation behaviour in the high-temperature range. AF demagnetisation was attempted to avoid thermal alteration, however, in most cases, this method failed to completely separate the components of magnetisation which were observed during thermal cleaning. The failure of the AF-technique is most likely due to the presence of the high-coercivity mineral goethite, which is indicated by a characteristic decay in magnetisation intensity of 40% up to 90% after heating to ca. 120 °C in almost all samples. Therefore, the results presented here are based almost exclusively on thermal treatment. The site mean results are listed in Table B.1 and four examples of the demagnetisation behaviour are shown in Fig. 9.2.

During thermal demagnetisation up to three components of magnetisation were identified, which are called A, B, and C and represent the low, intermediate and high laboratory unblocking temperature components, respectively. Component A (A in Fig. 9.2) can be identified in almost all samples and is removed below 300 °C. This magnetisation generally parallels the present-day Earth's magnetic field in the sampling area and is interpreted to be of recent age. 123 samples from 18 sites then show removal of magnetisation B with a shallow, southerly direction (B in Fig. 9.2). Due to mineralogical alteration during heating, this component could generally only be identified up to 480 °C (Fig. 9.2 a). However, in a few samples, component B is stable up to 580 °C, indicating magnetite as a carrier of magnetisation. In red limestones from site LODB and MRA, B is removed at demagnetisation tem-

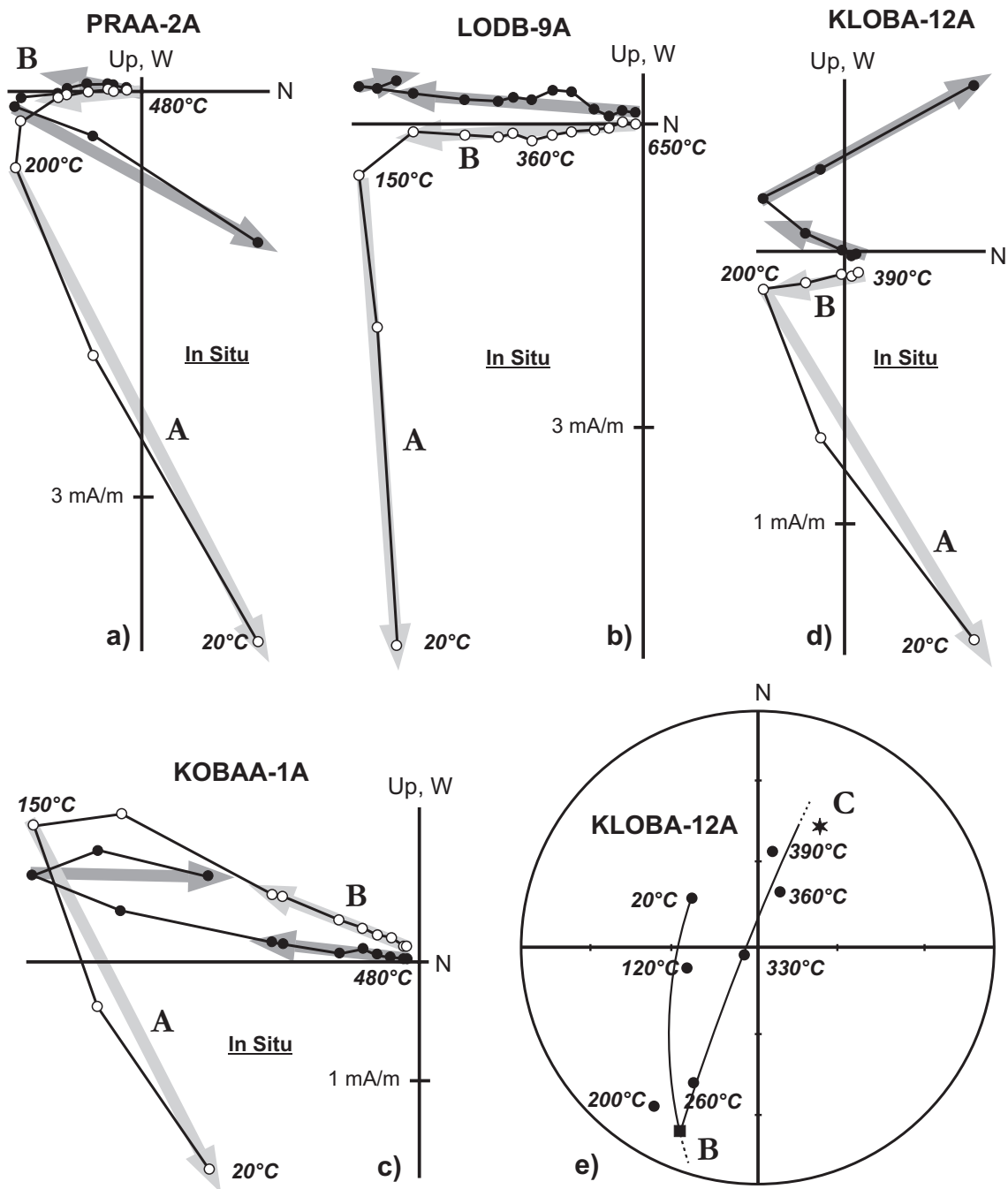


**Figure 9.2** Thermal demagnetisation behaviour of four samples in orthogonal (a-d, open and solid circles are vertical and horizontal planes, respectively) and stereographic projection (e, lower hemisphere). Three components of magnetisation are observed: Component A parallels the present-day field and is removed below 300°C. B has a southerly, shallow direction and is observed in the majority of samples (a-d). The presence of a third component (C) is indicated in samples, where B does not reach the origin (c,d). During demagnetisation of Late Silurian limestones (e), the magnetic vector moves from the direction of component B (square) towards the Silurian reference direction (star, TAIT et al., 1994b).

peratures above 620 °C (Fig. 9.2 b). Here, the magnetisation resides in magnetite and hematite. In red limestones of site KOBAA, component B is removed at temperatures below 580 °C and no component of magnetisation could be identified at higher temperatures. This indicates, that contribution of hematite (specularite) is not significant in these rocks. In one site from Silurian carbonate rocks (LODD), component B has a northerly direction with shallow inclination, which is antiparallel to the direction of B, observed elsewhere in the Barrandian. This suggest, that component B was acquired by these rocks before or after the Earth's magnetic field had reversed its polarity.

Frequently, component B does not directly demagnetise towards the origin (Fig. 9.2 c,d), indicating the presence of a third component of magnetisation (C). In limestones from the auxiliary type section of the Silurian/Devonian boundary (KLO), the vector of magnetisation moves on a great circle towards a northerly direction with an intermediate positive inclination during demagnetisation of component B (Fig. 9.2 e). This demagnetisation behaviour is similar to that of samples from the same section, studied by TAIT *et al.* (1994b). In fact, the great circle lies close to the mean direction of the high-temperature component (Dec: 28°, Inc: 40°, star in Fig. 9.2 e), which was interpreted by TAIT *et al.* (1994b) to be of Late Silurian age. In some samples of Devonian carbonates, the magnetisation vector also moves on a great circle towards a northerly direction during demagnetisation of component B. Here, however, the great circles are too scattered to allow a directional interpretation of this, possibly primary, Devonian magnetisation.

## 9.2.2 Results of fold tests

The open, upright folding of the Barrandian results in two general orientations of fold limbs with average bedding direction of 146°/47° and 320°/46° (dip direction/dip). The fold axis strikes to the southwest and it is virtually horizontal (strike: 233°, plunge: 2°, Fig. 9.3). Consequently, no correction for plunging fold axis had to be applied.

Fold tests using parametric resampling (WATSON & ENKIN, 1993) were performed with the ENKIN (1990) software package. The behaviour of FISHER'S (1953) precision parameter  $k$  for 20 resampled datasets during unfolding is shown in Figs. 9.4 a-c (continuous lines). The histograms in Figs. 9.4 a-c show the distribution of the maxima of  $k$  from 1000 resampling trials in 3% increments of unfolding. Bedding orientation was assumed to be accurate within 3°.

The fold test for all site mean results from Silurian and Devonian rocks, yields an optimum degree of unfolding at ca. 13% (Fig. 9.4 a). For a more detailed analysis, the site mean directions of component B were subdivided into two groups, repre-

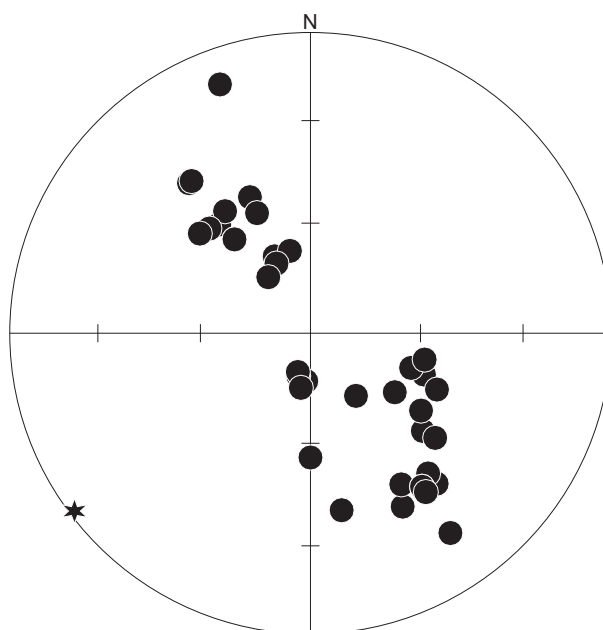


**Figure 9.3** Poles of bedding planes in stereographic projection show two clusters, indicating two general orientations of fold limbs with average bedding direction of  $146^{\circ}/47^{\circ}$  and  $320^{\circ}/46^{\circ}$  (dip direction/dip). The fold axis (star) is subhorizontal and strikes to the southwest ( $02^{\circ}/233^{\circ}$ ).

senting the different ages of the rocks studied (see also Table B.1). The fold test of Ludlovian to Lochkovian sedimentary and volcanic rocks, yields an optimum degree of unfolding at ca. 16% (Fig. 9.4 b), while component B in Devonian (Praghiian) limestones is clearly postfolding in origin (Fig. 9.4 c).

The distributions of the site mean directions in geographic coordinates (Fig. 9.5 a) and after optimum degree of unfolding (Fig. 9.5 b) show relatively high scatter and yield  $\alpha_{95}$  in the range of  $8^{\circ}$  -  $10^{\circ}$  (Table 9.1). The different mean directions for component B might indicate a different age of this remagnetisation in Silurian and Devonian rocks. However, the resolution of the palaeomagnetic results is not sufficient to distinguish between both mean directions of magnetisation B. Consequently, the unit mean direction for all sites were used for palaeopole and palaeolatitude determination (Table 9.1).

### 9.2.3 Interpretation of palaeomagnetic results

The fold test of all site mean directions from Ordovician to Devonian sedimentary rocks yields an optimum degree of unfolding at ca. 15% (Fig. 9.4 a). The interval of 95% confidence of the degree of unfolding (9% - 18%) suggests that B is a secondary overprint, which was acquired during a late stage of the main deformation phase. However, the difference in FISHER's (1953) precision parameter  $k$  in

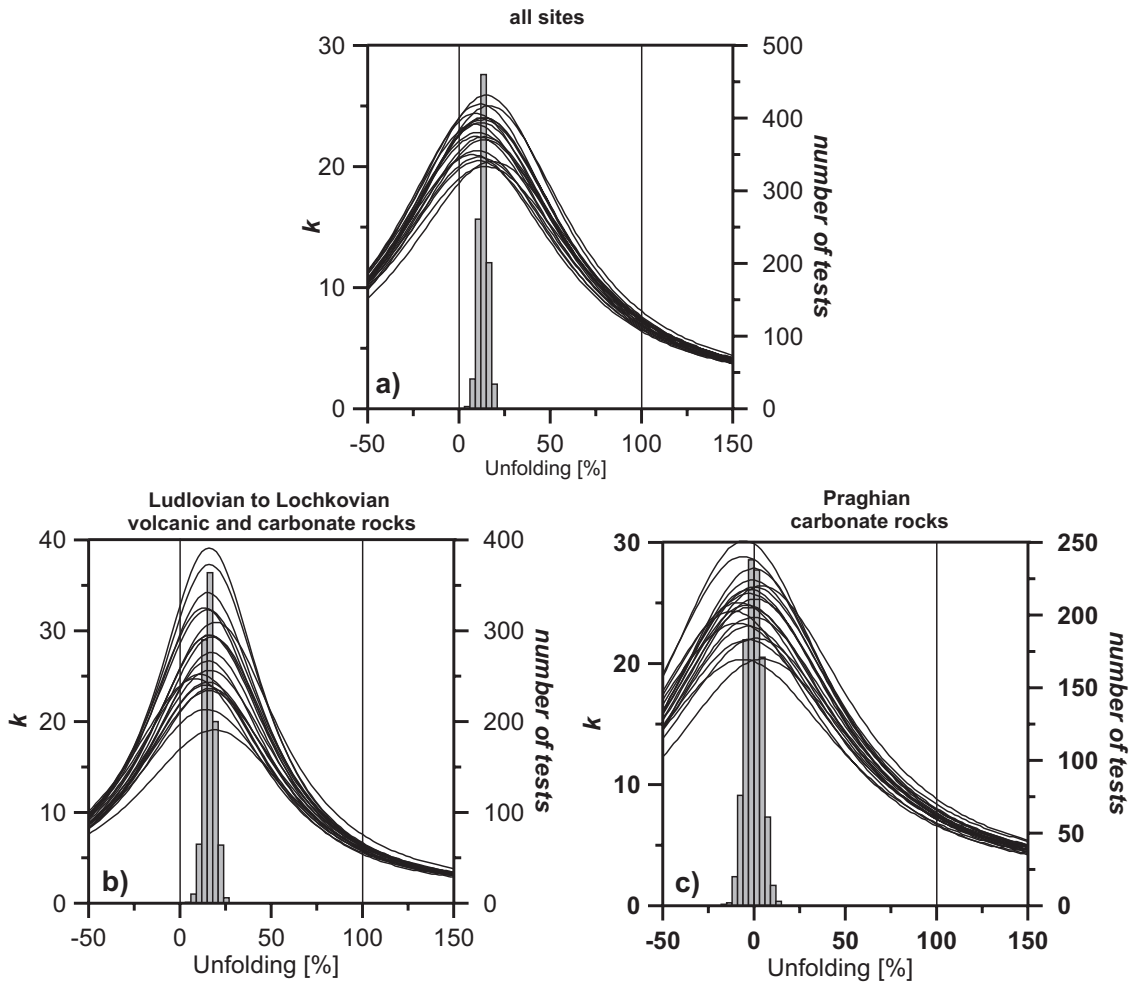


**Figure 9.4** Results of fold tests for component B. a) all sites , b) Ludlovian to Lochkovian carbonate and volcanic rocks and c) Praghan limestones. The continuous curves show the value of FISHER'S (1953) precision parameter  $k$  as a function of unfolding degree for 20 examples of parametric resampling. The histograms give the distribution of the maxima from 1000 trials in groups of 3%. Accuracy of bedding attitude was estimated to be within  $3^\circ$ .

geographic coordinates (23) and after partial untilting (25) is not large (Table 9.1). The interpretation of component B as a late synfolding remagnetisation depends on this small difference in  $k$ .

Rotation about multiple axes during folding and incomplete separation of magnetic components can result in synfolding patterns during fold test analysis of a postfolding magnetisation. In location KLO, a high-temperature component (C) primary in origin was identified. However, the thermal demagnetisation behaviour of these samples does not indicate overlapping unblocking temperature spectra and incomplete separation of both components is thought to be unlikely. Furthermore, the open, upright folding with a subhorizontal fold axis in the Barrandian area does not support rotations about multiple axis.

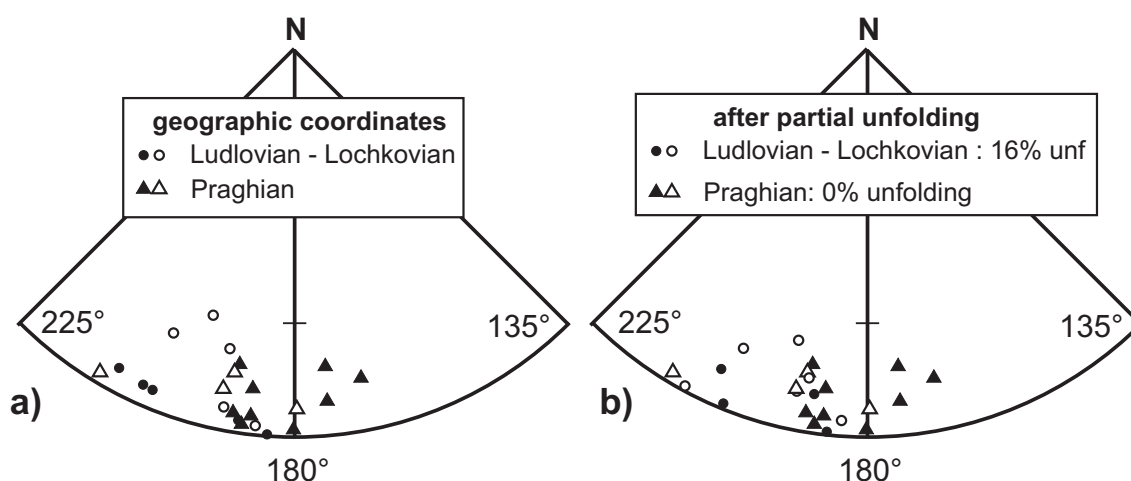


**Figure 9.5** Site mean directions in stereographic projection. a) in geographic coordinates and b) after optimal degree of unfolding

The fold test results from Silurian rocks could also be caused by a multi-phased deformation, where the remagnetisation event was followed by minor deformation, such as block rotation or tilting. Component B from Devonian rocks is unambiguously postfolding in origin. This implies that either the later deformation did only affect Silurian sedimentary and volcanic rocks, or component B was acquired at different times in Silurian and Devonian strata and the second deformation occurred between both remagnetisation events. A "selective", late deformation of Silurian rocks only is highly unlikely, especially since the sampling sites of Silurian and Devonian rocks are evenly distributed in the core of the Barrandian, which shows rather uniform deformation. A different timing of any remagnetisation event in rocks of different stratigraphic levels could be indicated by the different unit mean directions of component B in the Silurian and Devonian samples. However, since this difference is not statistically significant, the palaeomagnetic results do not support this interpretation.

An alternative, more hypothetical interpretation involves the migration of the remagnetisation from lower stratigraphic levels (Silurian) at a late stage of the main deformation into overlaying Devonian rocks after deformation. This would explain the observed differences in fold test results and would not rely on the postulation of a second deformation phase and large temporal differences in remagnetisation acquisition in Silurian and Devonian rocks.

However, the fold test results are generally ambiguous and component B could be either postfolding or synfolding in origin. A further common method for the age estimation of remagnetisation events is the comparison of the palaeopole with a reference apparent polar wander path (APWP). Since the Bohemian Massif un-

Unit mean directions (stratigraphic age)	N'	Geogr. coord.				partially unfolded					
		Dec [°]	Inc [°]	$\alpha_{95}$ [°]	k	oduf	95% confidence	Dec [°]	Inc [°]	$\alpha_{95}$ [°]	k
Ludl - Lochk	10	196	-6	10	27	16%	10% - 22%	195	-5	9	31
Praghian	13	186	4	8	27	0%	-8% - 8%	186	4	8	27
all sites	23	<b>190</b>	<b>0</b>	<b>6</b>	<b>23</b>	13%	9% - 18%	190	0	6	25
<b>resulting palaeopole:</b>	PLAT: 29°S; PLONG: 1°E; dp: 3°; dm: 6°										
<b>palaeolatitude:</b>	0°N <sup>+3°</sup> / <sub>-3°</sub>										

**Table 9.1** Unit mean directions for component B identified in the rocks from the Barrandian. For palaeopole calculation, the unit mean of all sites in geographic coordinates was used. Ludl, Ludlovian; Lochk, Lochkovian; N', number of site mean directions used; oduf, optimum degree of unfolding with its interval of 95% confidence and corresponding declination (Dec), inclination (Inc), radius of cone of 95% confidence  $\alpha_{95}$  and FISHER (1953) precision parameter (k); PLAT and PLONG, latitude and longitude of the palaeo(south)pole; dp and dm, semiaxes of the oval of 95% confidence.

derwent large-scale rotation during Devonian and Carboniferous times (TAIT *et al.*, 1994b), only the inclination of component B can be used for comparison with existing palaeomagnetic data for Baltica and Laurentia.

The palaeolatitude for the Barrandian resulting from the unit mean direction of all sites in geographic coordinates (Fig. 9.6) corresponds to the Late Devonian and Late Carboniferous palaeolatitudinal position of the sampling area (reference point: 50°N, 14°E), based on mean palaeopoles for Baltica and Laurentia (VAN DER VOO, 1990). Since the deformation in the Barrandian occurred during 382 Ma - 362 Ma (FRANKE, 2000, and references therein), a Late Devonian age of component B would support a late synfolding remagnetisation event, while a late Carboniferous remagnetisation would be clearly postfolding in origin (Fig. 9.6). Consequently, both interpretations of the fold test results are supported by the comparison of the palaeolatitude with the palaeomagnetic reference frame.

In the majority of sites, component B has a southerly declination indicating an inverse polarity of the geomagnetic field, which is consistent with the constantly inverse polarity during the PCRS in the Late Carboniferous. However, the observation of one site with normal polarity (LODD) can be taken as evidence against a Late Carboniferous age of the remagnetisation, since the existence of normal polarity intervals during the PCRS is still a matter of debate, whereas the reversal rate was rather high during Late Devonian times (HURLEY & VAN DER VOO, 1990).

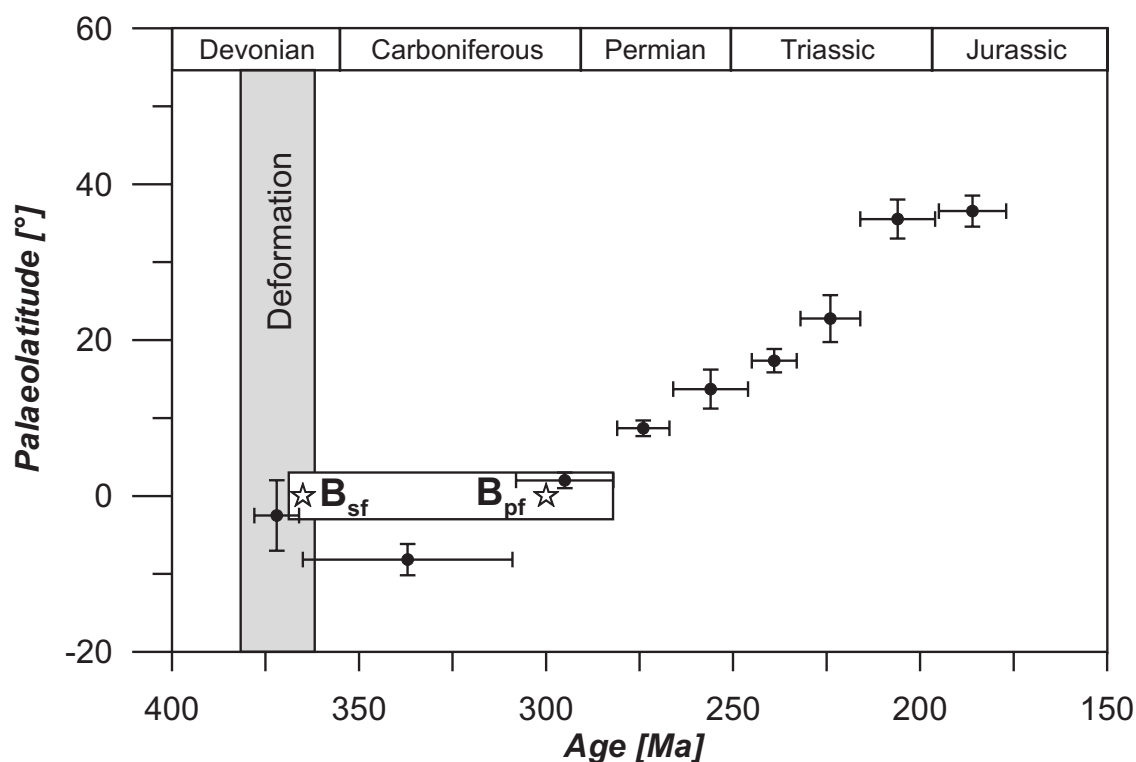


**Figure 9.6** Palaeolatitude for component B (stars) plotted against the predicted palaeolatitudinal drift history for the Rhenish Massif (reference location:  $50^{\circ}\text{N}$ ,  $14^{\circ}\text{E}$ ), based on mean palaeopoles for Baltica and Laurentia (VAN DER VOO, 1990) which are shown with their errors ( $\alpha_{95}$ ) and the time span over which the poles have been averaged. The shaded area indicates the age of deformation in the Barrandian (ca. 382 - 362 Ma, DALLMEYER & URBAN, 1998). The white rectangle indicates the latitudinal uncertainty of component B and its relative age with respect to the deformation.

### 9.3 Magnetomineralogy

IRM acquisition and hysteresis measurements were carried out to identify the magnetic minerals in the samples from the Barrandian. Three hysteresis curves are shown in Fig. 9.7, which are characteristic for the sample set. Samples LODB7 and MRAA6 do not reach saturation at 1 T, which indicates the presence of high coercive minerals. The strong decrease in magnetic intensity temperatures of ca.  $120^{\circ}\text{C}$  during thermal demagnetisation experiments is characteristic for high amounts of goethite in samples from LODB. In the red limestones from LODB and MRAA, magnetisation B is demagnetised above  $620^{\circ}\text{C}$ , indicating the presence of hematite. Both curves are constricted at low fields, which is indicative for a third, low coercive magnetic phase, which is thought to be magnetite.

Samples from sites KLO, PRA and RAD reached saturation in external fields below 300 mT (KLOAB1, Fig. 9.7). Here, magnetite is the dominating magnetic phase and contribution from high coercive minerals is low. The hysteresis ratios

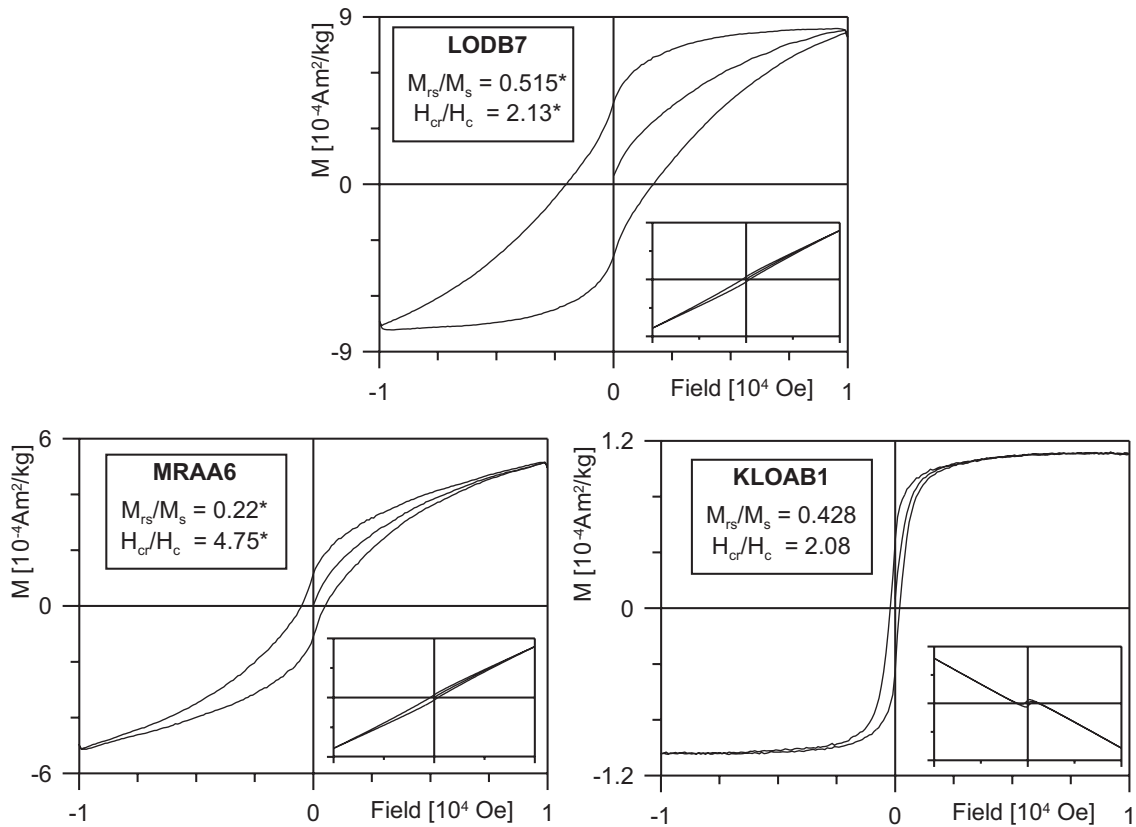


**Figure 9.7** Hysteresis curves of three samples from the Barrandian. The insets show the original shape of the hysteresis loops before correction for paramagnetism (LODB7 and MRAA6) and diamagnetism (KLOAB1). \* due to the presence of high coercive minerals, the hysteresis ratios are not shown in Fig. 9.8.

$M_{rs}/M_s$  and  $H_{cr}/H_c$  of these samples (Fig. 9.8) fall between the the SD-MD mixing line after PARRY (1982, line a) and the line of remagnetised North American remagnetised carbonate rocks (JACKSON, 1990, line b). Similar hysteresis properties were reported by MCCABE & CHANNELL (1994) from remagnetised Palaeozoic limestones from England. The high ratios of  $M_{rs}/M_s$  and  $H_{cr}/H_c$  are interpreted to reflect the presence of superparamagnetic (SP) magnetite.

SEM studies of rock fragments and polished sections indicate the oxidation of pyrite to magnetite in Late Silurian limestones (KLO). Magnetite replaces framboidal pyrite and occurs in close spatial relation to clay minerals (Fig. 9.9 a,b). The replacement of pyrite framboids by magnetite has also been observed in remagnetised limestones from North America (SUK *et al.*, 1990, 1991, 1993a). The oxidation of pyrite to magnetite is also indicated by the presence of Fe-sulphide (pyrite) cores of larger Fe-oxide (magnetite) grains (Fig. 9.9 c).

SEM and BSE images of polished sections from locality LODB show the replacement of baryte by calcite and Fe-oxides (Fig. 9.9 d-f). Large altered grains show a

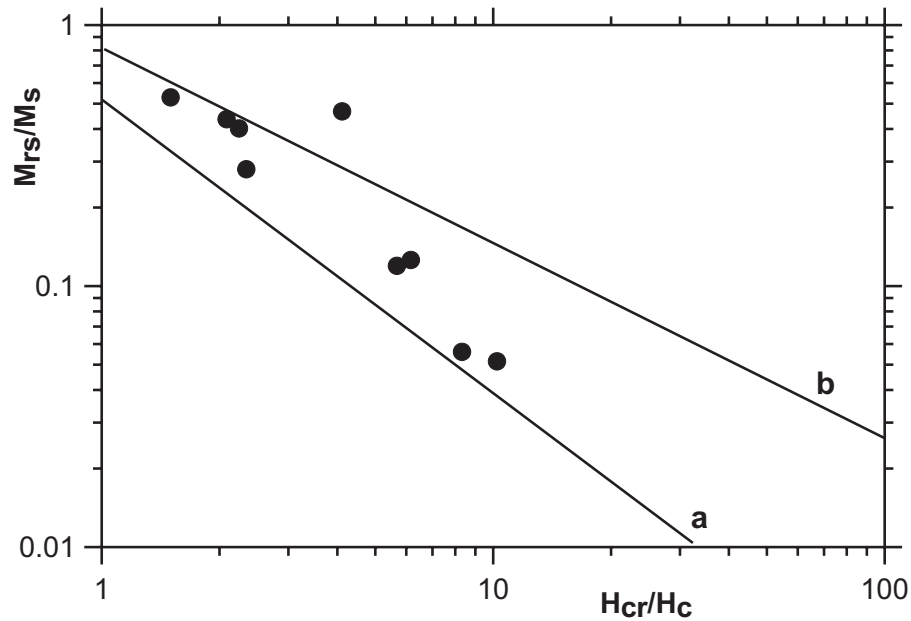


**Figure 9.8** Plot of the hysteresis ratios  $M_{rs}/M_s$  and  $H_{cr}/H_c$  of samples which reach saturation during hysteresis measurement. The samples from the Barrandian fall between the SD-MD mixing line after PARRY (1982, line a) and the line of remagnetised North American remagnetised carbonate rocks (JACKSON, 1990, line b).

complex paragenesis of calcite, baryte and Fe-oxide (Fig. 9.9 d). Idiomorphic calcite is overgrown by Fe-oxide crusts, which are covered by small platy to needle-shaped Fe-oxides. Ba-sulphates are always observed in xenomorphic, rounded shapes and are probably the remnants of a large baryte grain (Fig. 9.9 e). Fe-oxides also overgrow aggregates of clay minerals (illite and chlorite) and fill cavities of dissolved baryte (Fig. 9.9 f). The Fe-oxide in this paragenesis is thought to be hematite, carrying the remagnetisation component in site LODB.

## 9.4 K-Ar dating and trace element geochemistry

### 9.4.1 Preparation and characterisation of clay fractions

The effects of sample preparation and grain size on the apparent K-Ar ages was studied on four pilot samples from the NE Rhenish Massif (Section 7.2.1, page 73ff). Based on these results, the  $< 0.2\mu\text{m}$  fractions are thought to best represent the authigenic clay minerals in the samples. Consequently, the same separation techniques were used for four limestone samples (KOBAA, KLOAB, LODB, MRAA) from the Barrandian.

XRD analysis shows that illite is the dominating clay mineral in the  $< 0.2\mu\text{m}$  fractions (Table D.2). In all samples asymmetry of the (001) reflection of illite and

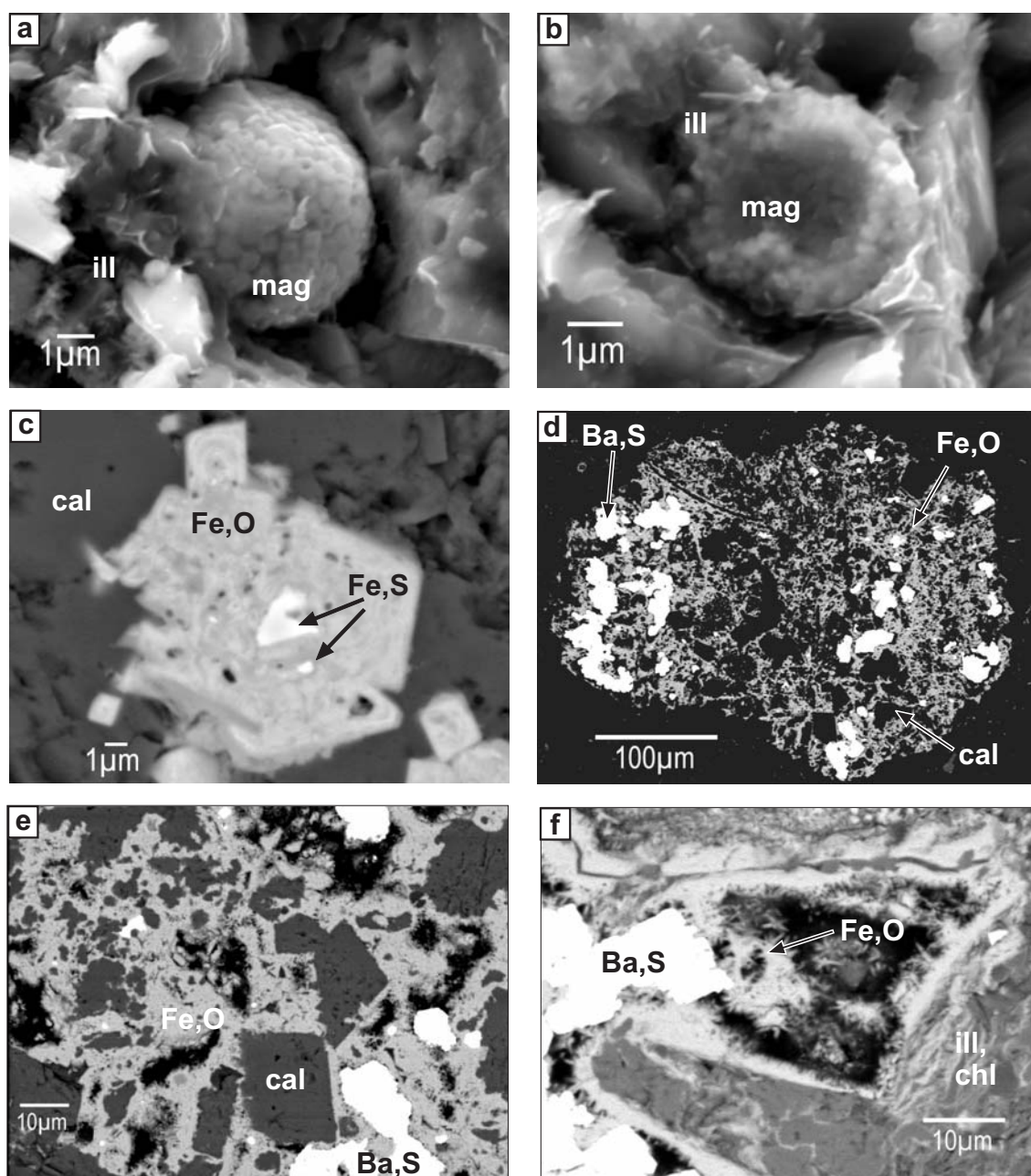


**Figure 9.9** Scanning electron micrographs of rock fragments and polished surfaces from locality KLO (a-c) and LODB (d-f). a) framboidal magnetite (mag) surrounded by small flakes of sheet silicates (ill, illite). b) hollow spherule of framboidal magnetite in close contact to illite. c) BSE image of Fe-oxide grain with sulphide core (cal, calcite). d) BSE image of large altered grain showing complex paragenesis of calcite, baryte and Fe-oxides. e) Detail of altered grain: replacement of baryte by idiomorphic calcite overgrown by Fe-oxides. f) growth of platy to needle-shaped Fe-oxides in small cavities, surrounded by clay minerals (ill, illite; chl, chlorite). All analyses shown in BSE images were made using secondary electrons in SEM mode.

slightly higher diffraction angles after treatment with glycol indicate illite - smectite interstratification. Chlorite was identified in fractions from samples KOBAA and MRAA, which also contain traces of quartz and albite. The  $< 0.2\mu\text{m}$  fraction of

sample KLOAB is characterised by high amounts of smectite interstratification and almost no contribution from other minerals.

The ICI of the  $0.2 - 2\mu\text{m}$  air-dried fractions ranges between 3 mm and 7.5 mm FWHM ( $0.3 - 0.75^\circ 2\Theta$ , Cu  $K_\alpha$ , Table D.1). It is highest in red limestones from site KOBAA, where evidence for fluid alteration was observed in the field. It should be noted, that the ICI of  $< 0.2\mu\text{m}$  fractions is significantly lower and ranges from 9 mm to 13 mm FWHM ( $0.9 - 1.3^\circ 2\Theta$ , Cu  $K_\alpha$ ).

### 9.4.2 K-Ar dating of $< 0.2\mu\text{m}$ clay fractions

The apparent ages of the  $< 0.2\mu\text{m}$  fractions fall within the range from  $356 \pm 12$  Ma (KLOAB) to  $390 \pm 9$  Ma (KOBAA, Table E.2). While the apparent K-Ar ages of fractions from KLOAB, LODB and MRAA are clearly younger than the sedimentation age of the limestones (Praghian, ca. 412 Ma - 400 Ma), the apparent K-Ar age of sample KOBAA is similar to the age of the Praghian/Emsian boundary (400 Ma).

In a plot of  $^{40}\text{Ar}/^{36}\text{Ar}$  versus  $^{40}\text{K}/^{36}\text{Ar}$  (Fig. 9.10 a), the analytical K-Ar data of samples KLOAB, LODB and MRAA fall on a regression line ( $386 \pm 7$  Ma) with an initial  $^{40}\text{Ar}/^{36}\text{Ar}$  ratio of  $253 \pm 10$  and a very low MSWD (0.065). The initial  $^{40}\text{Ar}/^{36}\text{Ar}$  ratio is significantly different from the present-day value, suggesting either an anomalously low  $^{40}\text{Ar}/^{36}\text{Ar}$  ratio during illitisation or subsequent loss of  $^{40}\text{Ar}$ . However, since this regression is only defined by three data points, further interpretation of the low initial  $^{40}\text{Ar}/^{36}\text{Ar}$  ratio does not seem justified.

The apparent ages of samples KLOAB, LODB and MRAA are not significantly different from each other and yield a weighted mean apparent age of  $365 \pm 13$  Ma (Fig 9.10 b). This is thought to indicate that the  $< 0.2\mu\text{m}$  fractions of these samples consist of one illite generation. Given the significant difference between the isochron age ( $386 \pm 7$  Ma,  $(^{40}\text{Ar}/^{36}\text{Ar})_{ini} = 253 \pm 10$ ) and the apparent age ( $365 \pm 13$  Ma,  $(^{40}\text{Ar}/^{36}\text{Ar})_{ini} = 295.5$ ), the age of this illite generation remains unclear. However, it seems reasonable to speculate, that the illitisation occurred closer to 365 Ma than to 386 Ma. The time interval from 365 Ma to 386 Ma is similar to the range of isotopic  $^{40}\text{Ar}/^{39}\text{Ar}$  ages on hornblendes and white micas from the Teplá-Barrandian (382 Ma - 362 Ma, DALLMEYER & URBAN, 1998), which are related to the deformation in the Barrandian (FRANKE, 2000).

Sample KOBAA does not fall on the regression line and yields higher ratios of  $^{40}\text{Ar}/^{36}\text{Ar}$  and  $^{40}\text{K}/^{36}\text{Ar}$  reflecting the high apparent age of  $390 \pm 9$  Ma for this sample. This could be caused by the presence of detrital K-bearing minerals, such as K-feldspar or muscovite. Alternatively, the isotopic system of clay minerals could have been disturbed by fluid alteration, which is evidenced by reduction halos along

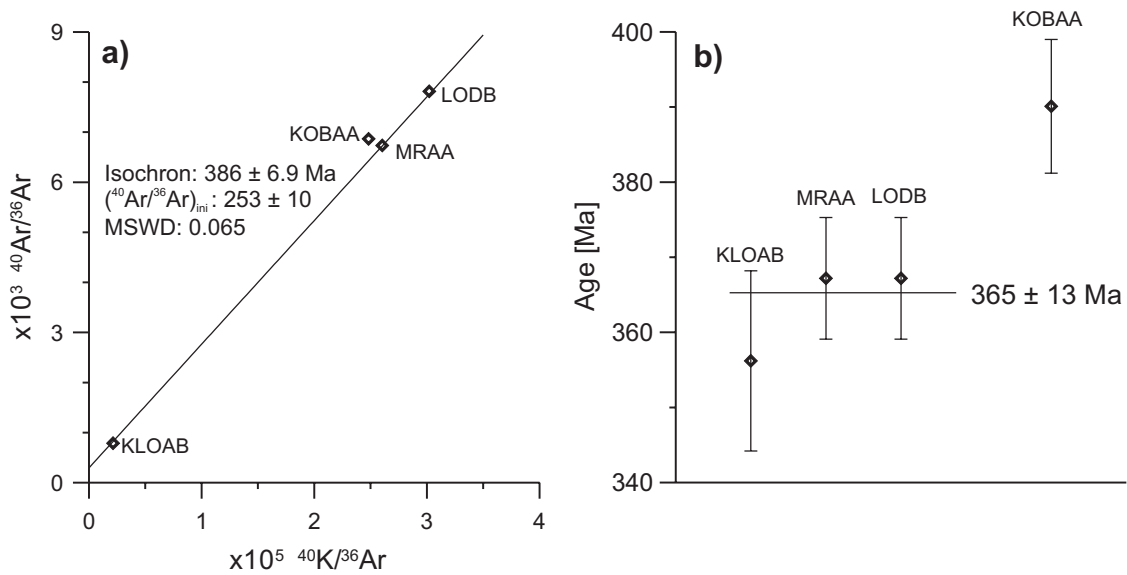


**Figure 9.10** a) K-Ar isochron and b) apparent ages of  $< 0.2\mu\text{m}$  fractions. The weighted mean apparent ages for samples KLOAB, LODB and MRAA yields  $365 \pm 13 \text{ Ma}$ . Sample KOBAA does not fall on the regression line and yields a significantly higher apparent K-Ar age.

fractures in the red limestones.

### 9.4.3 Trace and REE geochemistry of $< 0.2\mu\text{m}$ fractions and Fe-oxide leachates

The NASC normalised REE patterns of untreated  $< 0.2\mu\text{m}$  fractions of samples from the Barrandian are rather heterogeneous (Fig. 9.11 a). Two fractions (KLOAB, LODB) are depleted in HREE and show slight enrichments in MREE. Sample KOBAA is characterised by an increasing fractionation of REE with increasing atomic weight and a pronounced positive Ce-anomaly. The REE patterns of leachates from samples KLOAB, KOBAA and LODB are strongly enriched in MREE (Fig. 9.11 b). MRAA has the lowest REE content in the  $< 0.2\mu\text{m}$  fraction and the Fe-oxide leachate. Its REE patterns are generally flat with a slight depletion of MREE in the untreated clay fraction.

The enrichment in MREE of leachates from samples LODB, KOBAA and MRAA is correlated to the Ba-content. A similar relation between Ba-content and REE patterns of leachates was observed in the rocks from the NE Rhenish Massif (Section 7.3.2, page 81ff).

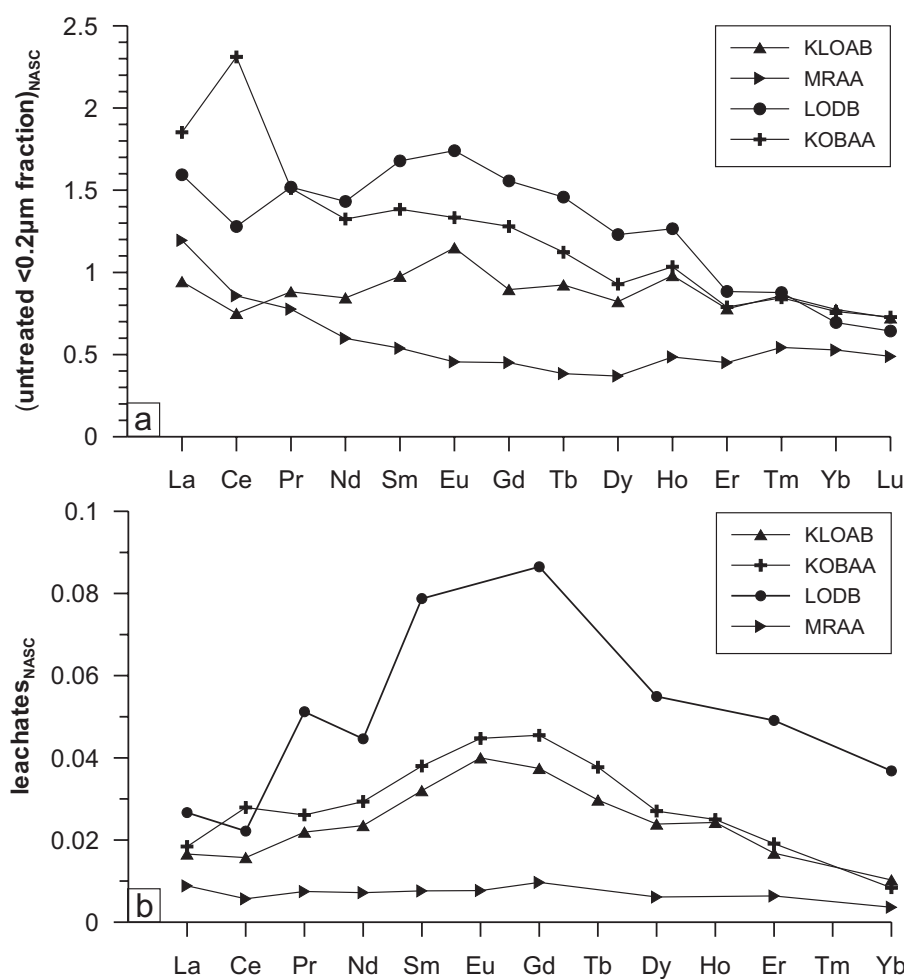


**Figure 9.11** NASC normalised REE patterns of a) untreated < 0.2µm fractions and b) Fe-oxide leachates.

## 9.5 Discussion of results

A remagnetisation was identified in the Barrandian, which is predominantly carried by magnetite in all localities, except for site LODB and MRA, where the magnetisation resides in magnetite and hematite.

Fold test analysis and comparison of the resulting palaeolatitude with the palaeomagnetic reference frame (VAN DER VOO, 1990) yields ambiguous results. Based on palaeomagnetic evidence, the remagnetisation event could have occurred during the late stage of the Variscan deformation in the Late Devonian or the remagnetisation could be postfolding in origin and of Late Carboniferous age.

The K-Ar ages of < 0.2µm fractions indicate a diagenetic event somewhere between 386 Ma and 365 Ma. This age interval is almost identical to the age of deformation, inferred from geological evidence and isotopic  $^{40}\text{Ar}/^{39}\text{Ar}$  ages on hornblendes and white micas from surrounding areas in the Teplá-Barrandian (DALLMEYER &

URBAN, 1998). Therefore, the illite diagenesis is likely to be related to the deformation in the Barrandian. The REE patterns of Fe-oxide leachates show a distinct enrichment in MREE, which is generally correlated to the Ba-content. A similar relationship between MREE enrichment and Ba-content was observed in remagnetised sedimentary rocks from the NE Rhenish Massif.

SEM studies indicate oxidation of framboidal pyrite to magnetite in grey Late Silurian limestones and the formation of Fe-oxides in red Devonian limestones. Magnetite pseudoframboids and authigenic illite form a characteristic parageneses. Since oxidation of framboidal pyrite is a possible mechanism of remagnetisation, the K-Ar ages of illite are thought to constrain the remagnetisation to be Late Devonian in age. The SEM studies also indicate, that authigenesis of magnetic minerals in red Devonian limestones is related to dissolution of baryte.

# Chapter 10

## Multiple remagnetisations in Devonian carbonate rocks, SW Holy Cross Mountains, Poland

### 10.1 Geology and sampling

The Holy Cross Mountains (HCM) in SE Poland are part of the Trans-European Suture Zone (TESZ), which forms the boundary between Baltica and the Palaeozoic mobile belts of Central Europe. The Palaeozoic core of the HCM consists of two tectonostratigraphic units, which are separated by the Holy Cross Dislocation. The southern unit (Kielce unit, Fig. 10.1) belongs to the Malopolska Massif (BELKA *et al.*, 2000, and references therein), which forms the Precambrian and Palaeozoic basement of southeastern Poland and is limited by the Cracow fault in the south. The Kielce unit is characterised by a thick succession of folded Precambrian to Middle Cambrian clastic rocks, which are discordantly overlain by Ordovician sandstones and carbonate rocks and Silurian shales. The Devonian comprises clastic and carbonate rocks, which rest discordantly on Lower Palaeozoic units. Provenance studies have shown that the Malopolska Massif constitutes the first Gondwana-derived microplate that accreted to the margin of Baltica in Middle Cambrian times. The facies pattern along the Holy Cross Dislocation suggests the amalgamation of the Kielce unit with the northern unit of the HCM (Lysogory) during late Silurian times (BELKA *et al.*, 2000, and references therein).

The intensive folding of the Palaeozoic strata in both units of the HCM mainly results from Variscan tectonics after the Viséan. The Palaeozoic structure is covered by flat lying Permian conglomerates. In the Maastrichtian and Palaeocene, the HCM were uplifted as a result of a shortening event during Alpine orogeny (LAMARCHE *et al.*, 1999). This tectonic phase is associated mainly with brittle deformation along

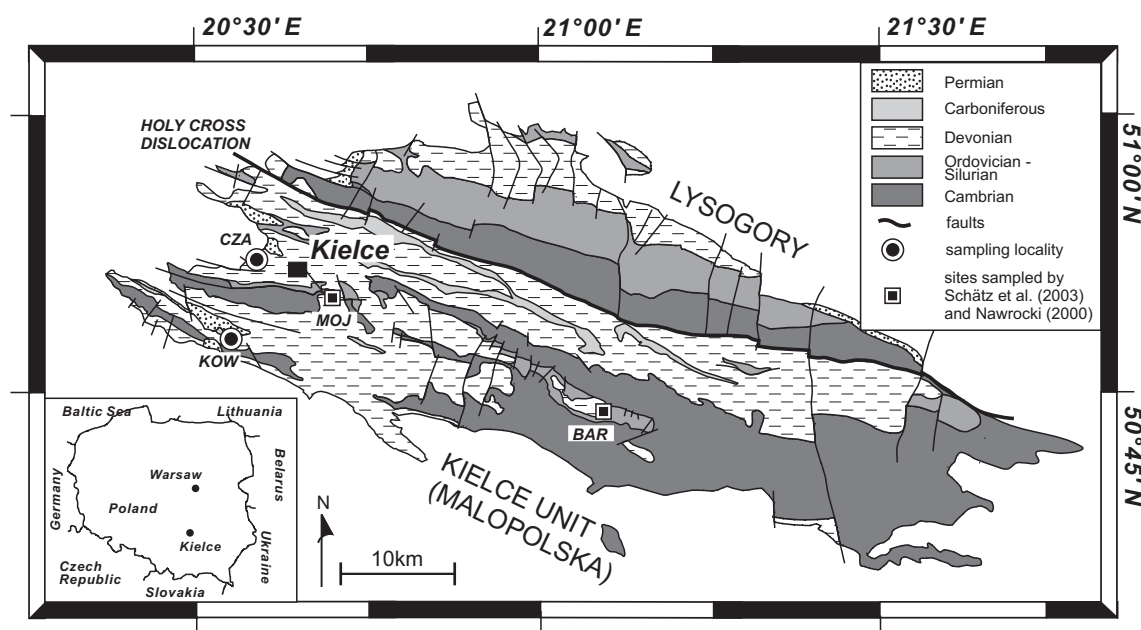


**Figure 10.1** Geological sketch map of the Holy Cross Mountains and location of the palaeomagnetic sampling sites (CZA, KOW). Previous palaeomagnetic results were reported from Ordovician carbonates (MOJ, SCHÄTZ *et al.*, 2003) and Silurian volcanic rocks (BAR, NAWROCKI, 2000) further to the east.

strike-slip and reverse faults and could have caused rotation and tilting of crustal blocks, while the Variscan age folds were not refolded (LAMARCHE *et al.*, 1999).

The timing and scale of movements along TESZ are still a matter of debate. Based on palaeomagnetic data from Devonian and Ordovician rocks, which indicate large-scale clockwise tectonic rotations, a major Variscan dextral strike-slip displacement of the southern Kielce unit was proposed along the SW margin of the East European Craton (LEWANDOWSKI, 1993). However, more recent palaeomagnetic data from Ordovician carbonates (SCHÄTZ *et al.*, 2003, MOJ in Fig. 10.1) and Silurian volcanic rocks (NAWROCKI, 2000, BAR in Fig. 10.1) in the central HCM indicate that no differential movements have occurred since Middle to Late Ordovician times between the HCM and Baltica.

The identification and analysis of tectonic events in the HCM by the means of palaeomagnetic methods is hampered by the observation of multiple remagnetisation events (GRABOWSKI & NAWROCKI, 1996) and evidence for strain modification of magnetic directions (GRABOWSKI & NAWROCKI, 2001). A remagnetisation of uncertain age was observed in Late Devonian limestones from the Czarnow (Sluchowice) Quarry (M. SCHÄTZ, unpublished data).

In order to study the timing and characteristics of this remagnetisation event, new palaeomagnetic samples were taken from Late Devonian (Frasnian) limestones at Czarnow Quarry (CZA in Fig. 10.1) and at a railroad cut in Kowala Quarry (KOW

in Fig. 10.1). The section at Czarnow comprises predominantly micritic limestone turbidites of Late Frasnian age. At Kowala, biogenic limestones (amphipora limestone), laminated limestones and debris flow deposits are exposed at the base of the limestone turbidites. Both sections are characterised by nearly pristine conodont colours (CAI 1-1.5), which demonstrate that the rocks were not affected by any thermal alteration (BELKA, 1988). However, the upper part of the Kowala section is characterised by reddish alteration colours (Liesegang rings). This is thought to reflect penetration of oxidising fluids from the Permian palaeosurface into the uppermost part of the Palaeozoic sequences.

In total, about 115 palaeomagnetic samples (16 sites) were taken from beds with varying bedding attitudes and the unpublished data (M. SCHÄTZ) from Czarnow (CZA1-3 in Table B.1) were reanalysed. Hand samples for isotopic and geochemical studies of clay minerals were taken from turbidite limestone (CZA3,5; KOW12), biogenic limestones (KOW1), and red and grey marl interlayers (KOW9r,g). One hand sample was taken from Ordovician limestones at Mojzca (MOJ in Fig. 10.1) to study the different geochemical and isotopic signatures of clay minerals in rocks, where a primary magnetisation is preserved.

## 10.2 Palaeomagnetism

### 10.2.1 Demagnetisation behaviour and fold test results

The demagnetisation behaviour of the samples from the HCM is similar to the samples from the Barrandian (section 9.2.1). Thermal demagnetisation is more effective in separating the components of magnetisation and was routinely used on all specimens. Fold test analysis was performed using the ENKIN (1990) software package.

After removal of a viscous overprint and/or a magnetisation parallel to the present day field in the sampling area, three components of magnetisation (A, B, and C) were identified during stepwise thermal demagnetisation (Fig. 10.2a-d). The site mean directions are shown in Table B.1.

Component A is present in most samples from CZA as a stable endpoint direction between 200 °C and 500 °C (Fig. 10.1 a). In some samples, however, A does not reach the origin (Fig. 10.2 b) and free linear segments were used for principal component analysis (PCA, KIRSCHVINK, 1980). The site mean directions fail the fold test, indicating that A is secondary in origin, postdating the folding event (Fig. 10.3 a). The demagnetisation behaviour of samples where A does not reach the origin, suggests the presence of a high temperature component (B\*) in CZA. Interpretation of great circle trajectories (MCFADDEN & MCELHINNY, 1988) yields a subhorizon-

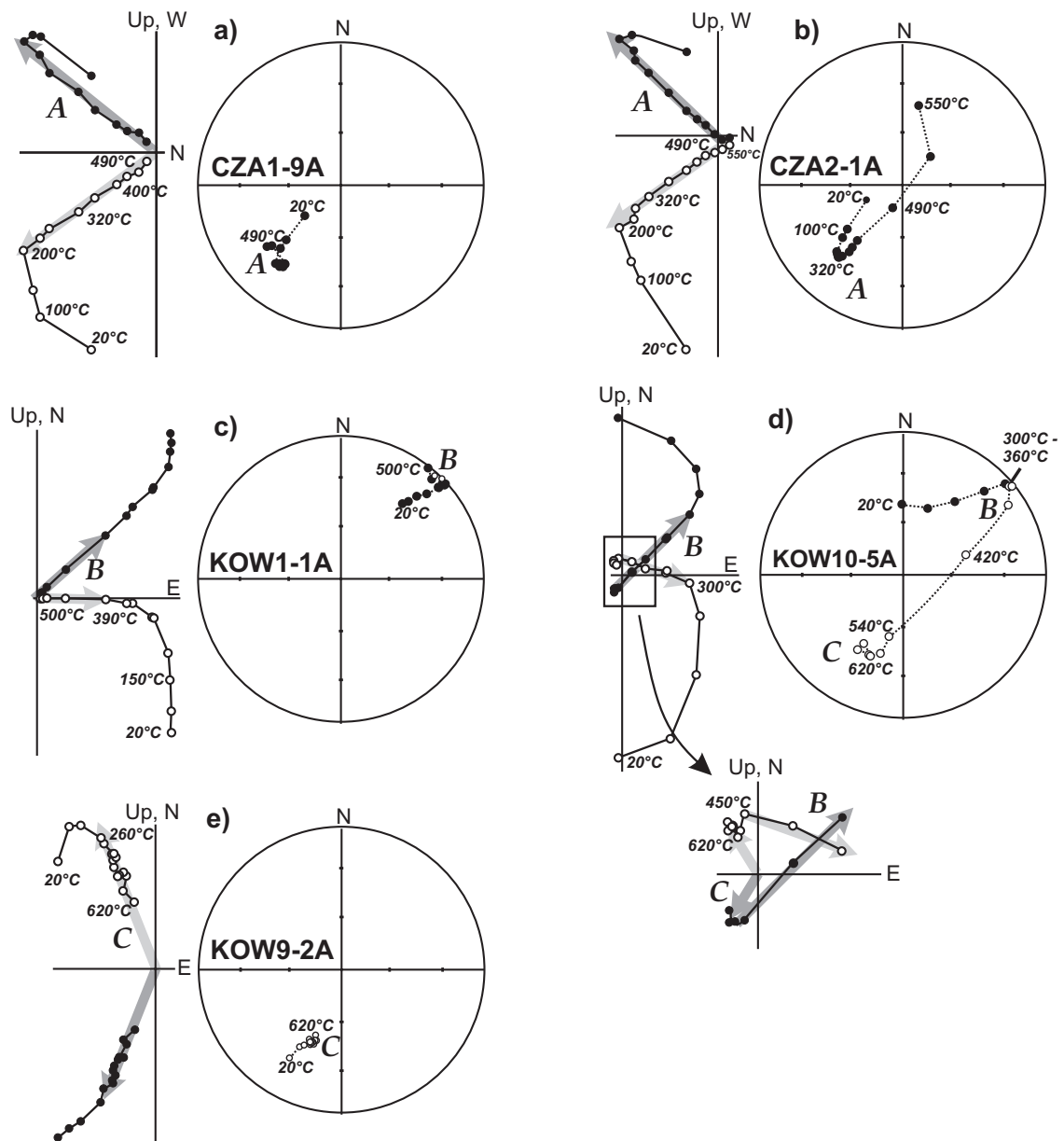


**Figure 10.2** Results of thermal demagnetisation experiments in orthogonal and stereographic projection. Orthogonal Projection in geographic coordinates, solid (open) circles: horizontal (vertical) plane. Stereographic Projection in geographic coordinates, solid (open) circles: lower (upper) hemisphere. Three components of magnetisation (A,B,C) were identified.

tal, northeasterly direction, with maximum precession (k) at 46% unfolding (Fig. 10.3 b).

A component of magnetisation (B) with a subhorizontal, northeasterly direction is also observed in samples from KOW. Here, B is demagnetised between 300°C and 500°C (Fig. 10.3 c,d) during thermal demagnetisation. The best distribution of site mean direction is reached at 59% unfolding (Fig. 10.3 c). Although component B\* from Czarnow is only identified by great circle interpretation, its similar unit

mean direction and fold test results indicate that it has the same age and origin as component B from Kowala (Table 10.1).

In many samples from the upper part of the Kowala section, a third component C with southwesterly declination and intermediate, negative inclination is demagnetised above 600 °C (Fig. 10.2 d,e). In most cases, the magnetisation follows a great circle toward the direction of C during demagnetisation of component B (Fig. 10.2 d). The fold test shows that C is clearly postfolding in origin (Fig. 10.3 d). The high unblocking temperatures of more than 600 °C indicate that C is carried by hematite.

Unit mean directions (Component)	N'	Geogr. coord.				partially unfolded					
		Dec [°]	Inc [°]	$\alpha_{95}$ [°]	k	oduf	95% confidence	Dec [°]	Inc [°]	$\alpha_{95}$ [°]	k
A	6	220	17	5	176	4%	0% - 8%	-	-	-	-
B*	14(s)	42	-14	6	173	46%		41	3	4	327
B	10	50	4	6	71	59%	41% - 77%	47	5	4	219
C	6	218	-38	6	147	10%	-1% - 21%	-	-	-	-

**resulting palaeopoles:**  
**Component A:** PLAT: 21 °S; PLONG: 22 °W; dp: 3 °; dm: 5 °  
**Component B:** PLAT: 27 °S; PLONG: 35 °W; dp: 3 °; dm: 6 °  
**Component C:** PLAT: 48 °S; PLONG: 39 °W; dp: 4 °; dm: 7 °

**Table 10.1** Unit mean directions for components A,B and C identified in the rocks from the Holy Cross Mts. For palaeopole calculation of components A and C, the unit mean in geographic coordinates was used. For palaeopole calculation of component B, the unit mean after 59% of unfolding was used. N', number of site mean directions used; oduf, optimum degree of unfolding with its interval of 95% confidence and corresponding declination (Dec), inclination (Inc), radius of cone of 95% confidence ( $\alpha_{95}$ ) and FISHER (1953) precision parameter (k); PLAT and PLONG, latitude and longitude of the palaeo(south)pole; dp and dm, semiaxes of the oval of 95% confidence.

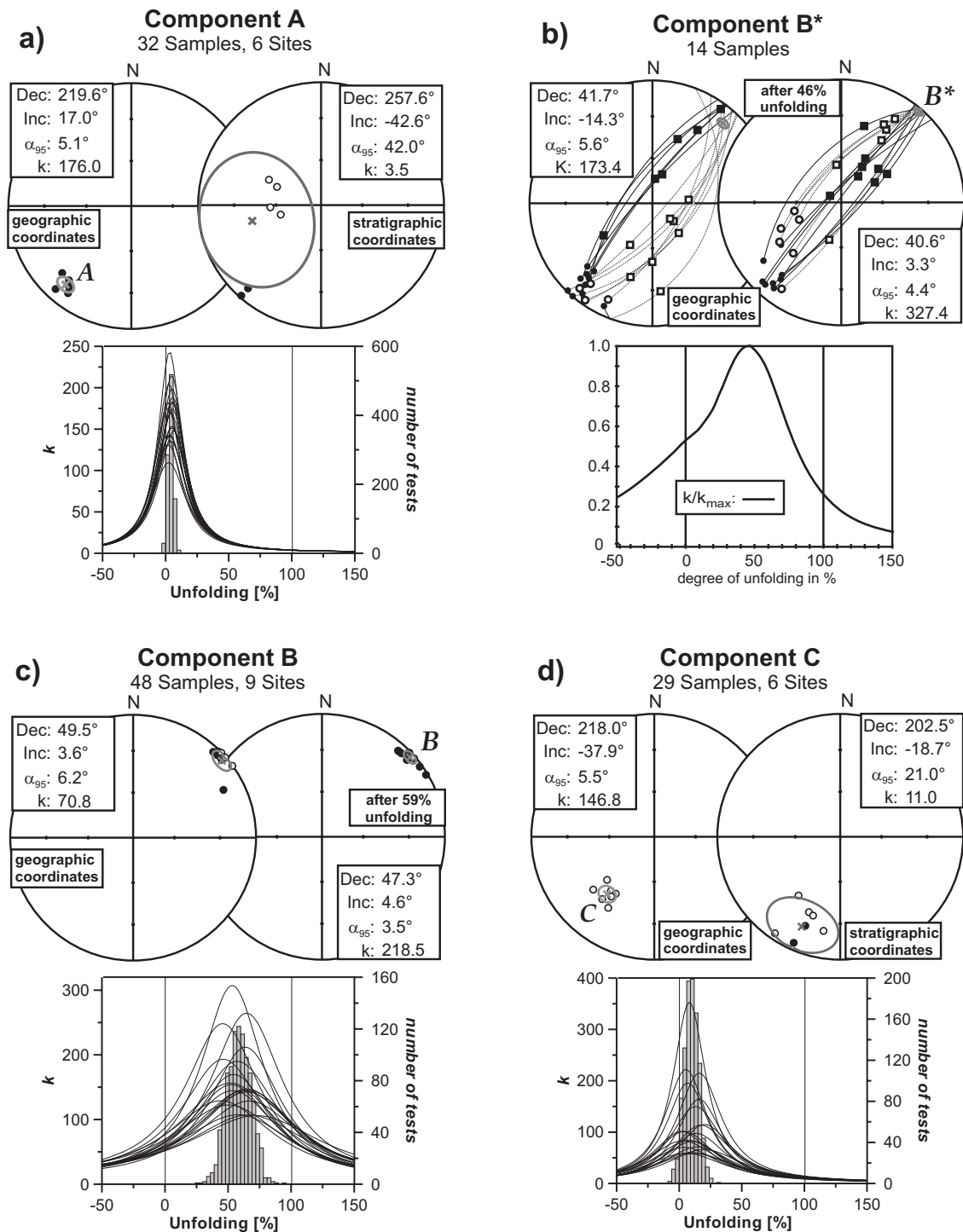


**Figure 10.3** a,c,d) Site mean directions of components A, B and C with fold test results. The histograms give the distribution of the maxima of 1000 trials in groups of 3%. Accuracy of bedding attitude was estimated to be within 3°. b) Great circle interpretation of high temperature tails observed in samples from the Czarnow Quarry, where Components A did not reach the origin upon demagnetisation. For fold test analysis, the algorithm by MCELHINNY (1964) was used. Here: circles (squares), start (end) point of great circle interpretation; solid (open) circles: lower (upper) hemisphere.

### 10.2.2 Interpretation of palaeomagnetic results

The results of the fold tests performed at the Kowala and Czarnow sections indicate at least two different remagnetisation events in the western part of the HCM. However, despite the fold test results, the age and geological significance of magnetisations A and B remain enigmatic.

Component A from Czarnow is postfolding in origin and was acquired after the main deformation in the Late Carboniferous. The resulting palaeopole (Table 10.1) plots close to the Early Carboniferous segment of the APWP for Baltica (SMETHURST *et al.*, 1998, Fig. 10.4). This palaeopole position implies a post-Variscan clockwise rotation of about  $20^\circ$  of the Czarnow area with respect to the East European Platform. It should be mentioned that palaeomagnetic results from Ordovician carbonate rocks (SCHÄTZ *et al.*, 2003) and Silurian volcanic rocks (NAWROCKI, 2000) do not indicate rotation of the HCM relative to Baltica since the Early Palaeozoic.

Component B appears to be synfolding in origin and it is therefore older than magnetisation A. The palaeopole for component B falls on the Late Devonian segment of the APWP, which indicates a primary age for component B. However, this is not consistent with the synfolding pattern of the fold test. A synfolding magnetisation with a nearly antiparallel direction was also reported by GRABOWSKI & NAWROCKI (2001) for Upper Frasnian limestones just south of the Holy Cross Dislocation.

Since the direction of B observed in CZA is not significantly different from the direction of B at KOW, any differential rotation between these two localities can be ruled out. Therefore the clockwise rotation of the Czarnow area indicated by component A must have also affected the Kowala region. If both palaeopoles are corrected for this rotation (arrows in Fig.10.4), B (synfolding in age) falls on a younger segment of the APWP than A (postfolding in age), which is difficult to explain, given the high quality of the data (small  $\alpha_{95}$  and high  $k$ ).

This interpretation relies on the significance of the great circle results from CZA and their validity might be challenged. In this case differential rotations between CZA and KOW cannot be ruled out and the correct chronological order of the palaeopoles for A and B on the APWP could be achieved by rotation of the Czarnow block about a horizontal axis during a period of brittle deformation in the Cenozoic (LAMARCHE *et al.*, 1999).

A more speculative explanation for a synfolding Late Devonian magnetisation is the possibility of a diachronous Variscan folding in the HCM (GRABOWSKI & NAWROCKI, 2001, and references therein). A late Devonian/Early Carboniferous deformation would support the palaeopole position of components A and B without

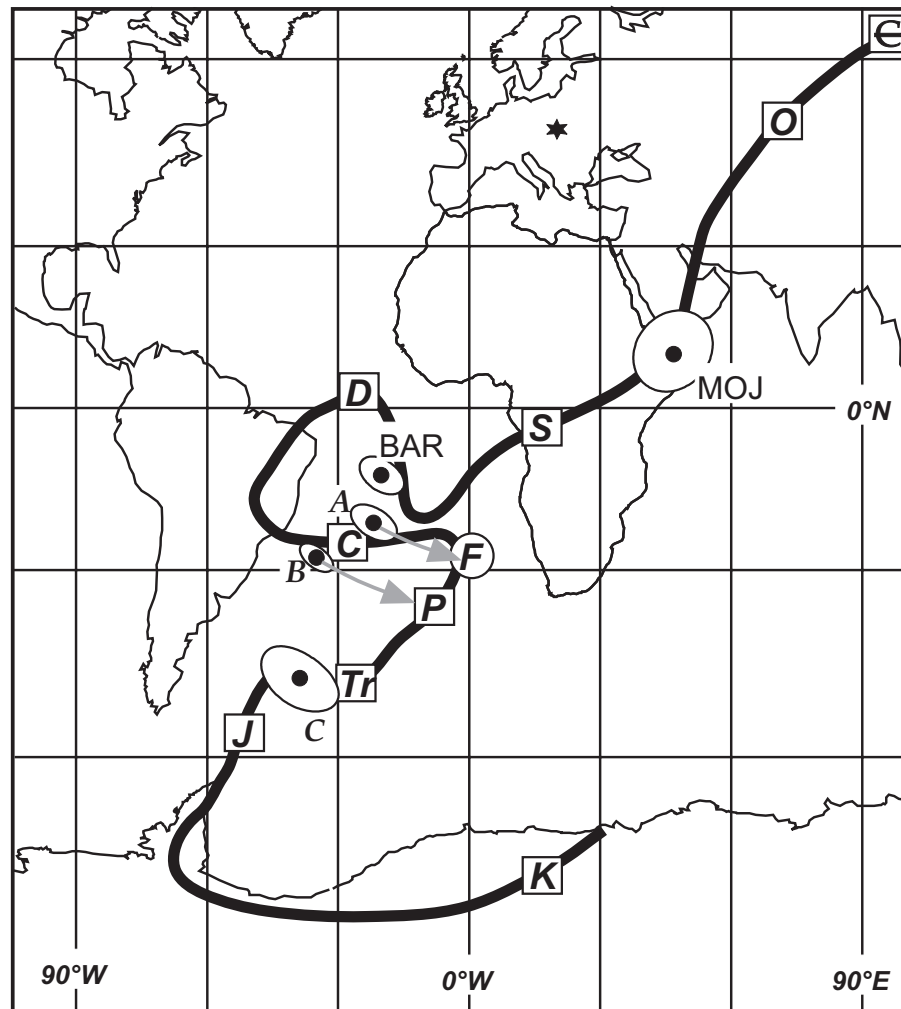


**Figure 10.4** Palaeopole positions with respect to the APWP for Baltica (SMETHURST et al., 1998). The arrows indicate the amount of rotation necessary to bring palaeopoles A and B into agreement with the APWP. O: Ordovician; S: Silurian; D: Devonian; C: Carboniferous; P: Permian; Tr: Triassic; J: Jurassic; K: Cretaceous; F: main deformation in the HCM. The star marks the location of the sampling area.

the requirement of post-Variscan block rotations. However, a diachronous deformation in the HCM is not supported by geological evidence.

The palaeopole for component C falls on the Triassic segment of the APWP. Component C is carried by hematite and mainly observed in the upper parts of the Kowala section, which shows evidence for oxidising fluid flow. This suggests, that C was caused by oxidising fluids, migrating from the Mesozoic weathering surface into the upper parts of the Palaeozoic strata.

### 10.3 Magnetomineralogy

IRM acquisition and hysteresis measurements were carried out to identify the magnetic minerals in the samples from the HCM. Two hysteresis curves are shown in Fig. 9.7, which are characteristic for the sample set. Both samples (CZA1-7, KOW12-2) do not reach saturation at 1 T, which indicates the presence of high coercive minerals. The strong decrease in magnetic intensity temperatures of ca. 120 °C during thermal demagnetisation experiments is characteristic for high amounts of goethite in samples from Czarnow. The hysteresis loop of sample CZA1-7 is constricted at low fields, which is indicative for a second, low coercivity magnetic phase, which is thought to be magnetite. Since components A and B are both demagnetised between 200 °C and 500 °C in the rocks from Czarnow and Kowala, magnetite is probably the carrier of magnetisation. In red limestones from site KOW12, magnetisation C is demagnetised above 620 °C, indicating the presence of hematite. The hysteresis curve of a sample from this site (KOW12-2 in Fig. 10.5) is not constricted at low fields, indicating the absence of, or only small amounts of, magnetite in this sample. Due to the presence of high coercivity minerals in almost all samples, the hysteresis ratios could not be used for further interpretation.

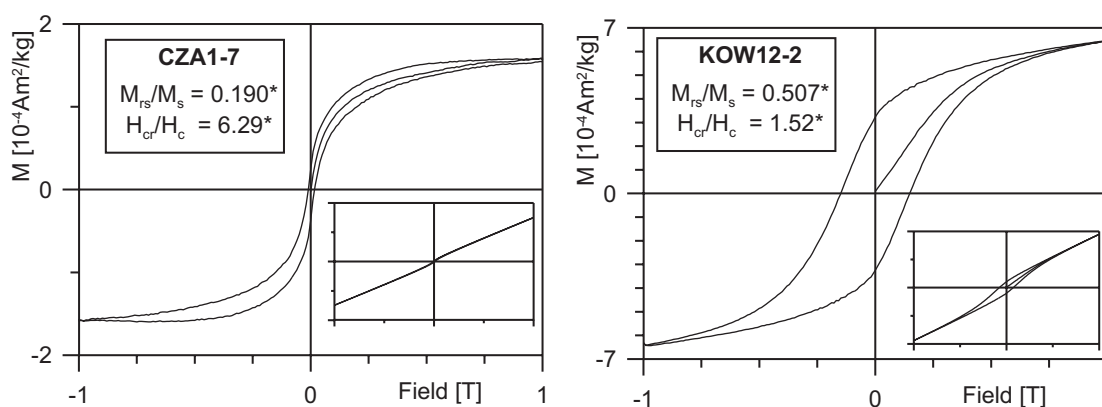


**Figure 10.5** Hysteresis curves of two samples from the HCM. The insets show the original shape of the hysteresis loops before correction for paramagnetism.\* due to the presence of high coercive minerals, the hysteresis ratios are not used for further interpretation.

In rocks from Czarnow, SEM studies of rock fragments indicate the occurrence of euhedral magnetite at the contact of micritic and sparitic calcite (Fig. 10.6 a). The oxidation of framboidal pyrite to magnetite is frequently observed (Fig. 10.6 b-d). The tiny depressions on the surfaces of magnetite crystals (arrows in Fig. 10.6 d) are thought to indicate small holes in the middle of the crystals, which have been described by SUK *et al.* (1993a) from pseudoframboidal magnetite in remagnetised

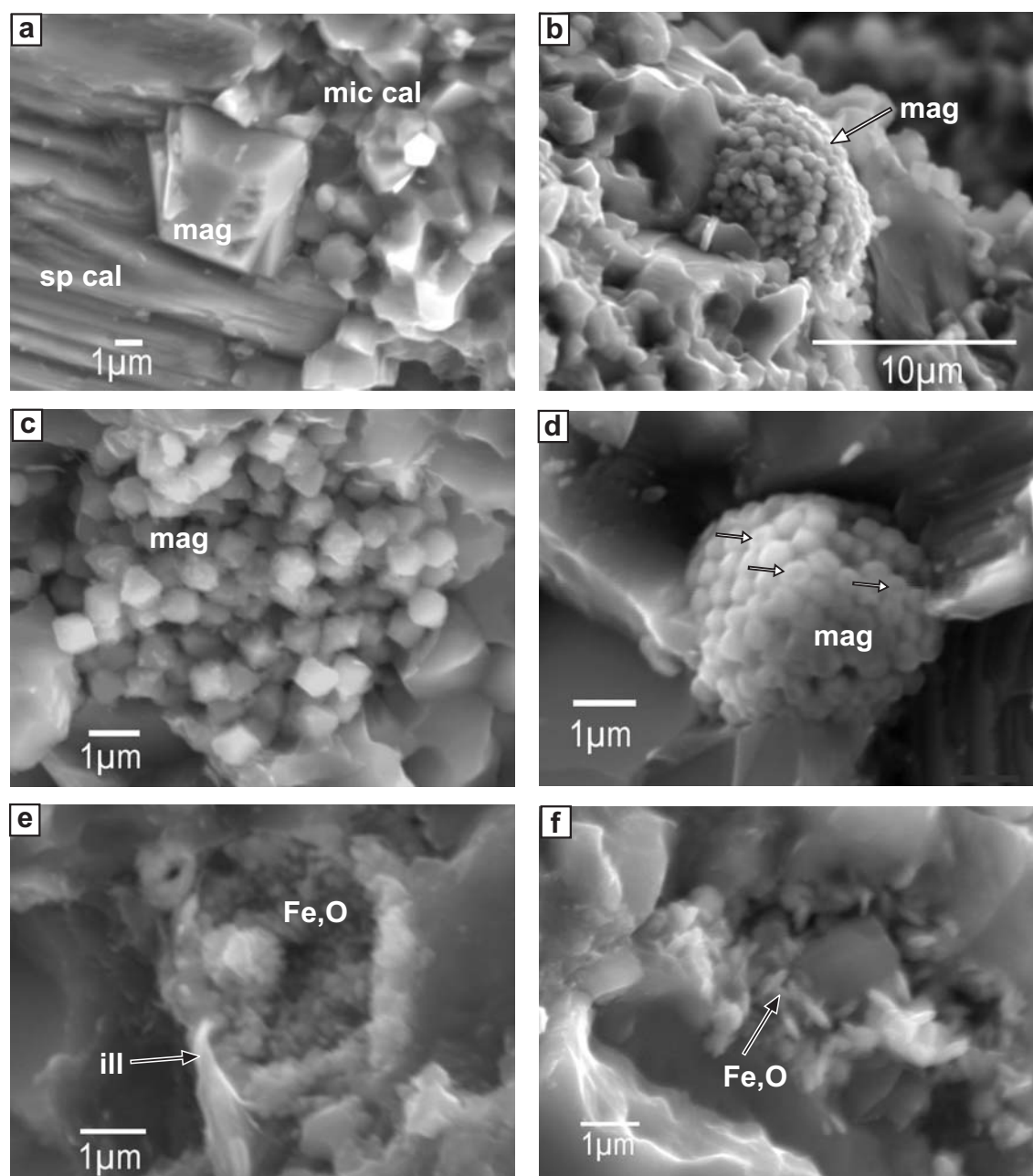


**Figure 10.6** Scanning electron micrographs of rock fragments from Czarnow (CZA3, a-d) and Kowala (KOW12, e-f). a) euhedral magnetite (mag) at the contact between micritic (mic cal) and sparitic calcite (sp cal). b-d) pseudoframboidal magnetite in calcite matrix. The arrows in d) indicate small depressions of the surfaces of magnetite crystals, which could indicate hollow magnetite grains. e,f) spherical pore space coated with platy Fe-oxide, which is thought to be hematite.

Early Palaeozoic limestones from New York State, USA. These holes could have been caused by dissolution of pyrite without subsequent crystallisation of magnetite. In site KOW12 from Kowala, spherical pore spaces are coated by small ( $< 1\mu\text{m}$ ) Fe-oxide crystals (Fig. 10.6 e,f). The platy morphology of these grains is similar to

the shape of hematite (specularite). The overgrowth of pore surfaces, indicates the secondary nature of this mineral. Hematite was identified during palaeomagnetic and rock magnetic experiments in samples from this site and carries component C, which is an Early Triassic magnetic overprint.

## 10.4 K-Ar dating and trace element geochemistry

### 10.4.1 Characterisation of clay fractions

The effects of sample preparation and grain size on the apparent K-Ar ages was studied on four pilot samples from the NE Rhenish Massif (Section 7.2.1, page 73ff). Based on these results, the  $< 0.2\mu\text{m}$  fractions are thought to best represent the authigenic clay minerals in the samples. Consequently, the same separation techniques were used for seven samples (CZA3, CZA5, KOW1, KOW9r, KOW9g, KOW12, MOJ) from the HCM.

The results of XRD analysis show that illite is the dominating clay mineral in the  $< 0.2\mu\text{m}$  fractions (Table D.2). Small amounts of mixed-layer illite - smectite is indicated by asymmetry of the (001) reflection of illite and slightly higher diffraction angles after treatment with glycol in the fraction of sample KOW1. Most samples contain traces of kaolinite, while chlorite was only observed in sample MOJ.

The ICI of the  $0.2 - 2\mu\text{m}$  air-dried fractions ranges between 4 mm and 9 mm FWHM ( $0.4 - 0.9^\circ 2\theta$ , Cu  $K_\alpha$ , Fig. 10.7, Table D.1). It is relatively constant in the  $0.2 - 2\mu\text{m}$  fractions of Devonian samples from Czarnow and Kowala, but significantly lower in the  $0.2 - 2\mu\text{m}$  fraction of the Ordovician carbonate rocks from site MOJ, where a primary Ordovician magnetisation is preserved (SCHÄTZ *et al.*, 2003). The ICI of the  $< 0.2\mu\text{m}$  fractions are generally higher in the limestones from Czarnow and the marls from KOW. It should be noted, that both grain size fractions of sample MOJ have similar ICI, indicating a rather homogeneous clay mineralogy in this sample.

### 10.4.2 K-Ar dating of $< 0.2\mu\text{m}$ clay fractions

The apparent ages of the  $< 0.2\mu\text{m}$  fractions fall within the range from  $333 \pm 7$  Ma (MOJ) to  $292 \pm 7$  Ma (KOW12, Table E.2) and are clearly younger than the sedimentation age of the Late Devonian and Ordovician carbonate rocks. In a plot of  $^{40}\text{Ar}/^{36}\text{Ar}$  versus  $^{40}\text{K}/^{36}\text{Ar}$  (Fig. 10.8 a), the analytical K-Ar data of all samples except MOJ define a regression line ( $318 \pm 41$  Ma;  $(^{40}\text{Ar}/^{36}\text{Ar})_{\text{imi}} = 295 \pm 320$ ), which is characterised by high uncertainties. The high MSWD value (192) indicates, that these samples do not represent a single illite generation but contain mixtures of

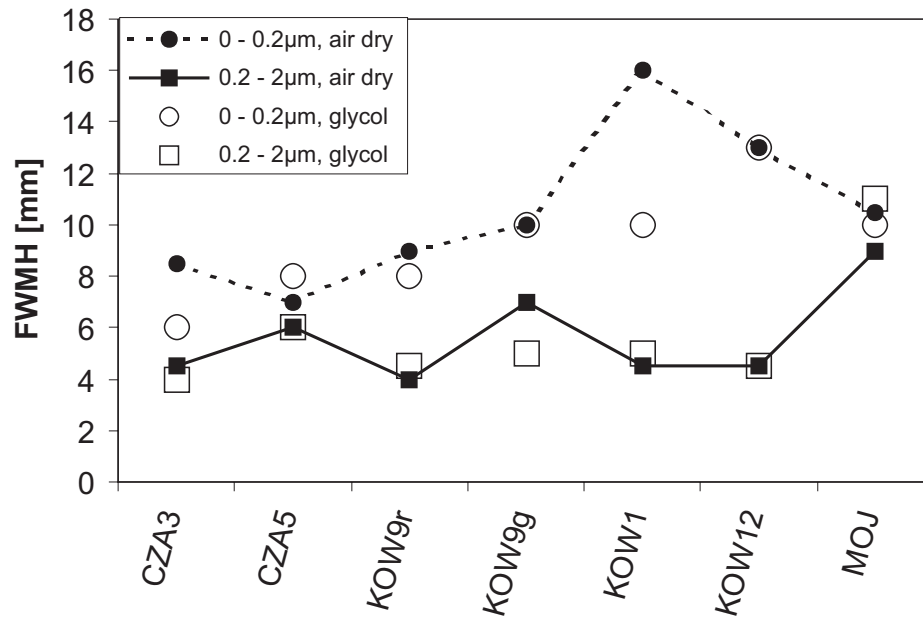


**Figure 10.7** The full width at half maximum (FWHM) of the illite  $10\text{\AA}$  peak in mm as a measure of the illite crystallinity index (ICI) of  $< 0.2\mu\text{m}$  (circles) and  $0.2 - 2\mu\text{m}$  (squares) fractions without treatment (solid symbols) and after treatment with ethylene-glycol (open symbols). 1 mm equals  $0.1^\circ 2\Theta$ , Cu  $K_\alpha$ . Glycol treatment did not significantly change the width of the  $10\text{\AA}$  peak.

two or more authigenic and possibly detrital sources. Alternatively, differential loss of radiogenic  $^{40}\text{Ar}$  could cause this high scatter. Neither the samples from Czarnow nor those from Kowala alone or any other chosen group of these samples define a regression line, which yields acceptable statistical parameters (MSWD  $< 5$ ).

The distribution of the apparent K-Ar ages (Fig. 10.8 b) shows a continuous trend between ca. 290 Ma and 330 Ma and the determination of a weighted mean apparent age is not justified. The  $< 0.2\mu\text{m}$  fraction of sample MOJ yields the highest apparent K-Ar age. In a plot of  $^{40}\text{Ar}/^{36}\text{Ar}$  versus  $^{40}\text{K}/^{36}\text{Ar}$ , the analytical K-Ar data of this sample plot far above the regression line defined by all other samples.

If the possibility of differential  $^{40}\text{Ar}$  loss is ignored, the different isotopic composition of MOJ can be explained by different age and origin of detrital muscovite, contaminating the clay fractions. In the simplest case, the apparent K-Ar ages of clay fractions from the HCM is a function of the relative amount of detrital minerals (muscovite) and one authigenic generation of illite. In this case, the youngest age of the  $< 0.2\mu\text{m}$  fractions (KOW12,  $292 \pm 7$  Ma) might be considered to be close to the maximum age of illitisation. Detrital muscovites in Lower Devonian clastic rocks from the Kielce unit (Malopolska) yield K-Ar ages of ca. 440 - 420 Ma (BELKA *et al.*, 2000). A similar or slightly younger age can be expected for detrital

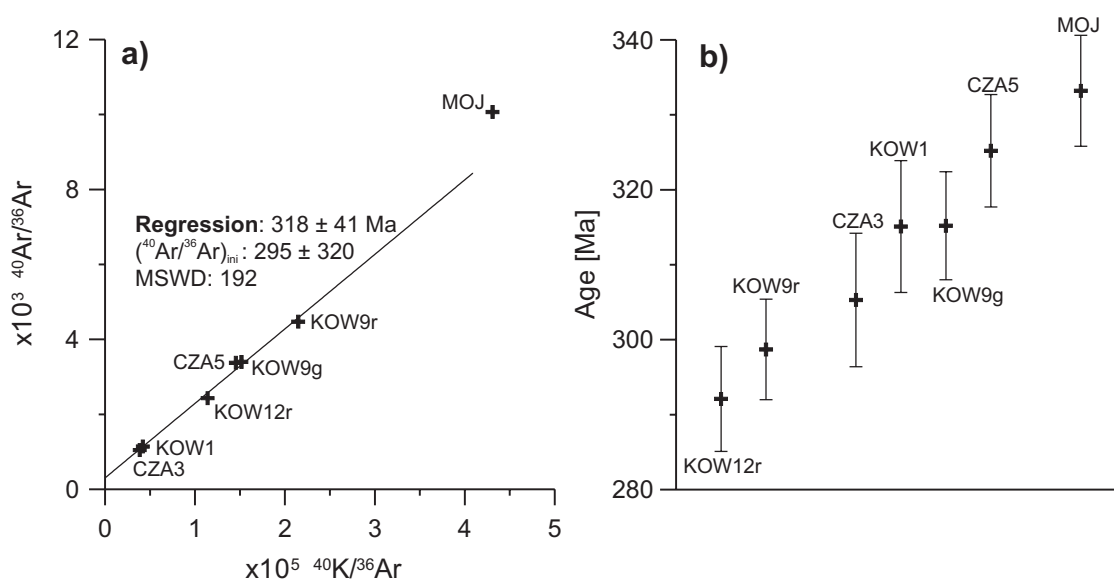


**Figure 10.8** a) K-Ar isochron and b) apparent ages of  $< 0.2\mu\text{m}$  fractions.

muscovite in the Late Frasnian limestones from Czarnow and Kowala. The detritus in the Middle Ordovician carbonates from MOJ must be considerably older and is likely to be similar to the age of detrital muscovite in Middle Cambrian clastic rocks in Malopolska (1745 Ma, BELKA *et al.*, 2000). A very small contamination from this detritus, which documents a clastic input from the Svecofenian basement of Baltica, would be sufficient to explain the high  $^{40}\text{Ar}/^{36}\text{Ar}$  ratio in the  $< 0.2\mu\text{m}$  fraction from MOJ.

This simple model is challenged by the fact that the fractions from marls (KOW9g) and biogenic limestones (KOW1) yield similar apparent K-Ar ages, while they can be expected to contain very different amounts of detrital material. Alternatively, it might be possible that the clay fractions are not contaminated by detrital minerals and that the apparent K-Ar ages reflect two or more illitisation events of different age (one older than ca. 330 Ma and another younger than ca. 290 Ma). Since MOJ was not affected by the remagnetisation events in the western HCM, it could also have been spared from a diagenetic event younger than ca. 290 Ma. This would imply that the remagnetisation event responsible for acquisition of component A occurred after 290 Ma. However, it must be stressed that this interpretation is highly speculative and relies on the assumptions that the Ar isotope system of illite in the HCM was not changed by diffusive processes and that remagnetisation and diagenesis in the HCM are connected.

### 10.4.3 Trace and REE geochemistry of $< 0.2\mu\text{m}$ fractions and Fe-oxide leachates

Three groups of REE patterns of untreated  $< 0.2\mu\text{m}$  fractions can be distinguished in the samples from the HCM (Fig. 10.9 a). The NASC normalised REE patterns of fractions from samples CZA3&5 and KOW9g are generally flat, while KOW1&12 show enrichment in MREE and fractionation of HREE. In sample MOJ, the REE pattern shows a positive trend with a pronounced fractionation of LREE. All leachates of samples from the remagnetised Frasnian limestones (CZA and KOW) show a strong enrichment in MREE, while the REE pattern of the leachate of sample MOJ from Ordovician carbonate rocks is almost flat (Fig. 9.11 b).

The enrichment in MREE of leachates of samples from the remagnetised limestones is correlated to the Ba-content of the leachates. A similar relation between Ba-content and REE patterns of leachates was observed in the rocks from the NE Rhenish Massif (Section 7.3.2, page 81ff). The sample MOJ, where a primary component of magnetisation was observed does not follow the trend of Ba-content and MREE-enrichment.

## 10.5 Discussion of results

The palaeomagnetic results from Late Devonian limestones of the HCM reveal a complex (re-)magnetisation history. Two remagnetisations are identified in rocks from Czarnow and Kowala, which are postfolding in origin and were acquired in Late Paleozoic (component A) and Mesozoic (component C) times, respectively. A third component of magnetisation (B) yields synfolding results during fold test analysis and is observed in both localities. Although remagnetisations A and B are likely to be Late Palaeozoic in age, the exact timing of remanence acquisition remains unclear.

Components A and B are carried by magnetite. SEM studies indicate the oxidation of framboidal pyrite to magnetite in rocks, where A and/or B are identified. The Triassic remagnetisation (C) resides in hematite, which is confirmed by the observation of secondary hematite (specularite) as coatings of spherical pore spaces.

The apparent K-Ar ages and isotopic compositions of  $< 0.2\mu\text{m}$  fractions indicate a mixture of different generations of sheet silicates. These results can be explained by the presence of a illite generation younger than ca. 290 Ma years, which is contaminated by different amounts of detrital material (muscovite). Alternatively, the K-Ar ages could indicate two or more diagenetic events in the HCM. However, diffusive loss of  $^{40}\text{Ar}$  from the illite crystal lattice subsequent to illite formation cannot be ruled out. Further studies are needed to better understand the diagenetic

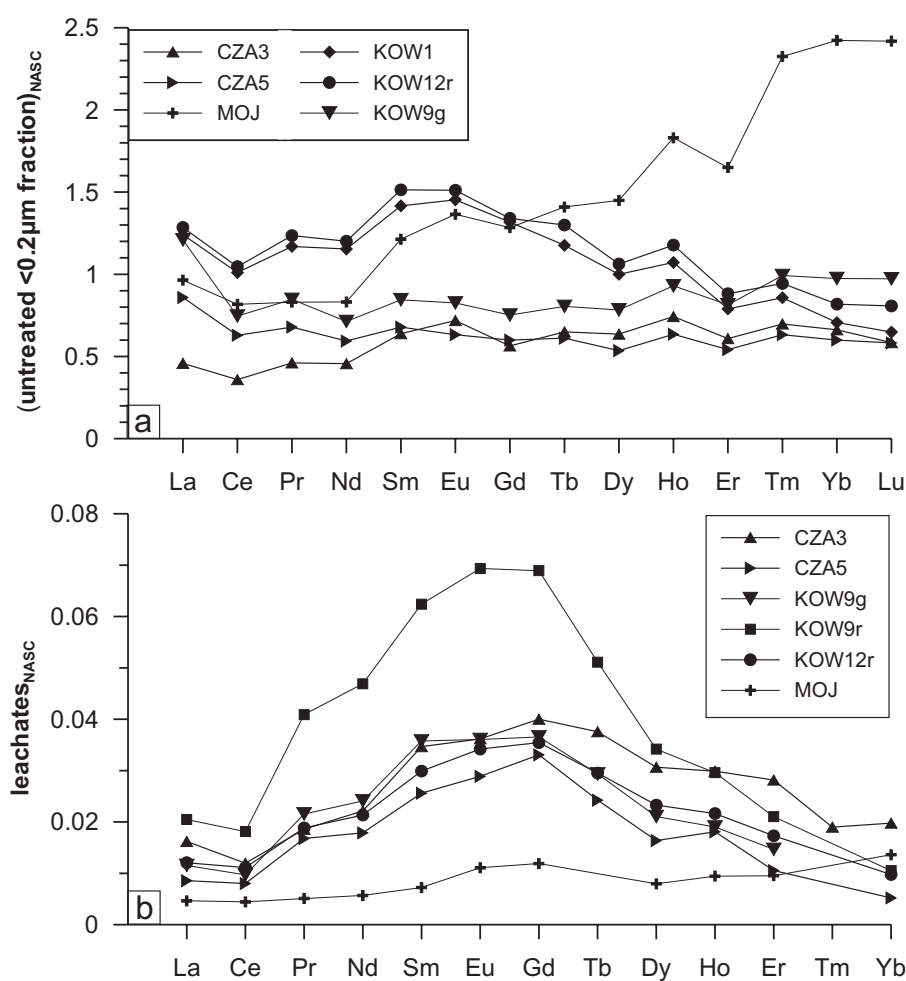


**Figure 10.9** NASC normalised REE patterns of a) untreated < 0.2 μm fractions and b) Fe-oxide leachates.

history of the Late Devonian limestones in the HCM.

The REE patterns of Fe-oxide leachates show a distinct enrichment in MREE, which is generally correlated to the Ba-content. A similar relationship between MREE enrichment and Ba-content was observed in remagnetised sedimentary rocks from the NE Rhenish Massif. One sample from Ordovician carbonate rocks (MOJ), which have not been affected by the remagnetisation events in the western HCM does not follow this pattern. However, the apparent K-Ar of the clay fraction from MOJ ( $336 \pm 7$  Ma) also indicates a diagenetic event in these rocks.

## Part IV

# Final conclusions and implications of this study

The present work combines palaeomagnetic and rock magnetic methods with clay mineralogy, isotope geochemistry of clay minerals and trace element geochemistry of Fe-oxide leachates to study remagnetised sedimentary rocks from Palaeozoic outcrops in Middle and Eastern Europe. The results yield important implications for the processes and mechanisms responsible for the Late Palaeozoic remagnetisation in the areas studied.

**Evidence for chemical remagnetisations:** Low palaeotemperatures of the sampled lithostratigraphic units, high demagnetisation temperatures of the characteristic components of magnetisation and the presence of SP magnetite indicate, that the remagnetisations were caused by authigenic growth or recrystallisation of magnetic minerals (magnetite), rather than by acquisition of a viscous partial thermoremanent magnetisation (VpTRM) carried by primary magnetite during periods of elevated temperatures.

**Palaeomagnetism and (isotope-) geochemistry of clay minerals:** In the predominantly carbonate rocks of Late Devonian and Early Carboniferous age from the NE Rhenish Massif, Germany, clay diagenesis ( $312 \pm 10$  Ma) and remagnetisation are coeval with respect to the main phase of deformation in the Late Carboniferous (ca. 320 - 310 Ma). In Middle Devonian clastic rocks, authigenic illites preserved an older diagenetic event ( $336 \pm 6$  Ma), while the age of remagnetisation is not different from the age of the remagnetisation event in the younger sequences. Therefore, the formation of secondary magnetite might be linked to chemical processes associated with the smectite/illite transition in the Late Devonian and Early Carboniferous rocks, while in Middle Devonian clastic rocks a different mechanism must be responsible for the growth of magnetite.

In Silurian and Devonian limestones from the Barrandian, Czech Republic, microscopic evidence suggests the cogenetic origin of illite and magnetite. Here, the K-Ar ages of authigenic illites constrain the age of remagnetisation to a period of ca. 386 - 365 Ma. This independent age control resolves the ambiguity of fold test results

in the Barrandian and indicates a late synfolding origin of the remagnetisation.

The palaeomagnetic results from Late Devonian limestones from the Holy Cross Mountains, Poland reveal a more complex remagnetisation history. Two remagnetisations of Late Palaeozoic age and a third magnetic overprint of Early Triassic age are identified. Due to the multiphase deformation in the Holy Cross Mountains, possibly involving rotations about vertical and horizontal axes, the fold tests yield ambiguous results. The presence of two or more generations of authigenic illite and the possible contamination of clay fractions by detrital material severely hampers the identification of diagenetic events in this region. Consequently, the exact timing of remanence acquisition in the Holy Cross Mountains in the Late Palaeozoic remains unclear.

**Leaching experiments:** The most important result of the leaching experiments is the observation of different REE pattern and Eu/Ce-anomalies in the rocks from the NE Rhenish Massif, which yield strong evidence against a fluid flow event on a regional scale triggered by orogenesis. The Fe-oxide leachates of all remagnetised rocks studied are enriched in MREE. The degree of MREE-enrichment is generally correlated with the amount of Ba in the leachates, which indicates the mobilisation and precipitation of baryte during diagenesis. This process is not necessarily connected to the remagnetisation event, since the REE spectra of leachates of Late Devonian and early Carboniferous rocks from the NE Rhenish Massif indicate the precipitation of Fe-oxides and apatite with flat REE spectra subsequent to the baryte mobilisation, which is probably connected to the older diagenetic event preserved in Middle Devonian rocks. However, it should be noted that Fe-oxides (hematite) and baryte occur in close relationship in red limestones from the Barrandian.

**Remagnetisation processes:** The processes and mechanism responsible for the remagnetisations in the areas studied are rather complex. The regional migration of orogenic-type fluids, which is thought to be responsible for widespread remagnetisations in Palaeozoic rocks of the Hercynian realm of North America, can be excluded for the NE Rhenish Massif and is not supported by the observations made in rocks from the Barrandian and the Holy Cross Mountains. Chemical changes associated with the smectite/illite transition could be responsible for the remagnetisation of Late Devonian and early Carboniferous rocks from the NE Rhenish Massif.

In limestones from the Barrandian and the Holy Cross Mountains, the observation of pseudoframboidal magnetite indicates the oxidation of pyrite to magnetite as a possible remagnetisation mechanism. This process requires the presence of a fluid phase, which could originate from pore fluids or local migration of fluids on fractures and faults.

In the Middle Devonian sequences of the NE Rhenish Massif the illite generation and the remagnetisation are not contemporaneous and oxidation of pyrite was not observed. Here, the remagnetisation must be related to a different mechanism. It can be speculated, that the remagnetisation mechanism in the Middle Devonian sequences could be related to pressure solution and changing pore fluid pressure during deformation. However, this does not agree with the spatial variation in timing of remagnetisation relative to the migration of the deformation front from south to north. More work is needed to elucidate the remagnetisation mechanism in the Middle Devonian clastic rocks from the NE Rhenish Massif.

The Mesozoic remagnetisations in the NE Rhenish Massif and the Holy Cross Mountains are carried by hematite and either related to hematite bearing mineralisation events during phases of uplift in the Mesozoic or caused by oxidising fluids percolating from the weathering surface and penetrating zones of enhanced permeability.

**Implications for further studies:** This study clearly demonstrates that the combination of palaeomagnetic and rock magnetic methods with clay mineralogy, isotope geochemistry of clay minerals and trace element geochemistry of Fe-oxide leachates opens a promising route towards the understanding of the processes controlling remagnetisations in sedimentary rocks. In Devonian limestones from the Barrandian, microscopic observation indicates the genetic relation between magnetite and illite. In Late Devonian and Early Carboniferous rocks from the NE Rhenish Massif the illitisation and remagnetisation are coeval and possibly connected. Although isotopic studies of clay minerals are commonly carried out on clastic lithologies, carbonate rocks and limestones turned out to be very well suited for this kind of studies. This is important, since these lithologies generally yield more reliable palaeomagnetic results than clastic rocks.

The use of plots of  $^{40}\text{Ar}/^{36}\text{Ar}$  versus  $^{40}\text{K}/^{36}\text{Ar}$  and the interpretation of K-Ar isochrons are essential in order to identify possible mixtures of illite generations with detrital material or diffusive loss of radiogenic  $^{40}\text{Ar}$ . The results of K-Ar dating of clay fractions from the Holy Cross Mountains reflect some typical problems connected with the presence of more than one illite generation and possible contamination with detrital material. Here, the amount of detrital contamination might be quantified by further K-Ar studies of clay minerals using multiple grain size fractions and the determination of illite polytypes.

The Fe-oxide leaching experiments represent a crucial link between carriers of magnetisation and the geochemistry of illite and other, more soluble phases and are a powerful method to characteristic the geochemical fingerprint of diagenetic events. However, contamination by detrital, REE-rich minerals, such as apatite or mon-

azite can severely hamper the interpretation of results from leaching experiments. By using a sequential leaching procedure, where carbonates, sulphates, phosphates and oxides are leached in different steps, the problems associated with detrital contamination could be avoided. Furthermore, the geochemistry of different groups of soluble minerals could be characterised independently. In the case of the rocks studied here, sequential leaching could also help to elucidate the relation of baryte and Fe-oxides and their REE-spectra.

Comparison of the geochemical fingerprint of leachates and clay fractions from remagnetised rocks and rocks, which did not experience a remagnetisation is an important aim of further studies. In the present work, only one sample could be studied, where the primary (Ordovician) magnetic information is preserved. The REE-spectra and geochemistry of the leachate from this sample (MOJ) is significantly different from other samples from the Holy Cross Mountains, although the K-Ar age of the clay fraction also indicates the presence diagenetic illite.

The separation of mineral carriers in quantity and purity sufficient for geochemical and isotopic studies is still unsolved. In this study high gradient magnetic separation was tested, but was not able to separate highly paramagnetic and ferromagnetic minerals. A successful separation of magnetic mineral carriers would allow to study the stable oxygen isotopes of the carriers of (re-)magnetisation and would yield more information on the conditions during remagnetisation. Comparison of stable oxygen isotopes of magnetite (hematite) and illite could also be used to test for a co-genetic growth of both minerals.

# Bibliography

- AHRENDT, H., N. CLAUER, J. C. HUNZIKER & K. WEBER, 1983. Migration of folding and metamorphism in the Rheinische Schiefergebirge deduced from K-Ar and Rb-Sr age determinations. In: Intracontinental fold belts; case studies in the Variscan belt of Europe and the Damara Belt in Namibia., edited by H. Martin & F. W. Eder, pp. 323–338. Springer-Verlag, Berlin, Federal Republic of Germany.
- BACHTADSE, V., F. HELLER & A. KRÖNER, 1983. Palaeomagnetic investigations in the Hercynian mountain belt of Central Europe. *Tectonophysics*, 91: 285–299.
- BACHTADSE, V., 1994. Paläomagnetische Untersuchungen an paläozoischen Gesteinen Afrikas - Implikationen für die Polwanderkurve Gondwanas. Unveröffentlichte Habilitationsschrift, Universität München, 30pp.
- BANDO, Y., M. KIYAMA, N. YAMAMOTO, T. TAKADA, T. SHINJO & H. TAKAKI, 1965. Magnetic properties of  $\alpha - Fe_2O_3$  fine particles. *J. Phys. Soc. Japan*, 20: 2086.
- BANERJEE, S., R. ELMORE & M. ENGEL, 1997. Chemical remagnetization and burial diagenesis; testing the hypothesis in the Pennsylvanian Belden Formation, Colorado. *J. Geophys. Res.*, 102(B11): 24,825–24,842.
- BELKA, Z., H. AHRENDT, W. FRANKE & K. WEMMER, 2000. The Baltica-Gondwana suture in central Europe: evidence from K-Ar ages of detrital muscovites and biogeographical data. In: Orogenic Processes: Quantification and Modelling in the Variscan Belt, edited by W. Franke, V. Haak, O. Oncken & D. Tanner, volume 179 of *Special Publications*, pp. 87–102. Geological Society, London.
- BELKA, Z., 1988. Thermal maturation and burial history from conodont colour alteration data, Holy Cross Mountains, Poland. In: First international Senckenberg conference and 5th European conodont symposium (ECOS 5), edited by W. Ziegler, volume 102 of *Courier Forschungsinstitut Senckenberg*, pp. 228–229. Frankfurt, Germany.

- BELOUSOVA, E., W. GRIFFIN, O. S.Y. & N. FISHER, 2002. Apatite as an indicator for mineral exploration: trace-element compositions and their relationships to host rock type. *Journal of Geochemical Exploration*, 76: 45–69.
- BETHKE, C. M. & S. MARSHAK, 1990. Brine migrations across North America - the plate tectonics of groundwater. *Annual Review of Earth and Planetary Science*, 18: 287–315.
- BONHOMME, M., R. THUIZAT, Y. PINAULT, N. CLAUER, R. WENDLING & R. WINKLER, 1975. Methodé de datation potassium-argon. Appareillage et technique. Technical report, Centre de Géochemie de la Surface, Université Louis Pasteur, 53 pp.
- BORRADAILE, G., 1994. Remagnetisation of a rock analogue during experimental triaxial deformation. *Phys. Earth Planet. Int.*, 83: 147–163.
- BRINDLEY, G. & G. BROWN, eds., 1980. Crystal structures of clay minerals and their X-ray identification, volume 5 of *Monograph*. Mineralogical Society, London, 495 pp.
- BROOKS, C., S. HART & T. WENDT, 1972. Realistic use of two-error regression treatments as applied to rubidium-strontium data. *Rev. Geophys. Space Phys.*, 10: 551–577.
- BROTHERS, L., M. ENGEL & R. ELMORE, 1996. The late diagenetic conversion of pyrite to magnetite by organically complexed ferric iron. *Chemical Geology*, 130(1-2): 1–14.
- BUGGISCH, W., 1972. Zur Geologie und Geochemie der Kellwasserkalke und ihrer begleitenden Sedimente (Unteres Oberdevon). *Abhandlungen des hessischen Landesamtes für Bodenforschung*, 62: 1–68.
- BUTLER, R., 1992. Paleomagnetism: Magnetic domains to geologic terranes. Blackwell Science, 238 pp.
- CHLŮPÁČ, I., 1994. Facies and biogeographic relationships in Devonian of the Bohemian Massif. *Courier Forschungsinstitut Senckenberg*, 169: 299–317.
- CLAUER, N. & S. CHAUDHURI, 1995. Clays in Crustal Environments, Isotope Dating and Tracing. Springer, Berlin, 359 pp.

- CLAUER, N. & S. CHAUDHURI, 1999. Isotopic dating of very-low grade metasedimentary and metavolcanic rocks: techniques and methods. In: Low-grade metamorphism, edited by M. Frey & D. Robinson, pp. 202–226. Blackwell Science, Oxford.
- COEY, J., 1988. Magnetic properties of iron in soil iron oxides and clay minerals. In: Iron in soils and clay minerals, edited by J. Stucko, B. Goodman & U. Schwertman, volume 217 of *NATO ASI Series. Series C: Mathematical and Physical Sciences*, pp. 397–466. D. Reidel Publishing Company, Dordrecht-Boston.
- COX, A. & G. DALRYMPLE, 1967. Statistical analysis of geomagnetic reversal data and the precision of Potassium-Argon dating. *J. Geophys. Res.*, 72: 2603–2614.
- CREER, K., 1964. A reconstruction of the continents for the Upper Paleozoic from paleomagnetic data. *Nature*, 203: 1115–1120.
- CREER, K., 1968. Paleozoic paleomagnetism. *Nature*, 219: 246–250.
- CROUZET, C., H. STANG & E. APPEL, 2001. Detailed analysis of successive pTRMs carried by pyrrhotite in Himalayan metacarbonates; an example from Hidden Valley, central Nepal. *Geophys. J. Int.*, 146(3): 607–618.
- DALLMEYER, R. & M. URBAN, 1998. Variscan vs Cadomian tectonothermal activity in the northwestern sectors of the Teplá-Barrandian zone, Czech Republic: constraints from  $^{40}\text{Ar}/^{39}\text{Ar}$  ages. *Geologische Rundschau*, 87: 94–106.
- DEKKERS, M., 1988. Magnetic properties of natural pyrrhotite Part I: Behaviour of initial susceptibility and saturation-magnetization-related rock-magnetic parameters in a grain-size dependent framework. *Phys. Earth Planet. Int.*, 52: 376–393.
- DEKKERS, M., 1989a. Magnetic properties of natural goethite - II. TRM behaviour during thermal and alternating field demagnetization and low-temperature treatment. *Geophys. J.*, 97: 341–355.
- DEKKERS, M., 1989b. Magnetic properties of natural pyrrhotite, Part II: High- and low-temperature behaviour of Jrs and TRM as a function of grain size. *Earth Planet. Sci. Lett.*, 57: 266–283.
- DEMING, D., 1992. Catastrophic release of heat and fluid flow in the continental crust. *Geology (Boulder)*, 20(1): 83–86. Geological Society of America (GSA). Boulder, CO, United States. 1992.

- DUNLOP, D., O. ÖZDEMİR, D. CLARK & P. SCHMIDT, 2000. Time-temperature relations for the remagnetization of pyrrhotite (Fe<sub>7</sub>S<sub>8</sub>) and their use in estimating paleotemperatures. *Earth Planet. Sci. Lett.*, 176(1): 107–116.
- DUNLOP, D. & O. ÖZDEMİR, 1997a. Rock magnetism: fundamentals and frontiers, volume 3 of *Cambridge studies in magnetism*. Cambridge University Press, Cambridge, 573 pp.
- DUNLOP, D., P. SCHMIDT, O. ÖZDEMİR & D. CLARK, 1997b. Paleomagnetism and paleothermometry of the Sydney Basin. 1. Thermoviscous and chemical overprinting of the Milton Monzonite. *J. Geophys. Res.*, 102(B12): 27 271–27 283.
- DUNLOP, D. & S. XU, 1994. Theory of partial thermoremanent magnetization in multidomain grains, 1. Repeated identical barriers to wall motion (single microcoercivity). *J. Geophys. Res.*, 99: 9005–9023.
- ELMORE, R., J. KELLEY, M. EVANS & M. LEWCHUK, 2001. Remagnetization and orogenic fluids: testing the hypothesis in the central Appalachians. *Geophys. J. Int.*, 144: 568–576.
- ELMORE, R., D. LONDON, D. BAGLEY, D. FRUIT & G. GAO, 1993. Remagnetization by basinal fluids; testing the hypothesis in the Viola Limestone, southern Oklahoma. *J. Geophys. Res.*, 98(B4): 6237–6254.
- ENKIN, R. & G. WATSON, 1996. Statistical analysis of paleomagnetic inclination data. *Geophys. J. Int.*, 126: 495–504.
- ENKIN, R., 1990. Formation et Déformation de l'Asie Depuis la Fin de l'Ere Primaire: Les Apports de l'Etude Paléomagnétique des Formations Secondaires de Chine du Sud. Ph.D. thesis, Université de Paris, 333 pp.
- EPSTEIN, A., J. EPSTEIN & L. HARRIS, 1977. Conodont Color Alteration - An Index to Organic Metamorphism. *Geol. Surv. Prof. Pap.*, 995: 1–27.
- FIALA, F., B. ČEJCHANOVÁ & J. MELKOVÁ, 1974. Confirmation of Silurian age of basaltic volcanics from Lodenice, Sv. Jan pod Skalou and Beroun. *Vestn. Ustred. Ustave Geol.*, 49: 331–341.
- FISHER, R., 1953. Dispersion on a sphere. *Proc. Roy. Soc. London*, A 217: 295–305.
- FÖRSTER, M., 1997. Paläomagnetische Untersuchungen in tektonisch schwach beanspruchten Serien des Rheinischen Schiefergebirges zum Nachweis präpermischer syngenetischer remanenter Magnetisierungen - Die mittel- und

- oberdevonische Kalke der Bergisch-Gladbacher Mulde. Diplomarbeit, Universität Köln, 105 pp.
- FRANKE, W., 1990. Rhenohercynian Basin and Mid-German Crystalline Rise - an introduction. In: Field Guide to the Mid German Crystalline Rise and Rheinisches Schiefergebirge, edited by W. Franke, IGCP 233, Terranes in the Circum-Atlantic Paleozoic Orogens, pp. 1–16. Göttingen-Giessen.
- FRANKE, W., 2000. The mid-European segment of the Variscides: tectonostratigraphic units, terrane boundaries and plate tectonic evolution. In: Orogenic Processes: Quantification and Modelling in the Variscan Belt, edited by W. Franke, V. Haak, O. Oncken & D. Tanner, volume 179 of *Special Publications*, pp. 35–61. Geological Society of London, London.
- GILL, J., D. ELMORE & M. ENGEL, 2002. Chemical remagnetization and clay diagenesis: testing the hypothesis in the Cretaceous sedimentary rocks of north-western Montana. *Physics and Chemistry of the Earth*, 27: 1131–1139.
- GOVINDARAJU, K. & I. ROELANDST, 1993. Second report (1993) on the first three GIT-IWG rock reference samples; anorthosite from Greenland, AN-G; basalte d'Essay-la-Cote, Be-N; granite de Beauvoir, MA-N. *Geostandards Newsletter*, 17(2): 227–294.
- GOVINDARAJU, K., 1994. 1994 compilation of working values and sample description for 383 geostandards. *Geostandards Newsletter*, 18(special issue): 158 pp.
- GRABOWSKI, J. & J. NAWROCKI, 1996. Multiple remagnetizations in the Devonian carbonates in the northwestern part of the Kielce region (Holy Cross Mts., southern part). *Geological Quarterly*, 40(1): 47–64.
- GRABOWSKI, J. & J. NAWROCKI, 2001. Palaeomagnetism of some Devonian carbonates from the Holy Cross Mts. (Central Poland): large pre-Permian rotations or strain modified palaeomagnetic directions? *Geological Quarterly*, 45(2): 165–178.
- HALLS, H., 1978. The use of converging remagnetization circles in paleomagnetism. *Phys. Earth Planet. Int.*, 16: 1–11.
- HAVLÍČEK, V., 1981. Development of a linear sedimentary depression exemplified by the Prague Basin (Ordovician - Middle Devonian; Barrandian area - Central Bohemia). *Sb. Geol. Ved.*, 35: 7–35.

- HEIDER, F. & D. DUNLOP, 1987. Two types of chemical remanent magnetization during oxidation of magnetite. *Phys. Earth Planet. Int.*, 46: 24–45.
- HILLIER, S. & M. HODSON, 1997. High-gradient magnetic separation applied to sand-size particles; an example of feldspar separation from mafic minerals. *J. Sedimentary Res.*, 67(5): 975–977.
- HIRT, A., A. BANIN & A. GEHRING, 1993. Thermal generation of ferromagnetic minerals from iron-enriched smectites. *Geophys. J. Int.*, 115: 1161–1168.
- HUDSON, M., R. REYNOLDS & N. FISHMAN, 1989. Synfolding Magnetization in the Jurassic Preuss Sandstone, Wyoming-Idaho-Utah Thrust Belt. *J. Geophys. Res.*, 94(B10): 13 681–13 705.
- HURLEY, N. & R. VAN DER VOO, 1990. Magnetostratigraphy, Late Devonian iridium anomaly and impact hypothesis. *Geology*, 18(3): 289–384.
- JACKSON, M., C. MCCABE, M. BALLARD & R. VAN DER VOO, 1988. Magnetite authigenesis and diagenetic paleotemperatures across the northern Appalachian Basin. *Geology (Boulder)*, 16(7): 592–595.
- JACKSON, M., P. ROCHETTE, G. FILLION, S. BANERJEE & J. MARVIN, 1993. Rock magnetism of remagnetized Paleozoic carbonates; low-temperature behavior and susceptibility characteristics. *J. Geophys. Res.*, 98(4): 6217–6225.
- JACKSON, M., 1990. Diagenetic source of stable remanence in remagnetized paleozoic cratonic carbonates: a rock magnetic study. *J. Geophys. Res.*, 95(B3): 2753–2761.
- KATZ, B., D. ELMORE, M. COGOINI, M. ENGEL & S. FERRY, 2000. Associations between burial diagenesis of smectite, chemical remagnetization, and magnetite authigenesis in the Vocontian Trough, SE France. *J. Geophys. Res.*, 105(1): 851–868.
- KENT, D., 1985. Thermoviscous remagnetization in some Appalachian limestone. *Geophys. Res. Lett.*, 12(12): 805–808.
- KIRSCHVINK, J., 1980. The least-square line and plane and the analysis of paleomagnetic data. *Geophys. J. R. astr. Soc.*, 62: 699–718.
- KODAMA, K., 1988. Remanence rotation due to rock strain during folding and the stepwise application of the fold test. *J. Geophys. Res.*, 93(B4): 3357–3371.

- KÖNIGSHOF, P., 1992. Der Farbänderungsindex von Conodonten (CAI) in paläozoischen Gesteinen (Mitteldevon bis Unterkarbon) des Rheinischen Schiefergebirges, volume 146 of *Cour. Forsch.-Inst. Senckenberg*. Senckenbergische Naturforschende Gesellschaft, Frankfurt a. M., 118 pp.
- KOSSMAT, F., 1927. Gliederung des varistischen Gebirgsbaues. *Abh. Sächs. Geol. Landesamt*, 1: 39.
- KREUZER, H. & W. HARRE, 1975. K/Ar-Altersbestimmungen an Hornblenden und Biotiten des Kristallinen Odenwaldes. *Der Aufschluß*, 27: 71–77.
- KÜBLER, B., 1966. La cristallinité de l'illite et les zones tout à fait supérieur du métamorphisme. In: Colloque sur les Etage Tectoniques, pp. 105–122. Neuchatel, Suisse.
- LAMARCHE, J., J. MANSY, F. BERGERAT, M. HAKENBERG, M. LEWANDOWSKI, E. STUPNICKA, J. SWIDROWSKA, B. WAJSPRYCH & J. WIECZOREK, 1999. Variscan tectonics in the Holy Cross Mountains (Poland) and the role of structural inheritance during Alpine tectonics. *Tectonophysics*, 313: 171–186.
- LARQUE, P. & F. WEBER, 1978. Sequences sedimentaires et lithostratigraphie de la serie Paleogene du Velay. Sedimentary sequences and lithostratigraphy of the Paleogene series of Velay. *Sciences Geologiques (Bulletin), Universite Louis-Pasteur, Institut de Geologie, Strasbourg, France*, 31(4): 151–155.
- LEE, D. & H. BASTRON, 1967. Fractionation of rare-earth elements in allanite and monazite as related to geology of the Mt. Wheeler mine area, Nevada. *Geochim. Cosmochim. Acta*, 31: 339–356.
- LEWANDOWSKI, M., 1993. Paleomagnetism of the Paleozoic Rocks of the Holy Cross Mts (Central Poland) and the Origin of the Variscan Orogen. *Publ. Inst. Geophys. Pol. Acad. Sci*, 265(A-23): 1–84.
- LIEWIG, N., N. CLAUER & F. SOMMER, 1987. Rb-Sr and K-Ar dating of clay diagenesis in Jurassic sandstone reservoirs, North Sea. *Am. Assoc. Petr. Geol. Bull.*, 71: 1467–1474.
- LOWRIE, W., 1990. Identification of ferromagnetic minerals in a rock by coercivity and unblocking temperature properties. *Geophys. Res. Lett.*, 17(2): 159–162.
- LUDWIG, K., 2001. Isoplot/Ex, rev. 2.49: a geochronological toolkit for Microsoft Excel. Berkeley Geochronology Center.

- LU, G., S. MARSHAK & D. KENT, 1990. Characteristics of magnetite carriers responsible for Late Paleozoic remagnetizations in carbonate strata of the mid-continent, U.S.A. *Earth Planet. Sci. Lett.*, 99: 351–361.
- LU, G., C. MCCABE, J. S. HANOR & R. FERRELL, 1991. A genetic link between remagnetization and potassium metasomatism in the Devonian Onondaga Formation, Northern Appalachian Basin. *Geophys. Res. Lett.*, 18(11): 2047–2050.
- MACDONALD, W., 1980. Net tectonic rotation, apparent tectonic rotation, and the structural tilt correction in palaeomagnetic studies. *J. Geophys. Res.*, 85(B7): 3659 – 3669.
- MATZKA, J., 2001. Besondere magnetische Eigenschaften der Ozeanbasalte im Altersbereich 10 - 40 Ma. Dissertation, Ludwig-Maximilians Universität München, 118 pp.
- MCCABE, C. & J. CHANNELL, 1994. Late Paleozoic remagnetization in limestones of the Craven Basin (northern England) and the rock magnetic fingerprint of remagnetized sedimentary carbonates. *J. Geophys. Res.*, 99(B3): 4603–4612.
- MCCABE, C., R. VAN DER VOO, D. PEACOR, C. SCOTESE & R. FREEMAN, 1983. Diagenetic magnetite carries ancient yet secondary remanence in some Palaeozoic sedimentary carbonates. *Geology*, 11: 221–223.
- MCELHINNY, M. & J. LOCK, 1990. IAGA global paleomagnetic database. *Geophys. J. Int.*, 101: 763–766.
- MCELHINNY, M. & N. OPDYKE, 1973. Remagnetization hypothesis discounted: A paleomagnetic study of the Trenton Limestone, New York State. *Geol. Soc. Am. Bull.*, 84: 3697–3708.
- MCELHINNY, M., 1964. Statistical significance of the fold test in palaeomagnetism. *Geophys. J. R. Astr. Soc.*, 8: 333–340.
- MCFADDEN, P. & M. MCELHINNY, 1988. The combined analysis of remagnetization circles and direct observations in paleomagnetism. *Earth Planet. Sci. Lett.*, 87: 161–172.
- MCLENNAN, S., 1989. Rare earth elements in sedimentary rocks: influence of provenance and sedimentary processes. In: *Geochemistry and Mineralogy of Rare Earth Elements*, edited by B. Lipin & G. McKay, volume 21 of *Reviews in Mineralogy*, pp. 170–200. Mineralogical Society of America.

- MEHRA, O. & M. JACKSON, 1960. Iron oxide removal from soils and clays by a dithionite-citrate system buffered with sodium bicarbonate. In: 7th Conference on Clays and Clay Mineralogy, pp. 317–327. Washington DC.
- MIDDLETON, M. & P. SCHMIDT, 1982. Paleothermometry of the Sydney Basin. *J. Geophys. Res.*, 87: 5351–5359.
- MOLINA GARZA, R. & J. ZIJDERVELD, 1996. Paleomagnetism of Paleozoic strata, Brabant and Ardennes massifs, Belgium; implications of pre-folding and post-folding Late Carboniferous secondary magnetizations for European apparent polar wander. *J. Geophys. Res.*, 101(B7): 15,799–15,818.
- MORRISH, A., 1994. Canted antiferromagnetism: Hematite. World Scientific, London, 192 pp.
- NAWROCKI, J., 2000. Late Silurian paleomagnetic pole from the Holy Cross Mountains; constraints for the post-Caledonian tectonic activity of the Trans-European suture zone. *Earth Planet. Sci. Lett.*, 179(2): 325–334.
- NÉEL, L., 1949. Théorie du trainage magnétique des ferromagnétiques en grains fins avec application aux terres cuites. *Ann. Géophys.*, 5: 99–136.
- NICK, K. & R. ELMORE, 1990. Paleomagnetism of the Cambrian Royer Dolomite and Pennsylvanian Collings Ranch Conglomerate, southern Oklahoma; an early Paleozoic magnetization and nonpervasive remagnetization by weathering. *Geological Society of America Bulletin*, 102(11): 1517–1525.
- ODIN, G. S., 1976. La glauconite GL-O, étalon inter-laboratoires pour l'analyse radiochronométrique. Glauconite GL-O, inter-laboratory standard for radiochronometric analysis. *Analusis*, 4(6): 287–291.
- OLIVER, J., 1986. Fluids expelled tectonically from orogenic belts: Their role in hydrocarbon migration and other geologic phenomena. *Geology*, 14: 99–102.
- ONCKEN, O., A. PLESCH, J. WEBER, W. RICKEN & S. SCHRADER, 2000. Passive margin detachment during arc-continent collision (Central European Variscides). In: *Orogenic Processes: Quantification and Modelling in the Variscan Belt*, edited by W. Franke, V. Haak, O. Oncken & D. Tanner, volume 179 of *Special Publications*, pp. 199–216. Geological Society of London, London.
- ONCKEN, O., C. VON WINTERFELD & D. DITTMAR, 1999. Accretion of a passive margin: The Late Paleozoic Rhenohercynian fold and thrust belt (Middle European Variscides). *Tectonics*, 18(1): 75–91.

- OPDYKE, N. & J. CHANNELL, 1996. Magnetic Stratigraphy, volume 64 of *International Geophysics Series*. Academic Press, London, 346 pp.
- PAPROTH, E. & M. WOLF, 1973. Zur paläogeographischen Deutung der Inkohlung im Devon und Karbon des nördlichen Rheinischen Schiefergebirges. *N. Jb. Geol. Paläont. Mh.*, 8: 469–493.
- PARRY, L., 1982. Magnetization of immobilized particle dispersions with two distinct particle sizes. *Phys. Earth Planet. Int.*, 28: 230–241.
- PLESCH, A. & O. ONCKEN, 1999. Orogenic wedge growth during collision; constraints on mechanics of a fossil wedge from its kinematic record (Rhenohercynian FTB, Central Europe). *Tectonophysics*, 309(1-4): 117–139.
- PULLAIAH, G., E. IRVING, K. BUCHAN & D. DUNLOP, 1975. Magnetization changes caused by burial and uplift. *Earth Planet. Sci. Lett.*, 28: 133–143.
- REUTER, A. & R. DALLMEYER, 1989. K-Ar and  $^{40}\text{Ar}/^{39}\text{Ar}$  dating of cleavages formed during very low-grade metamorphism: a review. In: Evolution of Metamorphic Belts. 1987 Joint Meeting of the Metamorphic Studies Group and IGCP Project 235, edited by J. Daly, R. Cliff & B. Yardley, volume 43 of *Geol. Soc. Spec. Publ.*, pp. 161–171.
- REUTER, A., 1985. Korngrößenabhängigkeit von K-Ar Datierungen und Illit-Kristallinität anchizonaler Metapelite und Metatuffe aus dem Rheinischen Schiefergebirge, volume 27 of *Göttinger Arbeiten zur Geologie und Paläontologie*. Georg-August-Universität Göttingen, Göttingen, 91 pp.
- REUTER, A., 1987. Implications of K-Ar ages of wholerock and grain size fractions of metapelites and intercalated metatuffs within an anchizonal terrane. *Contrib. Mineral. Petrol.*, 97: 105–115.
- ROBION, P. & G. BORRADAILE, 2001. Stress remagnetization in pyrrhotite-calcite synthetic aggregates. *Geophysical Journal International*, 144: 96–104.
- SCHÄTZ, M., A. ZWING & Z. BELKA, 2003. Middle-Late Ordovician magnetostratigraphy of the Mójcza Limestone and its paleogeographic implications for the Holy Cross Mountains, Poland. *in preparation*.
- SMETHURST, M., A. KHRAMOV & S. PISAREVSKY, 1998. Paleomagnetism of the Lower Ordovician Orthoceras Limestone, St. Petersburg, and a revised drift history for Baltica in the early Paleozoic. *Geophys. J. Int.*, 133: 44–56.

- STAMATAKOS, J., A. HIRT & W. LOWRIE, 1996. The age and timing of folding in the Central Appalachians from paleomagnetic results. *Geol. Soc. Am. Bull.*, 108(7): 815–829.
- STEIGER, R. & E. JÄGER, 1977. Subcommission on Geochronology: Convention on the use of decay constants in geo- and cosmochronology. *Earth Planet. Sci. Lett.*, 36: 359–362.
- SUK, D., D. PEACOR & R. VAN DER VOO, 1990. Replacement of pyrite framboids by magnetite in limestone and implications for paleomagnetism. *Nature*, 345: 611–613.
- SUK, D., R. VAN DER VOO, D. PEACOR & K. LOHMANN, 1993b. Late Paleozoic remagnetization and its carrier in the Trenton and Black River carbonates from the Michigan Basin. *Journal of Geology*, 101(6): 795–808.
- SUK, D., R. VAN DER VOO & D. PEACOR, 1991. SEM/STEM observations of magnetite in carbonates of Eastern North America: evidence for chemical remagnetization during the Alleghenian Orogeny. *Geophys. Res. Lett.*, 18(5): 939–942.
- SUK, D., R. VAN DER VOO & D. PEACOR, 1993a. Origin of magnetite responsible for remagnetization of early Paleozoic limestones of New York State. *J. Geophys. Res.*, 98(B1): 419–434.
- SUN, W. & M. JACKSON, 1994. Scanning electron microscopy and rock magnetic studies of magnetic carriers in remagnetized early Paleozoic carbonates from Missouri. *J. Geophys. Res.*, 99(B2): 2935–2942.
- TAIT, J., V. BACHTADSE, W. FRANKE & H. SOFFEL, 1997. Geodynamic evolution of the European Variscan foldbelt: palaeomagnetic and geological constraints. *Geologische Rundschau*, 86(3): 585–598.
- TAIT, J., V. BACHTADSE & H. SOFFEL, 1994a. New paleomagnetic constraints on the position of central Bohemia during the Early Ordovician times. *Geophysical Journal International*, 116: 131–140.
- TAIT, J., V. BACHTADSE & H. SOFFEL, 1994b. Silurian paleogeography of America: new palaeomagnetic data from Central Bohemia. *J. Geophys. Res.*, 99(B2): 2897 – 2907.
- TAIT, J., V. BACHTADSE & H. SOFFEL, 1995. Upper Ordovician palaeogeography of the Bohemian Massif: implications for Armorica. *Geophysical Journal International*, 122: 211–218.

- TAYLOR, S. & S. MCLENNAN, 1985. The continental crust: its composition and evolution. Blackwell, Oxford, 312 pp.
- TODT, W., U. ALTENBERGER & J. VON RAUMER, 1995. U-Pb data on zircons for the thermal peak of metamorphism in the Variscan Odenwald, Germany. *Geologische Rundschau*, 84(3): 466 – 472.
- VAN DER VOO, R. & R. FRENCH, 1977. Paleomagnetism of the Late Ordovician Juniata Formation and the remagnetisation hypothesis. *J. Geophys. Res.*, 82: 5796–5802.
- VAN DER VOO, R., 1990. Phanerozoic paleomagnetic poles from Europe and North America and comparisons with continental reconstructions. *Reviews of Geophysics*, 28(2): 167–206.
- VON DOBENECK, T., 1985. Gesteinsmagnetische Untersuchungen an Tiefseesedimenten des Südatlantiks. Diplomarbeit, Institut für Allgemeine und Angewandte Geophysik, Ludwig-Maximilians Universität München, 124 pp.
- WALLISER, O., 1981. The geosynclinal development of the Rheinische Schiefergebirge (Renohercynian zone of the Variscides; Germany). *Geologie en Mijnbouw*, 60: 89–96.
- WALTON, D., 1980. Time-temperature relations in the magnetization of assemblies of single domain grains. *Nature*, 286: 245 – 247.
- WATSON, G. & R. ENKIN, 1993. The fold test in paleomagnetism as a parameter estimation problem. *Geophys. Res. Lett.*, 20(19): 2135–2137.
- WEGENER, A., 1912. Die Entstehung der Kontinente. *Geologische Rundschau*, 3: 276–292.
- WERNER, W., 1989. Contribution to the genesis of the sedex-type mineralizations of the Rhenish Massif (Germany); implications for future Pb-Zn exploration. *Geologische Rundschau*, 78(2): 571–598.
- WERNER, W., 1990. The mineral deposits of Renohercynian zone in Germany. In: Field Guide to the Mid German Crystalline Rise and Rheinisches Schiefergebirge, edited by W. Franke, IGCP 233, Terranes in the Circum-Atlantic Paleozoic Orogens, pp. 55–73. Giessen - Göttingen.

- WILKEN, C., 1995. Paläo- und gesteinemagnetische Untersuchungen an paläozoischen Gesteinen aus dem Rheinischen Schiefergebirge. Diplomarbeit, Institut für Allgemeine und Angewandte Geophysik, Ludwig-Maximilians-Universität München, 134 pp.
- WOODS, S., D. ELMORE & M. ENGEL, 2002. Paleomagnetic dating of the smectite-to-illite conversion: Testing the hypothesis in Jurassic sedimentary rocks, Skye, Scotland. *J. Geophys. Res.*, 107(B5).
- XU, W., R. VAN DER VOO & D. PEACOR, 1994. Are magnetite spherules capable of carrying stable magnetizations? *Geophys. Res. Lett.*, 21(7): 517–520.
- YORK, D., 1969. Least-squares fitting of a straight line. *Can. J. Phys.*, 46: 1845–1847.
- ZEGERS, T., M. DEKKERS & S. BAILLY, 2003. Late Carboniferous to Permian remagnetization of Devonian limestones in the Ardennes: the role of temperature, fluids and deformation. In: EGS-AGU-EUG Joint Assembly, volume 5 of *Geophysical Research Abstracts*. Nice, France.
- ZIJDERVELD, J., 1967. AC-demagnetisation of rocks; analysis of results. In: *Methods in Palaeomagnetism*, edited by D. Collinson, K. Creer & S. Runcorn, pp. 254–287. Elsevier, New York.
- ZWING, A., V. BACHTADSE & H. SOFFEL, 2002. Late Carboniferous Remagnetisation of Palaeozoic Rocks in the NE Rhenish Massif, Germany. *Phys. Chem. Earth*, 27(25-31): 1179–1188.
- ZWING, A. & V. BACHTADSE, 2000. Paleoposition of the northern margin of Armorica in Late Devonian times: Paleomagnetic and rock magnetic results from the Frankenstein Intrusive Complex (Mid-German Crystalline Rise). *J. Geophys. Res.*, 105(B9): 21 445–21 456.

# Acknowledgements

This work was proposed and stimulated by Valerian Bachtadse, whom I owe most of my knowledge in palaeomagnetism. Our discussions in the field or in more civilised places and his encouragement to present and publish my results were invaluable for my (yet short) scientific career and beyond.

I would like to thank Norbert Clauer and Nicole Liewig for their great cooperation, vivid discussions and the possibility to use the facilities of the Centre de Géochimie de la Surface in Strasbourg. Nicole helped in many ways to make my visits in Strasbourg pleasant and I would like to thank her for the effort she invested in our project.

I would like to thank Heinrich Soffel for his interest in this work and for his support to raise funds from the DFG.

Jenny, Maria, Christoph, David, Jürgen, Roman and anyone else from the "best working group ever" deserve my special thanks for their friendship, support in not-so-good times and the many critical, controversial and silly discussions.

Uli Hambach, Christoph Obert and Florian Becker were great help in the field in the Rhenish Massif. Christian Wilken supplied palaeomagnetic data from this region, which I reanalysed. For my work in the Holy Cross Mountains, Poland, the information on local geology and practical advice ("Polish for idiots") by Zdislaw Belka was very helpful. I accompanied Michael Schätz on a first field trip to the Holy Cross Mountains and some of our joint work is presented here. Roman Leonhardt was a valuable field companion during later field work in the "Holy Cows" and the Barrandian. Jürgen Matzka helped me to get back on track, whenever I felt lost somewhere between the fundamentals and frontiers of rock magnetism.

Maunela Weiss took care of the instruments at the laboratory in Niederlippach, which would be a rather boring place without her. I would like to thank Nikolai Petersen for design and maintenance of the VFTB and many other palaeo- and rock magnetic instruments. Theresa Reinwald and Nico Hautmann carefully demagnetised many samples, for which I am very thankful.

The people from the workshop, especially Herr Reichl, are doing a great job to keep our drills running. I am very thankful to Horst Khek, who built the frame

of the magnetic separation system and who helped numerous other times, when a universal craftsman was asked for. Frau Schröer was always kind and helpful, whenever administrative puzzles had to be solved.

I would like to thank Mike Jackson, Jim Marvin and the entire IRM team for their support during my visit to their laboratory in Minneapolis. This visit was partly funded by a IRM visiting fellowship. The IRM is funded by the Keck foundation and the University of Minnesota.

Many people from the Centre de Géochimie de la Surface contributed to this work: Raymond Wendling and Miroslaw Honty in the Ar-lab, Thierry Perrone in the "salle blanche", Jean Samuel and Robert Rouault at the ICP-MS and ICP-AES, Daniel Million at the AAS, Jean-Luc Cézard and Phillipe Larqué in the XRD lab and Gill Morvan at the TEM. I am in great debt to Robert Wendling, for his enormous amount of work on the separation of clay fractions. Davy Rousset was invaluable for discussions on clay chemistry and reliable for the occasional pint at Nelson's. Special thanks go to Phillipe Karcher for his help on the SEM and his friendship. Thank you, Phillipe and Rolande for your hospitality in Bellefosse and Strasbourg.

Many thanks go to Davy, Jean, Olivier, Manu, Nathalie, petite Nathalie, Dom, Christoph and Benoit (and everybody I have forgotten to mention) for their company during so many lunches.

The manuscripts of two publications have greatly benefited from comments from Doug Elmore, Mark Dekkers and R. Molina-Garza.

Last but not least, I would like to thank Franziska for her great support and endurance during the last few month. This work is dedicated to her and Juliane Maria.

This project was funded by a grant of the Deutsche Forschungsgemeinschaft to Heinrich Soffel and Valerian Bachtadse (So72/62).

# Appendix A

## Samples

### *Barrandian and Holy Cross Mountains*

Site	Lat [°N]	Long [°E]	Location	Lithology	Stratigraphic unit	Strat. age
<i>Barrandian</i>						
KLO1-3*	49.933	14.178	SW of Karlštejn at Berounka river	lst		Prid
KLOA,B	49.933	14.178	SW of Karlštejn at Berounka river	lst		Prid
KOBAC	49.962	14.078	quarry S of Kobyle hill, Zlatý Kun	g/r cri lst	Slivenec	Prag
KOBJ	49.962	14.078	quarry S of Kobyle hill, Zlatý Kun	g/r cri lst	Slivenec	Prag
KRA1*	49.932	14.037	at Suchomasty river	basalt		Ludl-Prid
LIT3*	49.924	14.041	at Suchomasty river	basalt		Ludl-Prid
LODA-C	49.984	14.178	active quarry S of Loděnice	r/g lst	Loděnice	Prag
LODD,J	49.981	14.161	roadcut S of Loděnice	g lst		Prid
MOT3*	50.078	14.342	W of Motol	bas sill		420 Ma
MRA	50.002	14.267	abandoned quarry NE of Chynice	r nod lst	Loděnice	Prag
PRA	49.993	14.344	roadcut at Pragocement, Radotín	lst	Dvorce-Prokop	Prag
RAD	49.987	14.339	in Černá Rokle, road to Kosoř	lst	Radotín	Lochk
<i>Holy Cross Mountains</i>						
CZA1-5	50.888	20.588	abandoned quarry at Czarnow	turb lst		Frasn
KOW1-5	50.791	20.558	railroad cut in Kowala quarry	bioh lst	Kowala	Frasn
KOW6	50.791	20.558	railroad cut in Kowala quarry	deb fl	Kowala	Frasn
KOW7-9	50.791	20.558	railroad cut in Kowala quarry	r lst	Kowala	Frasn
KOW10-12	50.791	20.558	railroad cut in Kowala quarry	turb lst	Kowala	Frasn
KOW15	50.796	20.558	1km N of KOW section	cong	Kowala	Permian

**Table A.1** Sampling locations in the Barrandian, Czech Republic and the Holy Cross Mountains, Poland; \* previously studied by TAIT et al. (1994b). Lat and Long, Latitude and longitude. Lithologies: lst, limestone; g/r cri lst: grey/red crinoidal limestone; r/g lst, red/grey limestone; bas sill: basaltic sill; r nod lst, red nodular limestone; turb lst: turbiditic limestone; bioh lst: biohermal limestone; deb fl: debris flow; cong: conglomerate. Stratigraphic ages: Ludl, Ludlovian; Prid, Pridolian; Lochk, Lochkovian; Prag, Pragian; Frasn: Frasnian; 420 Ma: radiometric age using K-Ar methods (FIALA et al., 1974).

*Rhenish Massif*

Nr.	Site	Lat [°N]	Long [°E]	Location	Lithology	Stratigraphic unit	Strat. age
1	HEN	51.375	7.559	near Henkhausen	chy carb	Kulm-Plattenk.	Vis
2	LET2	51.375	7.561	Henkhausen, near public pool	chy carb	Kieselkalk-F.	Tour
3	LET3	51.375	7.561	Henkhausen, near public pool	chy carb	Kieselkalk-F.	Tour
4	STU	51.378	7.609	S of Stübbeken at B236	lst	Kulm-Plattenk.	Vis
5	GRU	51.378	7.643	N of A46 between AS45 and AS46	lst	reef complex	Fras
6	AMB	51.327	7.519	abandoned quarry at B54	qz sst	Brandenberg	Eif
7	LAS1	51.342	7.622	active quarry W of Lasbeck	qz sst	Brandenberg	Eif
8	LAS2	51.342	7.622	active quarry W of Lasbeck	qz sst	Brandenberg	Eif
9	LAS3	51.342	7.622	active quarry W of Lasbeck	qz sst	Brandenberg	Eif
10	HAC	51.373	7.976	abandoned quarry at B229	bit lst	Kulm-Plattenk.	Vis
11	BRU1	51.209	7.578	roadcut at B54, S of Brügge	sst	Honseler	Giv
12	BRU2	51.209	7.578	500m N of BRU1, below cementary	qz sst	Honseler	Giv
13	LOS1	51.219	7.586	active quarry near Lösenbach	greyw	Honseler	Giv
14	LOS2	51.219	7.586	active quarry near Lösenbach	greyw	Honseler	Giv
15	LOS3	51.219	7.586	active quarry near Lösenbach	greyw	Honseler	Giv
16	HAM	51.257	7.644	abandoned quarry at L530	sst	Honseler	Giv
17	ELV	51.285	7.712	road cut at B236 near power plant	qz sst	Brandenberg	Eif
18	NEU	51.272	7.778	aband. quarry near B229	qz sst	Honseler	Giv
19	GAR	51.316	7.814	abandoned quarry W of Garbeck	sst	Honseler	Giv
20	SOR	51.321	7.942	outcrop at lake, E of L687	greyw	Arnsberger	Nam
21	MET	51.337	8.048	road cut at junction, N of Westenfeld	greyw	Arnsberger	Nam
22	OLP1	51.366	8.164	roadcut at A46, S of Olpe	greyw	Arnsberger	Nam
23	OLP2	51.366	8.164	roadcut at A46, S of Olpe	greyw	Arnsberger	Nam
24	PLE	51.200	7.874	aband. quarry at L697	g/r slt	Herscheider	Ged
25	ALB1	51.106	7.823	roadcut SW of Albringhausen	slt	Wiedenester	Giv
26	ALB3	51.111	7.818	roadcut at L539, W of Albringhausen	sst	Selscheider	Eif
27	ATT1	51.111	7.879	roadcut at L708, S of Attendorn	g/r sst	U. Newberrien	Giv
28	AFI2	51.150	7.958	roadcut at L539, at Gut Ahausen	nod lst	reef complex	Fras
29	AFI7	51.143	7.949	roadcut at L539, 300m W of AFI2	r nod lst	reef complex	Fam
30	ATT2	51.149	7.957	roadcut at L539, S of Heggen	r nod lst	reef complex	Fam
31	ATT4	51.124	7.923	SW of Castle Schnellenberg	slt	Grevensteiner	Giv
32	STC	51.137	7.986	abandoned quarry, E of Sankt Claas	lst	reef complex	Fra
33	BOH1	51.024	8.387	active quarry near Raumland	qz sst	Raumländer	Eif
34	BOH2	51.024	8.387	active quarry near Raumland	qz sst	Raumländer	Eif
35	DOT1	51.017	8.402	roadcut at L553, N of Dotzlar	qz sst	Raumländer	Eif
36	DOT2	51.017	8.402	roadcut at L553, N of Dotzlar	qz sst	Raumländer	Eif
37	LAU	51.013	8.423	railroadcut near Laubroth	qz sst	Raumländer	Eif
A	LER	50.954	7.152	aband. quarry in park, Hotel Lerbach	bit lst	Hombacher	Fras
B	UTH	51.010	7.196	aband. quarry at L286 near Unterthal	lst	U. Plattenkalk	Giv

**Table A.2** Sampling locations in the NE Rhenish Massif. *Nr.* refers to numbers in Fig. 4.4; *Lat* and *Long*, Latitude and longitude. *Lithologies*: *chy carb*, cherty carbonate; *lst*, limestone; *qz*, quartzitic sandstone; *bit lst*; bituminous limestone; *sst*, sandstone; *greyw*, greywacke; *g/r slt*, grey/red siltstone; *slt*, siltstone; *g/r sst*, grey/red sandstone; *nod lst*, nodular limestone; *r nod lst*, red nodular limestone. *Stratigraphic ages*: *Ged*, Gedinian; *Eif*, Eifelian; *Giv*, Givetian; *Fras*, Frasnian; *Fam*, Famennian; *Tour*, Tournaisian; *Vis*, Viséan.

# Appendix B

## Palaeomagnetic data

*Barrandian and Holy Cross Mountains*

Site	n/N	Geogr.		Strat.		$\alpha_{95}$ [°]	k	Bedding	
		Dec [°]	Inc [°]	Dec [°]	Inc [°]			DD [°]	D [°]
<b>Barrandian, Component B</b>									
<i>Ludlovian - Lochkovian carbonate and volcanic rocks</i>									
KRA1*	7/6	186	-2	186	16	15	21	011	18
LIT3*	5/5	184	0	184	-29	12	42	185	29
MOT3*	7/3	203	-21	202	-1	9	195	005	21
LODD	10/9	23	-5	25	11	10	26	140	39
LODJ	22/15	191	-6	202	-33	7	31	153	39
KLOAA	6/4	204	6	211	36	15	40	360	34
KLOAB	6/3	188	4	199	50	16	61	350	50
KLOBA	7/6	209	7	321	-38	4	249	160	77
KLO1*	12/10	192	-22	192	22	6	49	332	55
KLO3*	7/4	197	-29	188	6	15	38	320	55
<i>Praghnian carbonate rocks</i>									
KOBAC	22/15	191	-17	190	-4	5	70	005	13
KOBJ	25/6	192	-12	192	-1	12	25	340	16
LODA	6/6	175	19	177	-23	8	69	141	54
LODB	7/6	180	-9	203	-46	13	28	142	54
LODC	6/4	180	3	193	-38	11	124	142	54
MRAA	6/4	190	19	188	-1	14	42	155	23
MRAB	7/6	188	3	189	-18	9	59	166	23
MRAJ	7/5	187	5	188	-12	12	44	154	21
PRAAC	6/8	175	10	196	50	12	30	325	50
PRAB	6/4	187	13	203	32	8	129	311	41
PRAJ	12/4	169	15	186	40	13	66	311	45
RADABC	12/7	190	6	191	9	13	27	293	32
RADJ	22/11	211	-3	186	5	10	66	294	30
<b>Holy Cross Mountains, Component A</b>									
CZA1	5/5	220	22	221	12	6	153	256	12
CZA2	5/5	225	22	297	-51	9	79	004	44 <sup>b</sup>
CZA3	6/6	216	13	269	-56	6	117	001	14 <sup>b</sup>
CZA4	6/6	222	9	222	3	4	267	197	7
CZA5	5/5	218	18	294	-58	7	109	006	32 <sup>b</sup>
CZA6	5/5	217	18	258	-63	4	311	011	32 <sup>b</sup>
<b>Holy Cross Mountains, Component B</b>									
KOW1	5/5	48	4	45	10	5	64	306	39
KOW2	5/5	49	-1	48	5	5	259	308	29
KOW3	5/6	54	0	44	4	4	414	308	22
KOW4	5/6	44	2	39	12	4	388	300	44
KOW5	4/5	49	-1	50	-2	14	46	320	33
KOW6	5/6	46	0	45	3	2	1063	310	35
KOW7&9	5/12	49	4	45	4	9	70	000	00
KOW8&10	8/11	67	20	56	-6	9	43	348	79
KOW11	6/6	431	5	186	40	8	71	305	28
<b>Holy Cross Mountains, Component C</b>									
KOW4&5	5/11	213	-32	192	-23	11	62	305	39
KOW6	4/6	229	-35	205	-32	15	45	310	35
KOW7	5/6	317	-42	217	-39	14	31	000	00
KOW9	6/6	215	-41	215	-4	12	35	000	00
KOW11&12	4/11	220	-34	201	-32	11	97	305	28
KOW10	5/6	214	-43	203	22	9	76	348	79

**Table B.1** Palaeomagnetic data for component B from the Barrandian and the Holy Cross Mountains. \* previously studied by TAIT et al. (1994b); Lat and Long, Latitude and Longitude of the site location; n, number of specimens; N, number of samples yielding palaeomagnetic results; Geogr., geographic coordinates; Strat., stratigraphic coordinates; Dec and Inc, declination and inclination;  $\alpha_{95}$ , radius of the cone of 95% confidence; k, FISHER'S (1953) precision parameter; DD and D, dip direction and dip of bedding; <sup>b</sup> overturned fold limb. There is no within site variation of bedding attitude and therefore  $\alpha_{95}$  and k are identical for site mean directions in geographical and stratigraphic coordinates.

*Rhenish Massif*

Nr.	Site	n/N/N <sub>o</sub>	Geogr.		Strat.				Bedding		Fold axis	
			Dec [°]	Inc [°]	Dec [°]	Inc [°]	$\alpha_{95}$ [°]	k	DD [°]	D [°]	PD [°]	P [°]
<b>Component B</b>												
<i>Remscheid anticline (RA)</i>												
1	HEN	8/8/8	180	-36	179	9	7	59	353	45	76	4
2	LET2	3/3/7	213	-23	211	16	13	95	333	50	265	3
3	LET3	3/3/5	211	23	215	-16	11	122	178	46	265	3
4	STU	6/6/6	175	-20	175	5	9	69	348	26	76	4
5	GRU	13/13/14	170	-35	168	4	6	56	340	40	76	4
6	AMB	7/7/8	170	-15	170	18	9	46	10	35	76	4
7	LAS1	5/5/7	178	-12	180	27	12	42	333	42	76	4
8	LAS2	7/7/7	168	-17	167	24	7	75	3	42	76	4
9	LAS3	5/4/6	163	-18	162	27	7	129	355	45	76	4
10	HAC	12/12/12	185	18	184	-14	2	594	164	34	67	3
<i>Lüdenscheid syncline (LS)</i>												
11	BRU1	8/8/9	193	14	188 <sup>a</sup>	-43	9	43	150	83	60	29
12	BRU2	10/10/13	190	16	172 <sup>a</sup>	-14	6	62	122	71	60	29
13	LOS1	6/6/6	187	25	171 <sup>a</sup>	-41	6	136	151	80	60	29
14	LOS2	4/4/8	185	15	175 <sup>a</sup>	-35	8	136	143	69	60	29
15	LOS3	7/7/7	188	15	172 <sup>a</sup>	-11	8	58	120	61	60	29
16	HAM	6/6/10	164	-8	164	15	11	35	325	24	242	3
17	ELV	7/7/11	174	-1	184	-48	10	41	155	51	242	3
18	NEU	6/6/11	196	5	187 <sup>a</sup>	-7	8	73	124	41	60	29
19	GAR	6/6/6	190	-6	188 <sup>a</sup>	-2	4	308	96	34	60	29
20	SOR	13/13/14	189	12	189	-16	7	48	155	35	67	3
21	MET	12/11/13	187	7	194	-32	9	61	155	48	67	3
22	OLP1	5/5/6	170	-2	177	62	9	87	343	65	67	3
23	OLP2	7/7/11	176	-15	184	59	8	62	346	75	67	3
<i>Attendorn and Wittgenstein synclines (AS/WS)</i>												
24	PLE	11/11/14	174	4	173 <sup>a</sup>	-25	4	119	118	58	75	14
25	ALB1	8/8/8	168	-11	174 <sup>a</sup>	-33	8	50	130	29	75	14
26	ALB3	8/8/10	175	2	173 <sup>a</sup>	-27	7	68	156	30	75	14
27	ATT1	8/8/8	174	-16	184 <sup>a</sup>	50	7	59	354	65	75	14
28	AFI2	7/7/7	188	-3	197 <sup>a</sup>	-41	8	58	151	51 <sup>b</sup>	75	14
32	STC	4/4/6	178	6	187 <sup>a</sup>	-41	8	131	140	64	75	14
33	BOH1	6/6/13	177	-1	198 <sup>a</sup>	-68	10	49	159	77	69	22
34	BOH2	6/6/8	191	11	261 <sup>a</sup>	58	15	22	338	75	69	22
25	DOT1	5/5/7	179	7	253 <sup>a</sup>	77	14	64	347	78	69	22
36	DOT2	7/7/10	186	12	178 <sup>a</sup>	-6	10	42	123	38	69	22
37	LAU	6/6/8	176	-6	189 <sup>a</sup>	-55	9	56	148	61	69	22
<b>Component C</b>												
<i>Lüdenscheid Syncline (LS)</i>												
19	GAR	6/6/6	216	-41	228 <sup>a</sup>	-20	12	40	96	34	60	29
<i>Attendorn syncline (AS)</i>												
27	ATT1	6/6/8	192	-38	198 <sup>a</sup>	25	11	54	354	65	75	14
29	AFI7	4/4/7	216	-46	231 <sup>a</sup>	-16	6	254	105	49 <sup>b</sup>	52	35
30	ATT2	9/9/10	201	-48	221 <sup>a</sup>	-24	6	86	151	51 <sup>b</sup>	75	14
31	ATT4	9/9/10	183	-50	243 <sup>a</sup>	69	7	57	153	47 <sup>b</sup>	75	14

**Table B.2** Palaeomagnetic data for components B and C. Nr, Site number in Fig. 4.4; Lat and Long, Latitude and Longitude of the site location; n, number of specimens measured; N, number of samples yielding palaeomagnetic results; N<sub>o</sub>, total number of samples obtained in the field; Geogr., geographic coordinates; Strat., stratigraphic coordinates; Dec and Inc, declination and inclination;  $\alpha_{95}$ , radius of the cone of 95% confidence; k, FISHER'S (1953) precision parameter; DD and D, dip direction and dip of bedding; PD and P, plunge direction and plunge of fold axis. There is no within site variation of bedding attitude and therefore  $\alpha_{95}$  and k are identical for site mean directions in geographical and stratigraphic coordinates. <sup>a</sup>plunge of fold axis is greater than 5° and uniplunging and untilting was performed simultaneously, <sup>b</sup>overturned fold limb.

# Appendix C

## Rock magnetic data

Sample	$M_s$ [ $10^{-6} \cdot Am^2/kg$ ]	$M_r$	$H_c$ [mT]	$H_{cr}$ [mT]	$M_{rs}/M_s$	$H_{cr}/H_c$	$S/M_r(10s)$ [ $s^{-1}$ ]	$\Delta J_{Verwey}$
<i>Reef carbonates</i>								
GRU1	193	55	8.00	38.5	0.288	4.81	0.027	0.117
STC1-1	83.0	12.4	3.56	74.3	0.149	20.9	0.032	0.155
STC1-2	–	–	–	–	–	–	0.030	0.155
WES1-4	9.24	3.84	16.8	64.4	0.416	3.83	0.025	0.156
<i>Detrital carbonates</i>								
HAC2-2	607	46.5	4.00	37.6	0.077	9.40	–	0.138
HAC2-3	554	37.0	3.17	37.9	0.067	12.0	–	0.138
HEN1-2	237	6.98	1.98	53.5	0.030	27.0	0.032	0.334
LET2-5	236	11.3	1.86	37.1	0.048	19.9	0.054	0.207
STU1-1	229	7.16	1.67	38.5	0.031	23.1	0.026	0.193
<i>Clastic rocks</i>								
ALB1-5	826	17.9	5.26	70.3	0.022	13.4	–	–
ALB1GM	622	37.5	5.95	56.5	0.060	9.50	–	–
ALB3-9	739	29.6	6.94	48.6	0.040	7.00	0.012	0.514
AMB1-5*	326	18.6	9.58	120	0.057	12.5	0.015	–
ATT1-1	–	–	–	–	–	–	0.025	0.149
<i>ATT4-5</i>	743	20.9	5.59	64.7	0.028	11.6	0.017	0.368
BOH1-14	237	8.96	6.58	141	0.038	21.4	0.007	0.417
BOH1-3	357	6.12	5.00	123	0.017	24.6	0.008	0.417
BRU1-6	699	26.4	6.11	50.6	0.038	8.28	0.020	0.244
BRU2-10	770	47.2	10.7	62.4	0.061	5.83	0.023	0.244
DOT2-7	386	13.3	8.53	109	0.035	12.8	0.006	–
<i>EDE3-3</i>	978	30.0	2.24	34.5	0.031	15.4	0.017	–
ELV1-9	662	21.1	5.40	61.1	0.032	11.3	0.008	0.215
<i>FIN1-1</i>	819	32.4	5.03	58.7	0.040	11.7	0.027	0.619
<i>FIN1-8</i>	983	14.2	3.07	47.0	0.014	15.3	–	0.619
HAM1-2*	538	19.0	5.83	68.9	0.035	11.8	0.015	0.238
LAS1-1	1125	54.2	7.85	52.5	0.048	6.69	–	0.366
LAU1-11*	344	7.08	6.98	150	0.021	21.5	0.031	–
LOS2-2	594	40.1	10.7	68.5	0.068	6.40	0.020	0.166
LOS3-4	800	121.9	15.0	85.1	0.152	5.67	0.018	–
MET1-5	350	17.1	6.61	56.5	0.049	8.55	0.011	–
NEU1-4	388	37.2	12.7	56.2	0.096	4.43	0.010	0.380
OLP2-10	436	21.2	6.64	48.1	0.049	7.24	0.011	0.382
PLE1-11	–	–	–	–	–	–	0.006	–
PLE1-8	–	–	–	–	–	–	–	0.045
PLE1-4	–	–	–	–	–	–	0.009	0.285
SOR3-7	370	19.4	8.89	63.8	0.052	7.18	0.028	–

**Table C.1** Rock magnetic results from the Rhenish Massif. \* not saturated at 1 T and not used for Fig. 6.4; samples from sites, where only component C was identified are shown in italic letters.

# Appendix D

## X-ray diffraction data

Sample	FWHM [mm]					
	air dried			glycolated		
	0 – 0.2 $\mu\text{m}$	0.2 – 2 $\mu\text{m}$	< 2 $\mu\text{m}$	0 – 0.2 $\mu\text{m}$	0.2 – 2 $\mu\text{m}$	< 2 $\mu\text{m}$
<i>Rhenish Massif</i>						
LETb	9.0	8.5		9.0	8.0	
LET	9.0	8.0		9.0	8.0	
HACb	5.5	5.0		5.5	5.0	
HAC	8.0	8.0		9.0	9.0	
LER	10.0	7.0	5.5	9.0	6.5	5.0
UTH	8.0	7.0	6.0	9.0	6.6	5.5
OLP	7.0	4.5	5.5	6.0	4.5	5.0
BRU	6.0	4.0	4.5	5.5	3.5	4.0
NEU	4.5	3.0	4.0	4.5	3.0	4.0
HAM	5.0	4.0	4.0	5.0	4.0	3.5
STC	5.5	4.0	4.5	6.0	4.5	4.5
ALB3	5.0	4.0	3.5	5.0	3.5	3.5
ALB1b	4.5	3.5		4.0	3.0	
ALB1	4.5	3.5		5.0	3.5	
ATT1b	4.0	3.0		4.5	2.5	
ATT1	4.5	3.0		4.5	3.5	
BOH	7.5	7.5		8.0	8.0	
<i>Barrandian</i>						
KOBAA	9.0	3.0	7.5	10.0	3.5	6.0
MRAA	11.5	6.0	9.0	8.5	3.5	7.0
KLOAB	12.0	5.0		11.0	3.5	
LODB	13.0	7.5		11.5	9.0	
<i>Holy Cross Mountains</i>						
CZA3	8.5	4.5	8.0	6.0	4.0	5.5
CZA5	7.0	6.0		8.0	6.0	
KOW1	16.0	4.5		10.0	5.0	
KOW9r	9.0	4.0	9.0	8.0	4.5	6.0
KOW9g	10.0	7.0	9.0	10.0	5.0	6.0
KOW12	13.0	4.5		13.0	4.5	
MOJ	10.5	9.0	9.0	10.0	11.0	8.0

**Table D.1** Illite crystallinity indices of the < 0.2 $\mu\text{m}$  fractions measured as full width at half maximum (FWHM) in mm of the 10 Å peak. 1 mm equals 0.1° 2 $\Theta$  Cu K $\alpha$ .

Sample	Position and intensity of major XRD peaks for < 0.2 $\mu$ m illite fraction										Mineralogy					
	$\text{\AA}$ [mm]	$\text{\AA}$ [mm]	$\text{\AA}$ [mm]	$\text{\AA}$ [mm]	$\text{\AA}$ [mm]	$\text{\AA}$ [mm]	$\text{\AA}$ [mm]	$\text{\AA}$ [mm]	$\text{\AA}$ [mm]	$\text{\AA}$ [mm]	ill	ill/sme	chl	kao	qz	alb
	<b>Rhenish Massif</b>															
LEtb	3.32 51	3.55 30	4.94 20	7.20 47	10.10 73	14.50 10	xx	x	(x)	x	(x)	x	(x)			
LET	3.35 20	3.57 27	4.16 20	7.20 35	10.10 59	14.25 24	xx	x	(x)	x	(x)	x	(x)			
HACb	3.32 39	4.24 15	5.00 20	10.10 69	10.20 120		xx	x								
HAC	3.35 45	3.48 20	5.08 25	10.50 88	10.10 128	14.25 32	xx	x	(x)	x	(x)					(x)
LER	3.31 29		5.10 35		10.00 80	14.50 24	xx									(x)
UTH	3.33 50		5.00 33		10.20 285	14.50 123	xx									(x)
OLP	3.32 28	3.51 25	4.70 15	7.20 55	10.10 128	14.25 32	xx									(x)
BRU	3.30 191	3.51 115	4.70 47	7.20 197	10.20 285	14.50 123	xx									(x)
NEU	3.31 31	3.52 23	4.68 12	7.10 64	10.00 82	14.40 35	xx									(x)
HAM	3.30 145	3.52 41	4.69 29	7.10 113	10.00 370	14.50 44	xx									(x)
STC	3.32 32		4.98 32		10.00 96	14.50 36	xx									(x)
ALB3	3.30 61	3.52 34	4.70 16	7.10 67	10.10 169	14.50 36	xx									(x)
ALB1b	3.30 28	3.50 13	4.70 9	7.10 35	10.00 96	14.25 29	xx									(x)
ALB1	3.32 78	3.55 35	4.65 14	7.20 78	10.10 206	14.25 53	xx									(x)
ATT1b	3.30 23	3.52 16	4.70 12	7.10 38	10.00 62	14.30 27	xx									(x)
ATT1	3.42 54	3.55 40	5.00 38	7.20 73	10.10 126	14.50 58	xx									(x)
BOH	3.29 63		5.10 43		10.40 167		xx									(x)
	<b>Barrandian</b>															
KOBAA	3.30 10	3.50 14	5.00 14	7.20 15	10.00 26	14.25 16	xx									(x)
MRAA	3.28 41		4.98 28	7.20 13	10.10 124	14.25 25	xx									(x)
KLOAB	3.35 27		5.00 32	7.20 21	10.10 67	15.00 74	xx									(x)
LODB	3.32 47		5.05 50		10.10 150		xx									(x)
	<b>Holy Cross Mountains</b>															
CZA3	3.28 20	3.98 14	5.00 17		10.10 62		xx									(x)
CZA5	3.31 33		4.98 32	7.20 19	10.10 106	14.25 34	xx									(x)
KOW1	3.33 55		5.05 55	7.20 22	10.10 163		xx									(x)
KOW9r	3.30 40		5.00 30	7.20 10	10.10 138		xx									(x)
KOW9g	3.28 38		4.49 30	7.20 11	10.10 97	14.75 20	xx									(x)
KOW12	3.32 38		5.00 29		10.10 115		xx									(x)
MOJ	3.31 105	3.54 53	4.18 20	7.20 104	10.10 257		xx									(x)

**Table D.2** XRD peaks and resulting mineralogy for < 0.2 $\mu$ m fractions. Minor peaks are not plotted (e.g. Feldspar,  $\sim$  3.2 $\text{\AA}$ ) Mineral content: ill = Illite, ill/sme = illite/smectite interstratification, chl = chlorite, kao = Kaolinite, qz = Quartz, alb = albite. xx = large amounts, x = abundant, (x) = very small amounts.

# Appendix E

## Geochemical and isotopic data of untreated $< 0.2\mu\text{m}$ clay fractions

Sample	Al <sub>2</sub> O <sub>3</sub> [wt %]	MgO [wt %]	CaO [wt %]	Fe <sub>2</sub> O <sub>3</sub> [wt %]	MnO [wt %]	TiO <sub>2</sub> [wt %]	Na <sub>2</sub> O [wt %]	K <sub>2</sub> O [wt %]	P <sub>2</sub> O <sub>5</sub> [wt %]
<i>Rhenish Massif</i>									
LETb	26.32	1.77	0.23	3.88	0.011	0.50	0.10	4.05	0.05
LET	23.49	1.64	1.31	3.73	0.015	0.48	0.09	3.20	0.83
HACb	22.27	1.66	0.20	3.54	0.004	0.28	0.19	3.72	0.06
HAC	22.49	1.75	0.44	2.63	0.003	0.27	0.17	3.70	0.49
LER	22.89	3.03	0.56	3.44	0.008	0.41	0.09	4.07	0.03
UTH	23.30	2.76	0.57	4.96	0.057	0.33	0.06	5.74	0.11
OLP	27.40	2.20	0.24	7.32	0.027	0.40	0.72	4.70	0.06
BRU	25.49	3.09	0.37	11.21	0.039	0.33	0.37	5.66	0.08
NEU	25.63	3.22	0.39	10.30	0.039	0.47	0.42	5.37	0.12
HAM	32.44	2.01	0.25	6.08	0.035	0.44	0.50	6.54	0.06
STC	29.64	0.97	0.44	5.54	0.069	0.30	0.66	4.82	bdl
ALB3	28.09	2.84	0.32	6.78	0.036	0.45	0.51	5.71	0.06
ALB1b	30.57	3.54	0.13	9.29	0.043	0.44	0.30	6.11	0.11
ALB1	27.63	3.18	0.33	8.21	0.028	0.44	0.29	5.86	0.11
ATT1b	25.30	4.27	0.24	10.85	0.044	0.41	0.31	5.63	0.08
ATT1	24.72	3.79	0.28	11.30	0.032	0.37	0.30	5.23	0.08
BOH	30.09	3.00	0.31	1.71	0.006	0.13	0.04	7.63	bdl
<i>Barrandian</i>									
KOBAA	23.75	2.56	0.66	20.62	0.113	0.83	0.11	4.04	0.17
MRAA	24.62	2.71	0.76	11.38	0.017	0.66	0.10	5.29	0.10
LODB	23.99	2.49	0.67	12.91	0.020	0.62	0.10	5.01	0.14
KLOBA	21.17	3.47	0.80	4.40	0.009	1.50	0.11	3.40	0.17
<i>Holy Cross Mountains</i>									
KOW1	23.41	3.00	0.68	3.82	0.009	0.70	0.10	5.18	0.03
KOW9r	24.52	2.58	0.44	8.16	0.011	0.80	0.08	5.98	0.02
KOW9g	25.02	2.75	0.41	4.32	0.012	0.74	0.09	6.11	0.04
KOW12r	23.07	3.32	0.70	5.95	0.015	0.71	0.10	5.66	0.23
CZA3	21.16	2.71	0.96	2.73	0.009	0.36	0.05	4.68	bdl
CZA5	24.23	3.75	0.55	5.50	0.014	0.59	0.09	5.91	0.09
MOJ	23.69	1.65	4.90	8.19	0.033	0.54	0.07	4.90	3.42

**Table E.1** Major element data (wt%) of  $< 0.2\mu\text{m}$  clay fractions. Analyses were made with ICP-AES. bdl = below detection limit.

Sample	K2O %	40Ar* %	40Ar* cc/g STP $\times 10^{-6}$	40K mol/g $\times 10^{-8}$	40Ar* mol/g $\times 10^{-9}$	36Ar mol/g $\times 10^{-12}$	Age Ma $\pm 2\sigma$	40Ar/36Ar	$^{40}\text{K}/^{36}\text{Ar} \times 10^3$	$^{40}\text{K}/^{36}\text{Ar} \times 10^3$	
<b>Rhenish Massif</b>											
LETa < 2 $\mu$ m	1.71	56.4	21.3	4.25	0.95	2.49	$\pm 13$	677.0	$\pm 3$	16.98	$\pm 0.214$
LETb	4.08	27.6	43.4	10.1	1.94	17.24	$\pm 22$	407.9	$\pm 2$	5.85	$\pm 0.02$
LET	3.63	49.4	37.3	9.02	1.66	5.76	$\pm 12$	584.0	$\pm 6$	15.53	$\pm 0.197$
HACa < 2 $\mu$ m	2.37	31.9	27.4	5.89	1.22	8.85	$\pm 21$	483.6	$\pm 1$	6.62	$\pm 0.054$
HACb	3.76	40.9	45.3	9.34	2.02	9.90	$\pm 17$	500.0	$\pm 1$	9.36	$\pm 0.044$
HAC	4.13	53.6	46.0	10.3	2.05	6.01	$\pm 12$	637.0	$\pm 2$	16.92	$\pm 0.063$
LER	4.56	82.0	53.6	11.3	2.39	1.78	$\pm 8.7$	1642	$\pm 4$	62.77	$\pm 0.228$
UTH	6.22	96.2	67.5	15.5	3.01	0.40	$\pm 6.8$	7827	$\pm 27$	366.0	$\pm 1.965$
OLP	4.60	91.9	50.9	11.4	2.27	0.68	$\pm 7.4$	3640	$\pm 23$	163.6	$\pm 1.599$
BRU	5.68	93.8	67.4	14.1	3.01	0.68	$\pm 7.6$	4747	$\pm 26$	201.8	$\pm 1.714$
NEU	5.24	94.9	61.8	13.0	2.75	0.50	$\pm 7.6$	5822	$\pm 50$	250.4	$\pm 3.618$
HAM	6.61	96.9	85.0	16.4	3.79	0.42	$\pm 7.8$	9382	$\pm 24$	369.1	$\pm 1.536$
STC	5.00	87.2	56.4	12.4	2.52	1.25	$\pm 7.8$	2315	$\pm 14$	97.69	$\pm 1.126$
ALB3	6.03	95.0	71.2	15.0	3.18	0.56	$\pm 7.5$	5920	$\pm 114$	254.1	$\pm 6.809$
ALB1a < 2 $\mu$ m	5.46	93.1	76.1	13.6	3.40	0.85	$\pm 8.9$	4285	$\pm 82$	158.5	$\pm 4.338$
ALB1b	6.32	96.3	80.2	15.7	3.58	0.46	$\pm 7.8$	8026	$\pm 43$	337.2	$\pm 3.716$
ALB1	6.70	92.0	81.4	16.6	3.63	1.07	$\pm 7.8$	3691	$\pm 14$	151.3	$\pm 0.804$
ATT1a < 2 $\mu$ m	5.07	92.8	66.9	12.6	2.98	0.78	$\pm 8.6$	4106	$\pm 13$	160.1	$\pm 0.872$
ATT1b	5.50	84.6	67.5	13.7	3.01	1.86	$\pm 8.6$	1916	$\pm 5$	73.17	$\pm 0.29$
ATT1	6.03	92.9	70.5	15.0	3.15	0.82	$\pm 7.5$	4148	$\pm 64$	177.8	$\pm 3.787$
BOH	8.48	98.7	94.2	21.1	4.20	0.19	$\pm 6.6$	17008	$\pm 48$	836.6	$\pm 3.642$
<b>Barrandian</b>											
KOBAA	4.78	95.7	67.1	11.9	3.00	0.46	$\pm 8.9$	6866	$\pm 35$	248.2	$\pm 2.187$
MRAA	6.25	95.6	82.1	15.5	3.66	0.57	$\pm 8.1$	6734	$\pm 77$	260.3	$\pm 4.451$
LODB	5.99	96.2	78.7	14.9	3.51	0.47	$\pm 8.1$	7816	$\pm 33$	302.1	$\pm 2.062$
KLOBAB	3.75	62.5	47.6	9.32	2.12	4.32	$\pm 12$	788.0	$\pm 2$	21.37	$\pm 0.078$
<b>Holy Cross Mountains</b>											
KOW1	5.88	74.1	65.3	14.6	2.91	3.44	$\pm 8.8$	1142	$\pm 3$	41.98	$\pm 0.147$
KOW12r	6.33	87.9	64.7	15.7	2.89	1.35	$\pm 7.0$	2432	$\pm 12$	114.0	$\pm 0.728$
KOW9r	6.71	93.4	70.3	16.7	3.14	0.75	$\pm 6.7$	4472	$\pm 17$	214.8	$\pm 0.894$
KOW9g	6.72	91.3	74.6	16.7	3.33	1.07	$\pm 7.2$	3400	$\pm 12$	151.6	$\pm 0.623$
CZA3	5.57	71.8	59.8	13.8	2.67	3.55	$\pm 8.9$	1047	$\pm 2$	38.57	$\pm 0.089$
CZA5	6.51	91.3	74.8	16.2	3.34	1.08	$\pm 7.5$	3376	$\pm 14$	145.4	$\pm 0.792$
MOJ	5.42	97.1	64.0	13.5	2.85	0.29	$\pm 7.4$	10067	$\pm 15$	430.9	$\pm 0.95$

Table E.2 K-Ar data of clay fractions. If not stated differently, data is given for < 0.2 $\mu$ m fractions

Sample	Sc	V	Cr	Co	Ni	Cu	Zn	Rb	Sr	Y	Zr	Nb	Mo98	Cd	Sn	Sb	Cs	Ba	Pb	Th	U
<i>Rhenish Massif</i>																					
LETb	6.23*	297*	268*	8.01	244*	86.3*	590*	194	24.0*	24.9*	254*	nm	30.3	nm	96.4	5.79	19.5	283*	125	5.56	21.0
LET	4.79*	277*	341	7.76	167	115	687	188	73.9	45.1	306	176	29.8	0.30	29.7	6.24	21.2	270	274	10.2	21.2
HACb	15.2*	985*	404*	14.0	232*	141*	177*	186	106*	20.7*	157*	nm	33.1	nm	43.4	43.0	56.6	828*	131	11.9	23.4
HAC	13.6*	944*	502	13.7	144	90.6	188	214	125	50.9	196	46.5	33.6	0.31	16.0	63.5	83.8	1099	203	12.6	27.0
LER	10.2*	237*	182	6.06	81.1	87.1	138	229	58.5	16.9	105	45.1	23.1	0.32	11.5	3.82	69.9	194	48.2	8.04	2.35
UTH	6.48*	185*	277	4.68	76.3	88.3	589	194	42.3	25.8	354	482	19.5	0.67	10.7	9.95	41.8	146	98.3	6.72	12.2
OLP	31.8*	187*	146*	18.1	66*	111*	207*	200	75.7*	22.2*	177*	nm	1.04	nm	10.0	0.60	11.3	560*	118	8.36	3.71
BRU	27.5*	197*	254*	21.6	78*	41.5*	171*	268	36.3*	16.6*	135*	nm	0.28	nm	10.3	0.55	19.0	628*	103	12.0	2.12
NEU	15.5*	251*	377*	16.1	106*	29.0*	164*	263	48.4*	22.7*	189*	nm	0.30	nm	14.3	0.51	26.7	658*	41.5	15.3	2.50
HAM	28.6*	221*	235*	23.6	73.7*	27.6*	83*	309	69.1*	17.1*	161*	nm	0.28	nm	16.5	1.04	25.9	783*	34.4	12.9	2.84
STC	bd1*	166*	222*	10.2	bd1*	222*	471*	200	27.7*	16.6*	166*	nm	5.18	nm	27.9	0.80	29.3	637*	260	4.54	20.7
ALB3	21.4*	190*	195*	15.1	74.3*	bd1*	116*	293	60.4*	30.6*	102*	nm	0.43	nm	20.8	0.80	37.7	905*	74.3	12.1	2.39
ALB1b	26.8*	194*	263*	18.4	124*	89.5*	179*	306	34.8*	17.4*	159*	nm	0.99	nm	18.6	1.99	29.0	711*	79.5	15.8	2.60
ALB1	24.4*	202*	313	16.3	86.7	96.4	193	341	49.3	20.9	219	57.8	0.14	0.13	26.6	1.75	30.6	888	62.9	12.9	1.66
ATT1b	20.8*	203*	330*	23.5	182*	71.0*	167*	243	35.5*	16.7*	137*	nm	0.54	nm	5.18	1.58	32.2	609*	104	14.4	2.75
ATT1	21.2*	192*	363	20.8	123	38.9	136	265	30.5	21.0	159	18.1	bd1	0.09	216	1.82	32.4	721	193	13.8	2.39
BOH	bd1	bd1	10	1.03	4.60	6.32	39	467	43.2	36.1	355	460	0.13	0.13	111	0.61	47.0	943	45.8	28.4	7.59
<i>Barrandian</i>																					
KOBAA	13.8*	312*	213	54.9	335	45.3	274	237	166	34.8	196	50.8	17.0	0.18	4.62	7.82	22.9	356	272	16.6	0.45
MRAA	27.0*	212*	195	21.6	90.4	50.2	176	274	132	15.6	205	25.5	0.06	0.09	9.36	3.51	25.1	284	44.4	27.4	bd1
LODB	10.1*	159*	133	14.5	129	64.7	184	239	88.8	48.6	148	27.4	0.18	0.11	106	3.57	14.9	305	71.0	26.7	bd1
KLOBA	11.3*	1251*	437	9.52	122	58.5	183	131	71.8	34.1	264	104	4.62	0.68	13.5	4.81	11.9	289	73.3	5.45	4.51
<i>Holy Cross Mountains</i>																					
CZA3	14.1*	171*	212	15.7	106	181	498	241	25.5	26.5	198	62.7	7.37	0.30	20.2	3.48	15.9	144	206	9.46	14.0
CZA5	10.5*	150*	144	7.00	78.9	74.3	530	282	42.7	19.5	147	73.4	1.66	0.10	13.7	3.64	31.1	259	93.9	12.1	2.80
KOW1	9.33*	187*	148	6.77	60.5	28.4	116	261	66.3	36.4	165	115	2.04	0.31	14.1	8.45	33.7	196	26.8	10.6	3.78
KOW9r	15.7*	2880*	420	6.14	79.2	51.3	517	286	58.6	61.8	532	177	2.87	0.38	6.43	24.8	38.8	188	39.1	20.8	13.0
KOW9g	17.0*	1860*	407	5.49	86.0	304	421	293	75.1	30.0	306	120	0.87	0.18	12.8	10.1	36.9	209	84.9	20.4	13.0
KOW12r	9.76*	537*	155	7.21	65.2	29.7	120	281	71.6	38.0	174	120	1.84	0.26	15.2	9.20	35.7	202	29.9	12.1	4.31
MOJ	11.1*	312*	260	27.0	120	42.7	661	203	102	77.4	415	209	0.60	0.25	31.0	8.78	13.9	385	64.1	9.18	65.0

**Table E.3** Trace element data (ppm) of < 0.2µm clay fractions. Analyses were generally made with ICP-MS. \* = analysed with ICP-AES, bdl = below detection limit, nm = not measured.

Sample	La	Ce	Pr	Nd	Sm	Eu	Gd	Tb	Dy	Ho	Er	Tm	Yb	Lu
<i>Rhenish Massif</i>														
LETb	8.38	12.4	1.50	6.00	1.58	0.53	1.79	0.44	3.48	0.84	2.59	0.50	3.04	0.46
LET	23.1	49.6	7.47	34.3	7.60	1.73	6.12	0.99	5.87	1.21	3.15	0.51	2.88	0.45
HACb	28.4	42.9	4.73	15.9	2.31	0.61	2.05	0.43	3.18	0.80	2.65	0.53	3.28	0.50
HAC	40.3	84.2	9.83	40.2	8.18	1.82	6.88	1.21	7.33	1.55	4.01	0.66	3.68	0.51
LER	18.3	26.9	3.23	12.3	2.50	0.59	2.27	0.37	2.45	0.55	1.44	0.27	1.49	0.24
UTH	10.1	24.4	2.50	10.0	2.24	0.44	2.23	0.45	3.20	0.75	2.25	0.43	2.49	0.36
OLP	26.5	54.9	6.45	24.6	5.14	1.20	4.05	0.65	3.97	0.87	2.50	0.46	2.92	0.44
BRU	21.5	47.2	5.93	23.4	4.61	1.02	3.33	0.54	3.10	0.66	1.90	0.32	2.32	0.35
NEU	26.8	59.0	6.78	25.6	5.54	1.33	4.66	0.79	4.75	0.96	2.75	0.46	2.83	0.42
HAM	30.4	63.3	7.16	25.8	4.49	0.98	3.43	0.54	3.28	0.68	2.07	0.36	2.54	0.40
STC	12.9	27.0	2.84	10.6	2.28	0.53	2.12	0.27	2.36	0.44	1.52	0.21	1.82	0.20
ALB3	21.4	47.6	6.35	26.9	6.66	1.30	5.21	0.98	5.91	1.15	3.08	0.51	2.90	0.38
ALB1b	15.0	29.9	3.39	13.4	2.81	0.70	2.53	0.49	3.25	0.72	2.17	0.40	2.56	0.40
ALB1	16.9	37.7	3.97	15.1	3.59	0.87	3.01	0.58	3.65	0.78	2.20	0.43	2.61	0.40
ATT1b	16.0	34.2	4.03	15.9	3.06	0.72	2.64	0.47	3.17	0.67	1.96	0.35	2.28	0.33
ATT1	16.3	39.3	4.42	17.7	4.05	0.92	3.28	0.57	3.77	0.78	2.05	0.39	2.19	0.34
BOH	18.8	50.8	5.47	19.9	5.26	0.34	4.64	1.12	7.47	1.38	3.77	0.73	4.41	0.67
<i>Barrandian</i>														
KOBAA	59.3	169	11.9	43.7	7.89	1.65	6.65	0.95	5.38	1.08	2.68	0.42	2.36	0.35
MRAA	38.2	62.6	6.13	19.8	3.07	0.57	2.34	0.33	2.14	0.51	1.53	0.27	1.64	0.23
LODB	51.0	93.4	12.0	47.2	9.57	2.16	8.09	1.24	7.13	1.32	3.01	0.44	2.16	0.31
KLOBA	30.2	54.8	6.97	27.9	5.56	1.43	4.66	0.78	4.77	1.02	2.65	0.43	2.40	0.35
<i>Holy Cross Mountains</i>														
KOW1	39.7	73.8	9.24	38.1	8.07	1.80	6.85	1.00	5.80	1.11	2.68	0.43	2.19	0.31
KOW12r	41.1	76.4	9.76	39.6	8.63	1.87	6.97	1.10	6.16	1.22	3.00	0.47	2.54	0.39
KOW9r	41.9	61.5	8.41	32.8	7.51	1.65	6.35	1.23	8.30	1.79	5.12	0.94	5.30	0.76
KOW9g	38.7	54.4	6.69	23.5	4.82	1.02	3.91	0.68	4.54	0.97	2.77	0.50	3.02	0.47
CZA3	14.7	26.2	3.64	15.1	3.64	0.89	2.93	0.55	3.69	0.77	2.07	0.35	2.05	0.28
CZA5	27.5	45.9	5.36	19.6	3.87	0.78	3.12	0.52	3.10	0.66	1.84	0.32	1.86	0.28
MOJ	30.9	59.7	6.56	27.4	6.92	1.69	6.68	1.20	8.41	1.90	5.61	1.16	7.51	1.16

Table E.4 Rare earth element data (ppm) of < 0.2 μm clay fractions. Analyses were generally made with ICP-MS.

# Appendix F

## Geochemical data of leachates

Site	SiO <sub>2</sub> [wt %]	Al <sub>2</sub> O <sub>3</sub> [wt %]	MgO [wt %]	CaO [wt %]	Fe <sub>2</sub> O <sub>3</sub> [wt %]	MnO [ppm]	TiO <sub>2</sub> [ppm]	K <sub>2</sub> O [ppm]	P <sub>2</sub> O <sub>5</sub> [ppm]
<i>Rhenish Massif</i>									
LET	0.196	0.104	0.077	0.350	2.314	114	0.09	276	1112
HAC	0.252	0.261	0.016	0.133	1.477	10.8	15.5	858	2826
LER	0.376	0.339	0.175	0.487	1.385	11.7	13.8	769	215
UTH	0.152	0.294	0.057	0.457	3.339	539	43.5	361	885
OLP	0.228	0.754	0.099	0.131	0.647	48.4	1.54	1026	86.5
BRU	0.097	0.636	0.100	0.253	2.159	151	15.8	903	236
NEU	0.251	0.482	0.129	0.240	0.867	114	16.1	601	175
HAM	0.232	0.453	0.091	0.167	0.662	97.8	2.88	818	121
STC	0.157	0.286	0.042	0.162	4.609	609	198	283	811
ALB3	0.249	0.360	0.082	0.215	0.762	67.2	9.40	653	236
ALB1	0.323	0.435	0.063	0.263	1.835	67.7	3.58	617	1096
ATT1	0.205	0.253	0.070	0.232	3.564	91.0	97.3	519	714
BOH	0.174	0.490	0.138	0.241	0.061	12.3	5.74	1422	bdl
<i>Barrandian</i>									
KOBAA	0.397	0.520	0.069	0.490	12.382	807	1729	482	1013
MRAA	0.280	0.358	0.060	0.616	4.742	783	295	658	636
LODB	0.323	0.466	0.083	0.560	7.215	116	414	799	847
KLOBA	0.228	0.169	0.218	0.595	1.464	35.0	14.1	417	536
<i>Holy Cross Mountains</i>									
KOW1	0.443	0.231	0.040	0.742	1.089	41.1	11.2	736	189
KOW12r	0.293	0.289	0.048	0.467	1.298	31.2	1.47	549	430
KOW9r	0.269	0.186	0.066	0.619	1.284	17.5	10.5	608	82.3
KOW9g	0.254	0.256	0.027	0.349	3.434	11.7	109	608	190
CZA3	0.401	0.269	0.050	0.323	0.352	4.42	37.2	857	77.7
CZA5	0.231	0.160	0.149	0.397	1.514	35.7	21.6	527	296
MOJ	0.302	0.496	0.042	0.759	4.537	267	43.6	508	3967

**Table F.1** Major element data (in w% of untreated < 0.2 $\mu$ m clay fraction) of leachates. Analyses were made with ICP-AES. bdl = below detection limit.

Site	Sr [ppm]	Ba [ppm]	V [ppm]	Ni [ppm]	Cr [ppm]	Zn [ppm]	Co [ppb]	Rb [ppb]	Y [ppb]	Zr [ppb]	Mo 98 [ppb]	Sn [ppb]	Sb [ppb]	Cs [ppb]	Pb [ppb]	Th [ppb]	U [ppb]
<b>Rhenish Massif</b>																	
LET	12.7	47.6	bdl	52.0	6.28	111	534	24.2	593	807	1007	7.58	92.0	bdl	109	153	200
HAC	11.1	97.2	13.1	52.4	11.2	101	897	470	1596	1345	1670	bdl	1576	265	7124	362	326
LER	20.1	23.4	7.14	31.25	5.36	64.4	184	131.25	532	813	203	1.55	124	66.1	460	271	60.7
UTH	18.0	19.8	37.7	40.4	35.0	393	291	23.3	610	5033	503	61.9	502	bdl	600	269	161
OLP	10.5	59.5	6.72	15.4	6.72	48.8	428	131	163	1617	16.3	bdl	5.94	bdl	474	50.8	44.2
BRU	8.58	189	8.66	8.66	9.52	9.35	90.3	75.3	394	3090	bdl	7.62	bdl	9.52	1459	238	45.9
NEU	13.9	41.9	8.06	4.48	10.8	0.86	181	72.6	530	3713	198	9.73	22.6	26.0	585	161	27.8
HAM	7.99	41.5	6.32	6.32	6.32	bdl	400	74.9	184	2487	bdl	29.7	18.0	11.7	397	113	14.4
STC	4.16	24.0	18.7	12.5	10.7	237	222	78.5	291	1855	221	249	197	13.4	821	46.6	584
ALB3	20.1	69.1	4.47	6.26	7.16	4.66	436	33.1	972	788	bdl	41.2	13.1	bdl	467	125	53.7
ALB1	13.0	52.5	bdl	7.75	6.78	32.8	625	90.1	502	4883	23.8	41.7	42.9	15.5	467	217	55.2
ATT1	9.56	58.3	9.39	4.69	12.2	4.15	138	62.9	583	3808	25.1	2715	57.1	18.8	1187	490	104
BOH	20.0	266	bdl	5.23	bdl	bdl	176	307	136	2616	18.9	26.0	0.99	49.7	1353	165	101
<b>Barrandian</b>																	
KOBAA	9.57	29.5	150	25.1	26.9	57.3	805	174	928	2491	1260	33.4	567	19.9	1537	321	34.7
MIRAA	6.93	18.2	62.4	13.0	21.7	19.1	321	221	228	2355	61.4	bdl	73.1	15.6	273	660	13.0
LODB	11.4	46.1	42.6	40.0	23.9	36.5	493	332	1755	2085	153	2837	200	128	555	880	96.3
KLOBA	18.7	112	26.2	35.5	8.42	53.3	434	34.6	804	3359	199	25.3	121	bdl	478	133	104
<b>Holy Cross Mountains</b>																	
KOW1	6.30	103	9.03	12.6	7.23	213	128	77.7	356	917	296	26.8	61.7	9.94	542	78.5	38.8
KOW9r	5.56	12.7	164	13.6	56.1	84.5	31.4	228	937	3641	243	16.3	414	36.2	945	861	86.9
KOW9g	4.25	7.72	46.4	9.46	6.02	35.1	15.8	158	593	1525	101	38.0	98.2	37.8	1085	885	61.0
KOW12r	5.11	21.6	28.5	7.79	11.2	19.7	89.4	85.7	761	733	76.7	88.1	117	20.8	823	175	102
CZA3	4.80	12.8	8.63	38.0	17.3	99.2	670	114	917	2430	176	49.4	45.1	11.2	1318	533	528
CZA5	8.93	46.5	5.37	19.7	4.48	132	80.9	87.7	546	990	99.9	9.54	67.4	20.6	1107	396	41.2
MOJ	7.26	112	41.2	46.1	30.4	383	978	217	439	1869	23.8	34.3	166	19.6	705	67.4	428

**Table F.2** Trace element data of leachates (in ppm and ppb of untreated < 0.2 μm clay fraction). Sr, Ba, V, Ni, Cr and Zn were analysed with ICP-AES, all other elements were analysed with ICP-MS. bdl = below detection limit.

Site	La [ppb]	Ce [ppb]	Pr [ppb]	Nd [ppb]	Sm [ppb]	Eu [ppb]	Gd [ppb]	Tb [ppb]	Dy [ppb]	Ho [ppb]	Er [ppb]	Tm [ppb]	Yb [ppb]	Lu [ppb]
LET	366	712	127	592	132	31.4	153	17.9	96.9	14.3	43.9	bdl	18.8	bdl
HAC	1177	2010	871	1450	392	139	421	116	343	117	184	82.3	132	69.2
LER	259	546	113	515	127	28.6	138	16.1	93.8	16.1	39.3	bdl	25.0	bdl
UTH	385	1079	128	561	126	17.0	112	14.3	95.1	17.9	55.6	bdl	48.4	bdl
OLP	121	290	43.2	201	53.8	12.5	55.7	bdl	45.1	bdl	22.1	bdl	19.2	bdl
BRU	145	420	57.1	284	76.2	22.5	95.2	13.9	84.0	18.2	45.0	bdl	45.0	bdl
NEU	207	538	89.6	369	104	40.3	142	31.4	120	34.9	65.4	22.4	60.0	19.7
HAM	168	426	47.8	234	50.5	17.1	54.2	bdl	45.1	bdl	28.0	bdl	20.8	bdl
STC	136	350	41.0	174	34.8	bdl	55.3	bdl	38.4	8.92	20.5	bdl	13.4	bdl
ALB3	214	699	113	573	199	42.9	209	32.2	173	32.2	83.2	9.84	61.7	8.94
ALB1	152	414	66.9	363	144	25.2	135	21.3	127	22.3	56.2	9.69	55.2	9.69
ATT1	275	700	107	545	188	35.7	177	25.4	139	21.6	56.3	bdl	43.2	bdl
BOH	74.0	181	21.8	88.0	23.5	bdl	30.5	bdl	33.1	bdl	22.6	bdl	16.6	bdl
<b>Barrandian</b>														
KOBAA	589	2038	206	969	217	55.5	237	32.1	157	26.0	65.0	bdl	26.0	bdl
MRAA	283	415	59.0	238	43.4	9.54	50.3	bdl	35.6	bdl	21.7	bdl	11.3	bdl
LODB	853	1618	405	1473	449	172	450	141	319	128	167	88.6	114	84.3
KLOBA	530	1148	173	775	182	49.6	195	25.3	138	25.3	57.1	bdl	31.8	bdl
<b>Holy Cross Mountains</b>														
KOW1	153	332	43.4	165	37.9	10.8	52.4	bdl	325	9.03	17.2	bdl	12.6	bdl
KOW9r	655	1323	323	1548	356	86.0	358	43.4	198	30.8	71.5	bdl	32.6	bdl
KOW9g	369	709	170	795	204	44.7	190	24.9	122	19.8	49.9	bdl	310	bdl
KOW12r	386	812	149	704	170	42.4	184	25.1	135	22.5	58.8	bdl	30.3	bdl
CZA3	519	873	147	731	198	44.9	208	31.9	178	31.1	95.8	9.49	61.3	8.63
CZA5	274	585	132	590	146	35.8	172	20.6	94.9	18.8	35.8	bdl	16.1	bdl
MOJ	148	324	40.2	187	41.2	13.7	61.8	bdl	46.1	9.81	32.4	bdl	42.2	bdl

**Table F.3** Rare earth element data (in ppb of untreated < 0.2µm clay fraction) of leachates. Analyses were made with ICP-MS. bdl = below detection limit.

# Lebenslauf

## Persönliche Daten

Alexander Zwing, geboren am 27.06.1970 in München

## Schulbildung

1976 - 1980            Grundschule an der Dorfstraße, Taufkirchen bei München  
 1980 - 1990            Gymnasium Unterhaching  
 Juli 1990              Erwerb der allgemeinen Hochschulreife

## Studium

1991 - 1998            Studium der Geologie/Paläontologie an der Ludwig-Maximilians-Universität (LMU) München  
 Okt. 93 - Juni 94      Auslandstudium Geologie an der University of Edinburgh, UK  
 November 1998        Erwerb des Diploms in Geologie/Paläontologie  
 1999 - 2002            Promotionsstudiengang in Geophysik an der LMU München

## Berufstätigkeit

Aug. 90 - Sept. 91    Zivildienst beim Ramersdorfer Seniorentreffpunkt Rogatekirche, München  
 Mai 95 - Aug. 95      Praktikum bei der Firma Uranerz Exploration and Mining Ltd, Saskatoon, Canada  
 Dez. 98 - April 99    wissenschaftliche Hilfskraft and den Instituten für Geophysik und Geologie, LMU München  
 April 99 - Mai 03     wissenschaftlicher Angestellter am Institut für Geophysik, LMU München